NTNU
Norwegian University of
Science and Technology

The Properties of Calcined Anthracite

Katrine Holm

Chemical Engineering and Biotechnology

Submission date:	June 2017
Supervisor:	Merete Tangstad, IMA
Co-supervisor:	Paul Beukes, North-West University Lars Lindstad, Elkem Carbon

Norwegian University of Science and Technology
Department of Materials Science and Engineering

I hereby declare that that this work has been carried out independently and in compliance with the examination regulations of the Norwegian University of Science and Technology, NTNU.

Trondheim, June 2017
Katrine Holm

Preface

This work is a part of the course *TMT4900 Materials Chemistry and Energy Technology, Master's Thesis* at the Norwegian University of Science and Technology (NTNU). This report describes an investigation of the properties of anthracite, coke and charcoal for the metal production industry, with a special interest of thermal behaviour.

This work has been a collaboration between NTNU, the North-West University (NWU) of Potchefstroom, South Africa and Elkem Carbon AS. The heat treatment and some characterization of the anthracite coal were carried out at Elkem Carbon Fiskaa and further investigated at the Department of Materials Science and Engineering at NTNU and at the School of Physical and Chemical Sciences at NWU.

I would like to thank Irene Bragstad at Sintef for performing the BET surface area and envelope density measurements. Ove Darell, also at Sintef, for his help with the dilatometer.

I am very grateful to Dr. Johan Jordaan at NWU for his help and guidance with the simultaneous thermal analysis instrumentation. To Yolindi Van Staden at NWU for her help with the thermomechanical instrumentation and guidance at the NWU campus. I would also like to thank all my office mates at NWU for their guidance, friendships and coffee breaks during my stay. Thank you for making me feel welcome in Potchefstroom.

I would like to thank my supervisor at NWU, Professor Paul Beukes, for all his help and guidance, for good discussions, and for his help with the multiple linear regression analysis. I would also like to thank my supervisor at Elkem Carbon AS, Dr. ing. Lars Lindstad, for his guidance and feedback during the last year.

Last but not least, I would like to thank my supervisor at NTNU, Professor Merete Tangstad, for the opportunity to work on this project, for the opportunity to spend time at NWU, for all her support and guidance during the last year and for good discussions along the way.

Trondheim, June 2017
Katrine Holm

Abstract

The aim of this thesis has been to look at the thermal behaviour of anthracite, coke and charcoal regarding their expansion during heating and their release of off-gases. Furthermore, to look at how the porosity and expansion of the anthracite is affected by the different temperatures during the calcining process. Two anthracites (A11 and A19), two cokes (C3 and C7) and one charcoal (BIO) were investigated.

The porosity and surface area of A11 calcined at different temperatures were investigated by porosity calculations from envelope and absolute density measurements, and from BET surface area measurements with N_2 gas adsorption. The porosity of A11 was found to decrease with increasing calcining temperature up to 1800 °C and increase between 1800 and 2650 °C. A significant difference in the surface area from 27.4 to $0.2\,\mathrm{m^2\,g^{-1}}$ was found between the materials calcined at 600 and 1100 °C, while an incremental increase was observed between 1100 and 2650 °C. The high surface area of the non-calcined A11 and A11 calcined at 600 °C can be explain the high porosity for these temperature samples.

Single grains of A11 calcined at 1100, 1800 and 2650 °C were heated to 1550 °C in a pushrod dilatometer in order to investigate the thermal expansion. The thermal expansion coefficient (TEC) was found to decrease with increasing calcining temperature. Both the material calcined at 1800 and 2650 °C had a TEC close to the TEC of graphite of about $3 \cdot 10^{-6}$ $°C^{-1}$, indicating graphitization. The material calcined at 1100 °C showed a higher TEC value of $15 \cdot 10^{-6}$ $°C^{-1}$.

The thermal expansion was also investigated with an Exstar SS6300 TMA, using pelletized material. Two heating cycles to 1400 °C were carried out. A shrinkage was found during the first heating above 600 °C due to volatiles leaving the carbon matrix. A linear relationship between the TEC from the first heating and the volatile content of the samples were found. The non-calcined A11 and A11 calcined at 600, 800 and 1000 °C revealed a trend where the shrinkage decrease with increasing calcining temperature. A linear relationship between the shrinkage and the volatile content was found in the temperature range where volatiles are driven off. Similar shrinkage was observed for the non-calcined A19, A19 calcined at 600 °C, C7 and BIO.

For the second heating all materials were found to contract the same amount dur-

ing cooling as they expand during heating. The expansion at 1400 °C was found to be between 0.6 and 0.9 % for all samples. For C3 and the anthracites calcined at 1200 °C or higher, no shrinkage occurred. The expansion was found to be similar for both temperature cycles, with only a small decrease in the average TEC values between the first and the second heating. The TEC values during the second heating were found to be very stable between 400 and 1100 °C. For all samples the TEC values were found to lay between 5 and 8 $\cdot 10^{-6}$ °C^{-1}, indicating graphitization. A high reproducibility was found for the thermal behaviour experiments carried out in the Exstar SS6300 TMA.

Mass loss and the derivative of mass during heating to 1500 °C was investigated for all samples by using an STA 449 F3 Jupiter and an Elite tube furnace. The STA was found to be more accurate and the results are reproducible. The mass loss of A11 and A19 during heating to 1500 °C comply with the mass losses during the calcining process. The derivative of mass curves showed the highest increase around 600-700 °C for all samples. The increase was found to be higher for A19 than for A11 samples due to the higher volatile content.

The off-gases during heating of all samples were investigated by connecting a Fourier transform infrared (FTIR) detector and a gas chromatography with mass spectrometry (GC-MS) to the STA. The FTIR spectra showed CO_2, CO and H_2O for all samples except C3, where only CO_2 and CO were detected. From the GC-MS analysis, only CO_2 was detected and these results correlates with the FTIR analysis. The amount of CO_2 was found to increase with increasing temperature for all samples, and the highest amount of CO_2 was found for BIO. CO appears around 700 °C and the amount was found to increase with increasing temperature. The FTIR spectra also indicated polycyclic aromatic hydrocarbons around 600-700 °C for the non-calcined anthracites, A19 calcined at 600 °C and BIO.

Finally, a multiple linear regression analysis was carried out to suggest correlations between different properties, how they affect each other and how they are affected by the thermal treatment. A root mean square error of zero was obtained for the total porosity of A11 with an optimum equation containing the hydrogen content, the ash content and the BET surface area. Similar results were obtained for the dimensional behaviour of the anthracites during the first heating to 1400 °C by including the sulfur, volatile and ash content in the equation.

Sammendrag

Målet med denne oppgaven har vært å se på termisk oppførsel av antrasitt, koks og trekull med hensyn til ekspansjon under oppvarming og utslipp av avgasser. Andre interesser var å se på hvordan porøsiteten og ekspansjonen av antrasitt påvirkes av de forskjellige temperaturene under kalsineringsprosessen. To antrasitter (A11 og A19), to koks (C3 og C7) og ett trekull (BIO) ble undersøkt.

Porøsiteten og overflaten av A11 kalsinert ved forskjellige temperaturer ble undersøkt ved porøsitetsberegninger fra konvolutt- og absolutt-tetthetsmålinger og fra BET-overflatearealmålinger med N_2 gassadsorpsjon. Det ble funnet at porøsiteten til A11 synker med økende kalsineringstemperatur opp til 1800 °C, og øker mellom 1800 og 2650 °C. En stor reduksjon av overflaten fra 27,4 til 0,2 $\mathrm{m^2\,g^{-1}}$ ble funnet mellom materialene kalsinert ved 600 og 1100 °C, etterfulgt av en liten, gradvis økning mellom 1100 og 2650 °C. Det høye overflatearealet for ukalsinert A11 og A11 kalsinert ved 600 °C kan forklare den høye porøsiteten for disse temperaturprøvene.

Enkeltkorn av A11 kalsinert ved 1100, 1800 og 2650 °C ble varmet til 1550 °C i et pushrod dilatometer for å undersøke termisk ekspansjon. Termisk ekspansjonskoeffisient ble funnet til å avta med økende kalsineringstemperatur. Både materialet kalsinert ved 1800 og 2650 °C hadde en TEC nær TEC av grafitt på ca. $3 \cdot 10^{-6}$ $°\mathrm{C}^{-1}$, som indikerer grafitisering. Materialet kalsinert ved 1100 °C viste en høyere TEC verdi på $15 \cdot 10^{-6}$ $°\mathrm{C}^{-1}$.

Termisk ekspansjon ble også undersøkt ved bruk av en Exstar SS6300 TMA, her ble pelletiserte materialer undersøkt. To oppvarminger til 1400 °C ble utført. Krymping ble observert under den første oppvarmingen over 600 °C på grunn av flyktige stoffer som forlater karbonmatrisen. Et lineært forhold mellom TEC fra den første oppvarming og det flyktige innholdet i prøvene ble funnet. Ukalsinert A11 og A11 kalsinert ved 600, 800 og 1000 °C viste en trend der krympingen avtar med økende kalsineringstemperatur. Et lineært forhold mellom krympingen og det flyktige innholdet ble funnet i temperaturområdet hvor flyktige stoffer drives av. Tilsvarende krymping ble funnet for ukalsinert A19, A19 kalsinert ved 600 °C, C7 og BIO.

For den andre oppvarming ble alle materialer funnet å trekke seg like mye sam-

men under avkjøling som de ekspanderer under oppvarming. Ekspansjonen ved 1400 °C ble funnet å være mellom 0,6 og 0,9 % for alle prøver. For C3 og antrasittene kalsinert ved 1200 °C eller høyere oppstod ingen krymping. Ekspansjonen viste seg å være lik for begge temperaturer, med bare en liten reduksjon i gjennomsnittlig TEC-verdi mellom første og andre oppvarming. TEC-verdiene under den andre oppvarmingen ble funnet å være svært stabile mellom 400 og 1100 °C. For alle prøver ble TEC-verdiene funnet å ligge mellom 5 og 8 $\cdot 10^{-6}$ $°C^{-1}$, som indikerer grafitisering. En høy reproduserbarhet ble funnet for eksperimentene utført i Exstar SS6300 TMA.

Termisk oppførsel som massetap og massetapsraten under oppvarming til 1500 °C ble undersøkt for alle prøver ved bruk av en STA 449 F3 Jupiter og en Elite tubeovn. STA ble funnet å være mer nøyaktig og resultatene er reproduserbare. Massetapet av A11 og A19 under oppvarming til 1500 °C samsvarer med massetapet under kalsineringsprosessen. Massetapsraten viste den høyeste økningen rundt 600-700 °C for alle prøver. Økningen ble funnet å være høyere for A19 enn for A11 prøver på grunn høyere innhold av flyktige komponenter.

Avgassene under oppvarming av alle prøver ble undersøkt ved å koble en Fourier transform infrarød (FTIR) detektor og en gaskromatografi med massespektrometri (GC-MS) til STA. FTIR-spektrene viste CO_2, CO og H_2O for alle prøver bortsett fra C3, hvor bare CO_2 og CO ble påvist. Fra GC-MS-analysen ble bare CO_2 oppdaget, og resultatene korrelerer med FTIR-analysen. Mengden CO_2 ble funnet å øke med økende temperatur for alle prøver. Den høyeste mengden av CO_2 ble funnet for BIO. CO vises først rundt 700 °C og mengden ble funnet å øke med økende temperatur. FTIR-spektrene indikerte også polysykliske aromatiske hydrokarboner rundt 600-700 °C for de ukalsinerte antrasittene, A19 kalsinert ved 600 °C og BIO.

En lineær regresjonsanalyse ble utført for å foreslå korrelasjoner mellom forskjellige egenskaper, hvordan de påvirker hverandre og hvordan de påvirkes av termisk behandling. Et root-mean-square avvik på null ble oppnådd for total porøsitet av A11 med en optimal ligning som inneholdt hydrogeninnholdet, askeinnholdet og BET-overflatearealet. Lignende resultater ble oppnådd for antrasittens dimensjonsadferd i løpet av den første oppvarmingen til 1400 °C ved å inkludere innholdet av svovel, flyktige komponenter og aske i ligningen.

Contents

Chapter 1

Introduction

1.1 Background

Carbon materials are widely used in the metal production industry today. Certain forms of carbon are chemically resistant, have high mechanical strength and can withstand high temperatures. Coal of bituminous rank is used to produce metallurgical coke, while the highest ranked coal, anthracite, is used used in the manufacturing of lining and electrode materials. Both the bituminous and anthracite coal have to undergo a thermal process in order to achieve the necessary properties for these applications.

The bituminous coal undergoes a coking process, where the coal is heated to about 1000-1100 °C to remove volatiles. For the anthracite used in electrodes and linings, a calcining process is conducted to temperatures ranging from about 1000 to 3000 °C in order to reduce impurities, increase the electrical conductivity and gain a more graphite-like structure.

The properties of the anthracite will be affected by the calcining temperature as the thermal treatment promotes thermal decomposition, phase transition, in particular graphitization, and removal of volatile components. In an electrical calcining furnace the temperature is inhomogeneous and there will be a temperature gradient across the furnace [1]. Thus, the anthracite grains will reach different temperatures depending on their position in the furnace, and hence achieve different properties.

When a new type of anthracite is implemented into production, there is a need to get an understanding of how this anthracite in particular is affected by the thermal treatment. Currently the anthracites are characterized as the average of the whole calcining furnace, but due to the temperature gradient across the furnace there will be a broad range of calcination degrees of the material. Because of this, it is of interest to develop a more accurate method in order to characterize individual grains and blends of carbon materials which have been heat treated to different temperatures.

During the period of June-July 2016, two types of anthracites were heat treated with different temperatures ranging from 600 to 2650 °C at Elkem Carbon Fiskaa. This was done in order to imitate the different positions in an industrial size calcining furnace. All anthracites should reach a temperature of at least 1200 °C in the calcining process, but heat treatment in the range of 600 to 1200 °C was done to see which properties the material would get if the flow comes out of control in the calcining furnace. Some analysis were carried out to characterize the calcined material.

These experiments along with the raw data from the analysis were a part of a summer project carried out at Elkem Carbon Fiskaa. The processing and the interpretation of the results were a part of TMT4500 Materials Technology, Specialization Project carried out at NTNU during the fall of 2016.

The specialization project also contained additional measurements of the calcined anthracite samples. The porosity was obtained from image analysis of optical micrographs and calculated from absolute and envelope density measurements. Surface areas were obtained by using the method of Brauner, Emmett and Teller (BET), and the linear thermal expansion of single grains were investigated by using a push-rod dilatometer.

An additional, related issue in the metallurgical industry is the release of polycyclic aromatic hydrocarbons (PAHs) into the environment. PAHs can be toxic and carcinogenic, hence unwanted in the environment. The PAHs first and foremost originates from the tar, but also from the coal during the thermal treatment. When electrodes, linings, etc. are produced, the carbon material is mixed with a binder of coal tar pitch.

1.2 Aim of Work

The aim of this thesis work is to continue the work of the specialization project and further investigate the calcined anthracites. Additional investigations of the porosity and the thermal expansion will be carried out, both for single grains and for pelletized material. Density measurements and surface area analysis will be used to investigate the porosity. For the expansion considerations, a pushrod dilatometer will be used for the single grains, while a thermomechanical analyzer will be used for the pelletized material.

Thermal behaviour of the carbon material is important due to the fact that a difference in expansion might lead to thermal stresses and a vulnerability of the electrode when baked for the first time. So in addition to the calcined anthracites, cokes and charcoal will also be considered in this work.

One objective of this work is also to consider the contribution that the carbon materials make to the PAH emissions during heating and re-heating of anthracites, cokes and charcoal. This will be done by evolved gas analysis.

Different experimental methods when considering the thermomechanical properties of the materials and the gas evolution during heating will be considered. Previously, these methods have not been used much for such materials, hence the methodology will be investigated.

The charcoal is included in this work to investigate the similarities and differences between the anthracite and cokes versus the charcoal. The use of charcoal is more environmental friendly, but the properties needs to be investigated further in order to consider the charcoal as a possible substitute for anthracite or coke in the metal production industry.

To summarize, the main objective of this work will be to investigate the thermal behaviour of anthracite, coke and charcoal regarding their expansion during heating and their release of off-gases. In addition, it will be of interest to look at how the porosity and expansion of the anthracite is affected by the different temperatures during the calcining process. A multiple linear regression analysis will be carried out in order to suggest correlations between different properties, how they affect each other and how they are affected by the thermal treatment.

Chapter 2

Theory

2.1 Carbon

2.1.1 The Properties and Structures of Carbon

Pure carbon exists in two crystalline forms in nature - graphite and diamond. In the diamond structure a carbon atom is bound to four other carbon atoms, in graphite this number of closest neighbours is three. The distance between each carbon atom in diamond is 1.54 Å, while the same distance in graphite is 1.42 Å. The distance between the layers, or the interlayar distance (d_{002}), in graphite is 3.35 Å [2]. This is demonstrated in Figure 2.1.

Within a layer in the graphite structure the carbon atoms are strongly bound together by covalent bonds, hence the smaller distance. The carbon-carbon bonding across the layers are weaker Van der Waals bonds, resulting in the greater distance. This distance makes it easier for electrons to move, making graphite a good electrical conductor parallel to the layers and an insulator across the layers. Hence, graphite is an anisotropic material. Diamond is a non-conductor of electricity, an insulator [3].

Carbon can also exist as non-crystalline or amorphous carbon in nature. This form of carbon occur as oil or coals. Oil is made from animal and plant remains, while coal is made from only plant remains. Accumulation of plants and/or animal

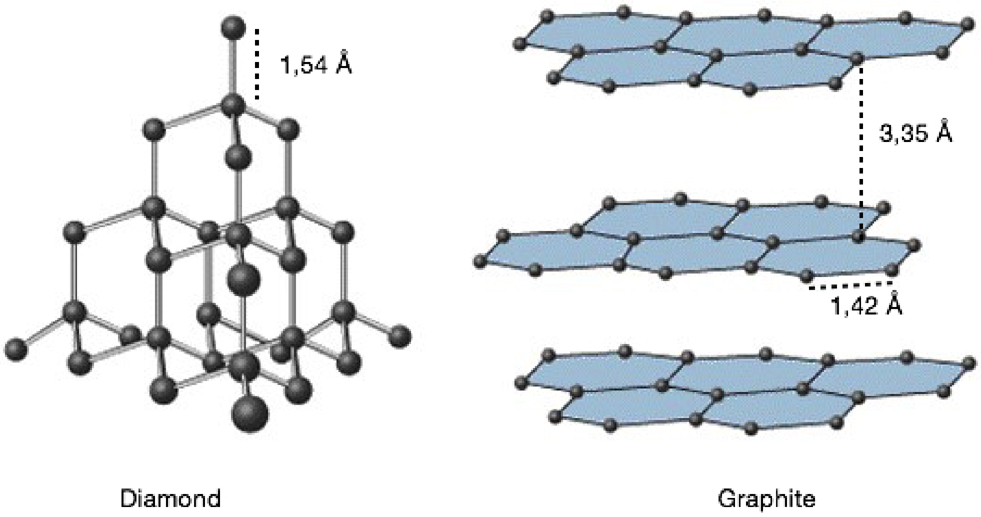

Figure 2.1: Diamond structure to the left with carbon-carbon distance equal to 1.54 Å. Graphite to the right with carbon-carbon distance within the layer equal to 1.42 Å and interlayar distance equal to 3.35 Å.

remains over time will lead to the formation of peat, the precursor material from which coals are derived. Peat contains less than 60 % of carbon [4].

During this coalification, volatiles are trapped within the coal-forming material. Inorganic matter will also be incorporated in the coal structure and is know as the mineral matter content or the ash content of the coal. High temperatures and high pressure will be obtained during the coalification.

Carbon atoms in coals are located in a three-dimensional network, bonding the carbon atoms in a highly complex structure compared to graphite. The lamellae in coals are randomly orientated and connected by cross-links. Voids and impurities such as the volatiles and inorganic material are placed within this structure [5].

2.1.2 Classification of Coals

According to The American Society for Testing and Materials [6] coals are divided into four main groups, or coal ranks:

- Lignitic coal
- Subbituminous coal
- Bituminous coal
- Anthracite coal

Where anthracite is defined as the highest ranked coal. The coal rank is a measure of the extent of coalification or metamorphism, and is determined by the content of moisture, volatile matter, ash and fixed carbon. During coalification, temperature mainly influences the development of coal rank, while geological pressure is a major factor in the development of physical properties such as structural anisotropy and porosity [7]. Table 2.1 shows the carbon content of the different ranked coals [8].

Table 2.1: Carbon content of the different coal ranks [8].

Rank	Carbon content [%]
Lingnite	60-70
Sub-bituminous	71-77
Bituminous	77-87
Anthracite	>87

The moisture content increases with decreasing rank, and typically ranges from 1 to 40 percent. It is determined by heating the coal to about 105-110 °C and calculating the weight loss. The volatile matter content can be measured by heating the coal to 950 °C for 7 minutes and determining the weight loss [9]. This content is typically below 12 percent for anthracitic coals.

By burning the coal at 800 °C for 12 hours and weighing the remaining residue, the mineral or ash content of the coal can be determined. This content is typically below 5 percent for anthracitic coals.

The amount of volatiles, ash and fixed carbon are usually given on a dry basis, where the amount of fixed carbon is the material left after subtracting the volatiles and the ash. The content of fixed carbon for anthracitic coals is typically around 90 percent on a dry basis.

Another way to predict the coal rank, is by measuring the Hardgrove Grindability Index (HGI) of the coal. The HGI is a unitless measure of the grindability, or the resistance to crushing, of the coal [10]. The lower the HGI, the harder and less grindable the coal is. HGI is measured by milling 50 g of coal in a calibrated grindability machine for 60 rounds. After milling the coal is sieved, and the HGI can be calculated from Equation 2.1.

$$H = 13 + 6.93 \cdot D \tag{2.1}$$

Where H is the Hardgrove Grindability Index and D is the fraction of coal passing through the sieve.

2.2 The Calcining Process

By heat treatment of e.g. anthracitic coal, the anthracite will gain a more graphite-like structure. This thermal treatment is used to reduce impurities, graphitize the carbon and physically stabilize the material [1]. This process is referred to as a calcining process and is often carried out by using an electrical calcining furnace. The anthracite which undergoes such a process is termed electrically calcined anthracite (ECA).

The most common way to calcine anthracite is to use a continuous shaft furnace with alternating current to heat the charge. A such furnace consists of a top and a bottom electrode, as illustrated in Figure 2.2.

The anthracite is fed at the top of the furnace and discharged at the bottom. The temperature within the furnace will vary from about 1000 °C at the furnace walls to 3000 °C in the centre. This will lead to an inhomogeneous thermal treatment of the anthracite. The furnace is considered a high-temperature chemical reactor where three critical transformations take place [1]:

- Carbonization
- Graphitization
- Densification

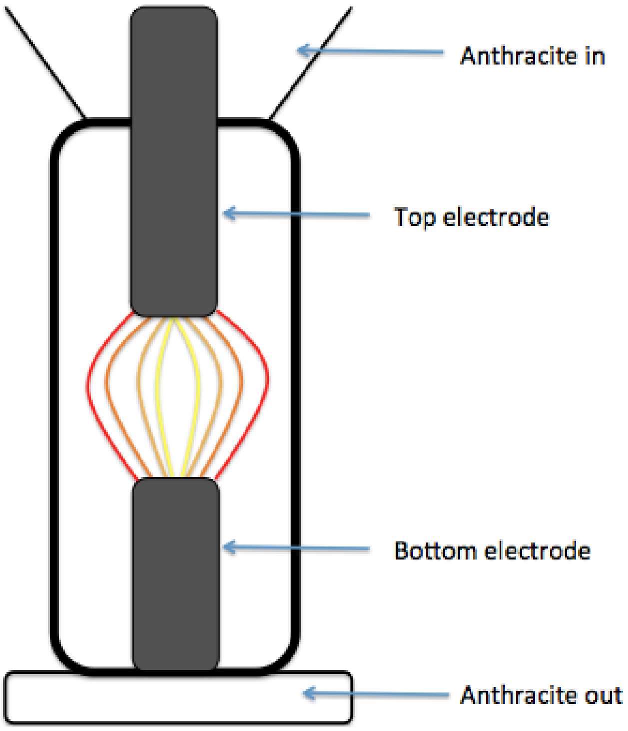

Figure 2.2: Scheme of an electrical calciner with top and bottom electrode. Anthracite is fed at the top of the furnace and discharged at the bottom.

Carbonization being the process where volatiles and ash are driven off, graphitization being a structural change where the anthracite structure is rearranged to a graphitic structure, and densification, which is a result of carbonization and graphitization. The material becomes more dense due to the the structural change and removal of ash components and volatile matter. The volatilization, ash vaporization and graphitization are all endothermic reactions.

2.2.1 Segregation

When anthracite grains are fed in at the top of the electrical calcining furnace, the bigger particles will segregate from the smaller particles. While the bigger particles will collect mainly closer to the wall, the smaller particles are found close to the center. This is illustrated in Figure 2.3. Big particles appear as yellow and small particles appear as red [11].

This segregation of anthracite grains in the calcining furnace will lead to a higher degree of calcination for the smaller particles due to the higher temperatures in the centre of the furnace. As the bigger particles are located closer to the furnace wall where the temperature is lower, they achieve a lower degree of calcination.

In order to achieve good packing of the carbon material when producing e.g. electrodes, a broad particle size distribution should be used. The difference in calcination between big and small particles might cause problems regarding the final properties of the produced electrode, where occasionally single grains will have higher electrical resistivity than the rest.

Figure 2.3: An example of segregation during filling due to particle size. The big particles are yellow, while the small particles are red [11].

2.2.2 Carbonization

Carbonization of coals involves the release of volatile organic components such as hydrogen, nitrogen and sulfur, and the vaporization and condensation of ash components [1].

The ash typically contains iron, aluminium and silicon among others. The Ellingham diagram in Figure 2.4 shows the Gibbs free energy of possible reactions of ash vaporization. This Ellingham diagram was constructed by using HSC Chemistry version 7. As can be seen from the diagram, the iron oxides are easiest to reduce, and hence will be reduced first. Calcium oxide is the hardest to reduce.

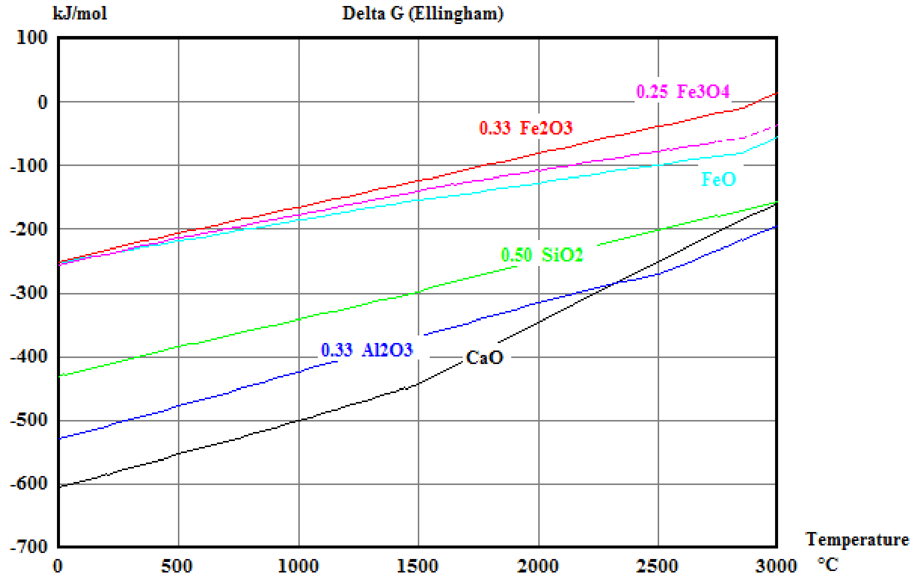

Figure 2.4: Ellingham Diagram constructed from HSC Chemistry. Gibbs free energy are given for the oxides of iron, silicon, aluminium and calcium.

In the hotter part of the furnace, the temperature will be sufficiently high for the metal to be vaporized. The metal vapour will be driven off to the cooler parts of the furnace where it will condense on the furnace wall and on the colder particles.

Possible vaporization and condensation reactions of the three oxides mainly found in anthracites are given in equation 2.2 - 2.9. The reactions are calculated by using HSC Chemistry 7.

- Iron (Fe):
  When in contact with carbon monoxide gas, iron(III)oxide will spontaneously be reduced to iron(II)oxide:

  $$\mathrm{Fe_2O_3(s) + CO\,(g) = 2\,FeO\,(s) + CO_2(g)} \qquad \Delta G^\circ < 0 \tag{2.2}$$

  The iron(II)oxide will be reduced to iron and vaporize through

  $$\mathrm{FeO\,(s) + C\,(s) = Fe\,(s) + CO\,(g)} \qquad \Delta G^\circ = 0 \text{ at } T = 750\,^\circ\mathrm{C} \tag{2.3}$$

  and

  $$\mathrm{FeO\,(s) + C\,(s) = Fe\,(g) + CO\,(g)} \qquad \Delta G^\circ = 0 \text{ at } T = 1678\,^\circ\mathrm{C} \tag{2.4}$$

  The Fe-gas will then be driven to the cooler zones of the furnace, where iron will condense at the furnace wall and at anthracite grains.

- Silicon (Si):
  The oxide vaporization of silica will occur around 1750 °C when silica is reduced to SiO-gas:

  $$\mathrm{SiO_2(s) = SiO_2(l)} \qquad T_{fus} = 1723\,^\circ\mathrm{C} \tag{2.5}$$

  $$\mathrm{SiO_2(s,l) + C\,(s) = SiO\,(g) + CO\,(g)} \qquad \Delta G^\circ = 0 \text{ at } T = 1743\,^\circ\mathrm{C} \tag{2.6}$$

  The SiO-gas will be driven to the cooler zones of the furnace, where it will condense at the furnace wall and at anthracite grains:

  $$\mathrm{2\,SiO\,(g) = SiO_2(s) + Si\,(s)} \tag{2.7}$$

- Aluminium (Al):
  The oxide vaporization of alumina will occur at around 2100 °C when alumina is reduced to Al_2O-gas:

  $$\mathrm{Al_2O_3(s) + 2\,C\,(s) = Al_2O\,(g) + 2\,CO\,(g)} \qquad \Delta G^\circ = 0 \text{ at } T = 2085\,^\circ\mathrm{C} \tag{2.8}$$

  The Al_2O-gas will be driven to the cooler zones of the furnace, where it will condense at the furnace wall and at colder anthracite grains:

  $$\mathrm{3\,Al_2O\,(g) = Al_2O_3(s) + 4\,Al\,(s)} \tag{2.9}$$

The vapour pressure of the various metals as a function of temperature is given in Figure 2.5, where the pressure is given on a logarithmic scale. The diagram is constructed by using HSC Chemistry 7.

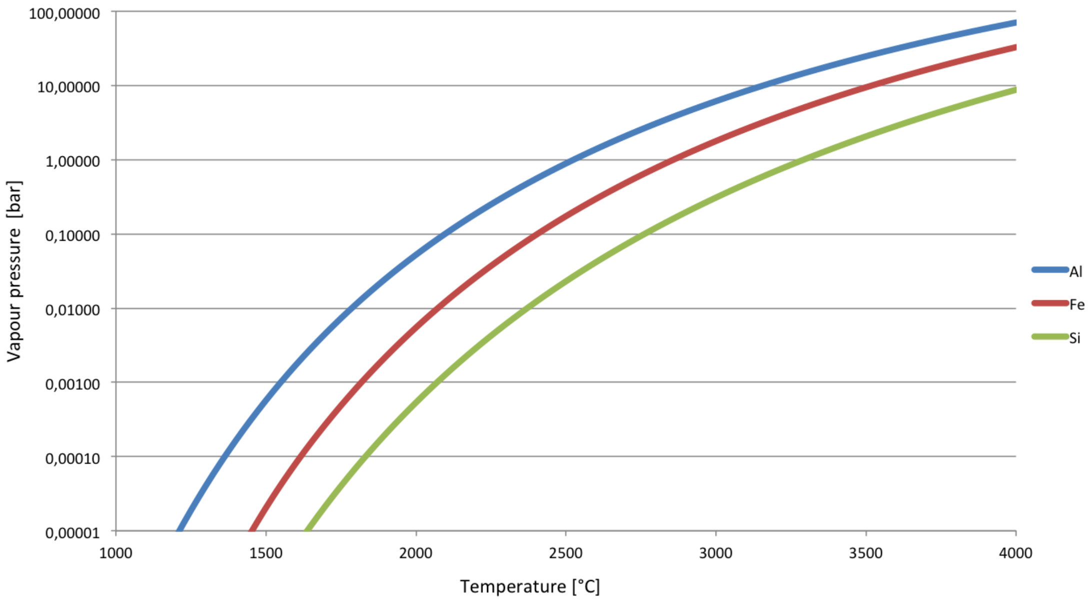

Figure 2.5: The vapour pressure of aluminium, iron and silicon as a function of temperature. The pressure is given on a logarithmic scale.

Oxygen, hydrogen, nitrogen and sulfur constitutes most of the volatiles, but some polycyclic aromatic hydrocarbons might also be found. Oxygen is found as oxides as previously mentioned, and humidity. Hydrogen and nitrogen are organically bound to the carbon matrix, whereas sulfur is bound both organically and inorganically to the carbon.

Hydrogen is mostly found as CH_4, water and other hydrocarbons at the surface of the anthracite particles, and is typically driven off around 800-1000 °C. Nitrogen and sulfur require higher temperatures in order to be removed due to the organic bonds to the matrix.

Sulfur is present in the coal in a number of both organic and inorganic forms. Inorganic forms include pyrite or marcasite (both FeS_2) and iron and calcium sulphate [7]. The desulfurzation leads to liberation of H_2S-gas.

2.2.3 Graphitization

Coals can undergo a graphitization process at elevated temperatures, were amorphous carbon is transformed to graphite-like carbon. The carbon will show a gradual change from the random layer structure to the ordered structure of crystalline graphite [7]. This is illustrated in Figure 2.6. This will increase the electrical conductivity of the coal and make it more suitable for use in the metal production industry. As the degree of graphitization increases, so does the elasticity of the material, and the electrical resistivity decreases.

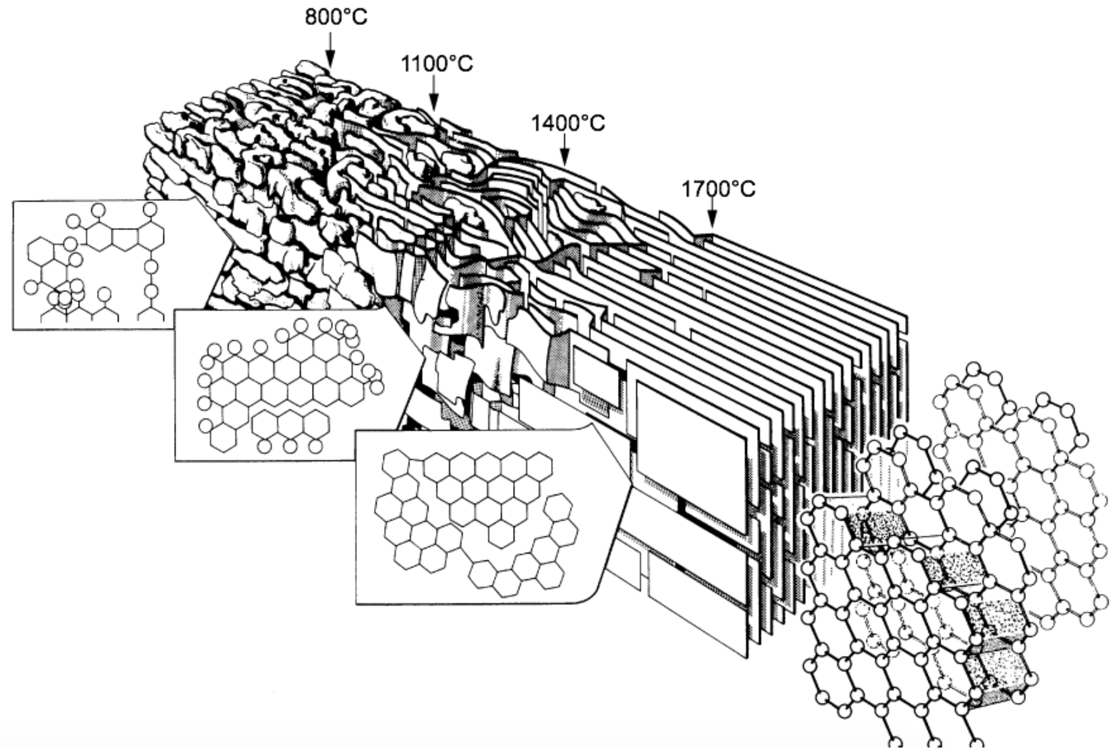

Figure 2.6: A model illustrating the effect of heat treatment on the structure of graphitizable carbon [12]. As the temperature increases the structure of the coal rearranges to a graphitic structure.

The graphitizaton process includes both the ordering of perfect graphite-like layers and removal of defects within the layers. Graphitic carbons can be described by the repetition of a structural unit, i.e. the carbon layer. A structural unit consists of several coherent domains with a coherent length in the plane, L_a, and a coherent height of the stack, L_c [13]. The structural unit is defect free, the defects are located between stacks, or between structural units. Figure 2.7 shows a coherent domain to the right and a structural unit of three coherent domains to the left. N being the number of layers in a stack, L_1 and L_2 being the defect free length and width of the unit. The stacking order is described by L_c and the mean interlayer spacing (d_{002}).

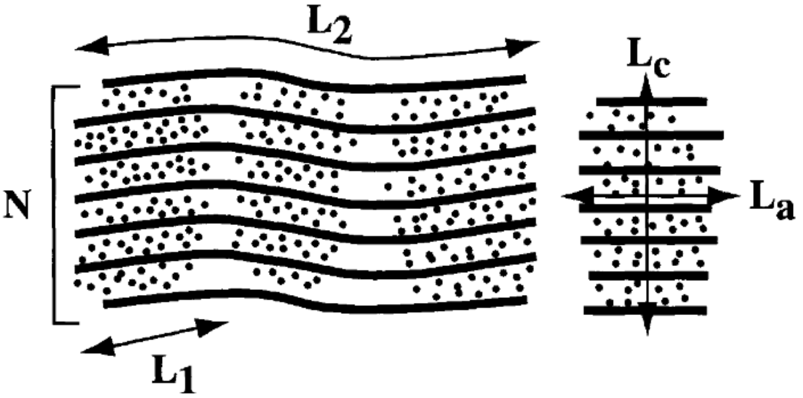

Figure 2.7: Coherent domain to the right and a structural unit of three coherent domains to the left. L_a is the length of the coherent domain, L_c is the height of the stack, N is the number of layers in a stack, L_1 is the length of the defect free unit and L_2 is the width of the defect free unit [13].

According to Bourrant [14] the graphitization process can be divided into four stages: the green-coke stage, the columnar stage, the coalescence stage and the graphitization stage.

In the first stage, up to about 500 °C, the coherent domains are small. These domains are less than 1 nm in diameter and only 2-3 graphene layers in a stack.

During the second stage the number of layers in stack increases. Neighbouring layers tend to be parallel within bent columns, hence this stage is called the columnar stage. The temperature in this stage is 800-1500 °C. Large inter-layar defects between stacks are swept away during this stage.

The third stage occurs above 1500 °C. This stage is referred to as the coalescence stage, where the lateral coalescence of the layers begin. Neighbouring columns coalesce edge-to-edge, entrapping defects within the graphene planes. The numbers of layers in a stack and the coherent length increases.

The graphitization stage occur at about 2000 °C. In this stage the temperature and hence the activation energy is sufficiently high to remove internal lattice defects. These defects can be oxygen, sulfur and nitrogen atoms, cross-links, vacancies and interstitial carbon atoms. Removal of defects will result in stiff and planar layers. The coherent length increases and the graphitization proceeds.

2.2.4 Densification

The calcined material becomes more dense due to the structural changes from the graphitization process and the removal of defects, volatiles and ash components from the carbonization process.

2.3 Use of Coal in the Metallurgical Industry

Coals have a lot of different applications in the metallurgical industry. Primarily the bituminous and anthracite coal are used. Thermal processes are necessary to obtain metallurgical coke from bituminous coal and electrically calcined anthracite from anthracite coal.

2.3.1 Bituminous Coal to Metallurgical Coke

One of the main applications of bituminous coal is as coking coal in the formation of metallurgical coke. The coke is produced by controlled heating, or coking, of coal in the absence of air, typically to temperatures around 1000-1100 °C [8]. During this process, the volatile materials will be driven off, and the carbon content will be concentrated.

Metallurgical coke is used primarily in the process of iron production in blast furnaces, as well as ferro-alloys in submerged arc furnaces and direct current furnaces. In these furnaces the metallurgical coke works as a a fuel, as a chemical reducing agent and as a permeable support [15].

Other applications might be as a substitute for anthracite in lining materials or electrodes.

2.3.2 Anthracite Coal in Lining and Electrodes

As previously mentioned, some of the main applications of electrically calcined anthracite are in lining material in e.g. submerged arc furnaces used in silicon production, in cathode blocks when producing primary aluminium and in electrodes, either pre-baked electrodes or self-baking Søderberg electrodes.

The electrically calcined anthracite is partly crushed, sieved and divided into different fractions. The anthracite is most often mixed together with a binder of coal-tar pitch according to a recipe. The composition of anthracite and binder will affect the packing and the density of the product and hence also the properties of the finished product [3].

The lining in a submerged arc furnace usually consists of three main layers. The outermost layer is a water-cooled steel shell which keeps the structure in place. This steel layer can not withstand very high temperatures, therefore a refractory layer is required. Hence, the middle layer consists of oxide refractory bricks, usually made of Al_2O_3, MgO or SiO_2. This layer can withstand the high temperatures, but is not necessarily chemically resistant. The innermost layer is a carbon lining, made to withstand high temperatures and wear from the furnace content [16]. In the lining the calcined anthracite needs to have high thermal conductivity to avoid being overheated. The lining will often due to high temperature become more graphitized. This will further increase the conductivity of the lining and hence increase the cooling of the hottest parts.

For the cathode blocks, it is important to withstand the combined effect of high temperatures and a tough electrochemical environment. When producing the cathodes anthracite calcined at about 1200 °C is typically used [17]. The anthracite is mixed with coal-tar pitch, formed and baked. The carbon purity requirement of the cathode is not as high as for the anode, since the metal contamination from the cathode is not significant.

The main task of an electrode is to conduct electrical current to the smelting zone of the furnace and to supply sufficient energy to the reaction zone so that the reduction reactions are maintained [3]. As they do so the electrode is consumed. This rises high requirement towards the purity of the carbon as the electrode will enter the metal melt. In the production of aluminium, the consumption rate is about 450 kg of electrode per ton aluminium produced [18]. Due to this consumption, the pre-baked electrodes have to be replaced and the electrode butt is recycled and used in new electrodes. A Søderberg electrode is a continuous electrode where carbon briquettes or cylinders are fed at the top of the electrode. Søderberg electrodes are also used in the ferroalloy industry, with similar requirements such as high electrical conductivity and low thermal expansion.

When producing pre-baked electrodes the anthracite is mixed with old electrode butts and coal-tar pitch. The mix is poured into moulds and transferred to a bake house where the electrode is baked at about 1100 °C for up to two weeks in order to increase the strength [18].

For the Søderberg electrodes, the electrodes are baked by the heat generated from the reduction process in the furnace. As the electrode is consumed, more anthracite/coal-tar pitch briquettes are fed at the top. When these briquettes move further down in the furnace, the temperature increases, causing the briquettes to soften, fill the mould and bake as it moves along. While baking, the electrical resistivity will decrease [3].

In order to work as a conductor of electricity, it is important for the electrodes to have low electrical resistivity. High density and high resistance to the furnace content is also important for all the carbon materials, as they will be exposed to high temperatures and molten metal and slag inside the furnace [2].

2.4 Polycyclic Aromatic Hydrocarbons

Polycyclic aromatic hydrocarbons (PAHs) are organic compounds consisting of two or more fused aromatic rings. These compounds originates mainly from human made sources, such as the burning and pyrolysis of coal, oil, wood and garbage among others [19], [20]. The metallurgical industry is one of the contributors to the total emissions of PAHs in the environment due to the release of PAHs during the coking of coal or the production of primary aluminium or electrode paste [21], [19].

Production of the Søderberg electrode paste involves the mixing of calcined anthracite with coal tar at temperatures around 170 °C [22]. During this mixing, PAHs are liberated into the atmosphere where production plant workers in particular are exposed. Bentsen et al. reported large amount of PAHs in the work environment of electrode paste workers, pointing out the importance of minimizing the release of PAHs [23], [22].

In 1983 Ramdahl et al. [21] stated that "As long as man has had fire, he has had PAH in his environment", emphasizing the human impact on the environment. When coal undergoes pyrolysis, physical and chemical changes occur, as mentioned in Section 2.2. As a consequence of the thermal process, aromatic clusters such as PAHs can be developed [24].

Most PAHs are considered carcinogenic and hence, inhalation of PAHs is a potentially serious risk. This is one of the main reasons to study PAH emissions, since once released into the atmosphere, they can easily be inhaled by humans [19], [20]. Figure 2.8 shows some examples of carcinogenic PAHs [25], where Benzo(a)pyrene (BaP) and 7,12-dimethylbenz(a)anthracene (DMBA) are concidered especially hazardous.

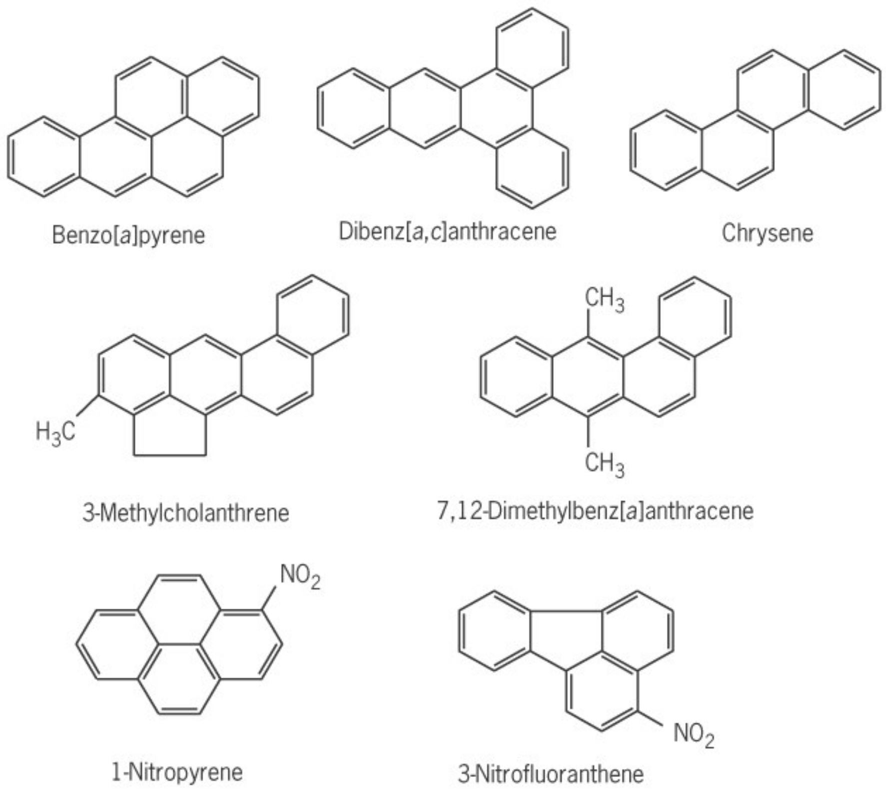

Figure 2.8: Some examples of carcinogenic polycyclic aromatic hydrocarbons [25].

Some methods used to analyze the PAH emissions from different materials are high-performance liquid chromatography with fluorescence detector (HPLC-FLD) and gas chromatography–mass spectrometry (GC-MS) [19]. Fourier transformed infrared (FTIR) spectroscopy is also a widely used technique in coal characterization [26].

By using simultaneous thermogravimetry–mass spectrometry Arenillas et al. [27] investigated the pyrolysis behaviour of a range of coals. One anthracite and three bituminous coals were investigated. One topic of interest during the experiments were the evolution of H_2. H_2 comes from the condensation of aromatic structures or the decomposition of heterocyclic compounds, processes that occur at higher temperatures [27]. The total amount of H_2 would give an indication of the PAH content of the coals.

Figure 2.9 shows the H_2 evolution curves for the four coals investigated by Arenillas et al. Very low H_2 emissions are observed for the anthracite due to the low volatile content of 4.2 % and the presence of highly condensed structures.

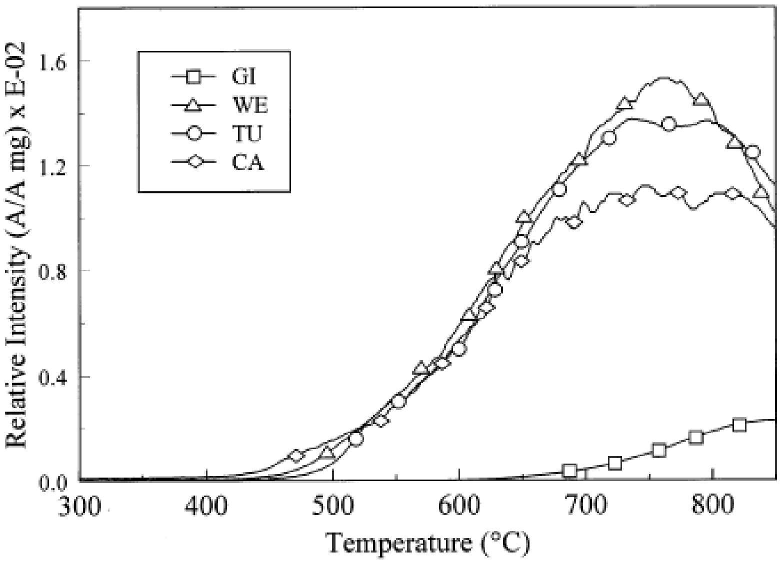

Figure 2.9: H_2 evolution curves for the four coals as a function of temperature investigated by Arenillas et al. GI represents the anthracite, while WE, TU and CA represent the bituminous coals [27].

Mastral et al. [28] investigated the influence of different combustion temperatures on the PAH emission of a low rank and a high rank coal. The temperatures ranged from 650 to 950 °C. The total amount of the PAH emitted is shown as a function of the combustion temperature in Figure 2.10. As can be seen from the figure, the highest amount of PAHs are emitted around 800 °C.

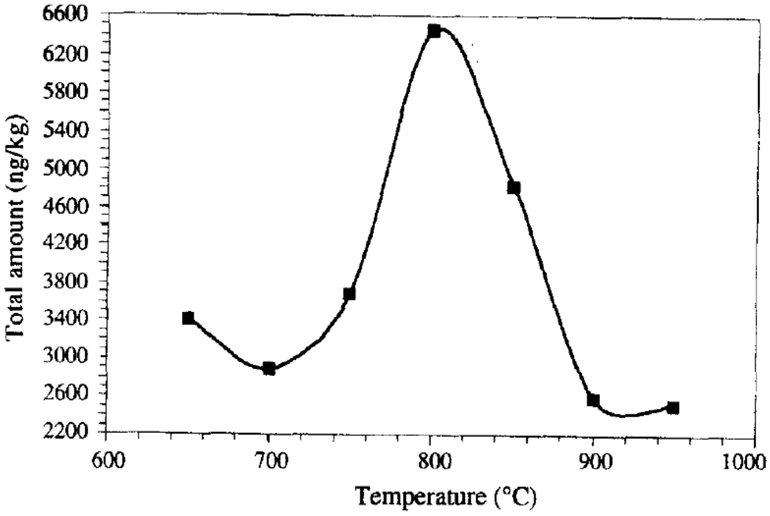

Figure 2.10: The total amount of PAHs emitted, given as a function of combustion temperature [28].

2.5 Porosity in Coals

Porosity is the ratio of pore volume over total volume. Coal is characterized by dual porosity, which consists of micropore and macropore systems. The micropores occur as a part of the coal matrix, whereas the fracture network establish the macropore system [29].

Microporosity is defined as pores with a diameter less than 2 nm, while macropores are pores with a diameter greater than 50 nm. The pores with a diameter less than 50 nm and grater than 2 nm are defined as mesopores [26], [30].

According to Rodrigues et al. [31] macropores, or primary porosity, predominate in lower rank coals. As the molecular structure changes through higher ranks, the porosity increases and the secondary porosity begins with the formation of meso- and micropores. Okolo et al. [30] stated that as the rank of the coal increases, the importance of macroporosity decreases and microporosity becomes increasingly significant. Microporosity is predominant in higher ranked coals.

Gas adsorption is a widely used technique to determine the surface area, pore structure and the porosity of coals. Among argon, carbon dioxide, helium, methane, nitrogen and water vapour, carbon dioxide and nitrogen are most commonly used [30]. Gas adsorption is less costly than more advanced techniques, but small angle x-ray scattering (SAXS), mercury intrusion porosimetry (MIP), helium pycnometry, scanning electron microscopy (SEM) are also used [26], [30], [31].

Okolo et al. [30] investigated different methods of measuring the surface area and porosity of coals. Low pressure gas adsorption with both CO_2 and N_2 were carried out, as well as MIP and SAXS.

For the gas adsorption, both the surface areas and the pore volumes decreases with increasing amount of fixed carbon in the four coal samples. According to Okolo et al. the N_2 adsorption underestimated the surface area and porosity compared to the results obtained by the other techniques, but provides a good insight into the pore size distribution of mesopores.

They found that each technique could only probe different pore size ranges, hence the overall porosity of a coal could not be described by only using one method. The CO_2 gas adsorption covers pores with a diameter of 0.3 - 0.5 nm in the lower micropore range, the N_2 gas adsorption covers pores with a diameter of 1.7 - 50 nm in the higher micropore and entire mesopore range, while MIP covers the meso- and macropore range with diameters of 3 - 60 000 nm. This means that pores with a diameter between 0.5 and 1.7 nm are not covered by any of these techniques, and pores with a diameter between 3 and 50 nm are covered by both N_2 gas adsorption and MIP. A more complete description of the porosity of the samples is obtained by combining the results for these tree techniques.

The surface areas and porosities determined from SAXS were larger than any of the values obtained by the other techniques. This is due to the large range of pore diameters covered by this technique. SAXS covers the micro- meso- and macroporosity with a diameter in the range of 0.3 - 60 000 nm, also including closed pores.

Rodrigues et al. used the Langmuir adsorption isotherms in order to determine the coal porosity of two coals in relation to the molecular size of different gases. The gases used in the experiments were He, N_2, CH_4 and CO_2. He is the gas with the smallest molecular size, hence the most precise measurement of the entire coal structure could be obtained by this gas. Although, there is only a small and insignificant change in the volume determination between N_2 and He.

For CH_4 and CO_2, shrinkage and swelling effects are induced when in contact with the coal molecular structure. For CO_2 this cause negative values in coal void volume calculations, however the changes are reversible. The effect when using CH_4 is less pronounced, but in this case the changes are irreversible and the coal volume is increased [31].

Liu et al. [32] investigated the porous structure of bituminous coals and found that there were two competing phenomena determining the evolution of the pore structure: growth of individual pores and coalescence of neighbouring pores. Pore walls might collapse and pores coalesce, leading to a decrease in the surface area.

Surface area and porosity experiments were performed on an anthracite, A11, in previous work [33], where low pressure N_2 gas adsorption, light microscopy and helium pycnometry were used as methods. Some of the results are shown in Figure 2.11 and 2.12.

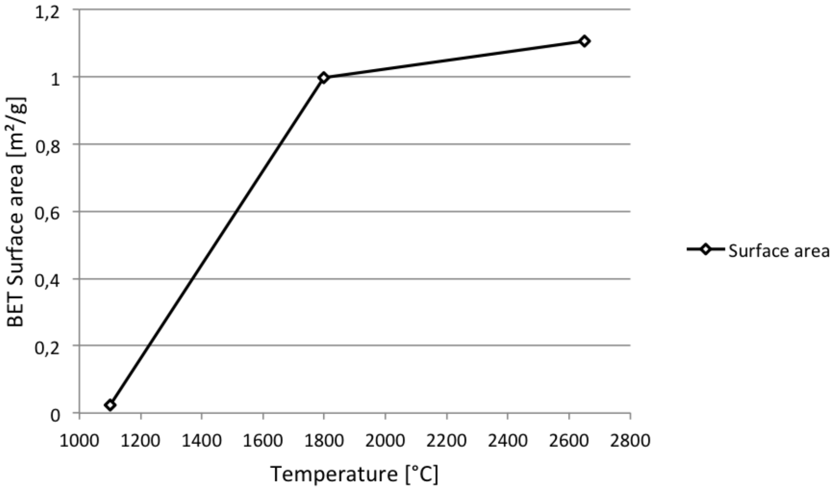

Figure 2.11: BET surface area of anthracite A11 as a function of calcining temperature [33].

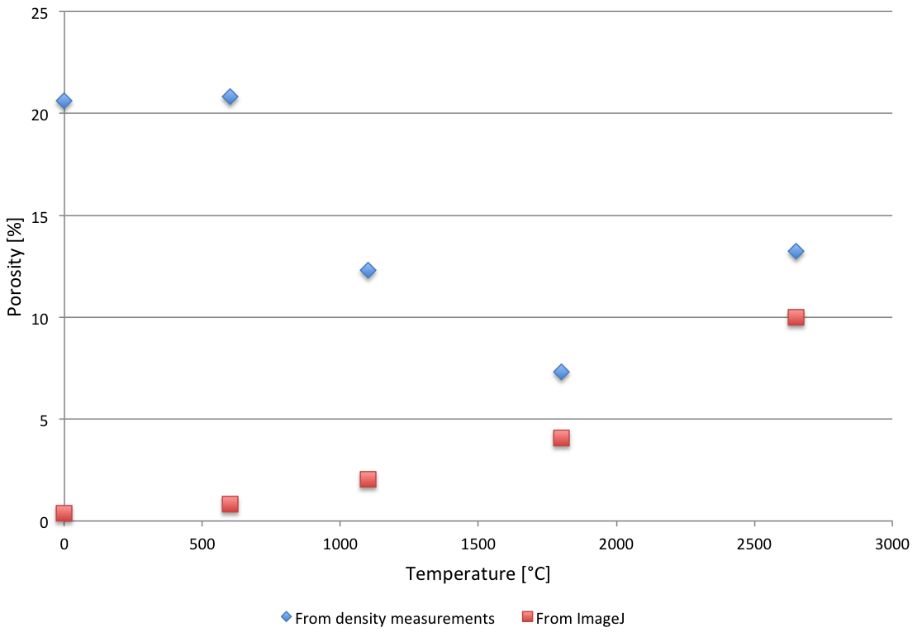

Figure 2.12: Porosities given as a function of calcining temperature. The red dots are the values given from image analysis of light micrographs, while the blue dots give the porosity values calculated from density measurements [33].

The BET surface area measurements of anthracite A11 are shown in Figure 2.11, where the surface area is given as a function of calcining temperature. The surface area increases with increasing temperature between 1100 and 2650 °C.

Figure 2.12 shows the porosities obtained from light micrographs and from density measurements of the A11 anthracite. The red dots are the values given from image analysis of light micrographs, and represent the macroporosity. Fluorescent dye was used to create a contrast between the carbon matrix, open- and closed porosity in order to conduct the image analysis. As can be seen from the figure, the porosity increases with increasing calcining temperature. The blue dots give the porosity values calculated from the pycnometric densities. Here, however, there is a decrease in the porosity value from the non-calcined material up to 1800 °C. Between 1800 and 2650 °C the porosity increases again.

In the previous work it was concluded that additional experiments should be carried out, to further investigate the porosity and the difference between the methods.

2.6 Dimensional Behaviour of Coals

The thermal behaviour of coal is vey important. As previously mentioned, when electrodes are produced, coke or anthracite fillers are used in a mixture with binder of coal tar pitch. While coal tar pitch tend to shrink [34] when exposed to high temperatures, coke and calcined anthracite tend to expand. This might cause stresses leading to failure of the electrodes under operation at high temperatures.

Beukes et al. [35] demonstrated how thermomechanical analysis can be used to characterize the thermal dimensional behaviour of Søderberg electrode paste raw materials, such as coal tar pitch and anthracite. The experiments were carried out by heating pressed pellets of anthracite from room temperature up to 1300 °C and measuring the dimensional changes in a thermomechanical analyser (TMA). Each experiment were carried out with three heatings up to 1300 °C. Three different anthracites where tested, both un-calcined and calcined at 1400 °C. One of the anthracites were also tested for different calcining temperatures, at 1200, 1300 and 1400 °C. Some of Beukes' results are shown in Figure 2.13, 2.14 and 2.15.

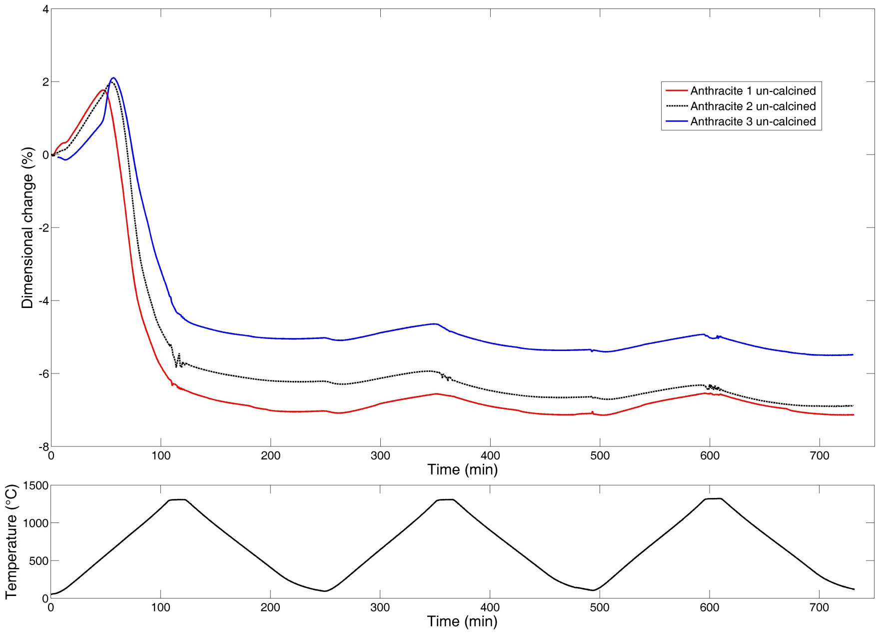

Figure 2.13: Thermomechanical analysis of the three un-calcined anthracites heated to 1300 °C [35].

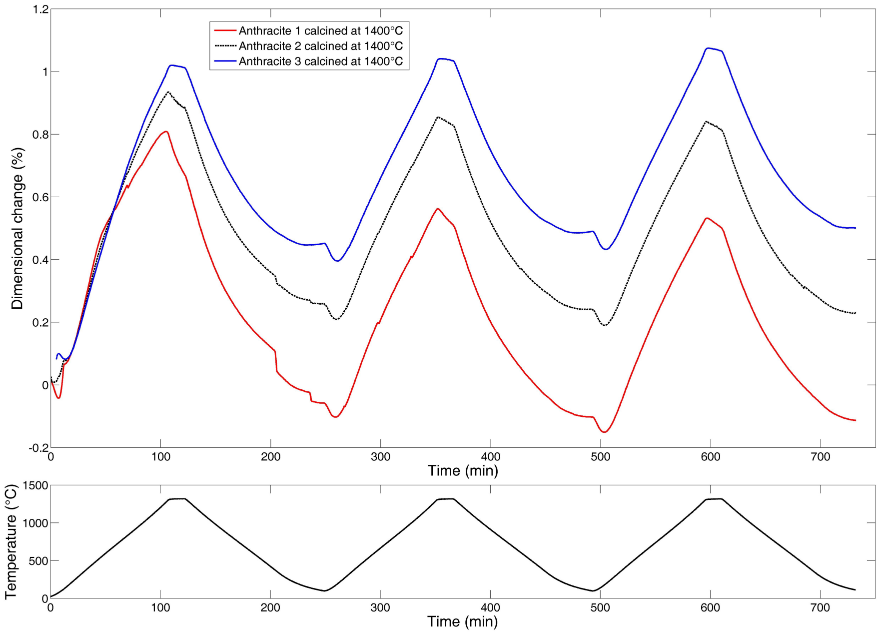

Figure 2.14: Thermomechanical analysis of the three anthracites calcined at 1400 °C. The graph shows the dimensional change as a function of time [35].

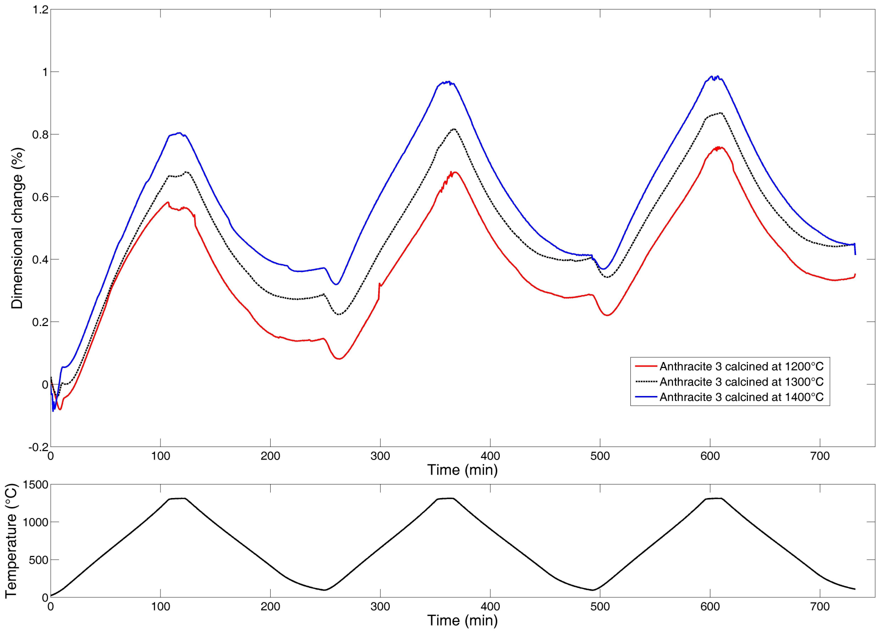

Figure 2.15: The influence of calcination temperature on the thermal dimensional behaviour of anthracite 3. The material is calcined at 1200, 1300 and 1400 °C [35].

Figure 2.13 shows the dimensional change of the three un-calcined anthracites as a function of time. The temperature profile is also given. As can be seen from the figure, there is a shrinkage during the first heating ranged from 6-8 % for the un-calcined samples.

From Figure 2.14 and 2.15, it can be seen that both the difference in the materials and a difference in the calcining temperature for the same material will affect the dimensional behaviour. Beukes et al. concluded that higher calcination temperatures resulted in smaller dimensional changes.

As Beukes addressed in his work, the difference in motion between the coal tar pitch binder and the anthracite filler for the Søderberg electrodes, indicates a vulnerability for the electrodes. While he found that the coal tar pitch shrunk about 12 % when exposed to temperatures up to 1300 °C, the anthracite calcined at 1400 °C expanded 0.6-1.0 % and the non-calcined material shrunk about 6-8 % when exposed to the same temperatures. The difference in thermal behaviour between the non-calcined anthracite and the anthracite calcined at 1400 °C underlines the importance of the calcining process of the anthracite prior to the electrode production, as it might cause dimensional instability to the electrode. Electrode graphite pre-baked at temperatures in the order of 3000 °C expand about 0.5 % at 1300 °C [35].

Experiments subjecting the thermal expansion of single grains of anthracite were performed in the previous work [33]. Non-calcined A11 and A11 calcined at 600, 1100 and 2650 °C were tested. Figure 2.16 shows the thermal expansion in terms of percentage of change in the longitudinal direction for each grain given as a function of time. In the figure, the dotted line illustrates the temperature, with a maximum temperature at about 1550 °C. The dilatation graph is shown in Figure 2.17, where the expansion is given as a function of temperature. The thermal expansion coefficients for the different samples are given in Table 2.2.

Thermal expansion for all samples and a shrinkage of the non-calcined material and the material calcined at 600 °C were observed. The TECs were found to be close to the TEC of graphite for the material calcined at 2650 °C and for the second heating of the material calcined at 600 °C. It was also indicated in the Specialization project report [33] that the change in TEC between 1100 and 1550 °C might be due to the the third stage of the graphitization process occurring at 1500 °C, where the neighbouring columns start to coalesce.

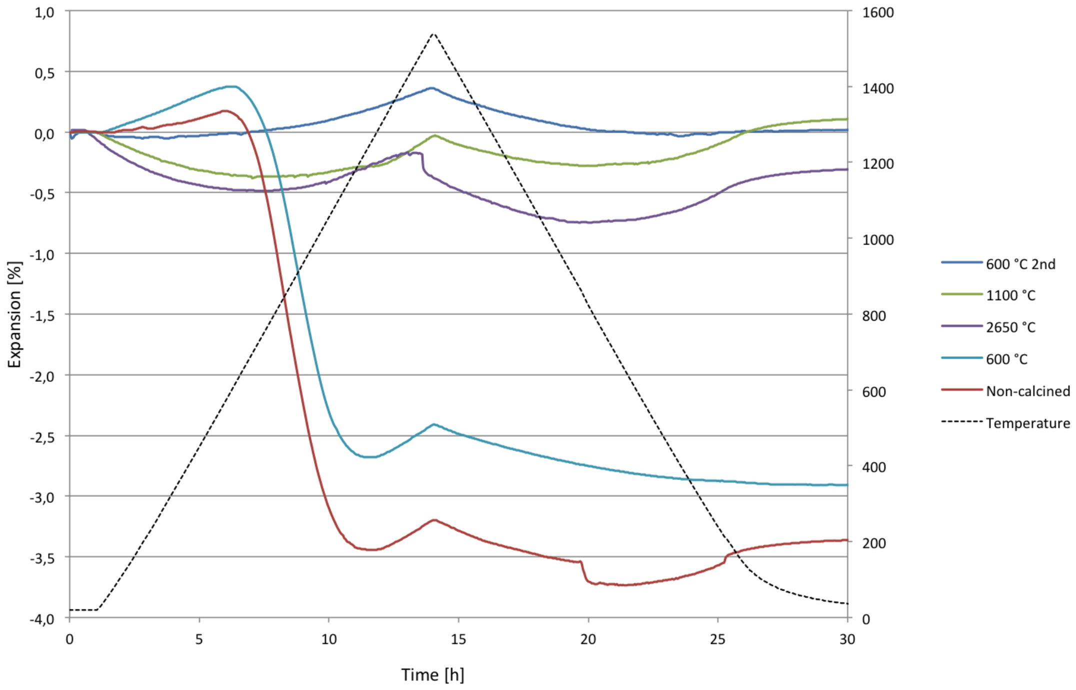

Figure 2.16: The linear thermal expansion measured for some selected samples of A11 given as a function of time during heating to 1550 °C. The temperature is given as the dotted line. [33].

Table 2.2: Thermal expansion coefficient (TEC) given for the A11 single grains [33]. The average TEC value is calculated in the temperature range of about 1200 to 1500 °C.

Temperature Sample [°C]	Thermal Expansion Coefficient (TEC) $[\cdot 10^{-6}\ \mathrm{m\,m^{-1}\,{}^{\circ}C^{-1}}]$
0	9.8
600	10.6
1100	10.0
2650	6.4
600, 2nd heating	6.2

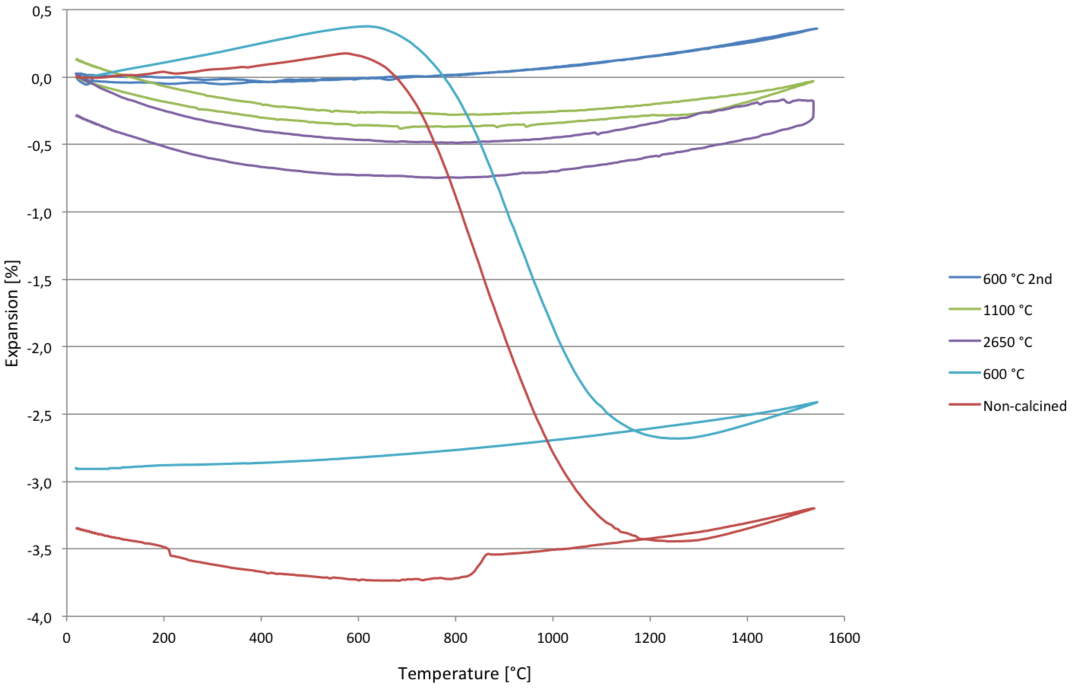

Figure 2.17: Dilatation graph, where the linear thermal expansion of A11 given as a function of temperature [33].

Chapter 3

Materials and Methods

The purpose of the experimental work presented in this chapter was to investigate the thermomechanical and thermogravimetric properties of the materials. Furthermore, to analyze the off-gases evolved from the materials during heating and re-heating.

Two anthracites, two cokes and one charcoal were investigated during these experiments. The two anthracites, A11 and A19, were calcined at different temperatures ranging from 600 to 2650 °C at Elkem Carbon Fiskaa during the period of June and July of 2016, and some characterizations were carried out. These results were interpreted and the anthracites were further investigated during the course of TMT4500 Materials Technology, Specialization Project, carried out at NTNU the fall of 2016 [33].

The two cokes, C3 and C7, were provided by Eramet. The charcoal, BIO, was provided by Elkem Thamshavn.

As a continuation of the Specialization Project, A11 was further investigated at the Norwegian University of Science and Technology, NTNU. Additional dilatometer experiments of single grains were carried out. Single grains calcined at 1100, 1800 and 2650 °C were tested. In order to further investigate the porosity calculations, additional envelope density measurements and BET analysis were carried out for the non-calcined material and the materials calcined at 600, 1100, 1800 and 2650 °C.

At North-West University the thermal expansion of pellets were investigated by using an Exstar SS6300 thermomechanical analyzer. Simultaneous Thermal Analysis (STA) or thermogravimetry (TG) and differential scanning calorimetry (DSC) were also carried out at NWU for all the materials. Further, the off-gases were investigated by using Gas Chromatography and Mass Spectroscopy (GC-MS), and Fourier Transform Infrared (FTIR) detector, connected to the STA.

The raw materials, the apparatus and the experimental procedures will be described in this chapter.

3.1 Materials

3.1.1 Anthracite

Two anthracites, A11 and A19, were calcined at Elkem Carbon Fiskaa during the course of June and July 2016. The material was crushed and sieved at +4 mm, −10 mm before the heat treatment. The amount of moisture, ash, volatiles and fixed carbon of the non-calcined materials are given in Table 3.1, where the amount of ash, volatiles and fixed carbon is given on a dry basis.

Table 3.1: Amount of moisture, ash, volatiles and fixed carbon in A11 and A19. The amount of ash, volatiles and fixed carbon are measured on a dry basis.

Sample	Moisture [%]	Ash [%]	Volatiles [%]	Fixed Carbon [%]
A11	8.51	2.98	2.45	94.57
A19	4.79	9.12	5.37	85.51

Two different high-temperature furnaces were used to carry out the heat treatments, denoted furnace 1 and furnace 2. The calcining temperatures, the retention times and the calcining atmospheres are given in Table 3.2. For heat treatment in furnace 1, the furnace was first heated to the given temperature before the anthracite was inserted into the hot furnace, held at the given temperature for the given time, and taken out of the hot furnace. For heat treatment in furnace 2, the anthracite was inserted into the furnace before heating to the given temperature, held at the given temperature for 1 hour, and taken out when the furnace had cooled down. The heating time to reach 1100, 1200, 1400 and 1600 °C was 30 minutes, 40 minutes for 1800 °C and 50 minutes for 2000, 2300 and 2650 °C. The cooling time was equal to the heating time for the given temperatures.

Table 3.2: Overview of the different heat treatments of A11 and A19.

		Retention time	
Furnace	Temperature [°C]	A11	A19
1, air	600	1h	1h
1, air	800	1h	1h
1, air	1000	1h	1h
1, air	1100	1h, 2h, 8h	1h, 2h, 8h
2, nitrogen	1100	1h	1h
2, nitrogen	1200	1h	-
2, nitrogen	1400	1h	-
2, nitrogen	1600	1h	-
2, nitrogen	1800	1h	1h
2, nitrogen	2000	1h	-
2, nitrogen	2300	1h	-
2, nitrogen	2650	1h	1h

Some characterizations of the non-calcined and calcined material were also carried out at Elkem Carbon Fiskaa. A selcetion of these results are presented graphically here, while the data is given in Appendix A.

The mass change during the course of the calcining process is shown in Figure 3.1, where the mass in percentage is given as a function of calcining temperature. A19 has a higher mass loss at 2650 °C of about 22 %, while A11 has a mass loss of about 10 % at 2650 °C. Both A11 and A19 show an even decrease in mass as the calcining temperature increases.

The total volatile content of A11 and A19 is shown in Figure 3.2, where the volatile content is given as a function of calcining temperature. The volatile content of the non-calcined material of A11 is 2.5 %, and 5.4 % for A19. Only a small decrease in volatile content of about 0.5 % is observed for A11, while A19 has a bigger change in volatile content between raw state and 800 °C of about 6 %.

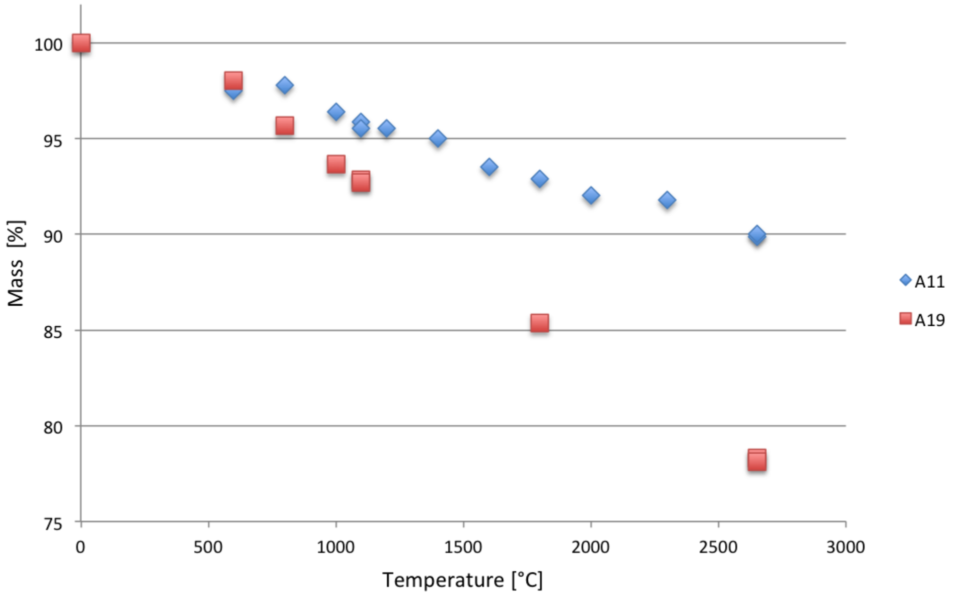

Figure 3.1: The mass of A11 and A19 as a function of calcining temperature.

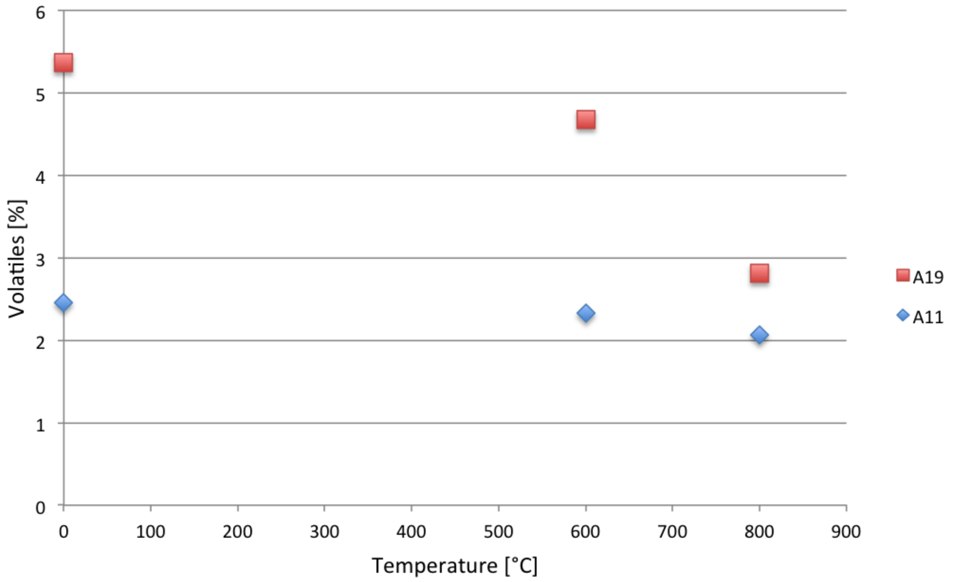

Figure 3.2: Volatile content of A11 and A19 given as a function of calcining temperature.

Absolute density measurements were carried out by using an AccuPyc 1330 and AccuPyc II 1340 with He gas. Figure 3.3 illustrates the absolute density measurments of A11 and A19 as a function of calcining temperature. The results are based on the average of five measurements, all given in Table A.3, Appendix A. The figure shows a higher increase in density for A19 than A11, but both anthracites follow the same trend where there is a small peak in the values around 1000 °C. It also shows that the density is getting closer to the density of graphite of 2.26 g cm^{-3} at high temperatures [36].

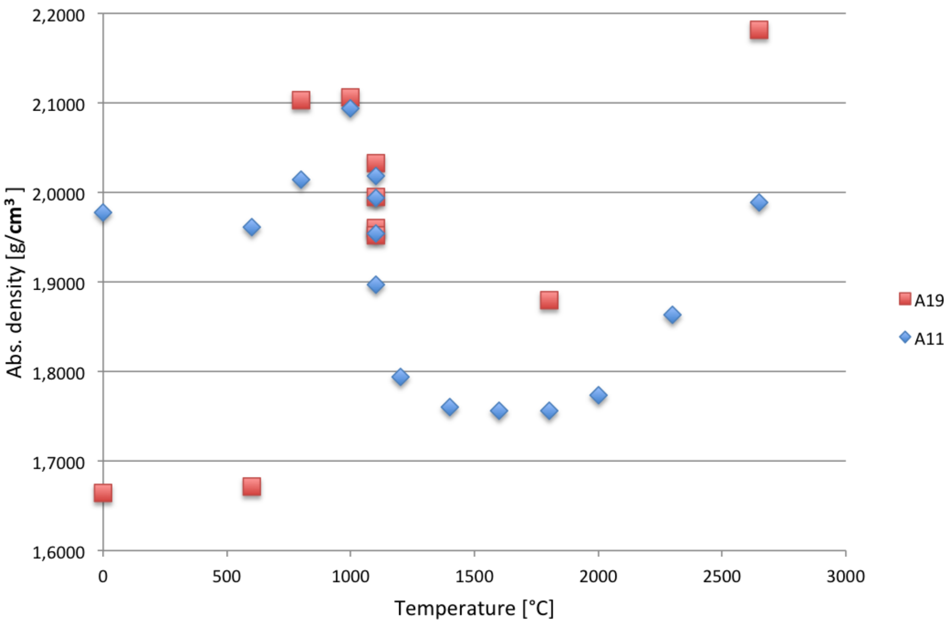

Figure 3.3: Absolute density measurements given as a function of calcining temperature for A11 and A19.

Figure 3.4 (a), (b) and (c) shows the weight percentage of sulfur, nitrogen and hydrogen, respectively. The weight percent is given as a function of the calcining temperature. An even decrease in the sulfur and nitrogen removal is observed for both anthracites, while most the hydrogen content is removed around 1000 °C. At 2650 °C all of the volatiles are removed for both anthracites.

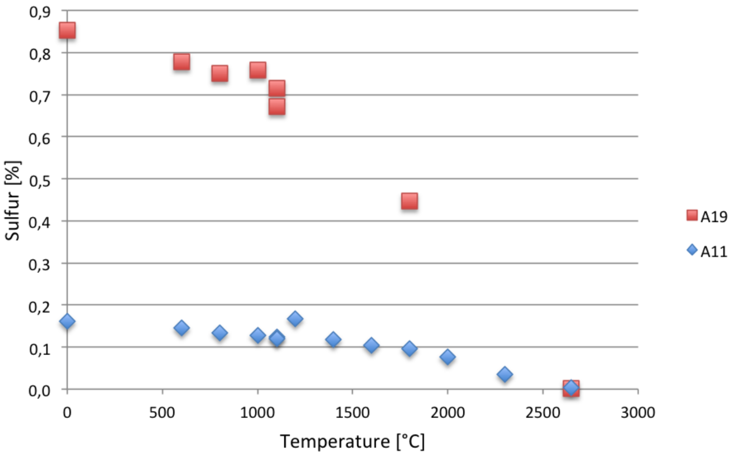

(a) Sulfur

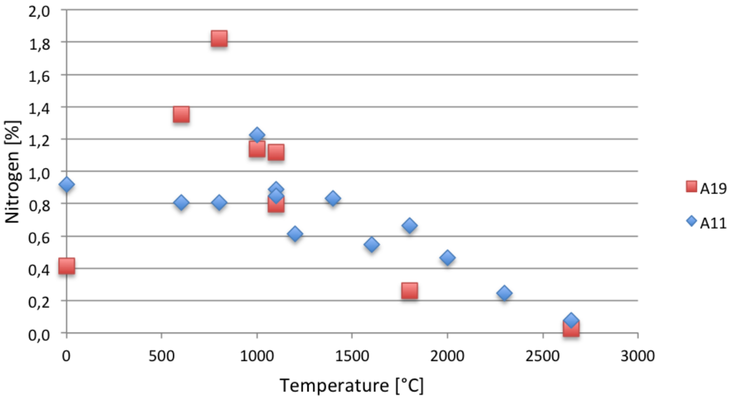

(b) Nitrogen

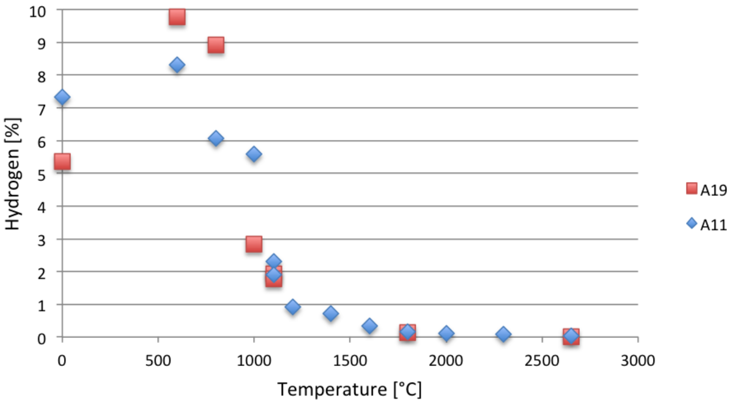

(c) Hydrogen

Figure 3.4: Sulfur, nitrogen and hydrogen content of A11 and A19 given as a function of calcining temperature.

The coherent height of the structural unit, L_c or the crystallite size and the interlayar spacing, d_{002}, were measured by using X-ray diffraction. The results are presented in Figure 3.5 (a) and (b), respectively. Both are given as a function of the calcining temperature.

As can be seen from the figure, the crystallite size increases with increasing temperature and is very similar for both A11 and A19 at lower temperatures. For the material calcined at 2650 °C there is a difference of about 80 Å, where A19 has the greater value.

The interlayar spacing decreases with increasing temperature, with an exception around 1000 °C where a sudden increase can be observed. At 2650 °C the interlayar spacing is 3.36 Å for both anthracites. This value is close to the interlayar spacing of graphite at 3.35 Å.

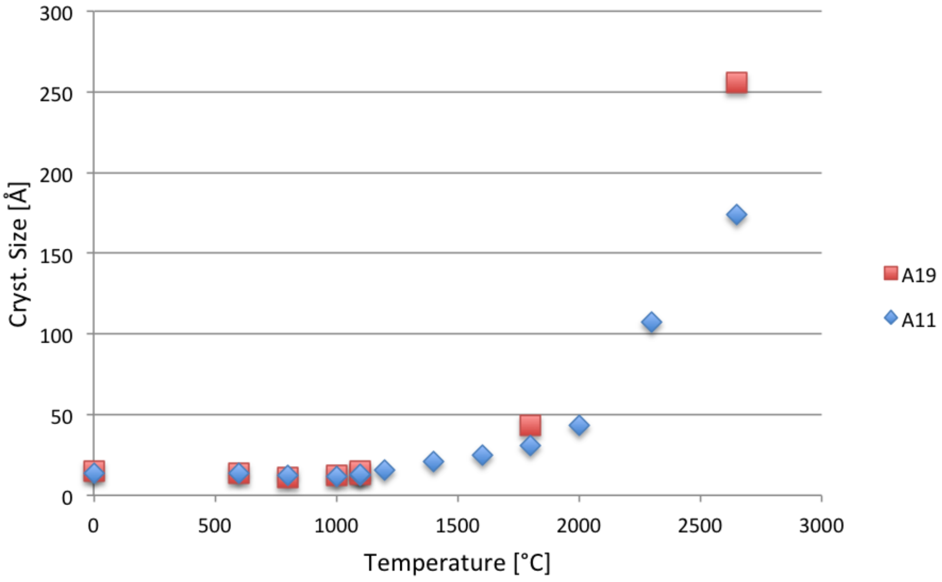

(a) Crystallite size, L_c

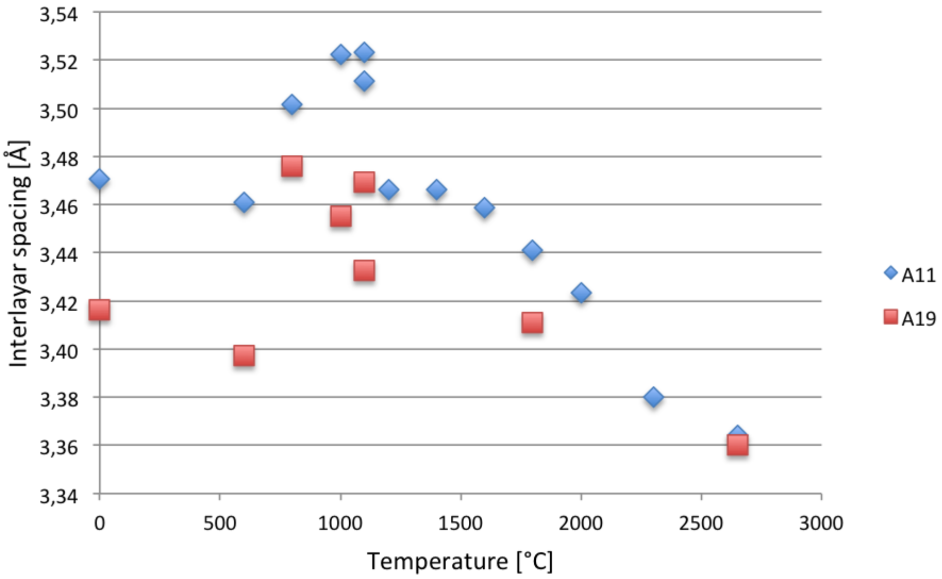

(b) Interlayar spacing, d_{002}

Figure 3.5: Crystallite size, L_c, and the interlayar spacing, d_{002}, from XRD given as a function of calcining temperature. Both measured in Å.

3.1.2 Coke

Two cokes, C3 and C7, were provided by Eramet. The amount of moisture, ash, volatiles and fixed carbon are presented in Table 3.3, where the amount of ash, volatiles and fixed carbon are given on a dry basis. The proximate analysis were preformed by Sintef molab.

Table 3.3: Amount of moisture, ash, volatiles and fixed carbon in C3 and C7. The Amount of ash, volatiles and fixed carbon are measured on a dry basis.

Sample	Moisture [%]	Ash [%]	Volatiles [%]	Fixed Carbon [%]
C3	4.47	13.29	1.43	85.28
C7	11.34	3.76	2.06	94.18

3.1.3 Charcoal

The charcoal, denoted BIO, was provided by Elkem Thamshavn. The amount of moisture, ash, volatiles and fixed carbon are presented in Table 3.4, where the amount of ash, volatiles and fixed carbon are given on a dry basis. The proximate analysis were preformed by Sintef molab.

Table 3.4: Amount of moisture, ash, volatiles and fixed carbon in BIO. The Amount of ash, volatiles and fixed carbon are measured on a dry basis.

Sample	Moisture [%]	Ash [%]	Volatiles [%]	Fixed Carbon [%]
BIO	2.2	2.6	14.0	83.4

3.2 Methods

3.2.1 Sample Preparation

For the envelope density measurements, single grains of non-calcined and calcined A11 were used, so no further sample preparation was required. The single grains of A11 were also used in the dilatometry experiments, and in order for the grain to sit in the instrument the grains had to be polished to achieve a parallell top and bottom side. The BET analysis required a smaller grain size, so some of the A11 material was crushed gently in a mortar.

The coke, charcoal, calcined and non-calcined anthracite were pulverized by using Siebtechnik ring mill for 30 seconds to achieve a particle size less than 150 µm. The materials where dried at 110 °C for about 24 hours prior to the pulverizing.

The pulverized samples were sufficient for use in the thermogravimetric analysis, but for use in the thermomechanical analysis, the pulverized samples were pelletized to cylidrical pellets.

Pelletizing of the materials were carried out by using a LRX Plus strength testing machine and a 10 mm die set, as shown in Figure 3.6 (a). About 0.65 g of pulverized material was placed in the die set. 3 drops of distilled water were added in order to ensure that the pellets had sufficient strength for handling and subsequent thermomechanical analysis.

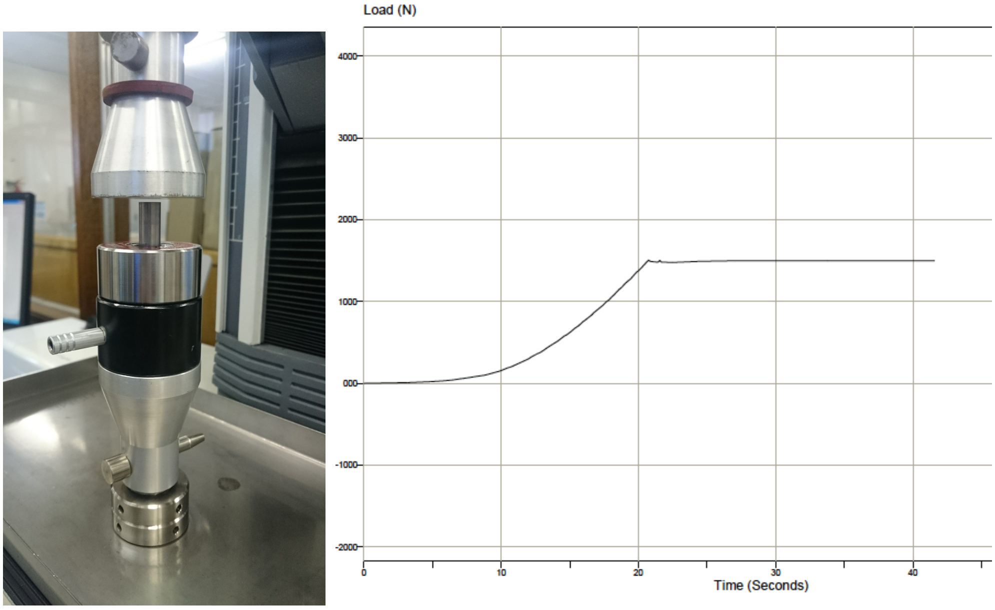

(a) (b)

Figure 3.6: (a) Set up for the pelletizing. A 10 mm die set in a LRX Plus strength testing machine. (b) Load as a function of time during pelletizing of the material.

The pellets were compressed until a load of 1500 N was reached, and was held at this load for 20 seconds. The load as a function of time during the pelletizing is shown in Figure 3.6 (b).

Sufficient amount of distilled water, compressing load and compressing time were determined by trial and error.

3.2.2 Dilatometry

Dilatometry is a thermo-analytical method for measuring the shrinkage or expansion of materials over a controlled temperature regime [37]. Dilatometry allows measurements of the thermal expansion of a material and the thermal expansion coefficient.

Thermal expansion is the tendency for a material to change in shape, area and volume in response to temperature. The degree of expansion divided by the change in temperature is called the material's coefficient of thermal expansion (TEC), and is given as the slope of the dilatation curve. For graphite the TEC is 2-6 $\cdot 10^{-6}$ $\mathrm{m\,m^{-1}\,°C}$ and 8.1 $\cdot 10^{-6}$ $\mathrm{m\,m^{-1}\,°C}$ for alumina [38].

Equation 3.1 shows the change in length with the change in temperature for solid materials.

$$dl = L_0 \cdot \alpha \cdot (T_f - T_0) \tag{3.1}$$

Where dl is the change in the objects length, L_0 is the initial length of the object, α is the linear expansion coefficient and T_0 and T_f are the initial and final temperature, respectively.

The thermal expansion of a solid material can be measured by using a pushrod dilatometer. The pushrod is connected to an inductive position transduser giving a voltage signal that is proportional to the dilatation [39]. The signal increases upon expansion and decreases upon contraction. The dilatometer measures the expansion difference i longitudinal direction between the sample holder and the sample:

$$\text{Measured values} = \text{Sample expansion} - \text{Holder expansion} \tag{3.2}$$

Where the expansion of the holder needs to be known in advance in order to find the expansion of the sample. If a displacement piece is used, the thermal expansion of this also has to be known. A scheme of the sample holder is given in Figure 3.7. Where the length of the holder, L_H, equals the length of the distance piece, L_D, plus the length of the sample, L_S. Usually both the holder and the distance piece are made of alumina.

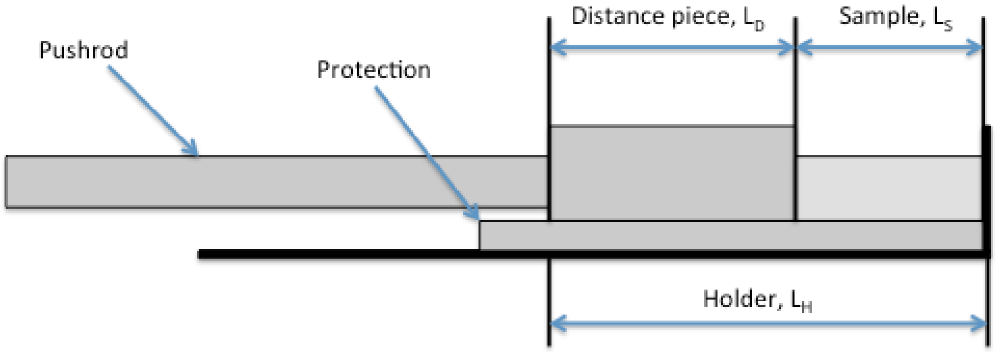

Figure 3.7: Scheme of the sample holder of a pushrod dilatometer, after Paulsen [39].

The measured dilatation, $\Delta L_{\text{Measured}}$, between the initial temperature T_0 and the temperature T can be expressed as:

$$\Delta L_{\text{Measured}} = \Delta L_S + \Delta L_D - \Delta L_H \tag{3.3}$$

where

$$\Delta L_{\text{Measured}} = L_{\text{Measured}}(T) - L_{\text{Measured}}(T_0) \tag{3.4}$$

$$\Delta L_S = L_S(T) - L_S(T_0) \tag{3.5}$$

$$\Delta L_D = L_D(T) - L_D(T_0) \tag{3.6}$$

$$\Delta L_H = L_H(T) - L_H(T_0) \tag{3.7}$$

By dividing the length of the holder, L_H, into two parts with the same length as the sample and the distance piece, L_{HS} and L_{HD} respectively, and applying it into equation 3.3, we get:

$$\Delta L_{\text{Measured}} = \Delta L_S + \Delta L_D - \Delta L_{HS} - \Delta L_{HD} \tag{3.8}$$

By rearranging and setting the length relative to the sample length at the initial temperature, the expansion of the sample can be expressed as:

$$\frac{\Delta L_S}{L_0} = \frac{\Delta L_{\text{Measured}} + L_{HS}}{L_0} - \frac{\Delta L_D - \Delta L_{HD}}{L_0} \tag{3.9}$$

Where the last term is the correction for the distance piece. If the holder and the distance piece have the same thermal expansion the correction will be zero [39]. Hence, the dilatation will be given by:

$$\frac{\Delta L_S}{L_0} = \frac{\Delta L_{\text{Measured}} + L_{HS}}{L_0} \tag{3.10}$$

The thermal expansion of some selected samples were investigated by using a Netzxch 402E Dilatometer in a nitrogen atmosphere, showed in Figure 3.8. The instrument is a classical pushrod dilatometer where all the ceramic parts are made from alumina. The instrument software makes the corrections automatically for the expansion of the alumina sample holder and distance piece.

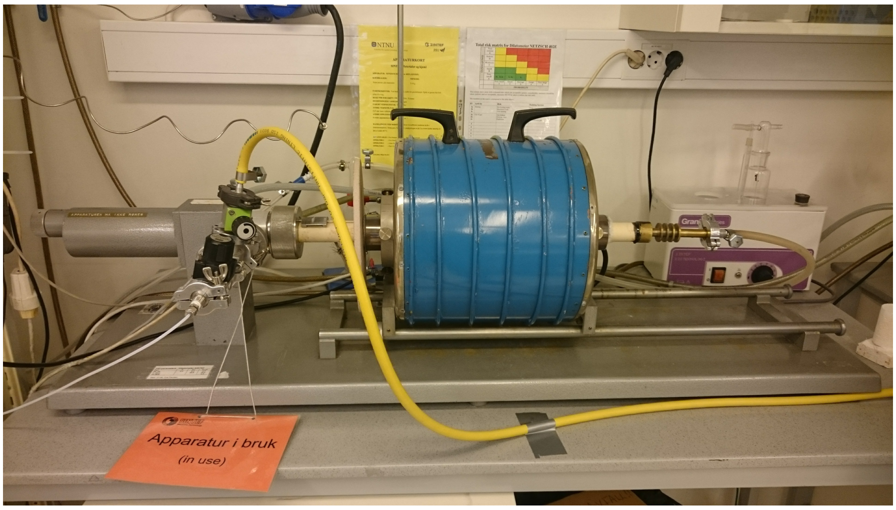

Figure 3.8: Netzsch 402E Dilatometer used in the thermal expansion experiments.

Thermal expansion measurements were carried out in order to supplement the experiments done the the Specialization Project [33]. Single grains of the material calcined at 1100, 1800 and 2650 °C were tested.

During the experiments, single grains were heated to about 1550 °C and cooled back down to room temperature with a heating and cooling rate of about 115 degrees per hour. Thermal expansion and dilatation graphs were created from the experimental data. The TECs were obtained from the slopes of the dilatation curves.

3.2.3 Envelope Density Measurements and Porosity Calculations

The porosity of a material can be calculated from measurements of absolute and envelope density. Absolute density is defined as the mass of a particle divided by its volume, where open and closed pores are left out. Envelope density is the external volume of a particle, such as would be obtained by tightly shrinking a film to contain it, divided by its volume. All pores and voids are included [40].

Combining absolute and envelope density allows for accurately calculations of percent porosity of a body, this is shown in Equation 3.11.

$$\%\text{Porosity} = \left(1 - \frac{\text{Envelope Density}}{\text{Absolute Density}}\right) \cdot 100\% \tag{3.11}$$

The densities can be measured by instruments based on Archimedes' displacement principle. Archimedes stated that for any body completely submerged in a fluid, the volume of displaced fluid is equivalent to the volume of the body [41].

For absolute density measurements a gaseous displacement medium is used, usually helium or other inert gases. This measurement can be carried out in a gas pycnometer.

Measurements of the envelope density utilizes a quasi-fluid displacement medium. This medium is composed of microspheres having a high degree of flowability that does not wet the sample or fill its pores [40]. The principle of this method is illustrated in figure 3.9.

To supplement and further investigate the envelope density measurements and porosity calculations carried out in the Specialization Project [33], additional envelope density measurements were carried out. The envelope density of the non-calcined material of A11 and A11 calcined at 600, 1100, 1800 and 2650 °C were measured. The envelope density measurements were carried out at Sintef Materials and Chemistry by using a GeoPyc 1365. A single grain was placed in the medium

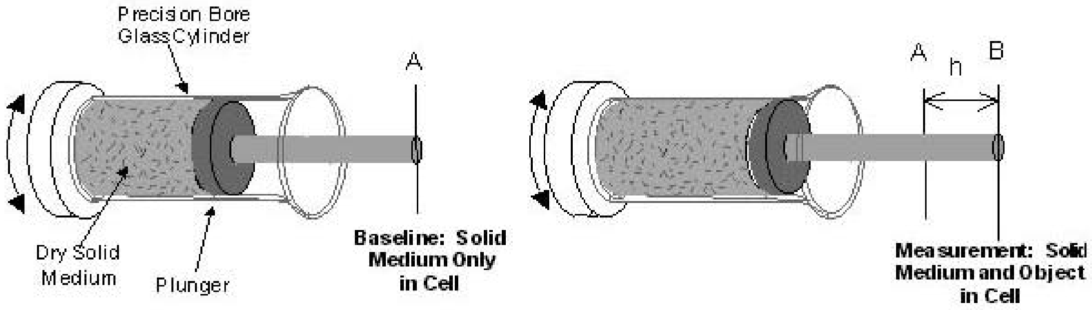

Figure 3.9: Illustration of Archimedes' metod. Volume determination by the displacement of a quasi-fluid [42].

with high degree of flowability and a grain size less than 500 µm. Compressed and displacement measurements were taken in order to allow computation of the samples' volume and the envelope density.

From these results, together with the absolute density measurements carried out at Elkem Carbon Fiskaa, the total porosity of the samples were calculated.

3.2.4 Surface Area Measurments

The specific surface area (SSA) of a material is defined as the total surface area per unit of mass, and can be measured by adsorption using the Bruaner-Emmett-Teller (BET) isotherm. This method measures the amount of gas adsorbed on the surface of the sample as a function of the adsorbate gas pressure. The BET adsorption isotherm is given in Equation 3.12 [43].

$$\frac{1}{V((P_0/P)-1)} = \frac{1}{V_mC} + \frac{C-1}{V_mC}\left(\frac{P}{P_0}\right) \tag{3.12}$$

Where V is the volume of adsorbed gas, V_m is the monolayer absorbed gas volume, P and P_0 are the equilibrium and the saturation pressure of adsorbates and c is the BET constant. The BET constant gives an indication of the magnitude of the adsorbent-adsorbate interactions, which is shown in Equation 3.13.

$$c = exp\left(\frac{E_1 - E_L}{RT}\right) \tag{3.13}$$

E_1 is the heat adsorption for the first layer, and E_L is the heat adsorption for the second and higher layers and is equal to the heat of liquefaction.

The specific surface area, S, is determined from V_m:

$$S = \frac{V_m \cdot N \cdot a}{m \cdot 22400} \tag{3.14}$$

Where N is the Avogadro constant, a is the effective cross-sectional area of one adsorbate molecule and m is the mass of the sample.

Specific surface area measurements were carried out in order to validate and further investigate the results of A11 from the Specialization Project [33]. The non-calcined material of A11 and A11 calcined at 600, 1100, 1800 and 2650 °C were tested. By using a Tristar 3000 Surface area and porosity analyzer the specific surface area were obtained from the BET method of adsorption of nitrogen gas. The experiments were carried out at Sintef Materials and Chemistry.

3.2.5 Thermomechanical Analysis

A thermomechanical analyzer (TMA) can be used to measure thermal mechanical characteristics such as thermal expansion, thermal contraction and softening [44]. The TMA used in these experiments were an Exstar SS6300 TMA. The TMA/SS module consists of two units: one measurement unit and one base unit for processing signals, coupled to Exstar 6000 software.

The measurement unit consists of a furnace, a sample unit, a force generator and a detector. A principle sketch is shown in Figure 3.10. A force is applied to the sample through the expansion probe, and the change in sample length is then detected by the detector.

The TMA sample unit is shown in Figure 3.11. Here, the sample is placed on the base plate in the sample tube during measurements and force is applied to the sample. The probe transmits the change in sample length to the detector, while the thermocouple measures the sample temperature. The thermocouple used is an R type thermocouple, which can measure temperatures ranging from - 50 to 1480 °C. The sample tube, the probe and the sample base plate are all made of alumina. The Exstar SS6300 software allows for alumina sample unit corrections after sample measurements.

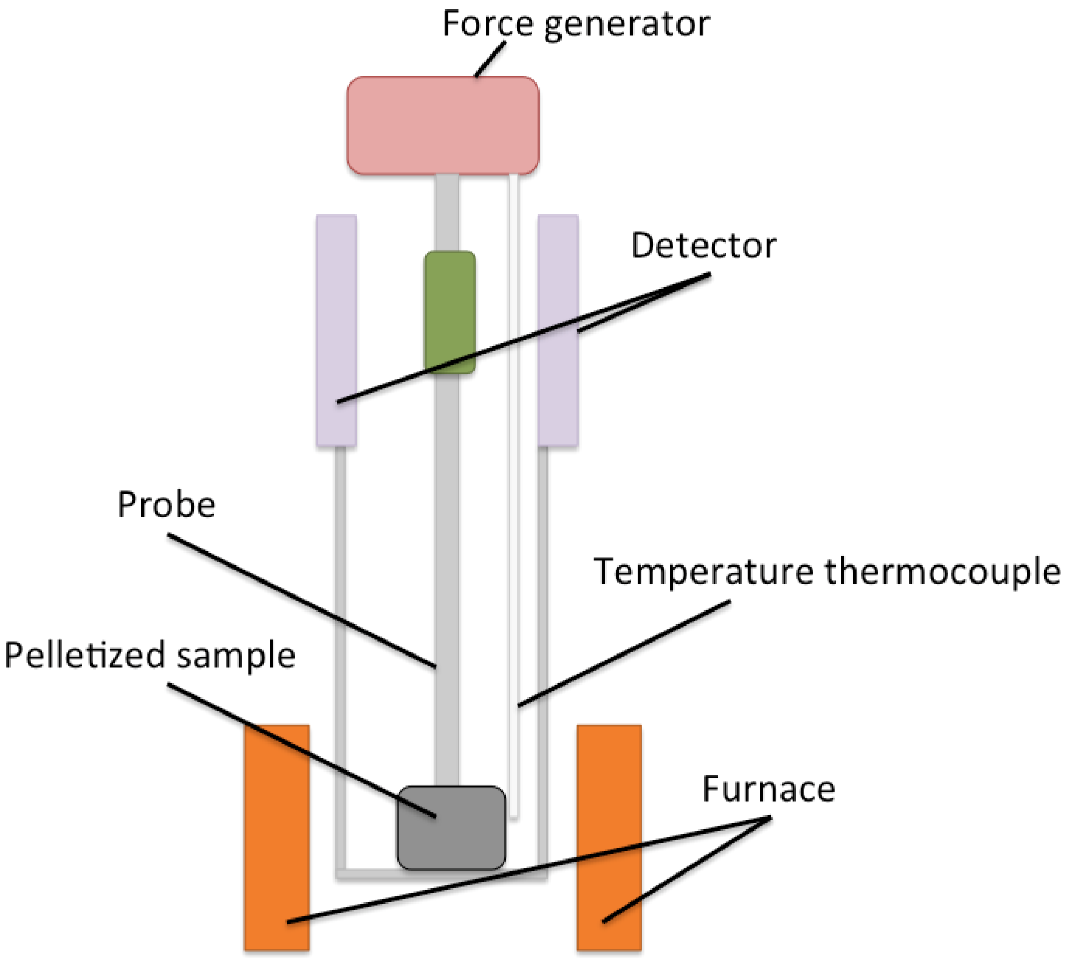

Figure 3.10: Principle sketch of the measurement unit of the TMA.

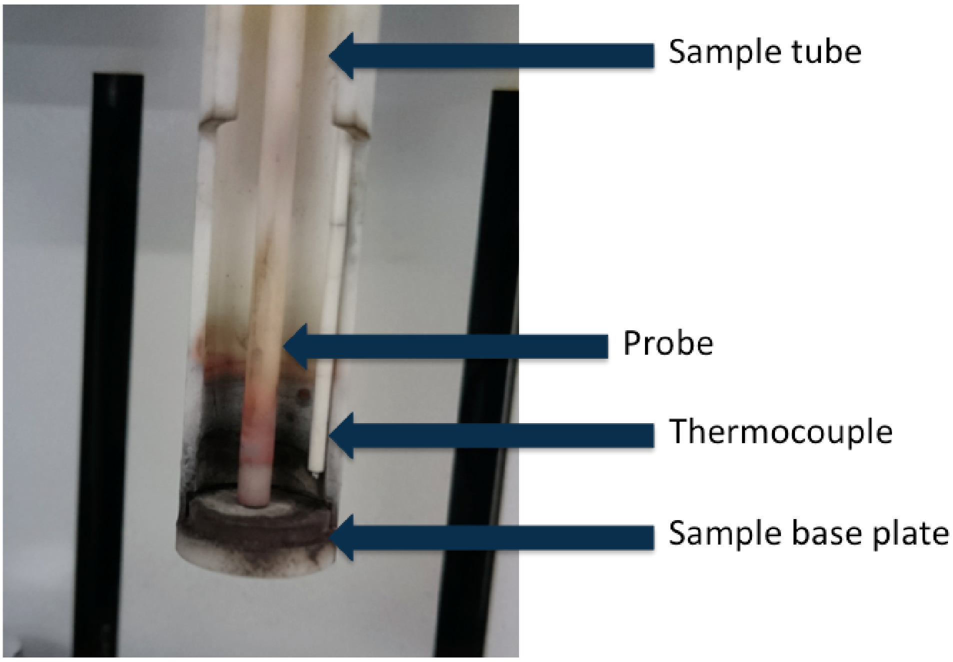

Figure 3.11: TMA sample unit showing the sample tube, the probe, the thermocouple and the sample base plate.

A furnace surrounding the sample unit is used to raise and lower the temperature around the sample unit. The furnace can be lifted up and down, for when placing the sample.

In order to protect the probe from getting contaminated by the sample, a small alumina crucible was used. The crucible was placed between the samle and the probe, surrounding the tip of the probe. The expansion data from the crucible were obtained in order to make corrections. The crucible expansion is given in Appendix B.

The thermal dimensional behaviour of A11, A19, C3, C7 and BIO were investigated by using an Exstar SS6300 thermomechanical analyzer (TMA). A constant N_2 flow rate of $500\,\mathrm{mL\,min^{-1}}$ was held throughout the experiments in order to prevent oxidation of the samples. Each sample was heated from room temperature up to $1400\,^{\circ}\mathrm{C}$ with a heating rate of $10\,^{\circ}\mathrm{C\,min^{-1}}$. The samples were then cooled back down to room temperature with a cooling rate equal to the heating rate, before the same temperature cycle was repeated. The full temperature program is given in Figure 3.12, where the temperature is given as a function of time.

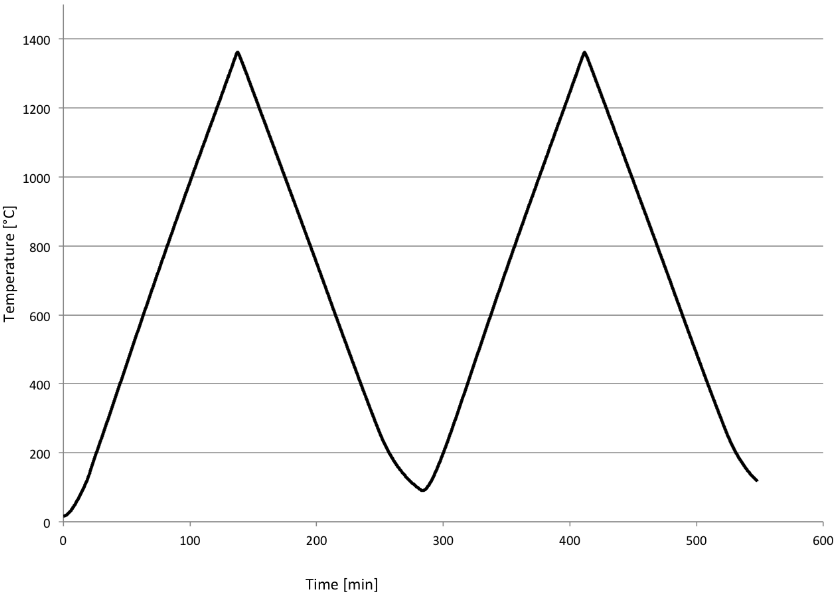

Figure 3.12: The temperature profile used for the TMA experiments. The temperature is given as a function of time. Heating and cooling rate is equal to 10 °C min^{-1}.

From the TMA data, thermal expansion and dilatation graphs were created. The results were corrected for the crucible expansion to obtain the expansion results from only the sample itself. Thermal expansion coefficients were obtained from the slopes of the dilatation curves. All results are base on the average of two measurements.

3.2.6 Thermogravimetry and Differential Scanning Calorimetry

Thermogravimetric analysis (TGA) is a useful technique employed in coal research, but according to Arenillas [27], coal is a very heterogeneous material and the temperature ranges of the various stages of decomposition overlap each other. Hence, only the overall process can be observed.

TGA measures the weight change of a substance, either as a function of increasing temperature, or isothermally as a function of time [45].

Differential scanning calorimetry (DSC) is a technique that measures the difference in the amount of heat required to increase the temperature of a sample and a reference. The result of a DSC experiment is a curve where heat flux is given as a function of temperature or time [46]. Positive and negative peaks in the DSC curve will indicate wether the reactions taking place are exothermic or endothermic.

A simultaneous thermal analysis (STA) combines the TGA and the DSC measurements in one instrument, and makes it possible to obtain TGA and DSC data from the same sample with identical conditions [47]. An STA 449 F3 Jupiter with two different furnaces, one steel furnace and one rhodium furnace, were used in the experiments. The instrument was coupled to Proteus software for data collection.

The Steel furnace runs in the temperature range from −150 °C to 1000 °C, while the rhodium furnace runs from room temperature up to 1650 °C. The cooling mediums for the two furnaces are liquid nitrogen and forced air, respectively. The sample carrier is connected to a type S sensor thermocouple which allows for TGA and DSC measurements from room temperature and up to 1650 °C. There are two seats in the carrier, one for the sample crucible and one for the empty reference crucible. The lids and crucibles are made of alumina. The furnace surrounds the sample carrier, and can be raised up and down for when placing the samples. The STA 449 F3 Jupiter used in the experiments and a sample carrier is shown in Figure 3.13 (a) and (b), respectively.

Thermogravimetric experiments were carried out in the rhodium furnace. The samples were heated from room temperature and up to 1500 °C with a heating rate of 20 $°\mathrm{C\,min^{-1}}$. The inert atmosphere of He was used. In order to be able to make corrections for the background-noise in the DSC curves, a blank sample was run to make a calibration curve. This calibration curve is found in Appendix C.

During some of the experiments, the lids fused to the crucibles and could not be reopened. Therefore, the non-calcined A11 was tested without a lid, to se wether this would have an impact on the results or not. The conclusion was to keep the lids on the crucibles and rather switch to a lower temperature furnace. The lid/crucible investigation is given in Appendix D.

For the rest of the experiments in the STA 449 F3 Jupiter, the rhodium furnace was replaced with the steel furnace. In order to obtain thermogravimetric results also from the rest of the samples at 1500 °C, an Elite tube furnace was used.

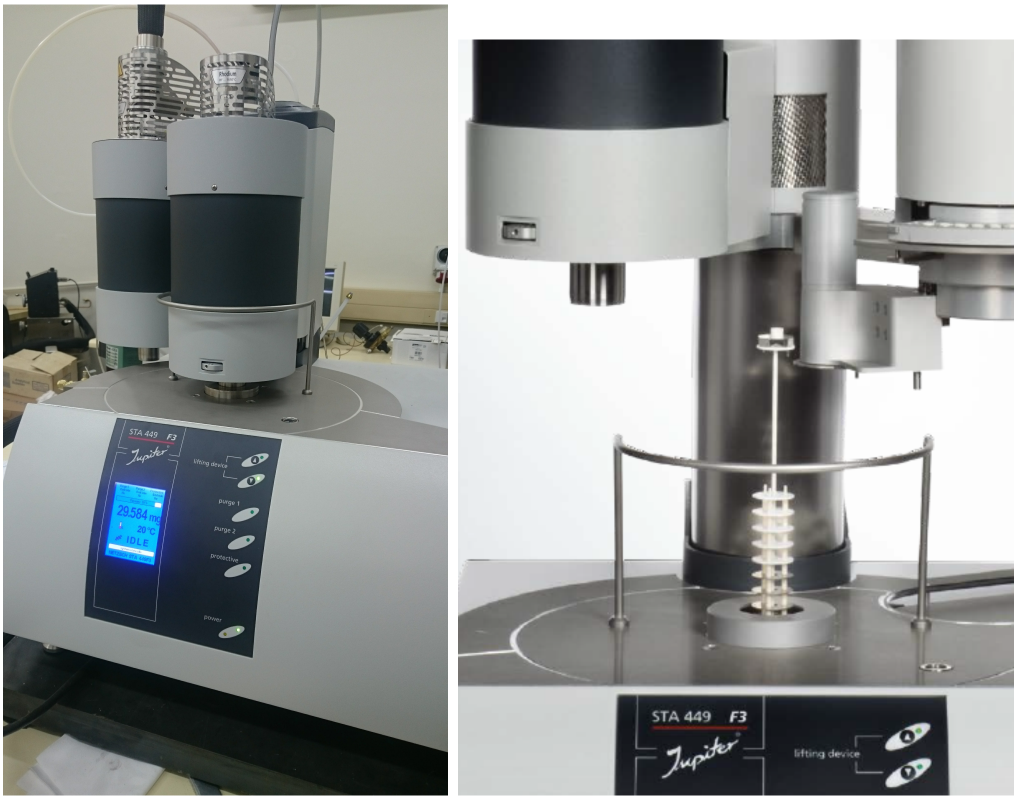

(a) (b)

Figure 3.13: (a) The STA 449 F3 Jupiter used in the experiments.
(b) Sample carrier [47].

For the high temperature thermogravimetric experiments, C3, the non-calcined anthracites and anthracites calcined at 600 and 1100 °C were tested in the STA 449 F3 Jupiter, while C7, BIO and the non-calcined A11 were tested in the Elite tube furnace. Both furnaces ran to about 1500 °C. The non-calcined A11 was tested in both instruments in order to determine the difference between the measurements.

Figure 3.14 shows the Elite tube furnace used in the experiments. Here, the sample is placed in alumina crucibles of about 4.5 cm in diameter and raised up into the furnace. The crucible sits on a sample carrier, connected to a scale which detects the mass change during the temperature run. This scale is very sensitive, and hence the experiments had to be carried out during weekends in order to limit air vibrations. The atmosphere inside the furnace is N_2.


(a) (b)

Figure 3.14: Thermogravimetric analyzer (TGA). (a) Alumina crucible placed on sample carrier. (b) Crucible raised up into the furnace. Sample carrier connected to scale to track the change in sample mass.

For the experiments carried out in the tube furnace, about 10 g of sample were placed in the crucible before raised up to the furnace. The furnace was pre-heated to 100 °C. The sample was then heated to 800 °C with a heating rate of 5 °C min^{-1}, held there for 30 minutes, then heated to 1450 °C with a heating rate of 10 °C min^{-1}. The temperature profile is illustrated in Figure 3.15, where the temperature is given as a function of time.

TG and DSC graphs were obtained from the STA data, and TG graphs were obtained from the tube furnace.

By coupling of the STA 449 F3 Jupiter to gas chromatography and mass spectrometer (GC-MS) and/or Fourier transform infrared (FTIR) spectrometer the off-gases from the thermogravimetric experiments could be analyzed. This evolved gas analysis allows for determination of the nature of volatile products formed during the

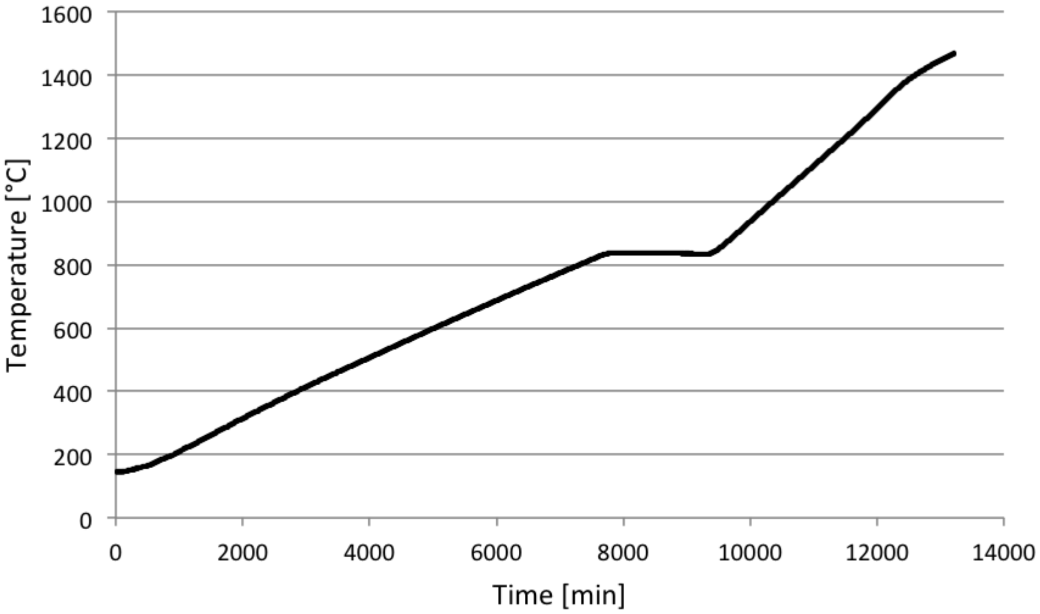

Figure 3.15: The temperature profile of the experiments carried out in the Elite tube furnace.

thermal degradation of the materials. The high temperature thermogravimetric results were used to determine the temperature program for GC-MS measurements.

The coupling of TG to GC-MS and FTIR allows for a simultaneously and continuously measurement of the mass loss and the gaseous products responsible for the mass loss, and the evolution profile can be determined. According to Xie et al. [48] this is the reason why this technique is so widely used in the study of coal pyrolysis and combustion. However, one disadvantage with these techniques is that all the evolved gases can not be distinguished due to possible overlap of either similar wavelengths in FTIR spectra or identical mass in MS spectra.

3.2.7 Gas Chromatography and Mass Spectrometry

Gas chromatography and mass spectrometry (GC-MS) can be used in combination with TGA to determine which decomposition products that evolve from the samples during heating according to their mass [48]. The gases released from the sample during heating in the TGA are transferred by a carrier gas to the GC, where the components can be collected. The components are then separated by GC in the GC-column, ionized and the peaks can be identified by MS [45]. The different retention times in the column allows the MS to detect the ionized molecules separately. This separation is done by using the ionized fragments mass-to-charge ratio, m/z. One downside by this method is that there might be some overlap in MS spectrum if the molecules have identical mass [48].

When the MS is directly coupled to the TGA, the detection limit is usually less than 1 ppm [48], but heavy molecules can not be detected. TG/GC-MS however, are capable of identifying high molecular mass compounds, although time- and temperature dependent gas evolution profiles can not be obtained in this case [48].

The STA 449 F3 Jupiter was coupled to Agilent Technologies 7890B GC System and Agilent Technologies 5977A MSD to obtain GC-MS data. Helium was used as carrier gas with a flow rate of $20\,\mathrm{mL\,min^{-1}}$. A flame ionization detector (FID) was used in the GC. The detection range used was 5-550 Da.

One method that can be used to determine the characteristics of the off-gases is to raise the temperature to a point where a reaction takes place and trigger the GC-MS at this point. Further, the sample should be quenched to a lower temperature and held there, in order to make sure that no new reactions take place. This will make is possible to obtain results for a specific temperature, where there is no overlap with higher temperatures.

This method was tested for the non-calcined material of A11, and the thermogravimetric data from the high temperature experiments were used to determine the temperature profile. The non-calcined A11 was first heated from about 100 °C up to 430 °C with a heating rate of $20\,\mathrm{°C\,min^{-1}}$, the GC-MS measurements were triggered at 430 °C before the temperature was quenched to 330 °C by the use of liquid nitrogen and kept at this temperature. The temperature profile is shown graphically in Figure 3.16.

Since this method did not give significant results, the GC-MS system was tested with a Grubbs Catalyst 1st generation to make sure that the system was functioning properly. The method was then changed to a continuous method, where the GC-MS was triggered already when the heating started. The samples were heated from room temperature and up to 900 and 1000 °C with continuous GC-MS mea-

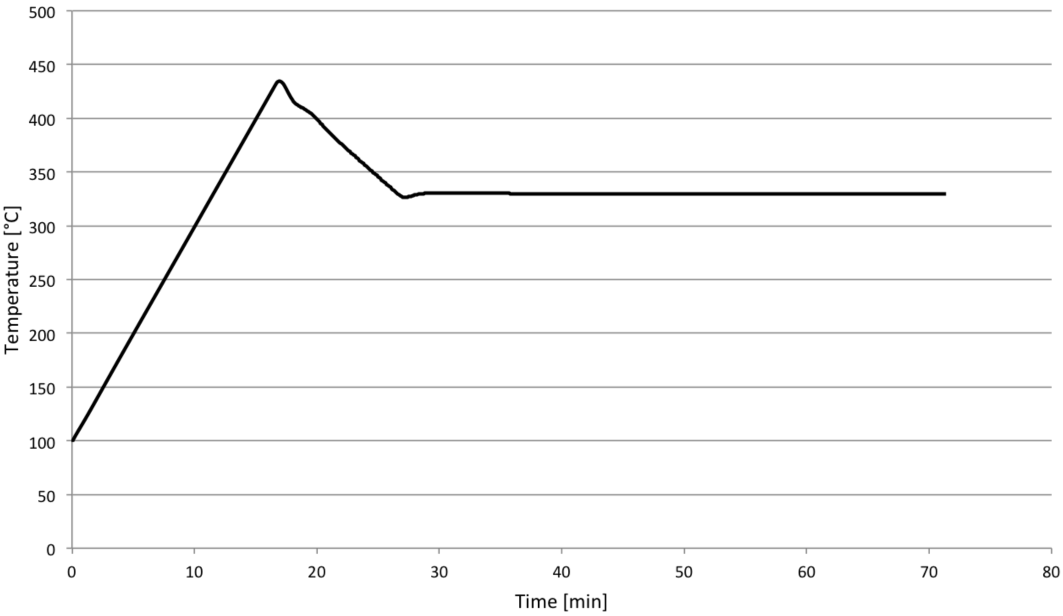

Figure 3.16: The temperature profile used for the GC-MS measurements of non-calcined A11. The GC-MS was triggered at 430 °C.

surements. Due to the overlap in m/z for N_2 and CO, infrared (IR) spectroscopy was also used for the continuous method. The off-gases from the STA 449 F3 Jupiter were split between the GC-MS and the IR to obtain both mass spectra and infrared spectra.

The intensity of the entire range of masses obtained from the GC-MS could then be summarised in a total ion current chromatogram (TIC) as a function of time. This chromatogram shows the total intensity of all masses, but by extracting m/z values, signals from a single mass can be studied as a function of time. In the extracted ion chromatogram (EIC) the value of 44 m/z, corresponding to the mass of CO_2, was extracted. By integrating the results as a function of time, a quality spectrum of the peaks could be produced. This integration and quality spectrum will give information about retention times, heights and areas of these CO_2 peaks at different times. The area under the GC peak is proportional to the amount of CO_2.

3.2.8 Fourier Transform Infrared Spectroscopy

In addition to the GC-MS instrument, the STA 449 F3 Jupiter was coupled to a Bruker TGA-IR to obtain Fourier transform infrared (FTIR) spectra. The TGA-IR utilizes infrared radiation in the mid-infrared region of 4000 to 200 cm^{-1}. Bruker Opus Spectroscopy software were used to collect and process the FTIR data from the experiments.

In Fourier transform infrared spectroscopy, radiation from a light source is divided into two beams by a beam splitter so that the paths of the two beams are different. The two beams are reflected onto one moving and one stationary mirror, before they are recombined. The recombined beam is then passed through the sample and detected by a detector [49]. The detector measures the difference in intensity of the two beams as a function of the difference of paths, and converts the analog spectral output into an electrical signal. This electrical signal is processed by using Fourier transformation to obtain the final spectrum [50].

When the beam is passed through the sample, the infrared radiation interacts with the vibrating dipole moments of the sample molecules, and absorbs the wavelengths which causes the change of dipole moment [49]. This interaction provides the characteristic spectrum from which structure information of a molecule can be obtained [50]. The final Fourier transform spectrum is a graph with infrared light absorbance on the y-axis and the absorbed wavelength on the x-axis. Comparison of the final spectrum with a spectra library will allow for identification of the molecules present in the sample.

Figure 3.17 and Figure 3.18 show examples of library spectra for comparison. Both figures are collected from the spectra library of the Bruker Opus Spectroscopy software. Figure 3.17 shows the characteristics of H_2O, with peaks at 3800 - 3500 cm^{-1} and 2000 - 1300 cm^{-1}. The characteristic peak of CO_2 can be found around 2400 - 2300 cm^{-1}, and the double peak of CO around 2300 - 2000 cm^{-1}, both given in Figure 3.18. CO_2 is given as the blue line, while CO appear as green.

Infrared spectra of PAHs include bands at around 3000 cm^{-1} [51], [52]. The strongest of these bands are due to C-H stretching modes. Other bands might also be observed at about 1600 and 1150 cm^{-1}.

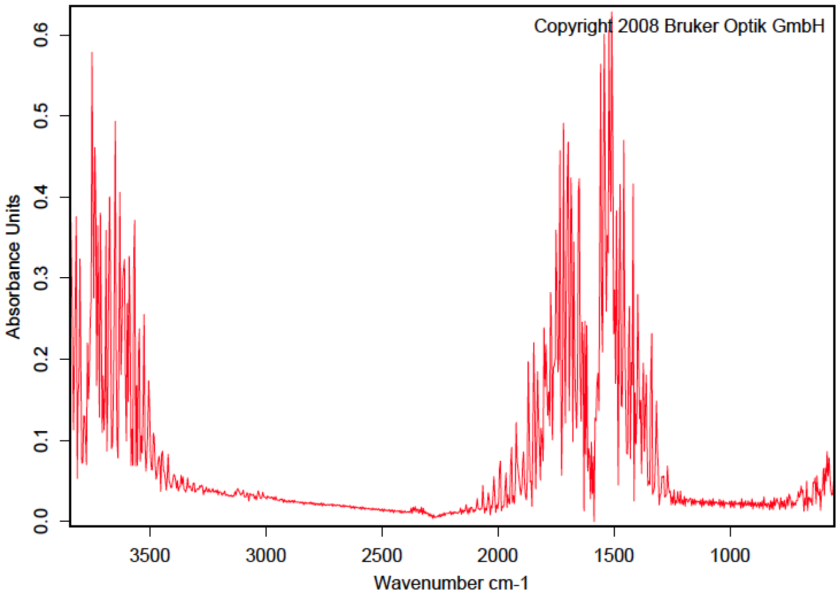

Figure 3.17: FTIR spectra of H_2O collected from the spectra library of the Bruker Opus Spectroscopy software.

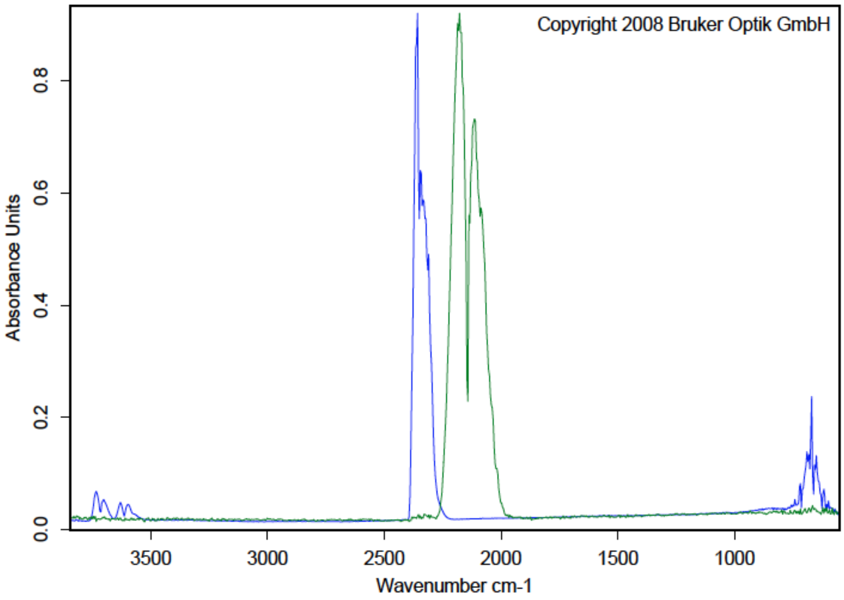

Figure 3.18: FTIR spectra of CO_2 and CO collected from the spectra library of the Bruker Opus Spectroscopy software.

In TGA-FTIR, Gram-Schmidt curves or chemigrams can be obtained. This curve presents the summarised intensities of the evolved gases as a function of time and temperature [49]. The Gram-Schmidt curves operate in arbitrary units, where an arbitrary unit is a relative unit of measurement to show the ratio of the amount of intensity to a predetermined reference measurement of the instrument. Hence, the unit only serves to compare multiple measurements performed in the same instrument, with the same conditions.

For the FTIR and GC-MS split experiments, the non-calcined A11 and A19 were tested from room temperature and up to 900 °C. Both of the non-calcined anthracites, the anthracites calcined at 600 °C, both cokes and the charcoal were tested from room temperature and up to 1000 °C. A heating rate of $20\,°\mathrm{C}\,\mathrm{min}^{-1}$ was used in both cases, He of $20\,\mathrm{mL}\,\mathrm{min}^{-1}$ were used as the carrier gas. The TGA-IR had to be cooled with liquid nitrogen before the experiments could be carried out.

From the Bruker Opus Spectroscopy software three-dimensional spectra could be obtained, where the absorbance is given as a function of both wavelength and time. Two-dimensional spectra could then be extracted at different times, to show the absorbance as a function of wavenumber at given times. By integrating the peaks of CO_2 and CO at different times, information about the amount of the species could be obtained.

3.2.9 Multiple Linear Regression Analysis

Multiple linear regression (MLR) analysis is a statistical method used to establish the relationship between different variables, and is a commonly applied method [53], [54], [55].

Relationships between a dependent variable and two or more independent variables are modeled by fitting a multi-linear equation to collected data. The relationship between the dependent variable, y, and the n independent variables, x, is denoted by the equation:

$$y_{\mathrm{modeled,\ i}} = c_0 + c_1 x_1 + c_2 x_2 + ... + c_n x_n \tag{3.15}$$

where c_n are the know parameters such as e.g. the sulfur, nitrogen or hydrogen content of the coal, the density or the interlayer spacing.

These parameters might be varied in order to minimize the root-mean-square error (RMSE) difference between the modeled and the experimental or measured values, and hence find the optimum equation to describe the desired dependent variable. The RMSE equation is given below:

$$RMSE = \sqrt{\frac{\sum_{i=1}^{n} (y_{\text{measured, i}} - y_{\text{modeled, i}})^2}{n}} \tag{3.16}$$

In order to relate the thermal expansion and the porosity of the anthracites to other coal characteristics, MLR was carried out by a fit-for-purpose Matlab program.

Chapter 4

Results

This chapter presents the results from the surface area analysis and porosity calculations, as well as evolved gas analysis during heating, and the thermomechanical analysis of both single grains and pelletized material. Optimum equations obtained from the multiple linear regression analysis will also be presented, correlating certain properties of the materials.

4.1 Dilatometry

The linear thermal expansion of single grains of A11 calcined at 1100, 1800 and 2650 °C are given in Figure 4.1. The thermal expansion is given in terms of percentage of change in the longitudinal direction for each grain, given as a function of time. The temperature is illustrated by the dotted line, with a maximum temperature of 1550 °C. The temperature is given as a function of time with a heating and cooling rate of about 115 degrees per hour.

Figure 4.2 shows the dilatation graphs for all samples, where the expansion is given as a function of temperature. The thermal expansion coefficients (TEC) were calculated from the dilatation graphs obtained from the thermal expansion experiments. The TECs are obtained from the slopes of the dilatation curves, in intervals of 50 degrees, and are shown in Figure 4.3. Table 4.1 give the average TEC values, calculated from the steepest part of the dilatation curves in the temperature range of about 1200 to 1500 °C.

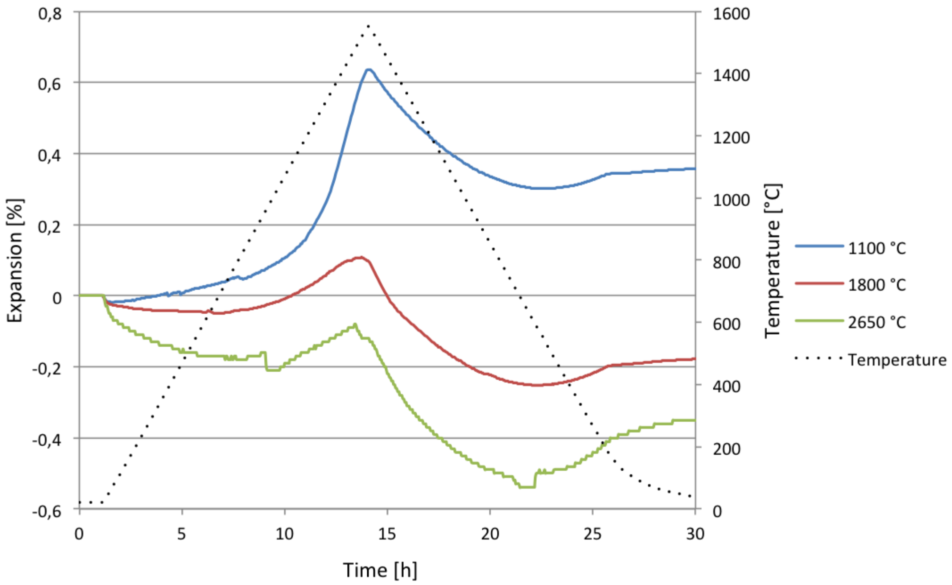

Figure 4.1: Linear thermal expansion of single grains of the material calcined at 1100, 1800 and 2650 °C given as a function of time. The temperature is illustrated by the dotted line.

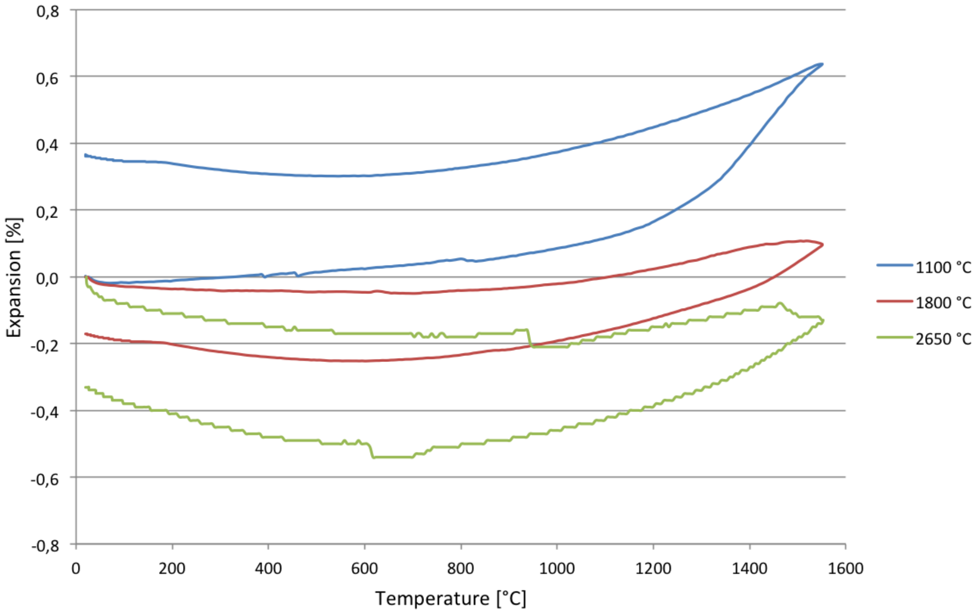

Figure 4.2: Dilatation curves where the expansion is given as a function of temperature.

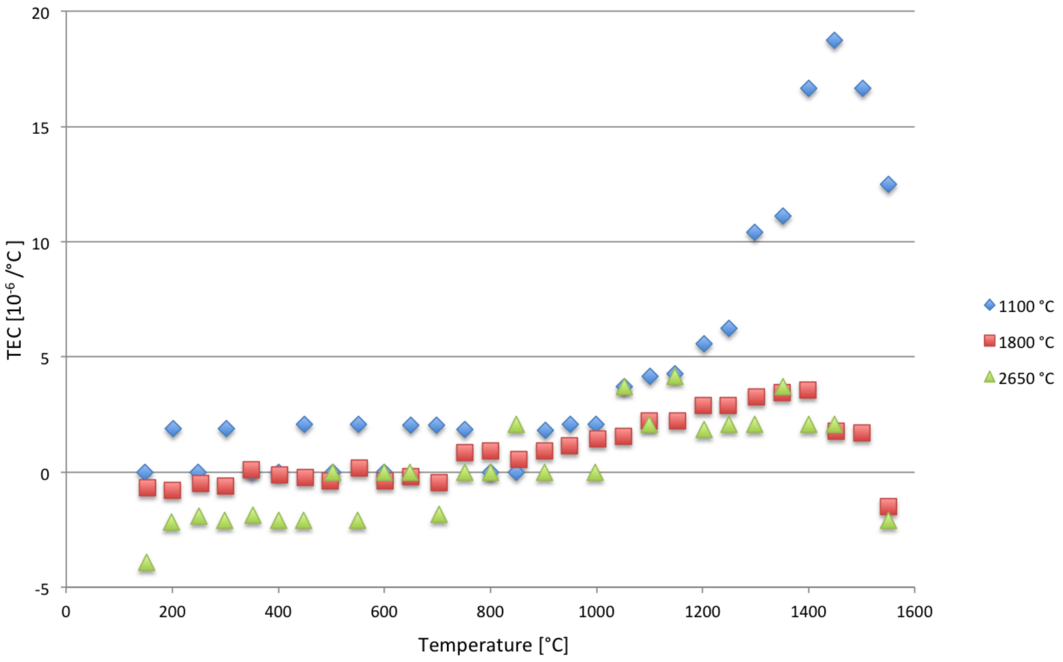

Figure 4.3: Thermal expansion coefficients (TECs) of the single grains calcined at 1100, 1800 and 2650 °C, calculated from intervals of 50 degrees.

Table 4.1: Average thermal expansion coefficients (TECs) calculated in the temperature range of 1200 to 1500 °C for all samples.

Temperature Sample [°C]	Thermal Expansion Coefficient (TEC) [$\cdot 10^{-6}$ °C^{-1}]
1100	15.4
1800	3.4
2650	2.6

As can be seen from Figure 4.3 and Table 4.1, the TEC decreases with increasing calcining temperature. For the material calcined at 1100 °C, the TEC increases with increasing temperature during the experiment, while the materials calcined at 1800 and 2650 °C are more stable. At the maximum calcining temperature of 2650 °C the average TEC is equal to $2.6 \cdot 10^{-6}$ $°C^{-1}$. The steepest slope, hence the highest TEC, is observed for the material calcined at 1100 °C.

From Figure 4.1 and 4.2, a lot of background noise can be observed in the results for the material calcined at 2650 °C. All the materials expand from about 800 °C and up to the maximum temperature, and shrink until the temperature again reaches about 800 °C.

The length of each grain before and after the experiment were measured with a caliper. The results are given in Table 4.2. The measurements show no change between initial and final length for any of the samples.

Table 4.2: The initial and final length of each grain measured with caliper.

Temperature Sample [°C]	Initial length [mm]	Final length [mm]	Change of length [%]
1100	10.17	10.17	0
1800	12.49	12.49	0
2650	12.01	12.01	0

4.2 Density Measurements and Porosity Calculations

The results from the GeoPyc envelope density measurements are given in Table 4.3. The average values are given from three measurements, and show a standard deviation of 3 % or less.

By applying Equation 3.11 and using the average envelope density from Table 4.3 and the absolute density given in Table A.3, the porosity was calculated. The calculated porosities are given in Table 4.4 and shown graphically in Figure 4.4.

Table 4.3: Envelope density measurements of A11 from GeoPyc with standard deviation.

Temperature Sample [°C]	1 [g cm^{-3}]	2 [g cm^{-3}]	3 [g cm^{-3}]	Average [g cm^{-3}]	Std. deviation [g cm^{-3}]
0	1.60	1.52	1.55	1.56	0.04
600	1.55	1.61	1.59	1.57	0.03
1100	1.73	1.83	1.77	1.78	0.05
1800	1.59	1.66	1.56	1.60	0.05
2650	1.68	1.74	1.68	1.70	0.04

Table 4.4: Absolute- and envelope density of A11 measured from AccuPyc and GeoPyc respectively and the calculated porosity.

Temperature Sample [°C]	Absolute density [g cm^{-3}]	Envelope density [g cm^{-3}]	Porosity [%]
0	1.978	1.56	21.30
600	1.962	1.58	19.28
1100	1.954	1.78	9.09
1800	1.756	1.60	8.71
2650	1.989	1.70	14.53

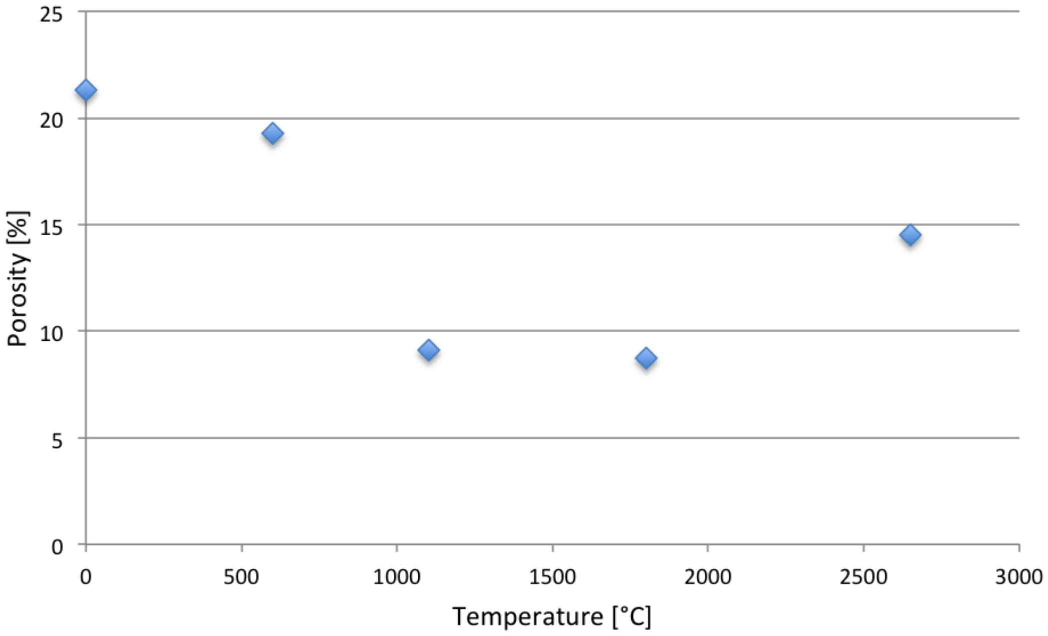

Figure 4.4: Percent porosity given as a function of calcining temperature for A11. The porosity is calculated from absolute and envelope density measurements.

As can be seen from the figure, the porosity decreases with increasing calcining temperature up to 1800 °C, and increases between 1800 and 2650 °C. The biggest decrease of about 10 % is observed between 600 and 1100 °C, where most of the volatiles evaporate and the crystal structure rearranges and densifies.

4.3 Surface Area Analysis

The results from the BET surface area analysis of A11 are given in Table 4.5 and shown graphically in Figure 4.5. The BET surface area is given as a function of calcining temperature.

Table 4.5: BET surface area of all samples.

Temperature [°C]	BET surface area [$\mathrm{m^2\,g^{-1}}$]
0	15.58
600	27.39
1100	0.16
1800	0.66
2650	2.47

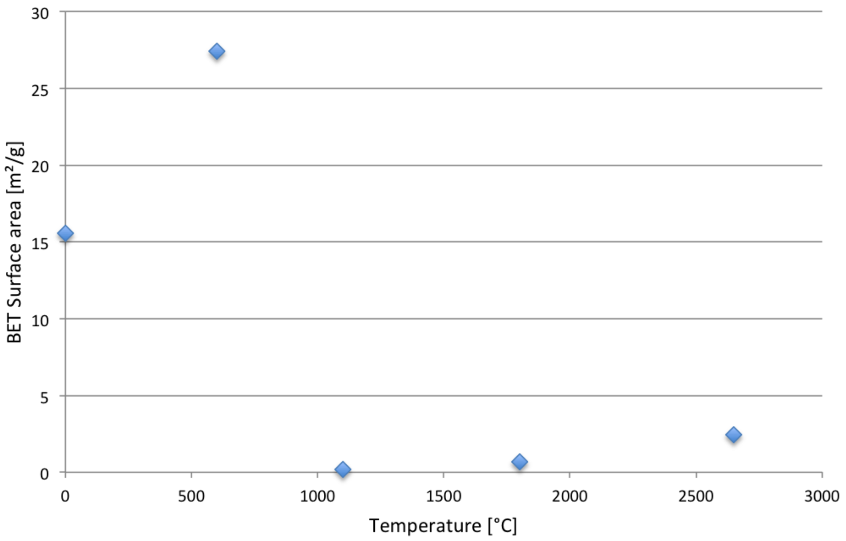

Figure 4.5: BET surface area of A11 given as a function of calcining temperature.

As can be seen from the figure, there is an increase in BET surface area between the non-calcined material and the material calcined at 600 °C. Between 600 and 1100 °C there is a large decrease where the BET surface area changes from 27.4 to $0.2\,\mathrm{m^2\,g^{-1}}$. From 1100 up to 2650 °C there is a small, incremental increase.

4.4 Thermomechanical Analysis

For all the thermomechanical analysis, the results are given as the average of two measurements. Only the average values are given in this chapter, while all the measurements are given in Appendix F in its full. The variation between the two measurements of each sample was found to be very small.

4.4.1 Anthracite, A11

The dimensional behaviour of the non-calcined material of A11 and A11 calcined at 600, 800, 1000, 1200 and 2000 °C are given in Figure 4.6. The expansion of the pellets is given in percentage and measured vertically. Both the expansion and the temperature are given as functions of time, where the expansion is given on the left y-axis and the temperature is given on the right. Figure 4.7 shows the dilatation curves from the same experiments, where the expansion is given as a function of temperature.

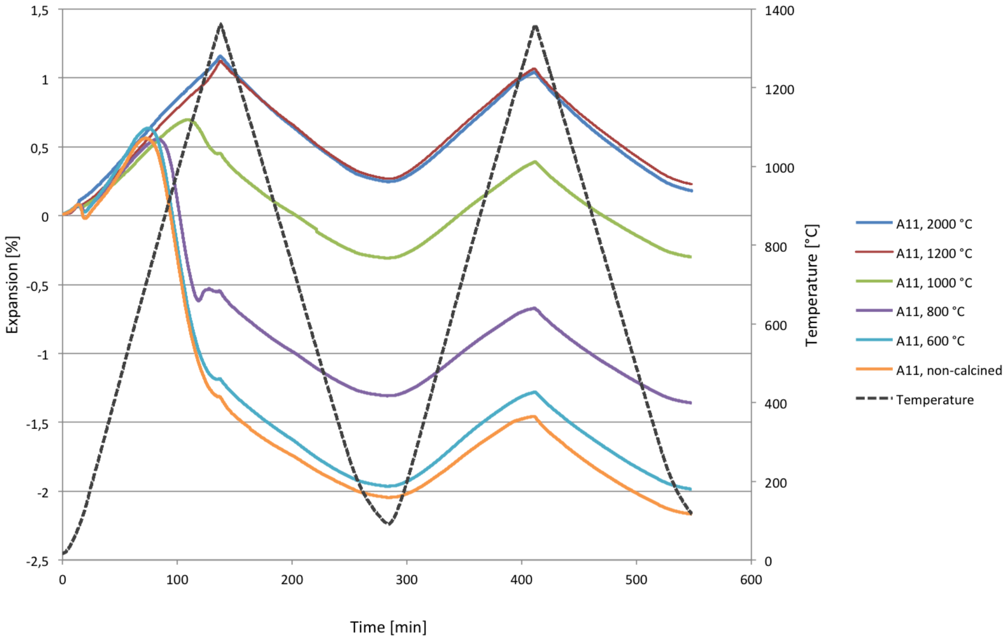

Figure 4.6: The dimensional behaviour of the A11 samples given as a function of time. The temperature profile is illustrated by the dotted line.

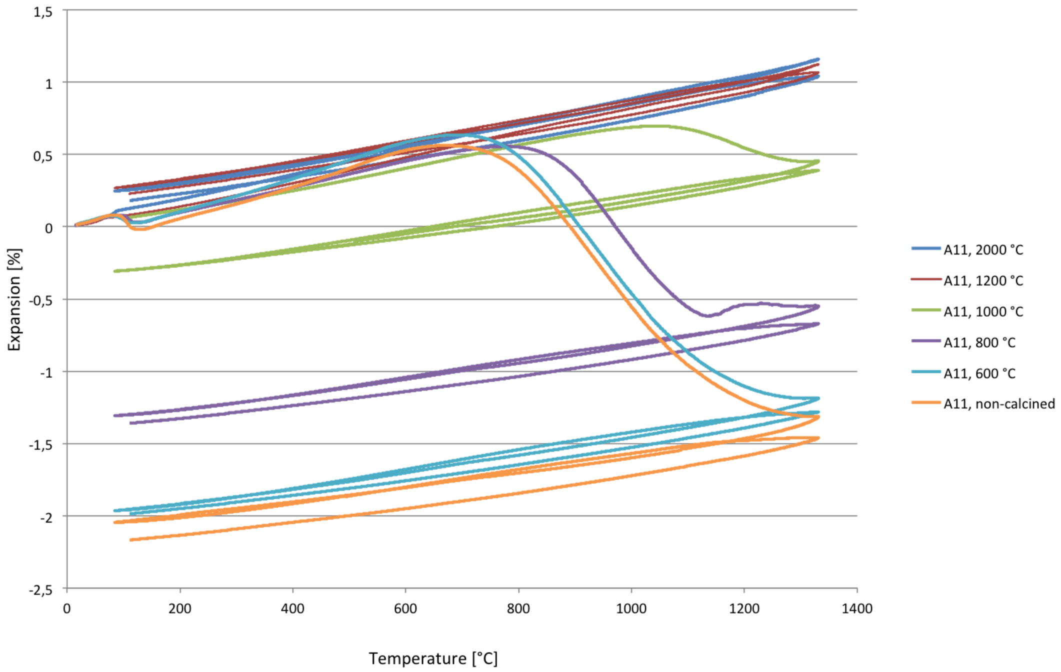

Figure 4.7: Dilatation graphs of all A11 samples. Expansion is given as a function of temperature.

As can be seen from Figure 4.6 and 4.7, there is a shrinkage of the non-calcined material and the materials calcined at 600, 800 and 1000 °C during the first heating to 1400 °C. First, there is an expansion up to about 800-1000 °C, before the shrinkage. At the maximum temperature there is also a small expansion, and the material continue to shrink as the temperature decreases.

For the second temperature cycle, all the materials contract the same amount during cooling as they expand during heating, with maximum expansion at the maximum temperature. For the materials calcined at 1200 and 2000 °C the pellets contract the same amount during cooling as they expand during heating for both temperature cycles. Both materials have a maximum expansion of about 1.1 % at 1400 °C.

The biggest shrinkage of about 2 % is observed for the non-calcined material, and the shrinkage decreases with increasing calcining temperature. For the material calcined at 1000 °C the shrinkage is about 0.3 %. There are no shrinkage observed for the materials calcined at 1200 and 2000 °C. The expansion of the pellets at the beginning of each temperature cycle as well as the expansion at the maximum temperature of about 1400 °C are given in Table 4.6.

Table 4.6: Expansion of the A11 pellets at the beginning of each temperature cycle and the the maximum temperature. Final Expansion is also given. All expansions are given in percentage of change from initial size.

Temp. [°C]	Start 1 [%]	Expansion 1 [%]	Start 2 [%]	Expansion 2 [%]	End [%]
0	0	-1.32	-2.05	-1.46	-2.17
600	0	-1.19	-1.96	-1.28	-1.99
800	0	-0.55	-1.31	-0.67	-1.36
1000	0	0.45	-0.31	0.39	-0.30
1200	0	1.12	0.27	1.07	0.23
2000	0	1.16	0.25	1.04	0.18

From the dilatation curves in Figure 4.7, the thermal expansion coefficients (TECs) were calculated. The TECs were calculated in intervals of 50 degrees and are shown graphically in Figure 4.8 and 4.9. The average value of TEC for each sample with standard deviation is given in Table 4.7. The values are given as the average between 200 and 500 °C for the first temperature cycle of the non-calcined material and the materials calcined at 600 and 800 °C. For the second temperature cycle of these materials, and for both temperature cycles of A11 calcined at 1000, 1200 and 2000 °C, the average TECs are calculated between 400 and 1100 °C.

For the non-calcined material there is a big difference between the TEC values for the first and the second temperature cycle. This is also true for the materials calcined at 600 and 800 °C. During the first temperature cycle, the TEC increases with increasing temperature between 200 and 600 °C, before the shrinkage occur and the TEC becomes negative. The maximum TEC of about 13 $\cdot 10^{-6}$ °C^{-1} is observed for the non-calcined material and the material calcined at 600 °C during the first temperature cycle around 600 °C.

For the second temperature cycle, a gradual increase in TEC up to about 400 °C is observed, followed by small variations in TEC values between 400 and 1100 °C. Finally, there is a decrease in TEC up to the maximum temperature.

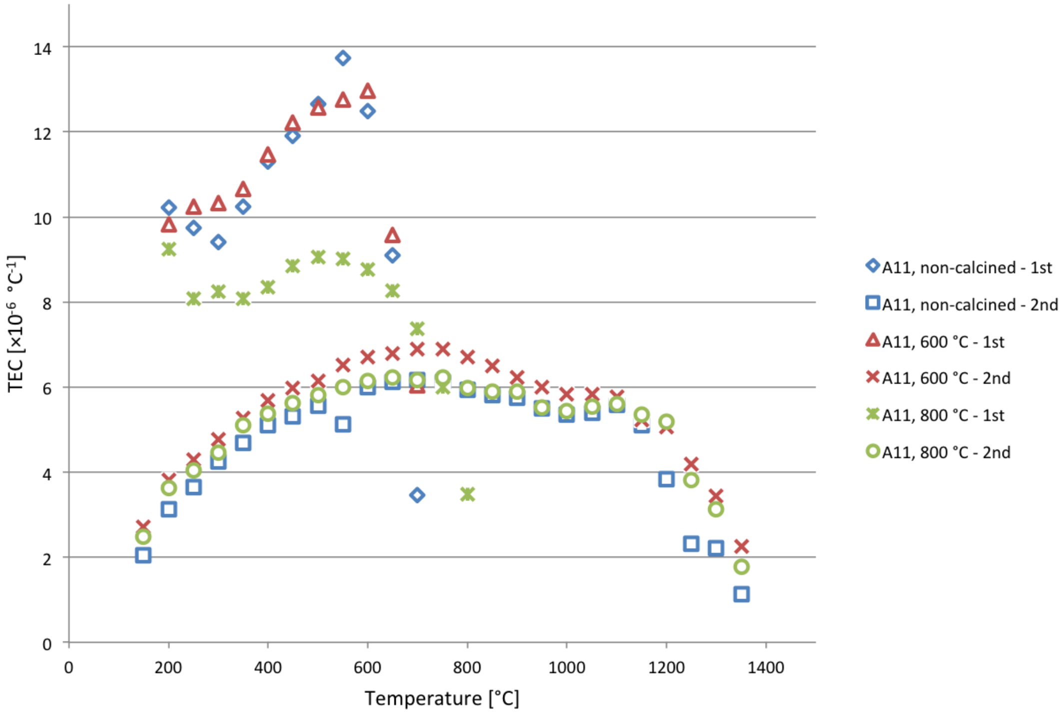

Figure 4.8: Thermal expansion coefficients given as a function of temperature during heating for both temperature cycles of the non-calcined material of A11, and A11 calcined at 600 and 800 °C.

Similar behaviour of the TEC is also observed for the material calcined at 1000 °C and for the second temperature cycle of the materials calcined at 1200 and 2000 °C. For the first temperature cycle of the materials calcined at 1200 and 2000 °C, the TEC values follow the same trend up to 1100 °C. However, as the TEC values of the other samples decrease from 1100 °C and up to the maximum temperature, the TECs now continue to increase. The materials calcined at 1200 and 2000 °C have similar TEC values of about 8.5 $\cdot 10^{-6}$ °C^{-1} for the first temperature cycle, and 7 $\cdot 10^{-6}$ °C^{-1} for the second temperature cycle. A small decrease in TEC values between the first and second temperature cycle can be seen for all three samples.

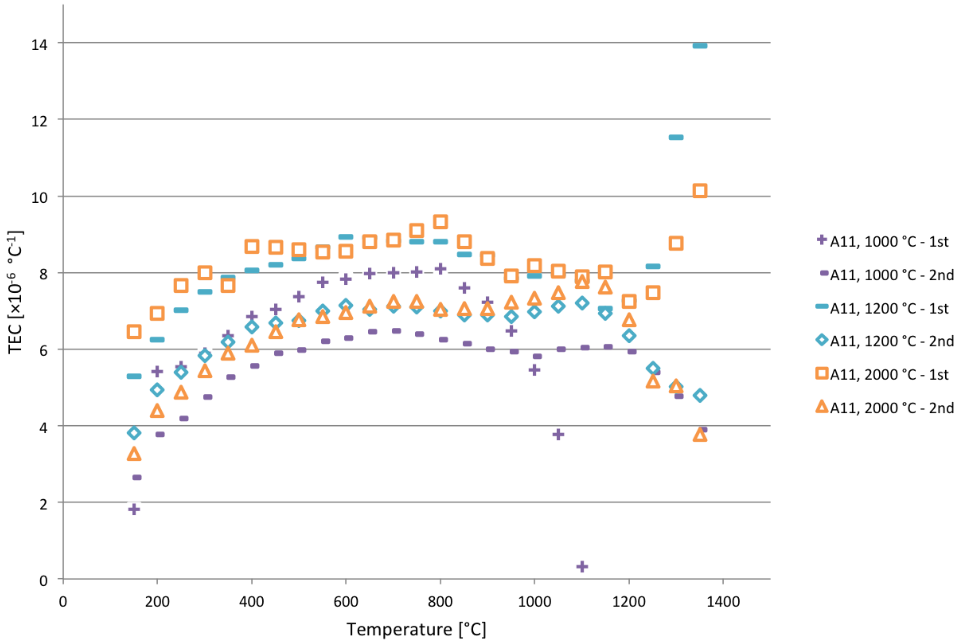

Figure 4.9: Thermal expansion coefficients given as a function of temperature during for both temperature cycles of A11 calcined at 1000, 1200 and 2000 °C.

Table 4.7: Average TEC for both temperature cycles of all A11 samples with standard deviation. The average for non-calcined and calcined at 600 and 800 °C during the fist temperature cycle is calculated between 200 and 500 °C. TECs of the second temperature cycle of these materials, and both temperature cycles of A11 calcined at 1000, 1200 and 2000 °C is calculated between 400 and 1100 °C.

Temperature [°C]	TEC 1 [$\cdot 10^{-6}$ °C^{-1}]	Std. deviation [$\cdot 10^{-6}$ °C^{-1}]	TEC 2 [$\cdot 10^{-6}$ °C^{-1}]	Std. deviation [$\cdot 10^{-6}$ °C^{-1}]
0	10.8	1.2	5.7	0.4
600	11.0	1.1	6.3	0.4
800	8.6	0.5	5.8	0.3
1000	6.6	2.1	6.1	0.3
1200	8.4	0.4	7.0	0.2
2000	8.6	0.4	7.0	0.4

4.4.2 Anthracite, A19

Figure 4.10 shows the dimensional behaviour of A19 during two temperature cycles from room temperature, up to about 1400 °C and back down to room temperature. In the figure, the temperature profile is illustrated as the black, dotted line.

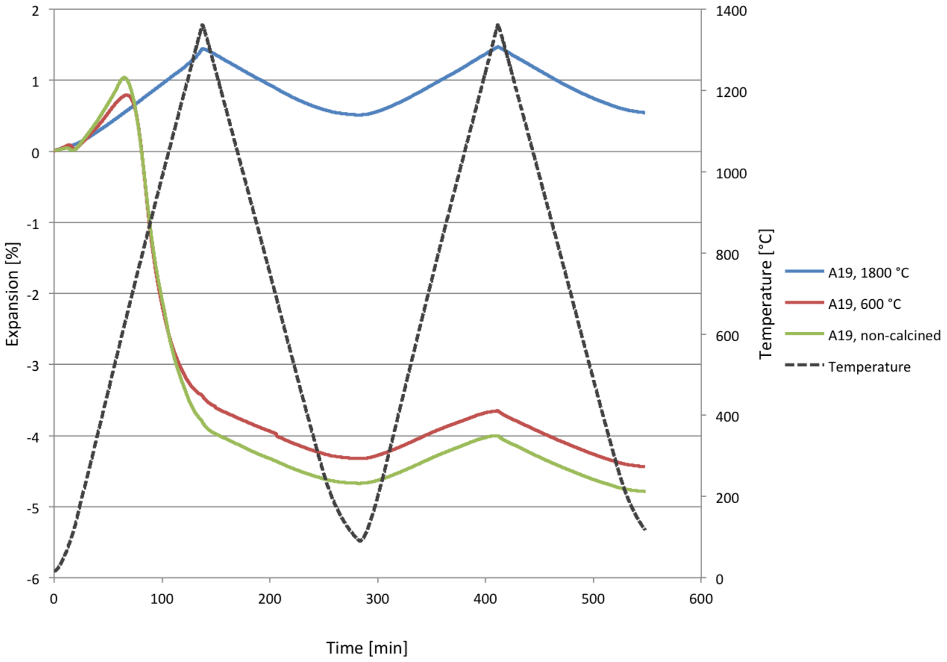

Figure 4.10: Expansion of pelletized A19 given as a function of time. The temperature profile is illustrated by the dotted line.

As can be seen from the figure, there is first a small expansion up to about 600 °C during the first temperature cycle for the non-calcined material of A19 and A19 calcined at 600 °C. From here, there is a big shrinkage up to the maximum temperature of about 4.5 % for both samples. During the second temperature cycle, both the non-calcined material and the material calcined at 600 °C contract the same amount during cooling as they expand during heating. For the material calcined at 1800 °C, the pellet contracts the same amount during cooling, as it expands during heating for both temperature cycles. The maximum expansion for the material calcined at 1800 °C is about 1.6 % for both temperature cycles. All the dimensional changes of the A19 samples are given in Table 4.8.

Table 4.8: Expansion of the A19 pellets at the beginning of each temperature cycle and the the maximum temperature. Final Expansion is also given. All expansions are given in percentage of change from initial size.

Temp. [°C]	Start 1 [%]	Expansion 1 [%]	Start 2 [%]	Expansion 2 [%]	End [%]
0	0	-3.81	-4.67	-4.00	-4.79
600	0	-3.44	-4.32	-3.65	-4.44
1800	0	1.56	0.66	1.58	0.69

The dilatation graphs of the A19 materials are given in Figure 4.11, where the expansion is given as a function of temperature. The TECs were calculated from the slopes of the dilatation curves in intervals of 50 degrees, and are shown graphically in Figure 4.12. Average TEC values are given in Table 4.9. Here, the TEC values from the first temperature cycle of the non-calcined material and the material calcined at 600 °C are given as the average of the TECs between 200 and 500 °C. For the second temperature cycle of these samples, and for both temperature cycles of the material calcined at 1800 °C, the values are given as the average of the TECs between 400 and 1100 °C. Standard deviation is also given in the table.

Table 4.9: Average TEC for both temperature cycles of each sample of A19. Standard deviations are also given. The average of the non-calcined and calcined at 600 °C is calculated between 200 and 500 °C. For the second temperature cycle of these samples, and for both temperature cycles of the material calcined at 1800 °C, the average is calculated between 400 and 1100 °C.

Temperature [°C]	TEC 1 [$\cdot 10^{-6}$ °C^{-1}]	Std. deviation [$\cdot 10^{-6}$ °C^{-1}]	TEC 2 [$\cdot 10^{-6}$ °C^{-1}]	Std. deviation [$\cdot 10^{-6}$ °C^{-1}]
0	20.4	2.1	6.0	0.3
600	16.1	1.7	6.0	0.4
1800	10.6	0.4	7.6	0.6

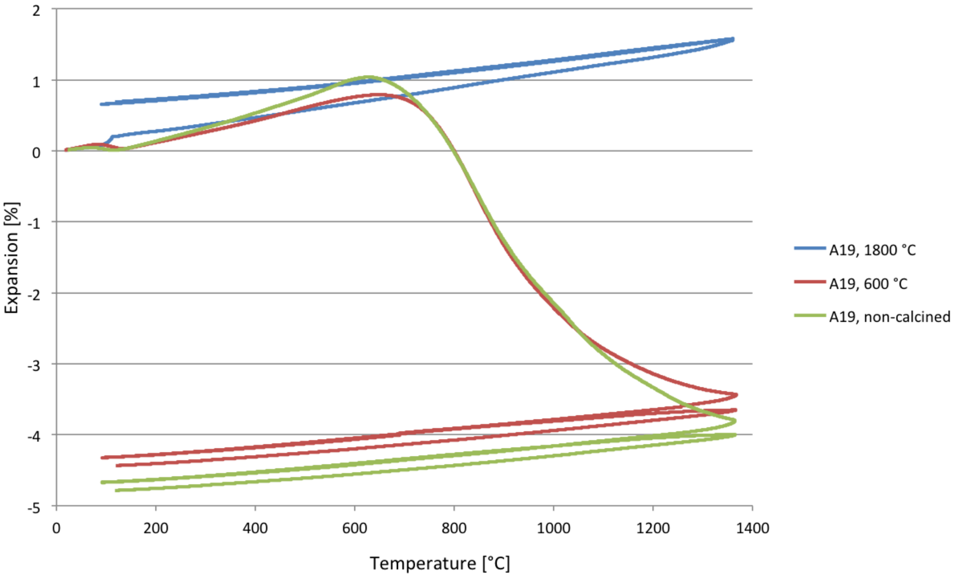

Figure 4.11: Dilatation graphs of all A19 samples. Expansion is given as a function of temperature.

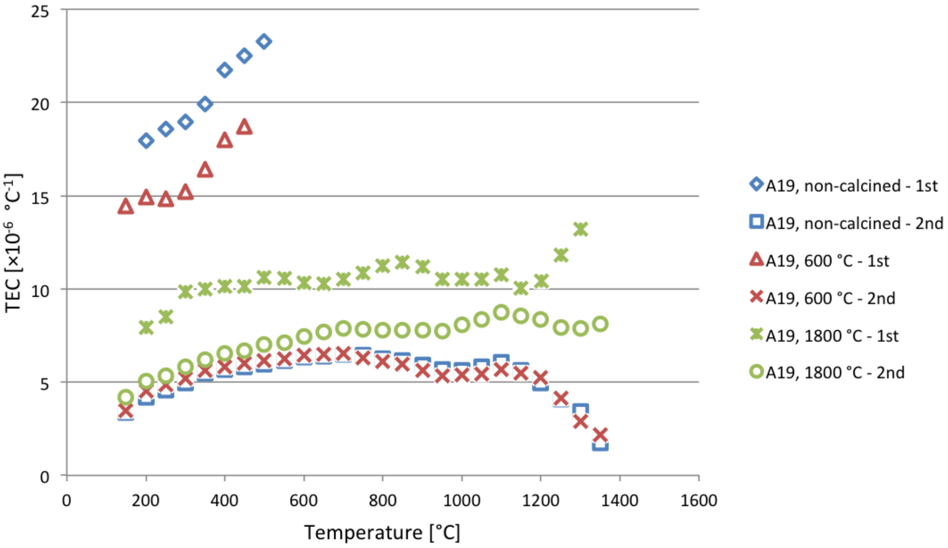

Figure 4.12: Thermal expansion coefficients given as a function of temperature during heating for both temperature cycles of the non-calcined material of A19, and A11 calcined at 600 and 1800 °C.

Figure 4.12 shows a significant difference in TEC values between the first and the second temperature cycle for the non-calcined material and the material calcined at 600 °C. During the first temperature cycle, the TEC increases with increasing temperature up to about 500 °C, and reaches about 26 $\cdot 10^{-6}$ $°C^{-1}$ for the non-calcined material and 19 $\cdot 10^{-6}$ $°C^{-1}$ for the material calcined at 600 °C. During the second temperature cycle, both samples show very similar behaviour with an average of 6 $\cdot 10^{-6}$ $°C^{-1}$ between 400 and 1100 °C. From 1100 °C and up to the maximum temperature there is a gradual decrease in TEC values.

For the material calcined at 1800 °C, there is a small decrease in the average TEC value between the first and the second temperature cycle. During the first temperature cycle, the TEC of the material calcined at 1800 °C increases from about 1200 °C and up to the maximum temperature.

4.4.3 Cokes and Charcoal

The dimensional behaviour of C3, C7 and BIO are given in Figure 4.13, where the expansion is given as a function of temperature throughout the experiment. The temperature profile is illustrated by the dotted line.

C7 shows similar behaviour to the anthracites, where there is a small expansion at about 700 °C in the first temperature cycle, before a shrinkage occur as the temperature reaches maximum. The total shrinkage of C7 during the first temperature cycle is about 1.2 %. For the second temperature cycle, C7 contracts the same amount during cooling as it expands during heating, this is about 0.7 %.

For the charcoal, the pellets have a much bigger expansion during the first temperature cycle of about 1.7 %. After reaching 700 °C the pellets shrinks as the temperature increases. When reaching the maximum temperature, a small expansion is again observed. The total shrinkage during the first temperature cycle of BIO is about 1.4 %. During the second temperature cycle, the material contracts the same amount during cooling as it expands during heating. This expansion is about 0.7 %, which is similar to C7.

C3, however, does not shrink during the first temperature cycle. It is observed that the material contracts about the same amount during cooling as it expands during heating for both temperature cycles. The expansion for the first cycle is

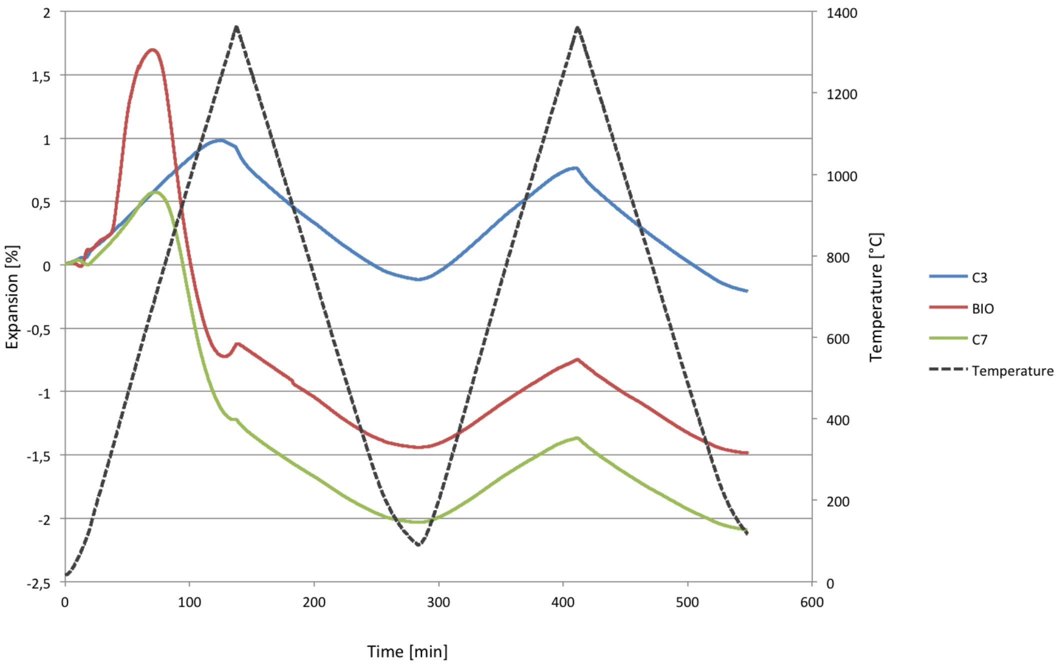

Figure 4.13: The dimensional behaviour of C3, C7 and BIO given as a function of time during heating and cooling. The temperature is illustrated by the dotted line.

about 0.9 %, while the expansion for the second temperature cycle is 0.7 %. All the dimensional changes of the cokes and the charcoal are given in Table 4.10.

Figure 4.14 shows the dilatation graphs of the cokes and charcoal, where the expansion in percentage is given as a function of temperature. From the dilatation graphs, the TEC of each sample was calculated. The TECs were calculated from intervals of 50 degrees, and are shown graphically in Figure 4.15. The average TEC of each sample is calculated from the TECs in the temperature range of 400 to 1100 °C with the exception of the first temperature cycle of C7 which is calculated from TEC values between 200 and 500 °C. The average TECs are given i Table 4.11.

As can be seen from Figure 4.15, the TEC values of BIO from the first temperature cycle are very high compared to the second temperature cycle and the cokes. The values vary a lot and reaches as high as 78 $\cdot 10^{-6}$ °C^{-1}. Hence, an average value for the first temperature cycle of BIO was not calculated.

Table 4.10: Expansion of the C3, C7 and BIO pellets at the beginning of each temperature cycle and the the maximum temperature. Final Expansion is also given. All expansions are given in percentage of change from initial size.

Temp. [°C]	Start 1 [%]	Expansion 1 [%]	Start 2 [%]	Expansion 2 [%]	End [%]
C3	0	0.89	-0.17	0.72	-0.24
C7	0	-1.22	-2.03	-1.36	-2.09
BIO	0	-0.63	-1.44	-0.75	-1.48

Table 4.11: Average thermal expansion coefficient for both temperature cycles of C3 and C7, and for the second temperature cycle of BIO. Standard deviations are also given. The first temperature cycle of C7 is calculated between 200 and 500 °C, while the rest are calculated from values between 400 and 1100 °C.

Temperature [°C]	TEC 1 [$\cdot 10^{-6}$ °C^{-1}]	Std. deviation [$\cdot 10^{-6}$ °C^{-1}]	TEC 2 [$\cdot 10^{-6}$ °C^{-1}]	Std. deviation [$\cdot 10^{-6}$ °C^{-1}]
C3	8.6	0.5	7.6	0.2
C7	10.4	1.0	6.0	0.4
BIO	-	-	6.1	0.3

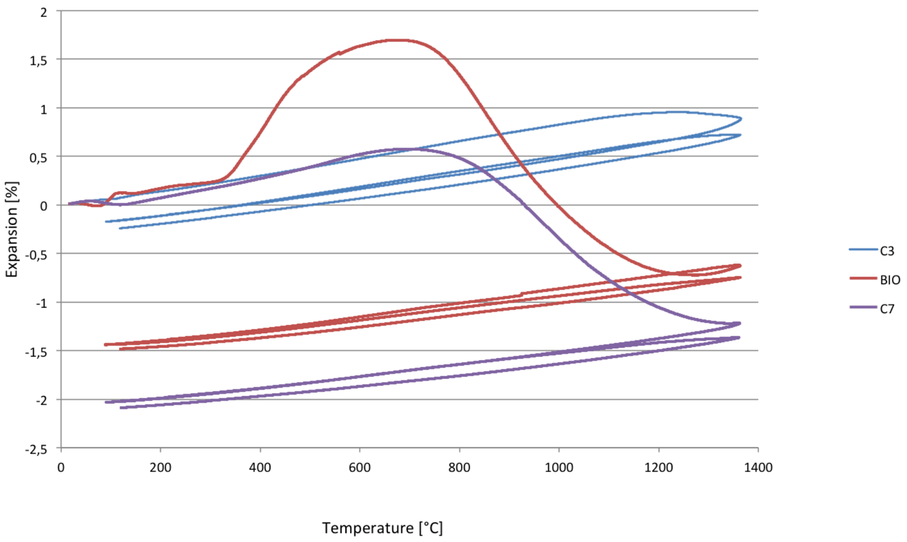

Figure 4.14: Dilatation graphs of C3, C7, BIO, where the expansion is given as a function of temperature.

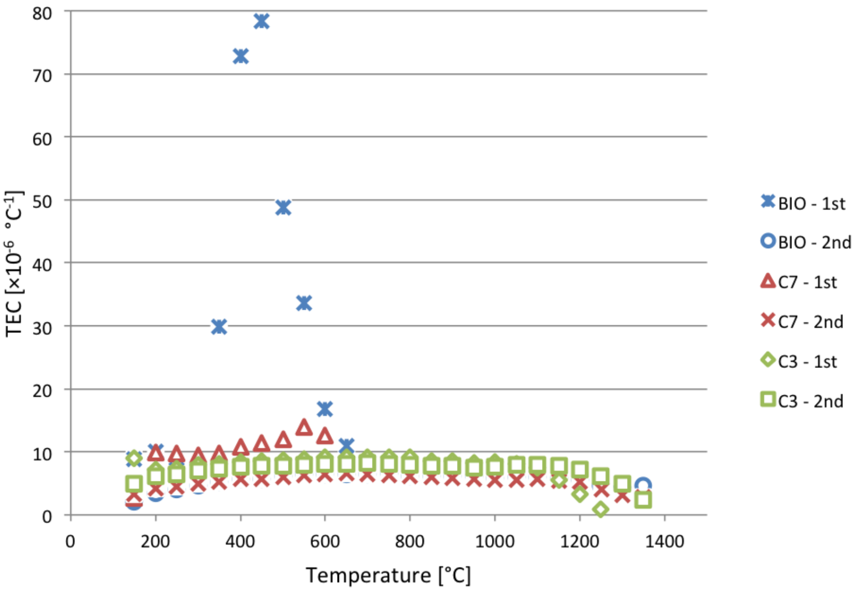

Figure 4.15: Thermal expansion coefficients given as a function of temperature during heating for both temperature cycles of the two cokes and the charcoal.

By changing the scale of the graph in Figure 4.15, the TEC of C3, C7 and the second temperature cycle of BIO can be seen more clearly. This is shown in Figure 4.16. For the first temperature cycle of C7, the TEC increases with increasing temperature, and reaches 14 $\cdot 10^{-6}$ °C^{-1} around 700 °C. The average value between 200 and 500 °C is about 10 $\cdot 10^{-6}$ °C^{-1}. For the second temperature cycle, lower values are observed, with an average of 6 $\cdot 10^{-6}$ °C^{-1} between 400 and 1100 °C. The same TEC average was also calculated for the second temperature cycle of BIO.

The C3 sample shows similar TEC average for both temperature cycles, with 8.6 and 7.6 $\cdot 10^{-6}$ °C^{-1} for the first and second heating, respectively. The C3 sample stands out from the other samples with a higher expansion, a higher TEC average and similar behaviour for both temperature cycles.

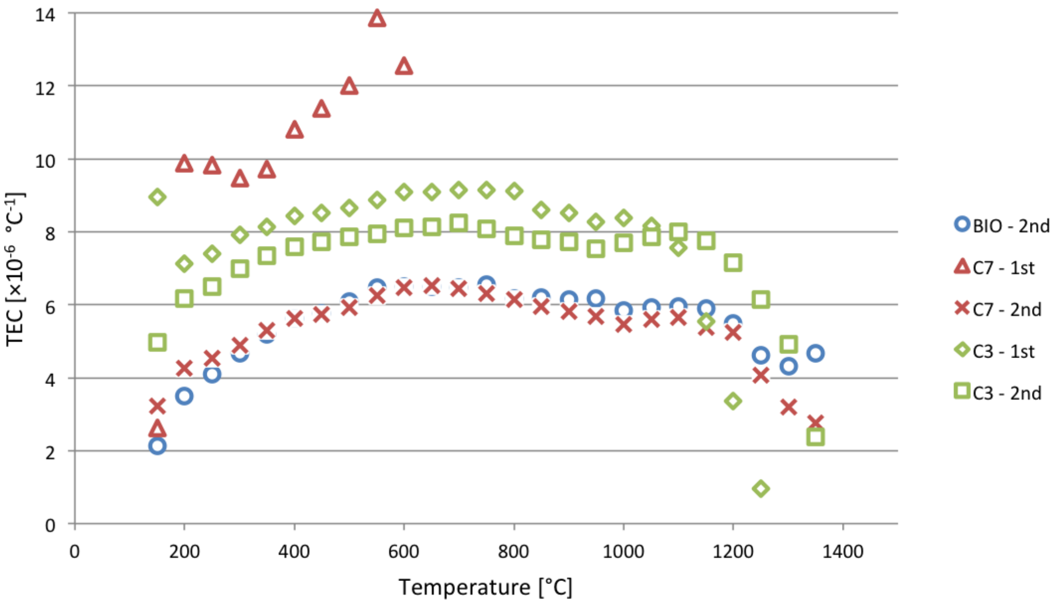

Figure 4.16: Thermal expansion coefficients given as a function of temperature during heating for both temperature cycles of C3 and C7, and for the second temperature cycle of BIO.

4.5 Thermal Analysis

4.5.1 Thermogravimetric Analysis

The results from the thermogravimetric analysis carried out at 1500 °C in the Elite tube furnace are given in Figure 4.17, where the mass loss in percentage is given as a function of time. The temperature profile is illustrated by the dotted line. Some noise in the mass-loss curves have been removed due to the sensitivity of the furnace. The un-smoothened curves can be found in Appendix G.

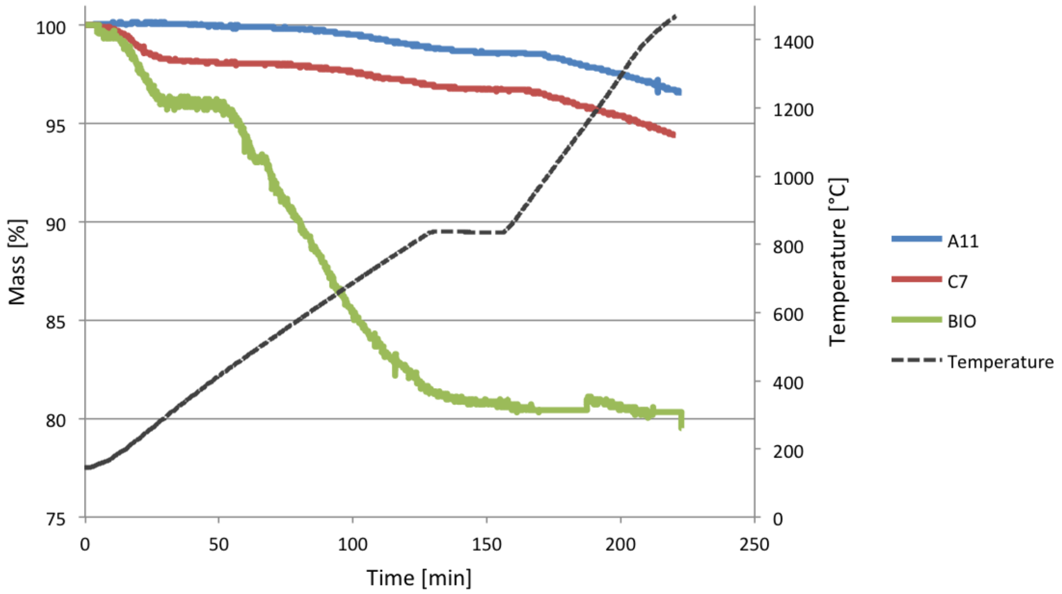

Figure 4.17: Thermogravimetric data from TG experiments carried out in the Elite tube furnace.

A gradual mass loss is observed for A11 and C7, with a mass loss at 1500 °C of 3.4 and 5.6 %, respectively. For the charcoal, there is a big mass-loss of about 20 % up to 800 °C, and only a small mass-loss up to the maximum temperature. The mass losses of the non-calcined A11, C7 and BIO at 1000 and 1500 °C are given in Table 4.12.

Table 4.12: The mass loss of A11, C7 and BIO from TG measurements at 1000 and 1500 °C in the Elite tube furnace.

Sample	Mass loss at 1000 °C [%]	Mass loss at 1500 °C [%]
A11, non-calcined	1.6	3.4
C7	3.5	5.6
BIO	19.5	20.5

4.5.2 Simultaneous Thermal Analysis

The mass losses from the thermogravimetric analysis carried out at 1500 °C in the STA 449 F3 Jupiter is given in Figure 4.18. The mass loss in percentage is given as a function of time. The temperature is illustrated by the dotted line. Due to the fact that the measurements starts while the furnace is still off, the furnace is believed to interrupt the scale when turned on. Therefore, all thermogravimetric results are zeroed at 10 minutes and 200 °C to have that as a reference point.

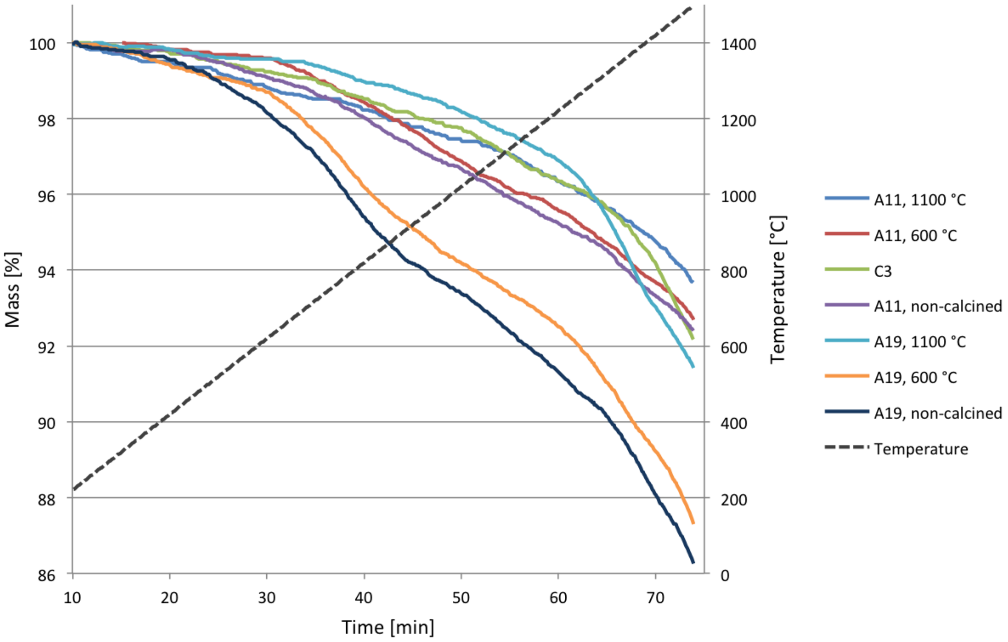

Figure 4.18: Thermogravimetric data obtained from the STA during heating of the materials to 1500 °C.

As can be seen from the figure, the non-calcined material of A19 and A19 calcined at 600 °C have the highest mass loss of about 13 % at 1500 °C, while A11 calcined at 1100 °C have the smallest mass loss of about 6 %. This complies with the volatile content of the samples as A19, non-calcined and calcined at 600 °C, have the highest volatile content and A11 calcined at 1100 °C has the lowest volatile content. The mass losses at both 1000 and 1500 °C for all samples are summarized in Table 4.13.

Table 4.13: Mass loss at 1000 and 1500 °C during heating in STA 449 F3 Jupiter for all samples.

Sample	Mass loss at 1000 °C [%]	Mass loss at 1500 °C [%]
A11, non-calcined	3.2	7.6
A11, 600 °C	3.0	7.3
A11, 1100 °C	2.5	6.3
A19, non-calcined	6.5	13.7
A19, 600 °C	5.7	12.7
A19, 1100 °C	1.7	8.6
C3	2.2	7.8

The differential scanning calorimetry (DSC) curves from the same STA experiments are given in Figure 4.19. The DSC in micro volts per milli gram is given as a function of time, with exothermic reactions in positive y-direction. The temperature is illustrated by the dotted line.

All the samples show similar behaviour, where the DSC increases up to about 400 °C, decreases to about 700 °C and increases again up to the maximum temperature. Some noise is observed around 1100 °C for the non-calcined A19 and A19 calcined at 600 °C. However, the DSC curves are not consistent results of endothermic or exothermic reactions at a given temperature. The reactions in the temperature range of 0 to about 1000 °C will be covered by background-noise. The background-noise shown in the calibration curve in Appendix C show much higher values, hence the DSC-curves might not be corrected with the calibration curve.

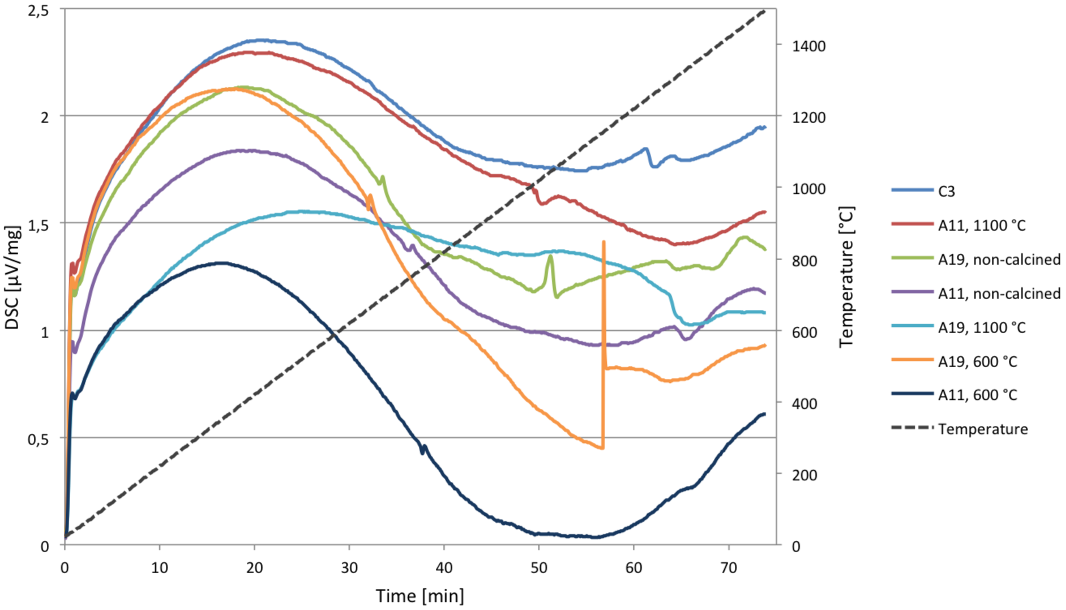

Figure 4.19: Differential scanning calorimetry (DSC) curves obtained from the STA measurements during heating of the materials to 1500 °C. The temperature is illustrated by the dotted line.

4.5.3 Simultaneous Thermal Analysis with Evolved Gas Analysis

No off-gases were detected from the experiments where the non-calcined A11 was heated to 430 °C. The thermogravimetric data obtained from these runs are given in Appendix E.

For the simultaneous thermal analysis coupled with Fourier transformed infrared and gas chromatography with mass spectroscopy, the non-calcined materials of A11 and A19, A11 and A19 calcined at 600 °C, C3, C7 and BIO were tested. First, the non-calcined materials of A11 and A19 were heated to 900 °C, then all samples were heated to 1000 °C. The mass losses at 1000 °C for all samples are summarised in Table 4.14, where C3 has the lowest mass loss of 1.2 % and BIO has the highest mass loss of 14.8 % at 1000 °C.

The thermogravimetric data for the non-calcined A11 heated to 900 and 1000 °C, as well as A11 calcined at 600 °C heated to 1000 °C is given in Figure 4.20. In (a),

Table 4.14: The mass loss at 1000 °C for all samples.

Sample	Total mass loss at 1000 °C [%]
A11, non-calcined	2.2
A11, 600 °C	2.4
A19, non-calcined	4.8
A19, 600 °C	3.9
C3	1.2
C7	3.0
BIO	14.8

the mass and the derivative of mass are given as functions of temperature, and in (b) the mass and the Gram-Schmidt curves are given as functions of temperature.

As can be seen from Figure 4.20, both the mass loss and the Gram Schmidt curves are are very similar for the three runs. The Gram-Schmidt curve shows a gradual increase as the temperature increases. As the temperature reaches about 700 °C, there is a higher increase in evolved gases. The derivative of the mass increases from about 600 °C and up to the maximum temperature for all samples.

Fourier transformed infrared spectrum from the evolved gas is given in Figure 4.21 for the non-calcined material of A11 heated to (a) 900 °C and (b) to 1000 °C. The FTIR spectrum of A11 calcined at 600 °C is given in 4.22. The absorbance is given as a function of time and wavenumber.

By extracting the absorbance as a function of wavenumber at given times, two-dimensional spectra where obtained. Figure 4.23, 4.24 and 4.25 shows such spectra where the absorbance is given as a function of wavenumber at the highest temperature of about 900 and 1000 °C, respectively.

As can be seen from the figures, the peaks are similar for both the heating of the non-calcined material to 900 and to 1000 °C. However, the absorbance is higher for the heating to 1000 °C. In the spectra there is one peak around 2400 - 2300 cm^{-1} corresponding to CO_2, and two peaks around 2300 - 2000 cm^{-1} corresponding to CO. Smaller peaks at 3800 - 3500 cm^{-1} and 2000 - 1300 cm^{-1} corresponding to H_2O can also be observed. The absorbance unit is higher for CO_2 than CO and H_2O, indicating a higher amount of CO_2 present.

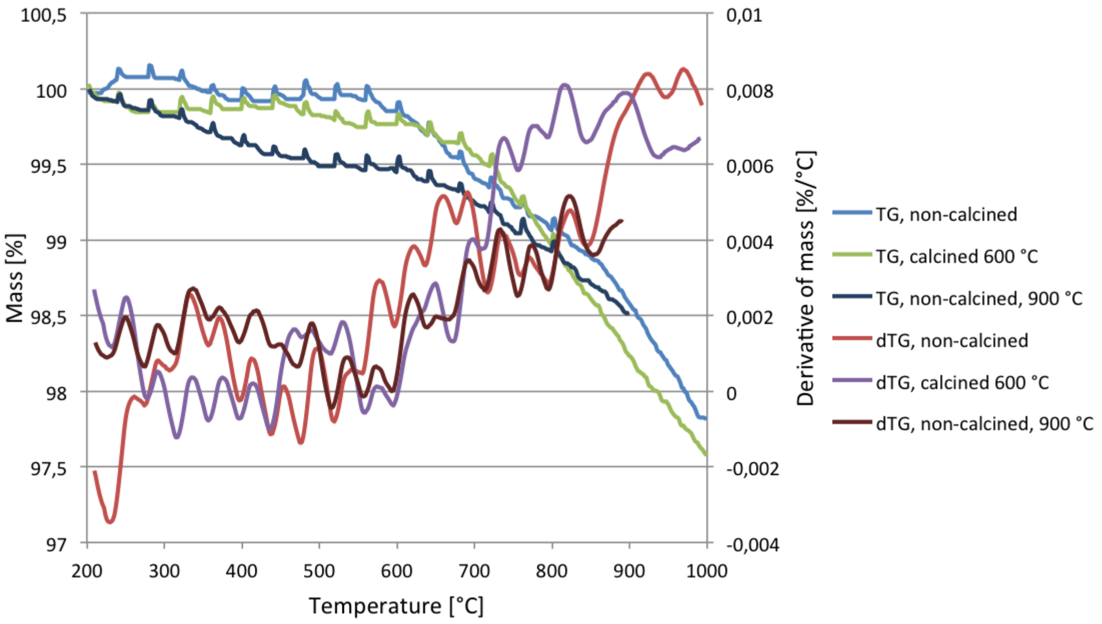

(a)

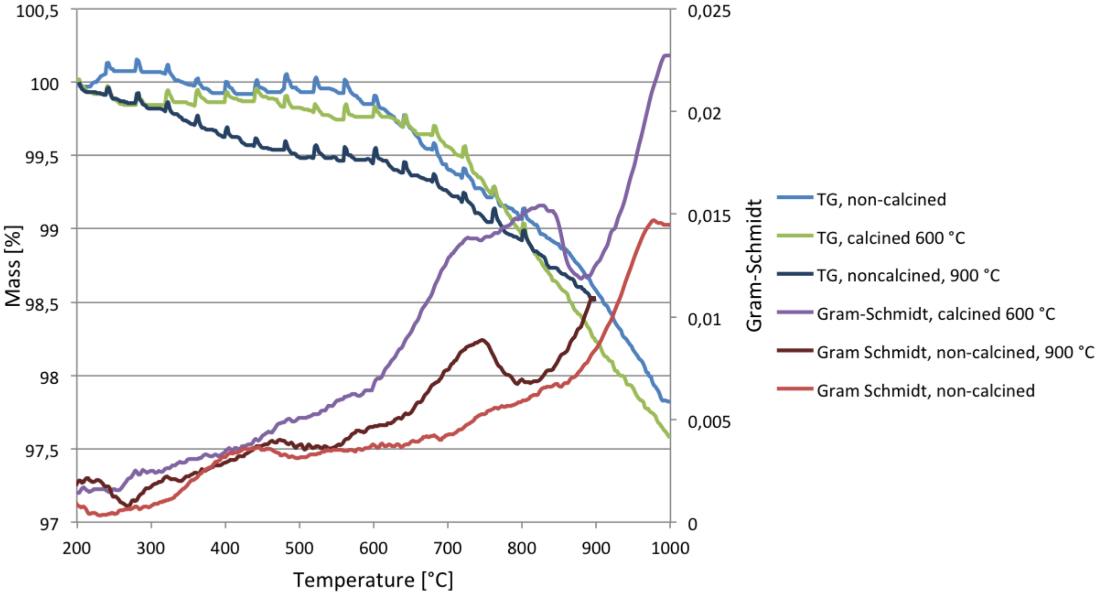

(b)

Figure 4.20: Thermogravimetric data of the non-calcined material of A11 heated to 900 and 1000 °C and A11 calcined at 600 °C heated to 1000 °C. (a) The mass loss and the derivative of mass given as functions of temperature. (b) The mass loss and the Gram Schmidt curve given as functions of temperature.

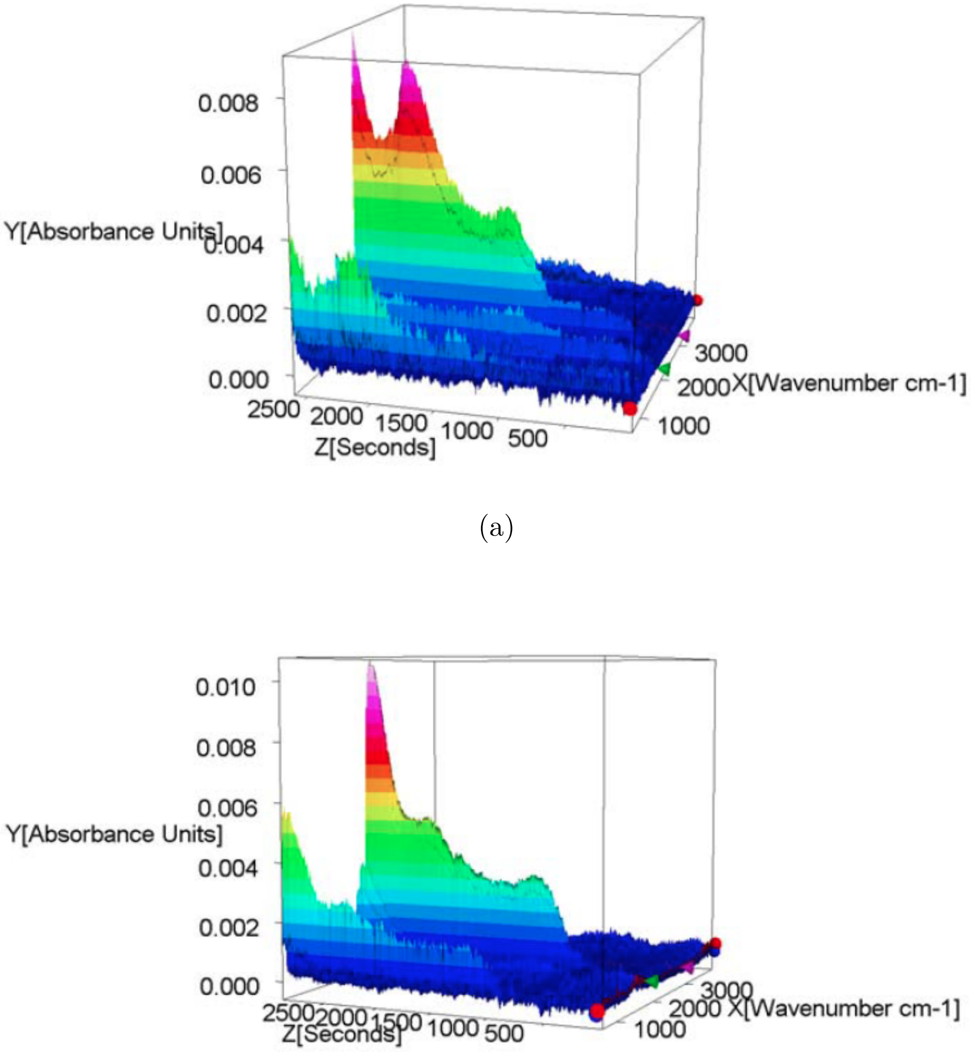

(a)

(b)

Figure 4.21: Fourier transformed infrared spectrum of the evolved gas from the non-calcined material of A11 heated to (a) 900 °C and (b) 1000 °C.

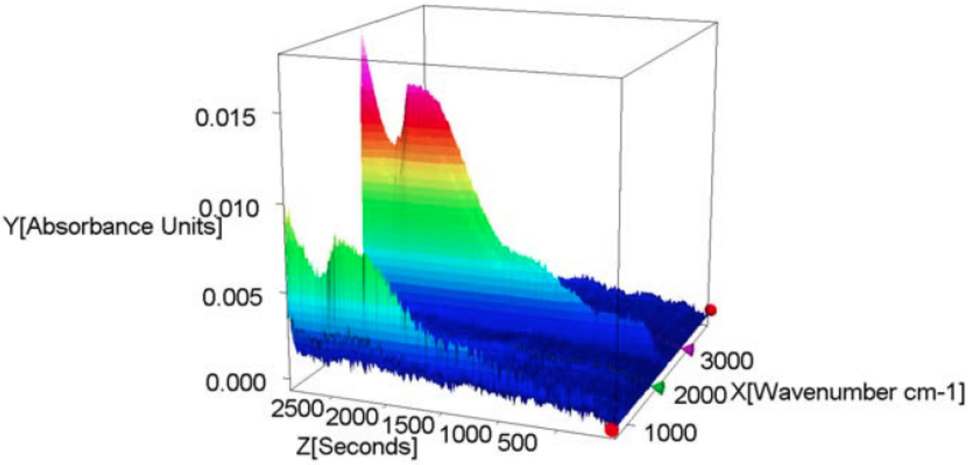

Figure 4.22: Fourier transformed infrared spectrum of the evolved gas from the A11 calcined at 600 °C heated to 1000 °C.

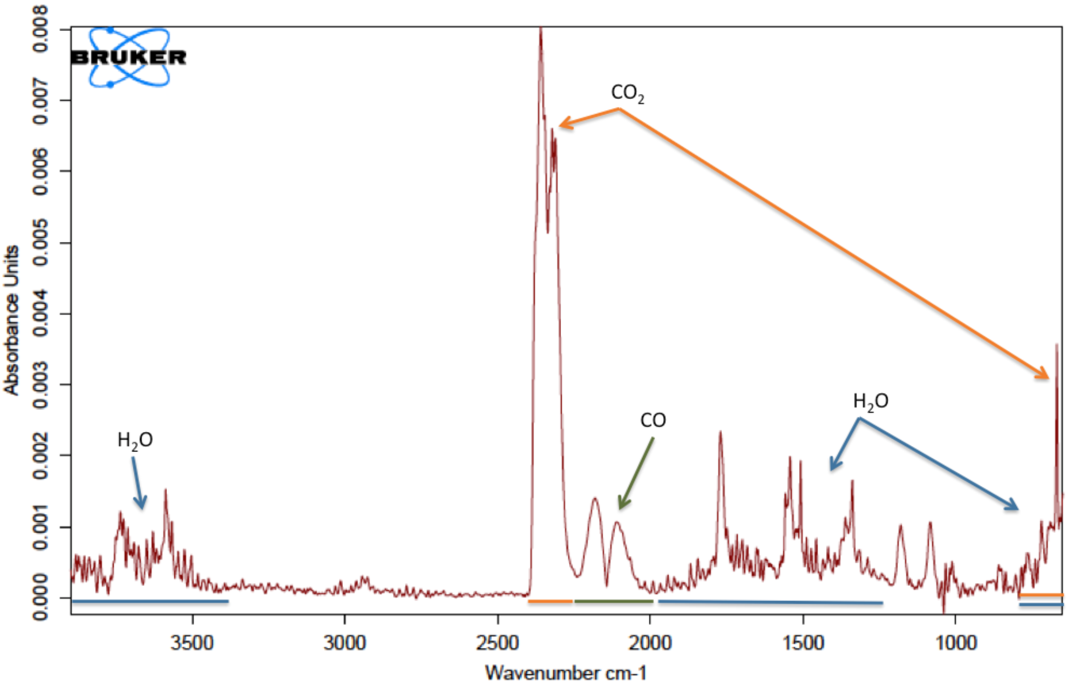

Figure 4.23: FTIR spectrum of the non-calcined material heated to 900 °C. The absorbance is given as a function if wavenumber at the time corresponding to the maximum temperature of 900 °C.

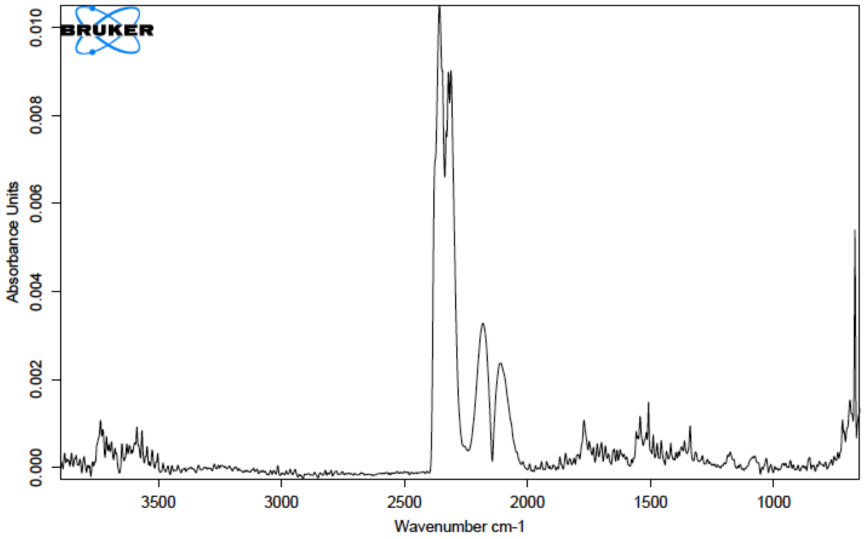

Figure 4.24: FTIR spectrum of the non-calcined material heated to 1000 °C. The absorbance is given as a function if wavenumber at the time corresponding to the maximum temperature of 1000 °C.

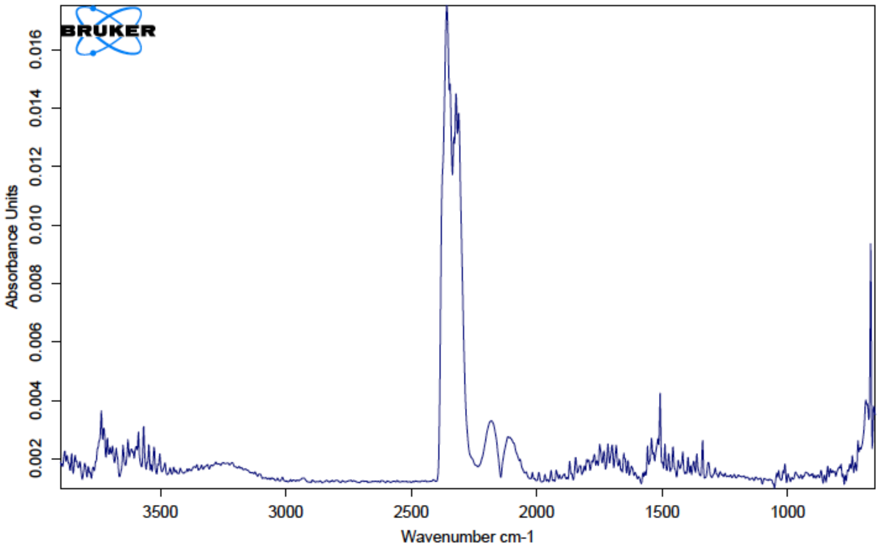

Figure 4.25: FTIR spectrum of the material calcined at 600 °C heated to 1000 °C. The absorbance is given as a function if wavenumber at the time corresponding to the maximum temperature of 1000 °C.

The peak areas corresponding to amounts of CO_2 and CO for the non-calcined A11 and A11 calcined at 600 °C heated to 1000 °C are given in Figure 4.26. Here, the values are normalized to the highest value of CO_2 for the non-calcined sample. All the two-dimensional absorbance vs wavenumber spectra at the different times from where the peak areas are calculated are given in Figure 4.27 and 4.28 for the non-calcined material and the material calcined at 600 °C, respectively.

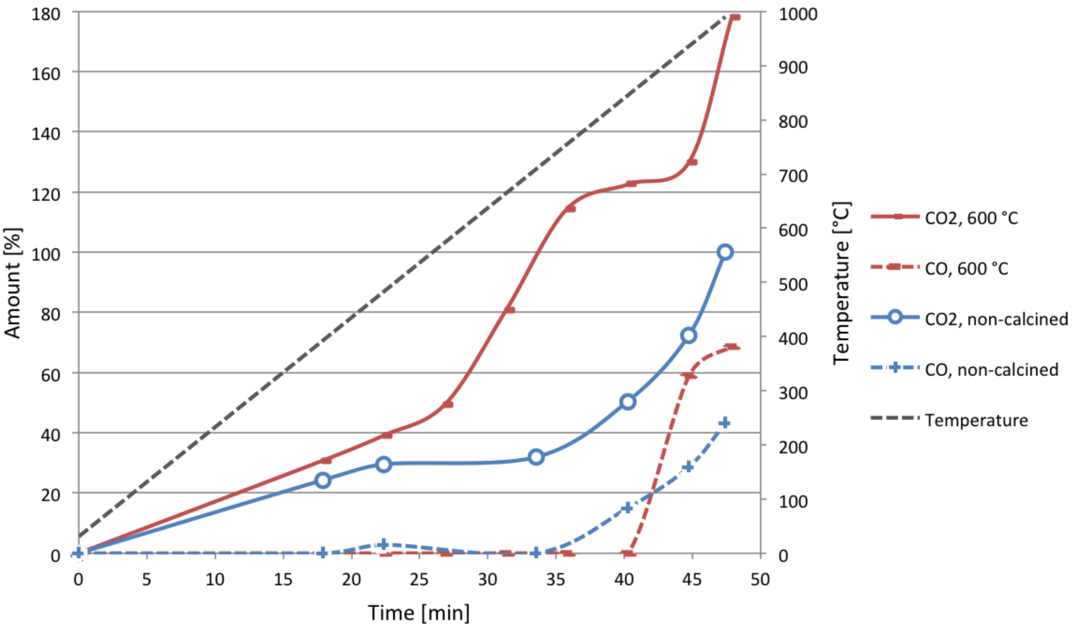

Figure 4.26: Amount of CO_2 and CO of the non-calcined A11 and A11 calcined at 600 °C given as a function of time during heating. The curves are normalized to the highest amount of CO_2 for the non-calcined material.

As can be seen from Figure 4.26, the first peak area calculation was carried out at around 18 minutes into the experiment, corresponding to a temperature of about 380 °C. As the temperature increases, so does the amount of both CO_2 and CO for both samples.

It can also be observed that CO only appear some place between 34 and 40 minutes into the experiment for the non-calcined material. This correspond to a temperature range of about 700 to 830 °C. For the material calcined at 600 °C, CO is only observed above 830 °C.

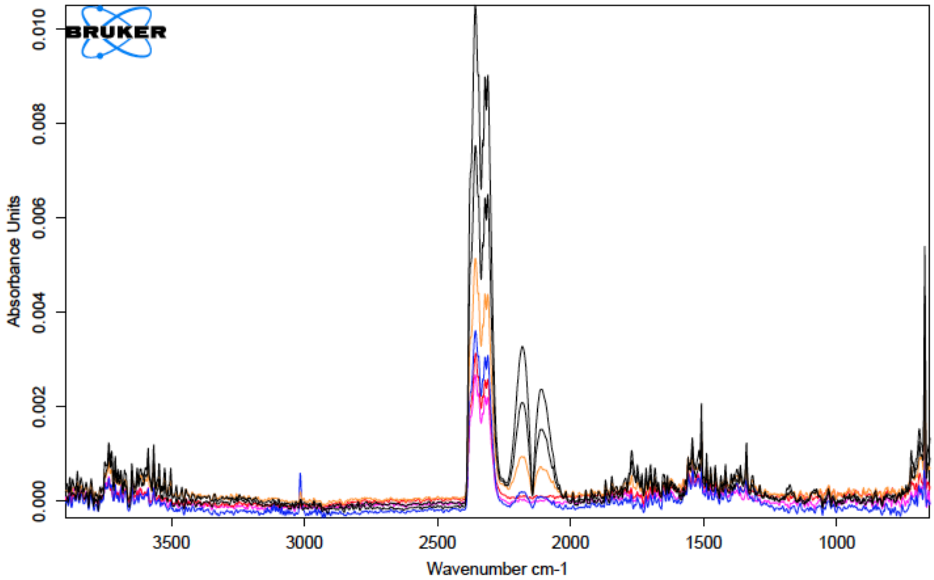

Figure 4.27: The two-dimensional FTIR spectra of the non-calcined A11 corresponding to the different times at where the peak areas are calculated.

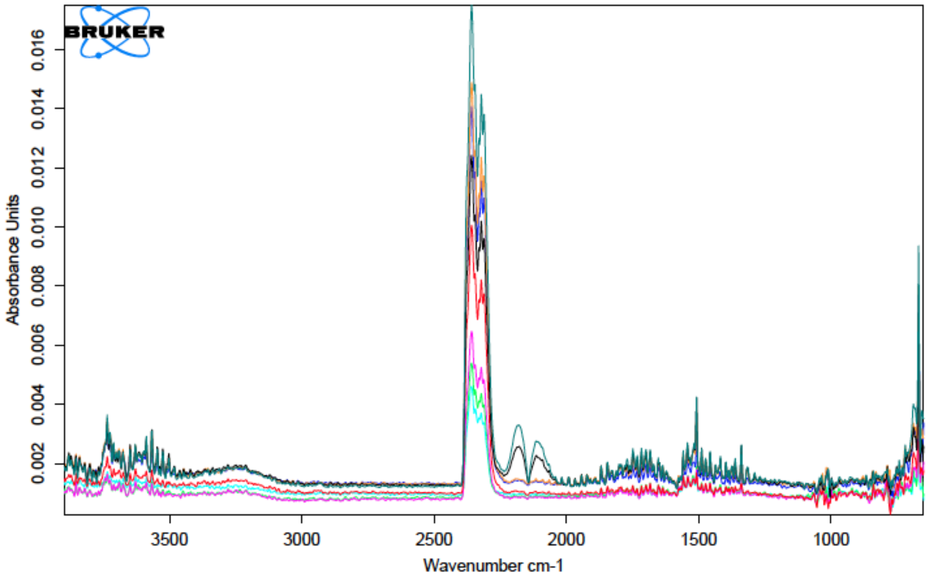

Figure 4.28: The two-dimensional FTIR spectra of A11 calcined at 600 °C corresponding to the different times at where the peak areas are calculated.

From Figure 4.27, a small peak around 3000 cm^{-1} for the blue line can be observed. This blue line represents the FTIR spectrum from about 34 minutes into the experiment, and a temperature of 700 °C.

Figure 4.29 shows the extracted-ion chromatograms (EICs) from the GC-MS, where the signal from CO_2 is given as a function of time during the heating of the non-calcined A11 up to 900 and 1000 °C in Figure (a) and (b), respectively. Figure (c) shows the EIC of the material calcined at 600 °C. As can be seen from the figures, the peak height and hence also the peak area increases with increasing temperature. The retentions times, peak heights and peak areas are given in Table H.1, H.2 and H.3 in Appendix H.

The peak areas obtained from the CO_2 EIC of the non-calcined A11 are given in Figure 4.30. The peak areas correspond to amount of CO_2, and the curves are normalized to the highest peak area during the heating to 1000 °C of the non-calcined material.

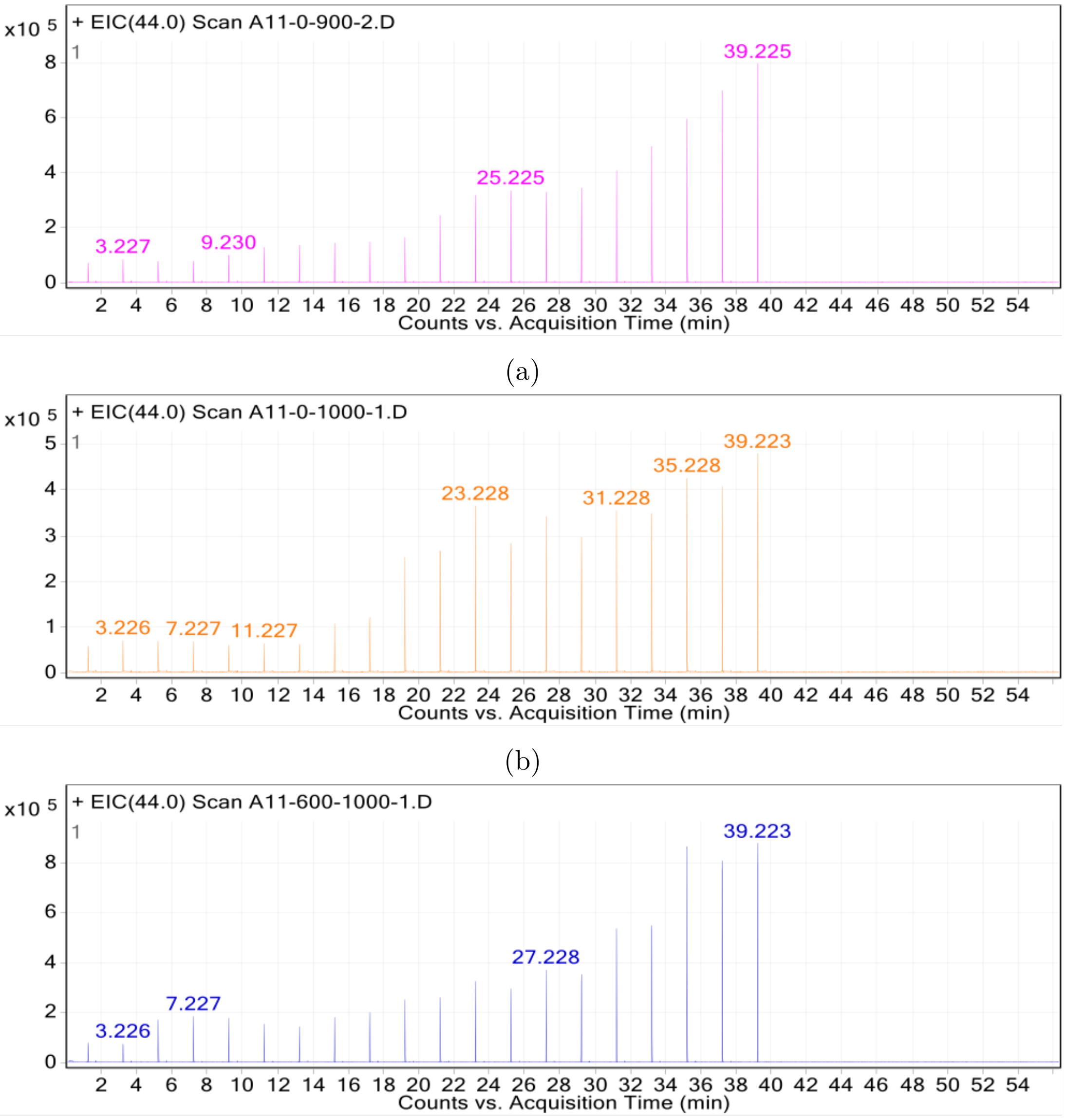

(a)

(b)

(c)

Figure 4.29: The extracted-ion chromatogram of CO_2 from the non-calcined A11 heated (a) 900 and to (b) 1000 °C, and of (c) the material calcined at 600 °C heated to 1000 °C.

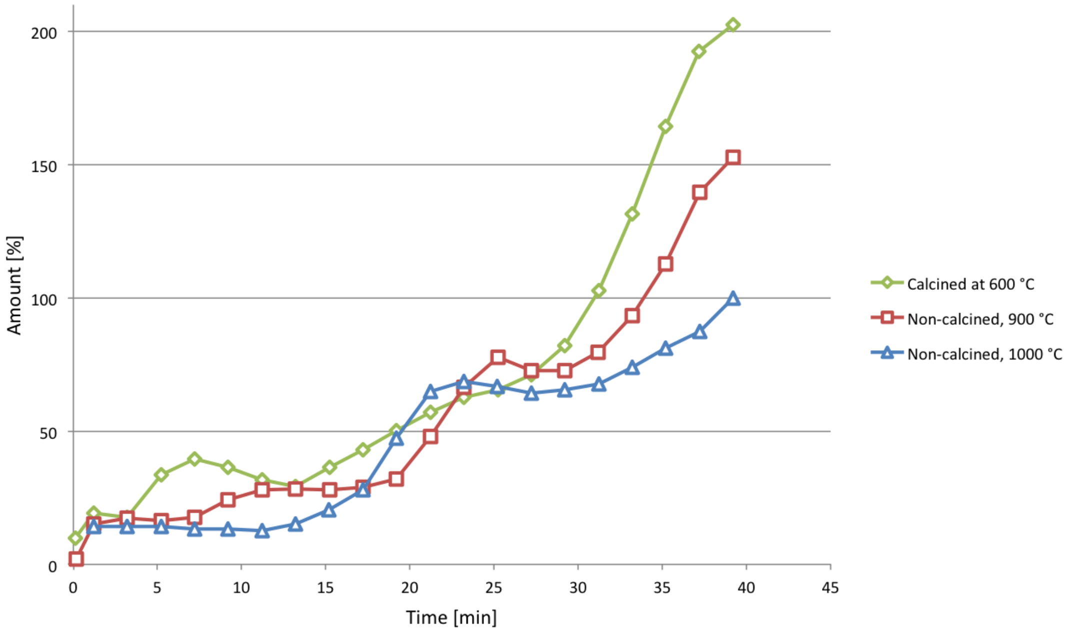

Figure 4.30: The peak areas obtained from the CO_2 extracted-ion chromatograms of the non-calcined A11 and A11 calcined at 600 °C corresponding to amount of CO_2. The amount is given as a function of time during heating to 900 and 1000 °C, and normalized to the maximum amount of CO_2 from the non-calcined material heated to 1000 °C.

The thermogravimetric data of the non-calcined A19 heated to 900 and 1000 °C and A19 calcined at 600 °C, heated to 1000 °C is given in Figure 4.31. In (a), the mass and the derivative of mass is given as functions of temperature, and in (b) the mass and the Gram-Schmidt curves are given as functions of temperature.

As can be seen from (a), the mass loss curve is very similar for the non-calcined material heated to 900 and 1000 °C. However, from (b) it can be seen that there is a higher intensity of evolved gas for the heating to 900 °C. For the material calcined at 600 °C, the mass loss doesn't start until reaching 600 °C, from this temperature an up, the derivative of mass is similar to the non-calcined material. From (b) it can be seen that there is a lower intensity of evolved gases for this sample. At about 700 °C there is a small peak in the Gram Schmidt curve and an increase in the mass loss derivative.

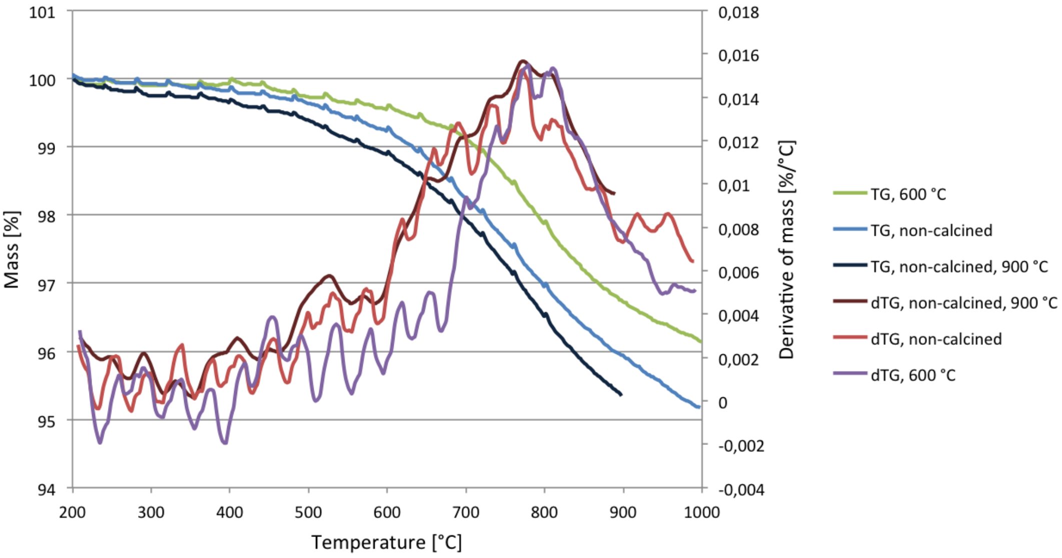

(a)

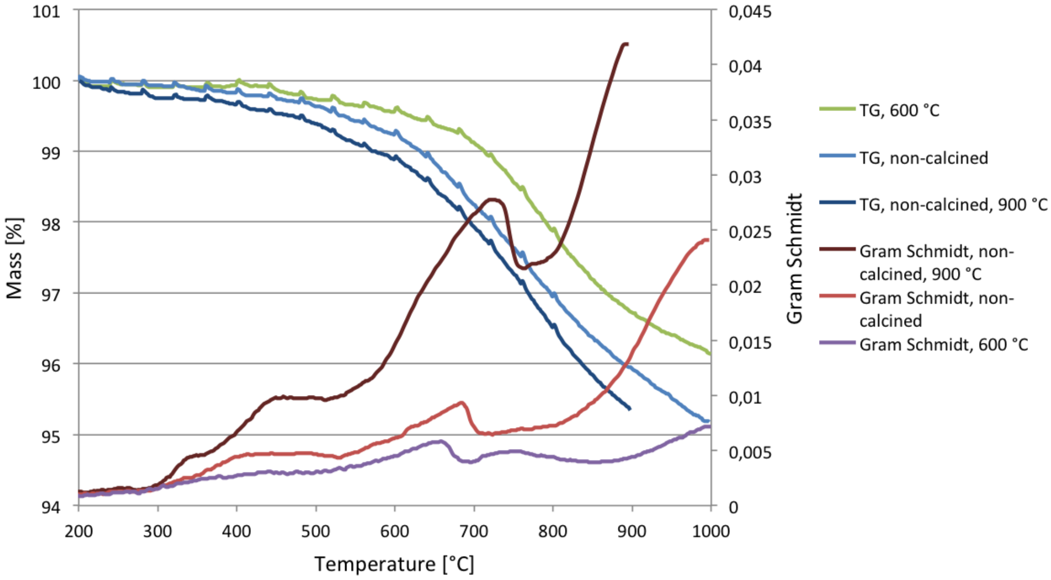

(b)

Figure 4.31: Thermogravimetric data of the non-calcined material of A19 heated to 900 and 1000 °C and A19 calcined at 600 °C heated to 1000 °C. (a) The mass loss and the derivative of mass given as functions of temperature. (b) The mass loss and the Gram Schmidt curves given as functions of temperature.

Fourier transformed infrared spectrum from the evolved gas is given in Figure 4.21 for the non-calcined material of A19 heated to (a) 900 °C and (b) 1000 °C. The FTIR spectrum of A19 calcined at 600 °C is given in Figure 4.33. The absorbance is given as a function of time and wavenumber.

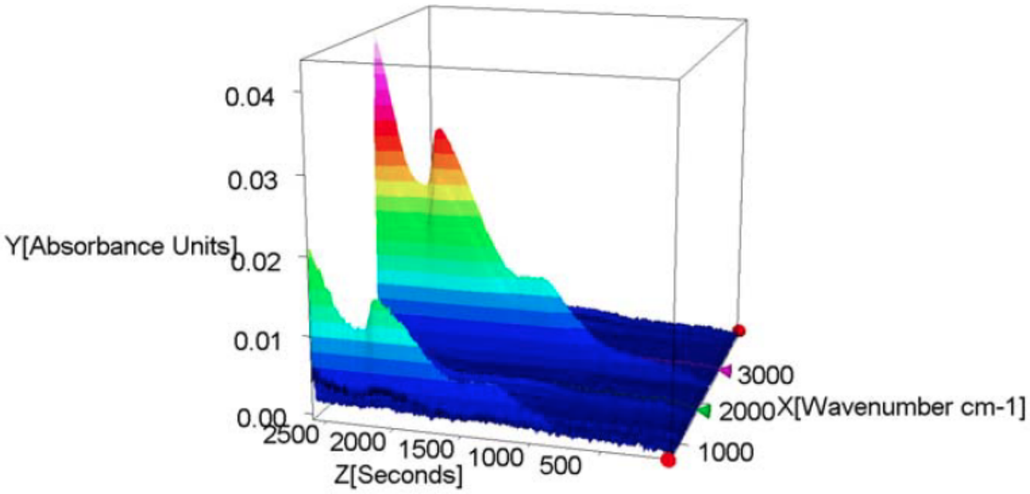

(a)

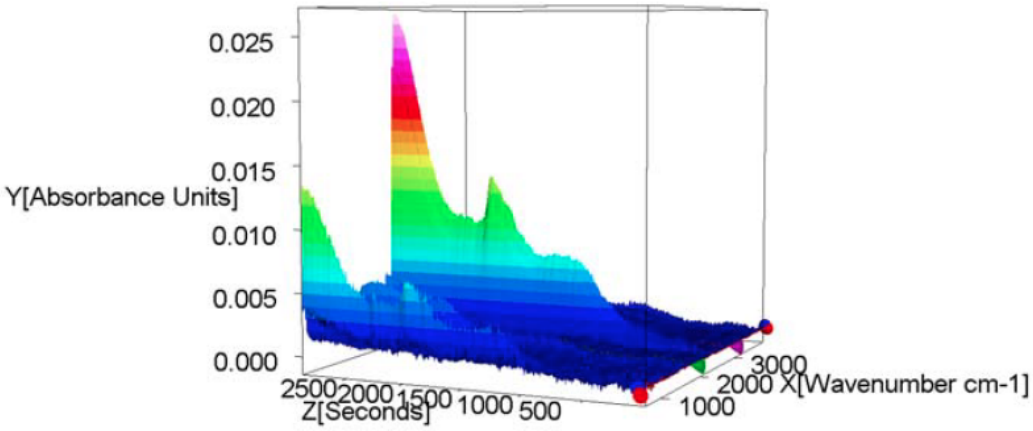

(b)

Figure 4.32: Fourier transformed infrared spectrum of the evolved gas from the non-calcined material of A19 heated to (a) 900 °C and (b) 1000 °C.

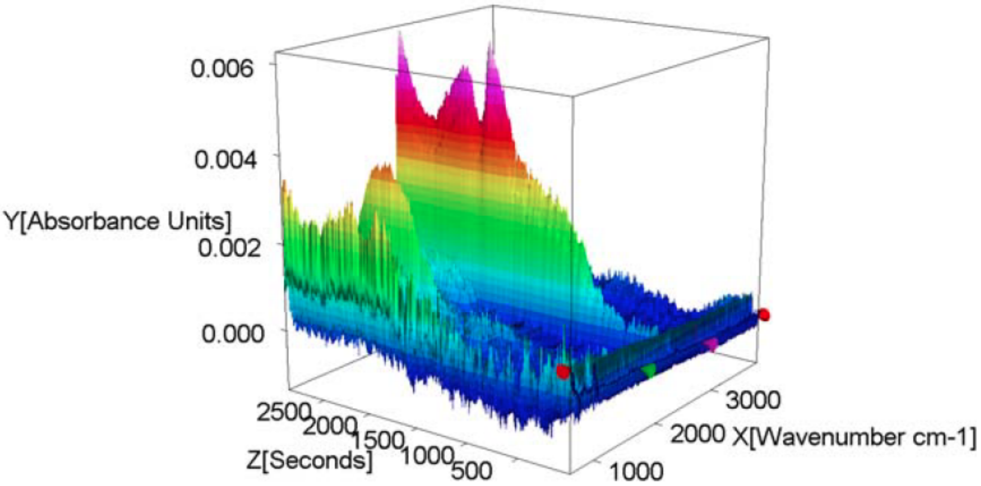

Figure 4.33: Fourier transformed infrared spectrum of the evolved gas from the A19 calcined at 600 °C heated to 1000 °C.

By extracting the absorbance as a function of wavenumber at given times, two-dimensional spectra where obtained. Figure 4.34, 4.35 and 4.36 shows such spectrua where the absorbance is given as a function of wavenumber at the highest temperature of about 900 and 1000 °C for the non-calcined materials and 1000 °C for the material calcined at 600 °C.

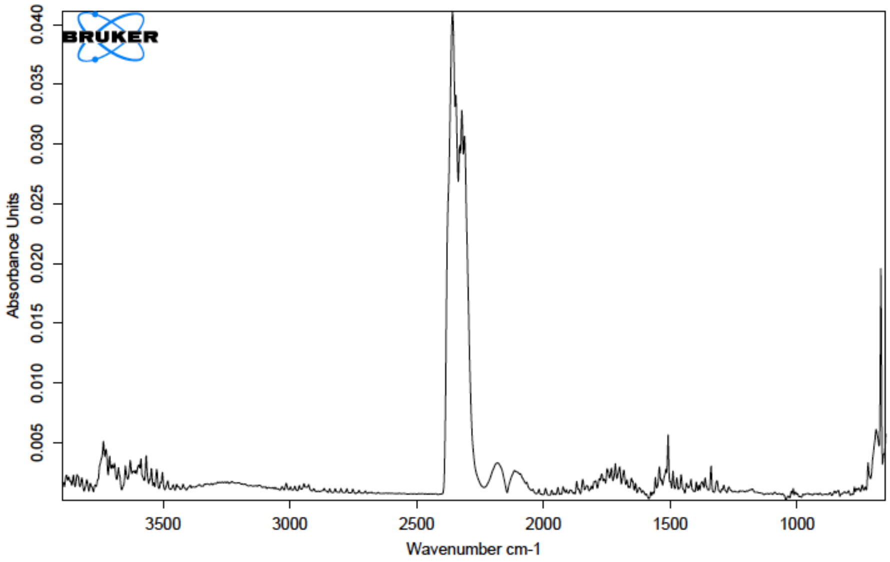

Figure 4.34: FTIR spectrum of the non-calcined material of A19 heated to 900 °C. The absorbance is given as a function if wavenumber at the time corresponding to the maximum temperature of 900 °C.

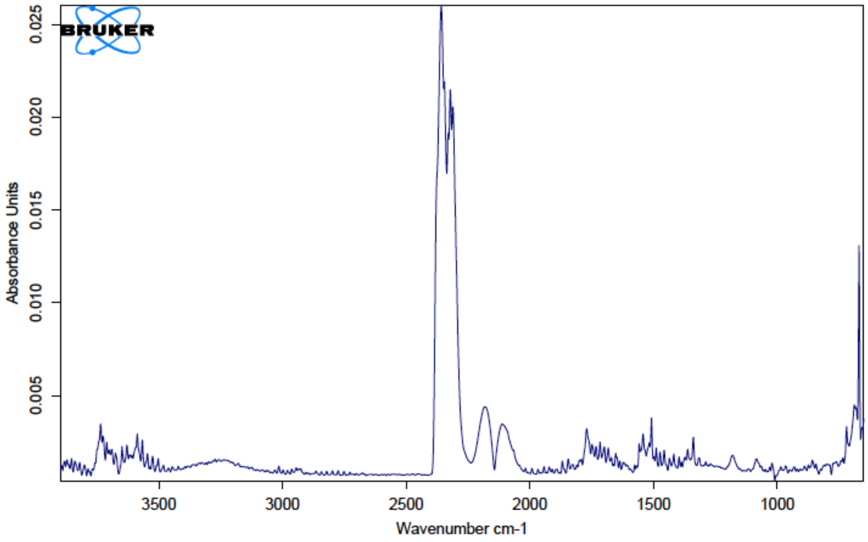

Figure 4.35: FTIR spectrum of the non-calcined material of A19 heated to 1000 °C. The absorbance is given as a function if wavenumber at the time corresponding to the maximum temperature of 1000 °C.

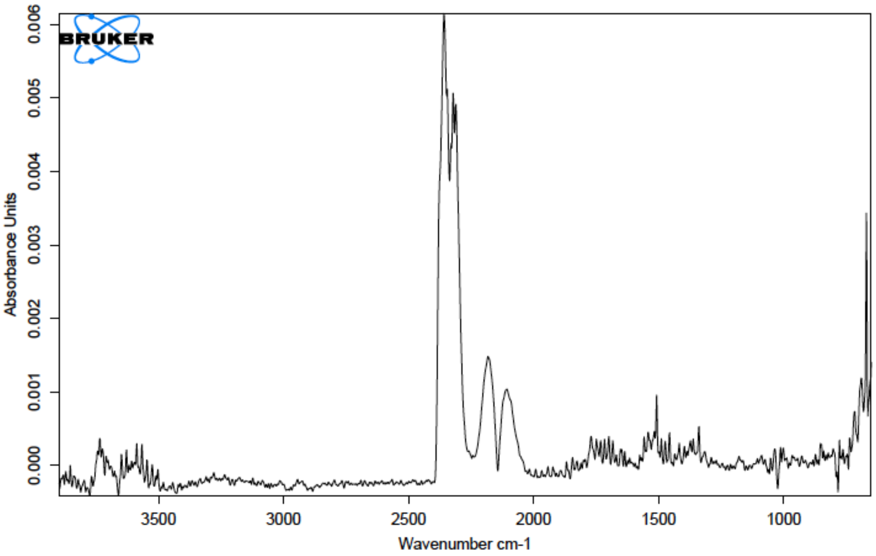

Figure 4.36: FTIR spectrum of A19 calcined at 600 °C heated to 1000 °C. The absorbance is given as a function if wavenumber at the time corresponding to the maximum temperature of 1000 °C.

As can be seen from these figures, the peaks are similar for both the heating to 900 and to 1000 °C for the non-calcined material, and the material calcined at 600 °C heated to 1000 °C. There is a difference in the absorbance, where the highest absorbance is observed for the non-calcined material heated to 900 °C and the lowest for the material calcined at 600 °C. The spectra obtained from A19 is similar to the ones from A11, where there is one peak around 2400 - 2300 cm^{-1} corresponding to CO_2, and two peaks around 2300 - 2000 cm^{-1} corresponding to CO. Smaller peaks at 3800 - 3500 cm^{-1} and 2000 - 1300 cm^{-1} corresponding to H_2O can also be observed.

The peak areas corresponding to the amount of CO_2 and CO are given in Figure 4.37. The values are normalized to the highest value of CO_2 for the non-calcined material. In the figure, the temperature is also given as a function of time.

All the two-dimensional FTIR spectra given at det different times from where the peak areas are calculated, are given in Figure 4.38 for the non-calcined A19 and Figure 4.39 for A19 calcined at 600 °C. The maximum temperature in both cases is 1000 °C, the absorbance is given as a function of wavenumber.

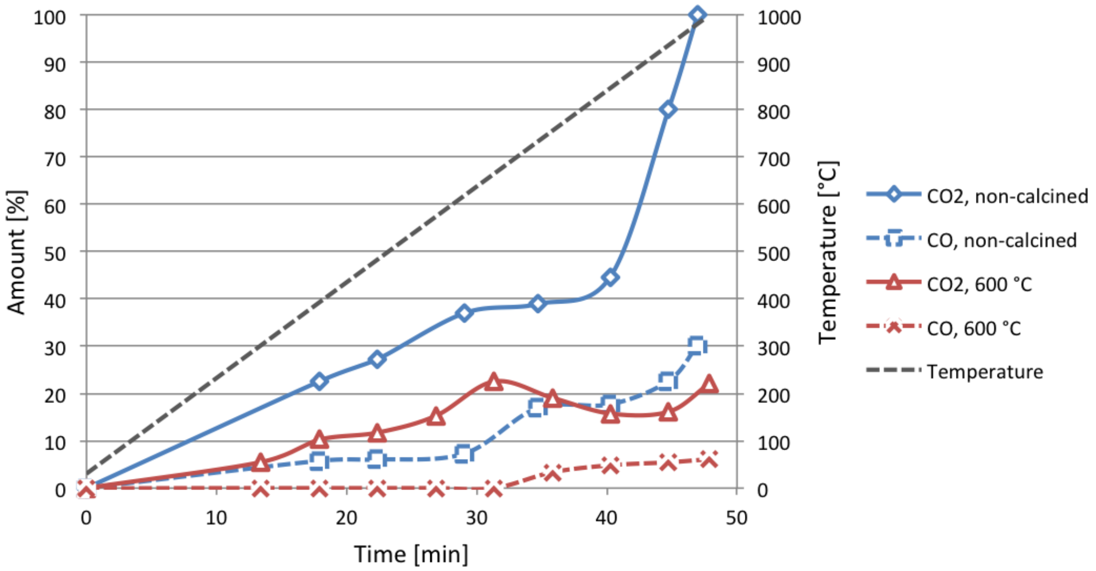

Figure 4.37: Amount of CO_2 and CO of the non-calcined A19 and A19 calcined at 600 °C obtained from FTIR given as a function of time during heating. The curves are normalized to the maximum amount of CO_2 of the non-calcined material.

As can be seen from Figure 4.37, the first peak area calculation was carried out at around 18 min into the experiment for the non-calcined material, corresponding to a temperature of about 380 °C. As the temperature increases, so does the amount of both CO_2 and CO.

For the non-calcined material, CO only appears in small amount up until 600 °C, and starts to increase between 600 and 700 °C. This is also the same place in temperature where CO appears for the material calcined at 600 °C as well. The amount of CO is higher for the non-calcined material than the material calcined at 600 °C. This is also true for the amount of CO_2.

The FTIR spectra of the non-calcined material in Figure 4.38 show a small peak around 3000 cm^{-1} for the blue, grey and green line, corresponding to about 600, 700 and 850 °C, respectively. This is also true for the turquoise, green and purple line of the FTIR spectra of A19 calcined at 600 °C, given in Figure 4.39. These lines correspond to about 650, 750 and 850 °C, respectively.

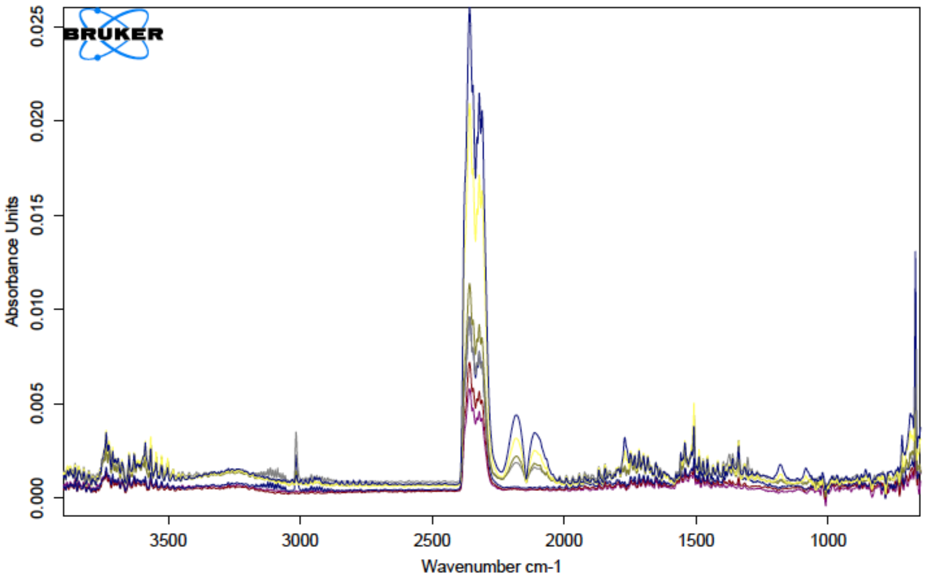

Figure 4.38: The two-dimensional FTIR spectra of the non-calcined A19 corresponding to the different times at where the peak areas are calculated.

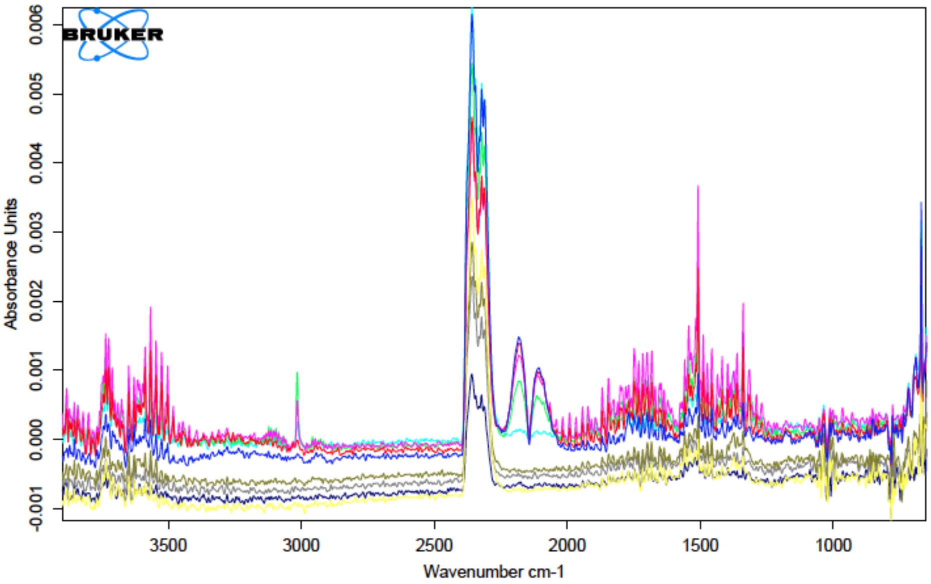

Figure 4.39: The two-dimensional FTIR spectra of A19 calcined at 600 °C corresponding to the different times at where the peak areas are calculated.

Figure 4.40 shows the EIC obtained from GC-MS. Here, the signal from the CO_2 is given as a function of the time during heating of the materials. Figure (a) and (b) show the heating of the non-calcined material up to 900 and 1000 °C, respectively, while figure (c) shows the material calcined at 600 °C during heating to 1000 °C. The peak height increases with time for all samples, but it is lower for the material calcined at 600 °C. The retention times, peak height and peak areas are given in Table H.4, H.5 and H.6 in Appendix H.

The peak areas obtained from the CO_2 EIC of A19 are given in Figure 4.41. The curves are normalized to the highest peak area of the non-calcined material during the heating to 1000 °C.

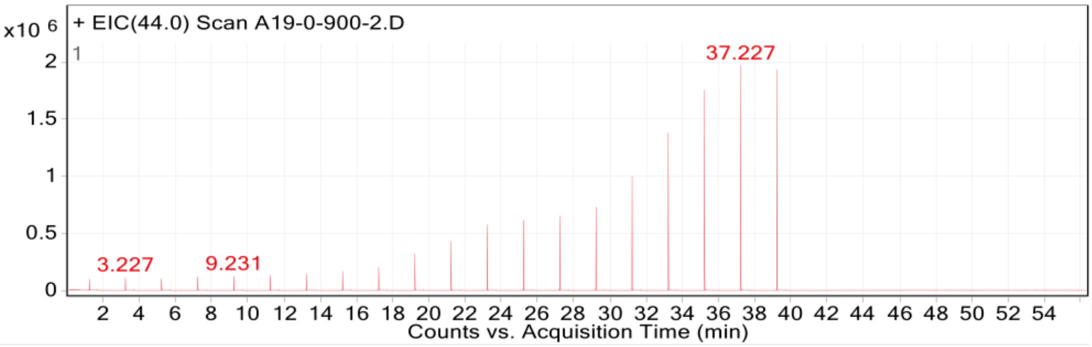

(a)

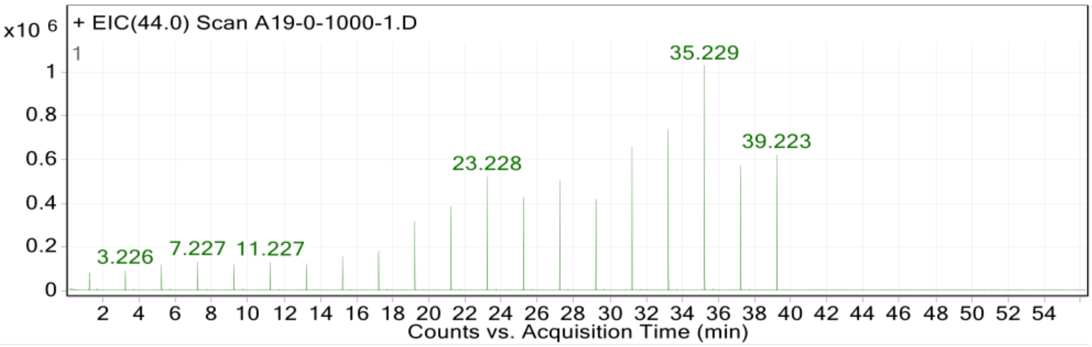

(b)

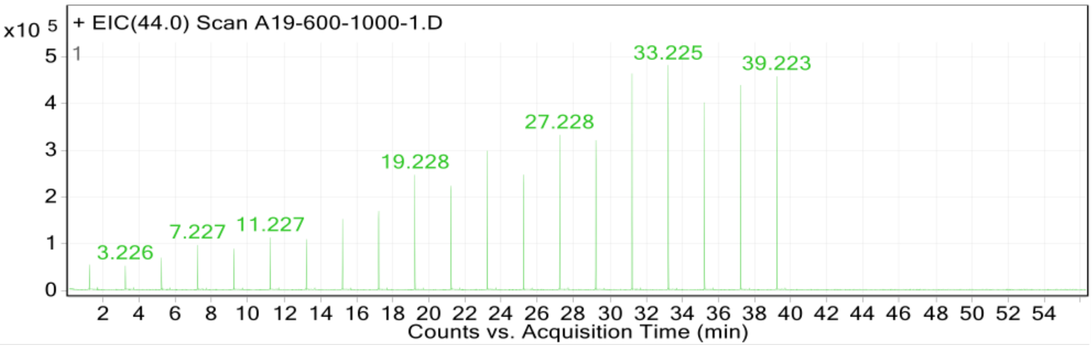

(c)

Figure 4.40: The extracted-ion chromatogram of CO_2 from the non-calcined A19 heated (a) 900 °C and to (b) 1000 °C, and (c) the material calcined at 600 °C heated to 1000 °C.

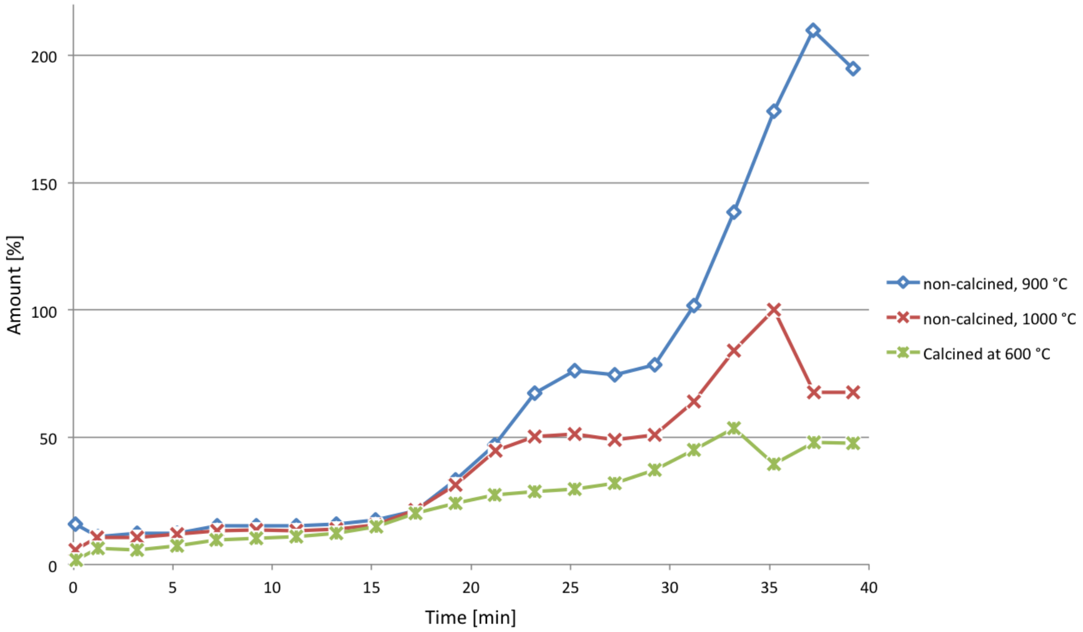

Figure 4.41: The peak areas obtained from the CO_2 extracted-ion chromatogram of the non-calcined A19 and A19 calcined at 600 °C corresponding to amount of CO_2. The amount is given as a function of time during heating to 900 and 1000 °C, normalized to the highest peak area of the non-calcined material during heating to 1000 °C.

Thermogravimetric data obtained from the heating of C3, C7 and BIO to 1000 °C is given i Figure 4.42. In (a), the mass and the derivative of mass are given as functions of temperature, and in (b) the mass and the Gram-Schmidt curves are given as functions of temperature.

From Figure 4.42 (a) it can be seen that the mass loss is a lot bigger for the charcoal, BIO, than for the two cokes. The two cokes have only a small gradual mass loss from about 500 °C for C7 and 700 °C for C3, and no big changes in the mass derivative is observed. BIO has a higher mass loss rate at about 350 and 600 - 700 °C. Figure 4.42 (b) shows that the intensity of evolved gas increases with increasing temperature for C3 and C7, and reaches a maximum at about 700 °C for BIO.

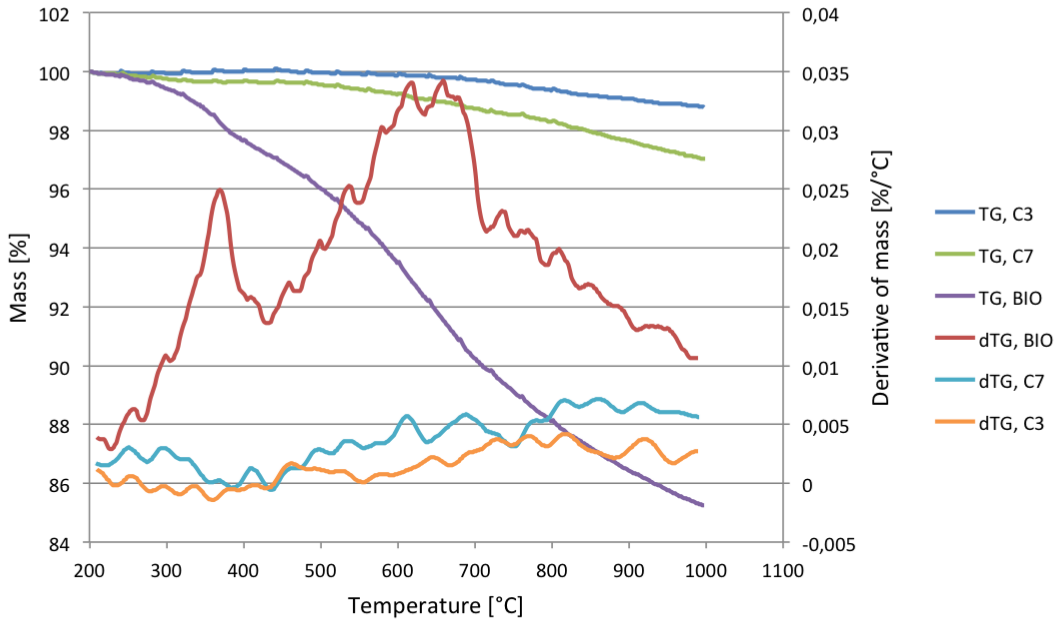

(a)

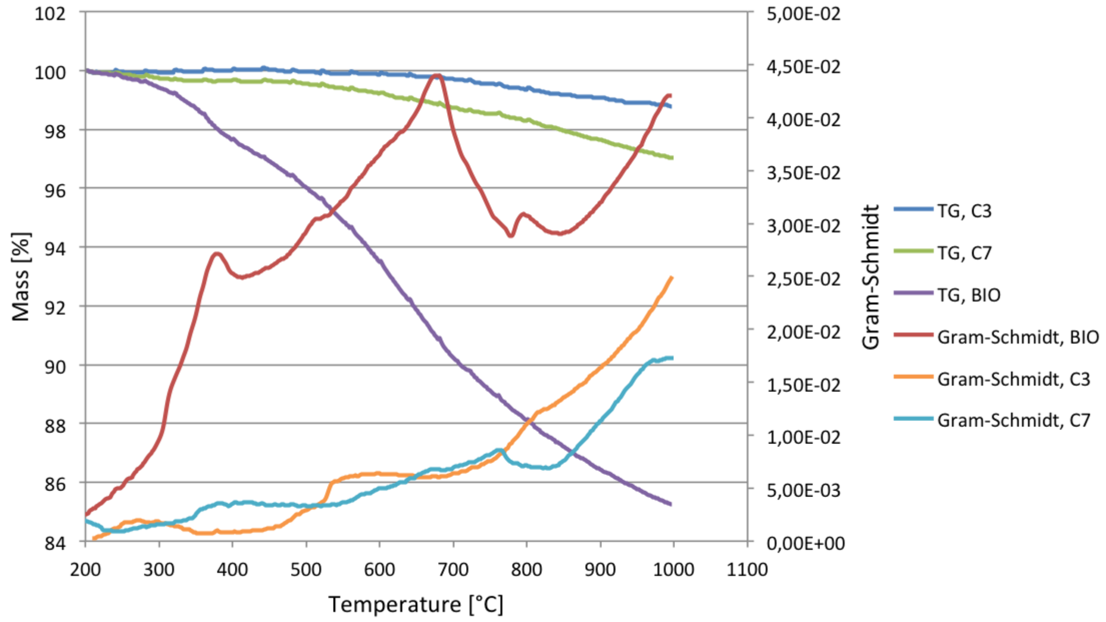

(b)

Figure 4.42: Thermogravimetric data of the charcoal and the two cokes heated to 1000 °C. (a) The mass loss and the derivative of mass given as functions of temperature. (b) The mass loss and the Gram Schmidt curves given as functions of temperature.

Figure 4.43 (a) and (b) show the FTIR spectra of the two cokes, C3 and C7 respectively. The FTIR specra of charcoal is shown in Figure 4.44. These FTIR spectra are obtained from the evolved gases during heating up to 1000 °C of the materials. The absorbance is given as a function of time and wavenumber.

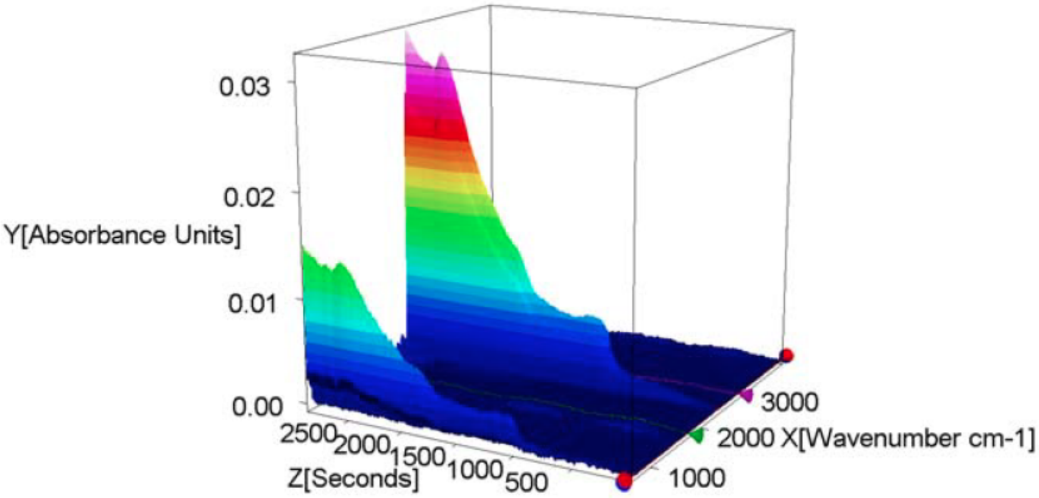

(a)

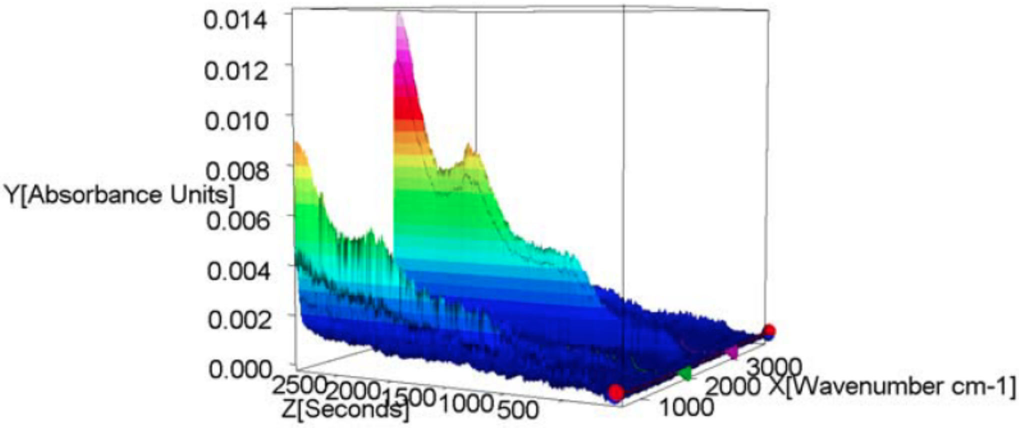

(b)

Figure 4.43: Fourier transformed infrared spectrum of the evolved gases from (a) C3 and (b) C7 during heating to 1000 °C.

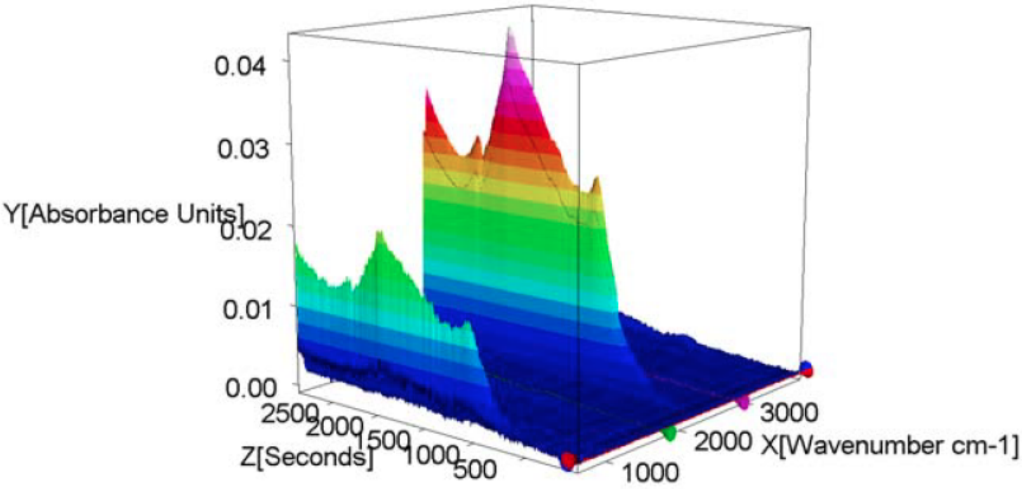

Figure 4.44: Fourier transformed infrared spectrum of the evolved gases from BIO during heating to 1000 °C.

The two-dimensional spectra given in Figure 4.45, 4.46 and 4.47 for C3, C7 and BIO, respectively, are obtained from the three-dimensional spectra in Figure 4.43 and 4.44. These spectra are given at the time corresponding to the maximum temperature of 1000 °C for all samples, and show the absorbance as a function of wavenumber.

For C3 only peaks corresponding to CO_2 and CO are observed, while for C7 and BIO, additional peaks corresponding to H_2O is also observed. The highest absorbance is observed for for the charcoal, while the lowest absorbance is observed for the C7 material.

The peak areas corresponding to the amount of CO_2 and CO are given in Figure 4.48. The values are normalized to the highest value of CO_2 for the charcoal. In the figure, the temperature is also given as a function of time.

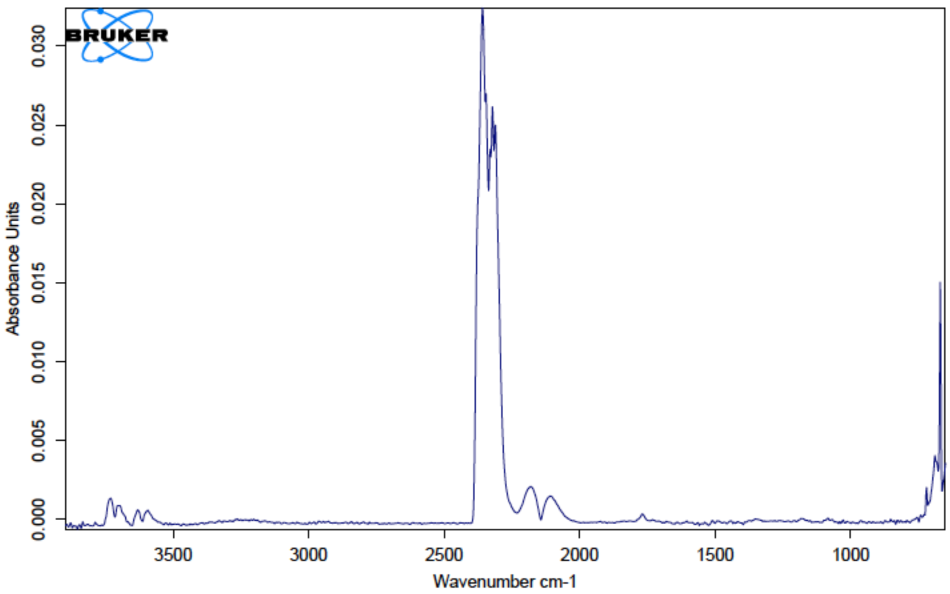

Figure 4.45: FTIR spectrum of the C3 heated to 1000 °C. The absorbance is given as a function if wavenumber at the time corresponding to the maximum temperature of 1000 °C.

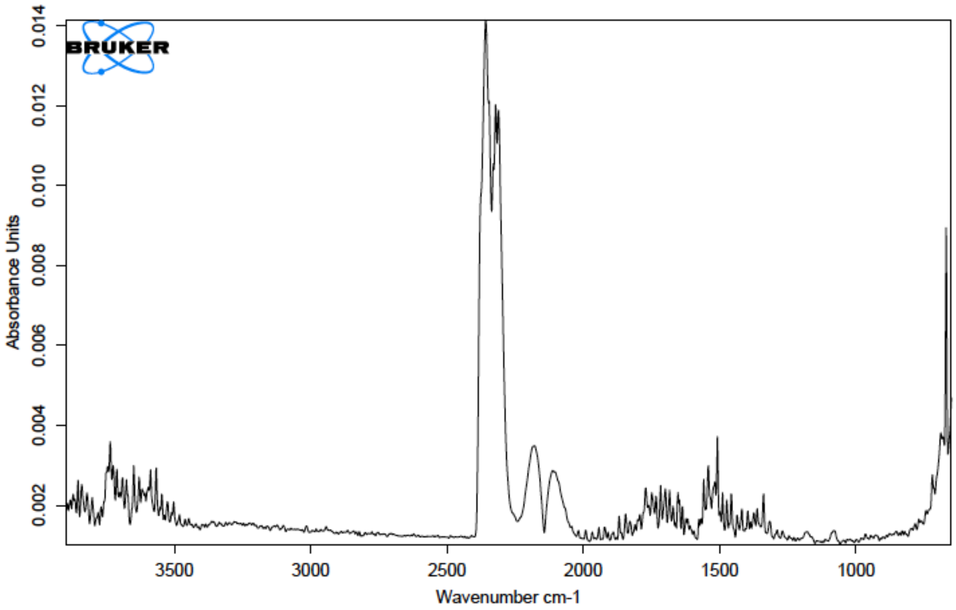

Figure 4.46: FTIR spectrum of C7 heated to 1000 °C. The absorbance is given as a function if wavenumber at the time corresponding to the maximum temperature of 1000 °C.

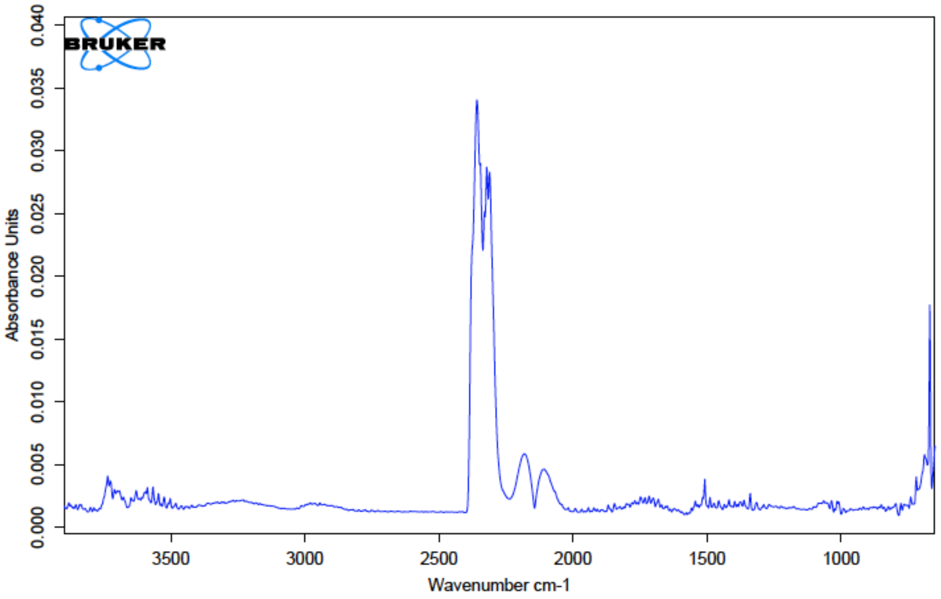

Figure 4.47: FTIR spectrum of BIO heated to 1000 °C. The absorbance is given as a function if wavenumber at the time corresponding to the maximum temperature of 1000 °C.

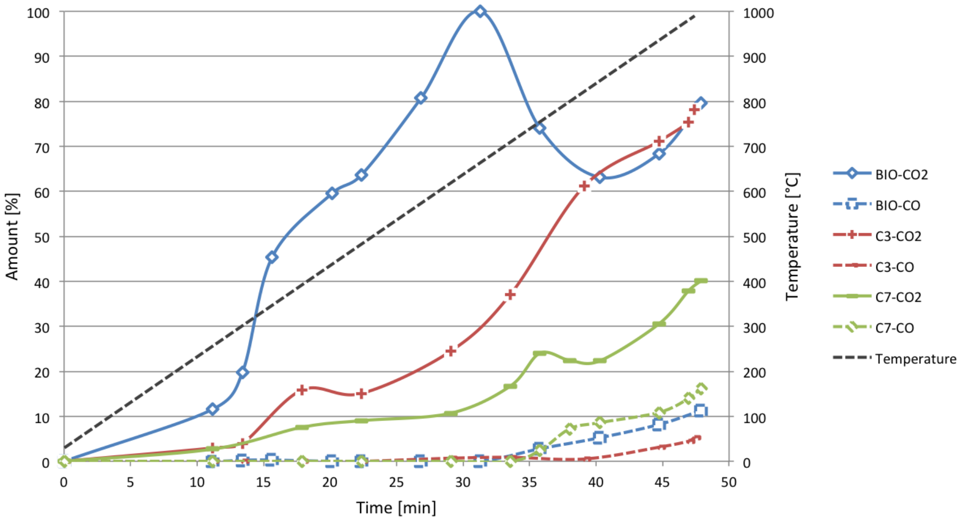

Figure 4.48: Amount of CO_2 and CO of C3, C7 and BIO obtained from FTIR given as a function of time during heating. The curves are normalized to the maximum amount of CO_2 of BIO.

All the two-dimensional FTIR spectra given at the different times from where the peak areas are calculated, are given in Figure 4.49 for C3, 4.50 for C7 and 4.51 for BIO. The maximum temperature is 1000 °C for all samples, the absorbance is given as a function of wavenumber.

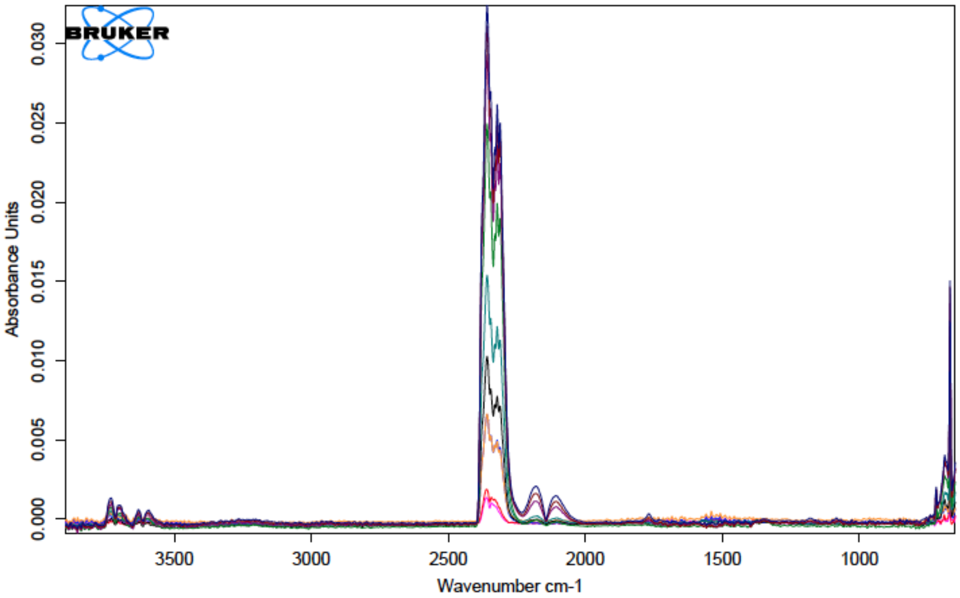

Figure 4.49: The two-dimensional FTIR spectra of C3 corresponding to the different times at where the peak areas are calculated.

From Figure 4.48, it can be seen that the first peak area calculations were carried out at around 11 minutes into the experiment for all samples. This corresponds to a temperature of about 250 °C. Some CO_2 is observed at this temperature for all samples, and the amount increases with increasing temperature. For BIO, the highest amount is observed at about 650 °C. CO only appears between 700 and 800 °C for all samples, and continue to increase with increasing temperature.

The FTIR spectra for the charcoal, given in Figure 4.51, also show small peaks around 3000 cm^{-1} for the green and the turquoise lines corresponding to about 550 and 650 °C, respectively.

Figure 4.52 shows the EICs from GC-MS. Here, the signal from the CO_2 is given as a function of the time during heating of the materials. The two cokes are given in (a) and (b), while the charcoal is given in (c).

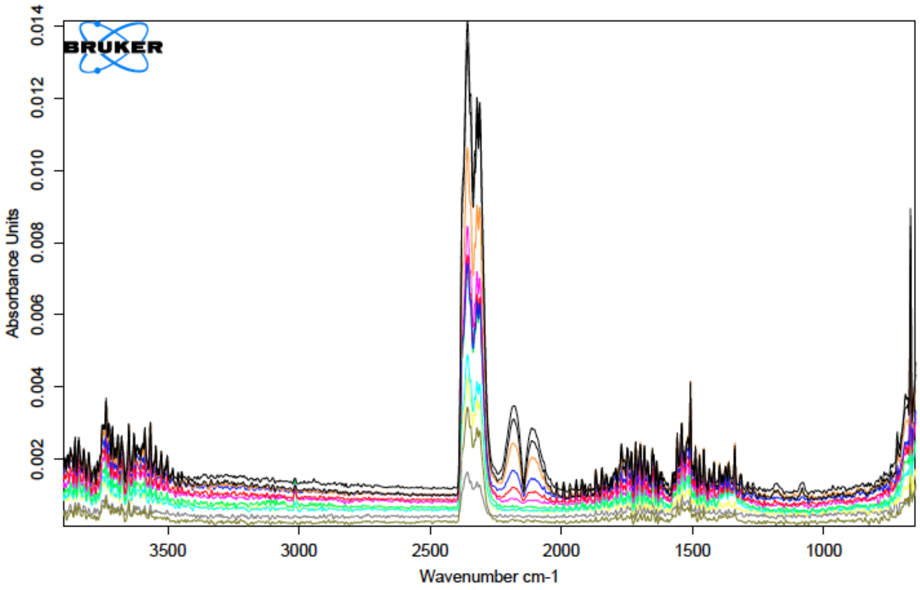

Figure 4.50: The two-dimensional FTIR spectra of C7 corresponding to the different times at where the peak areas are calculated.

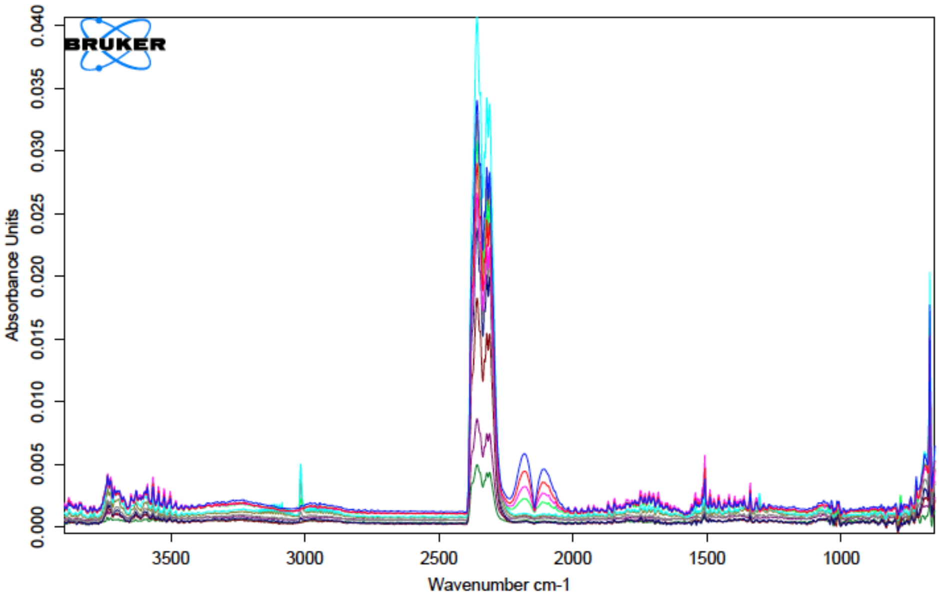

Figure 4.51: The two-dimensional FTIR spectra of BIO corresponding to the different times at where the peak areas are calculated.

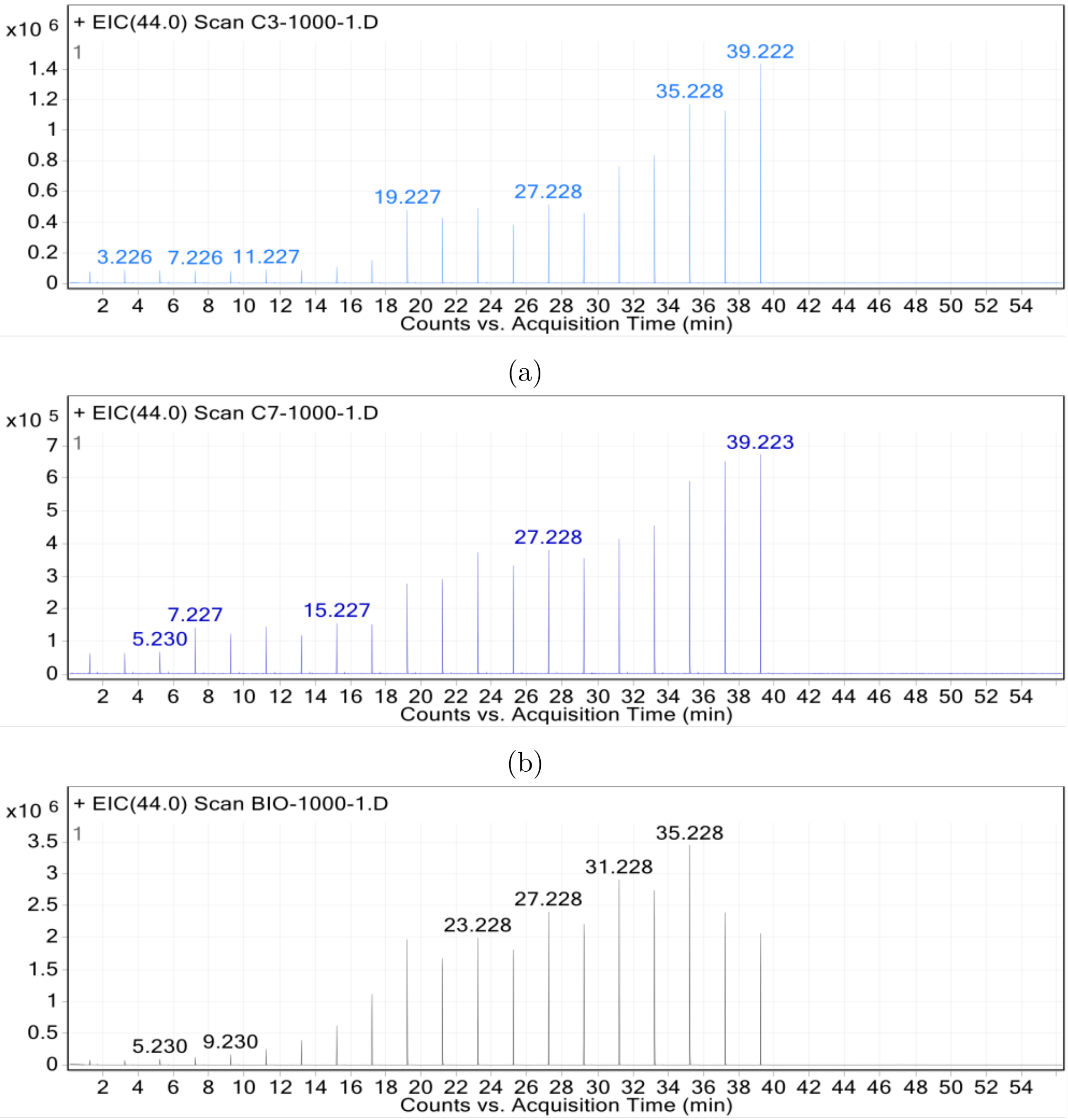

(a)

(b)

(c)

Figure 4.52: The extracted-ion chromatogram of CO_2 from (a) C3, (b) C7 and (c) BIO heated to 1000 °C.

The peak height increases with time and hence with increasing temperature for all samples, but is lower fro C7 than C3 and BIO. The retention times, peak height and peak areas are given in Table H.7, H.8 and H.9 in Appendix H.

The peak areas obtained from the CO_2 EIC of C3, C7 and BIO are given in Figure 4.53. The curves are normalized to the highest peak area of BIO during the heating to 1000 °C.

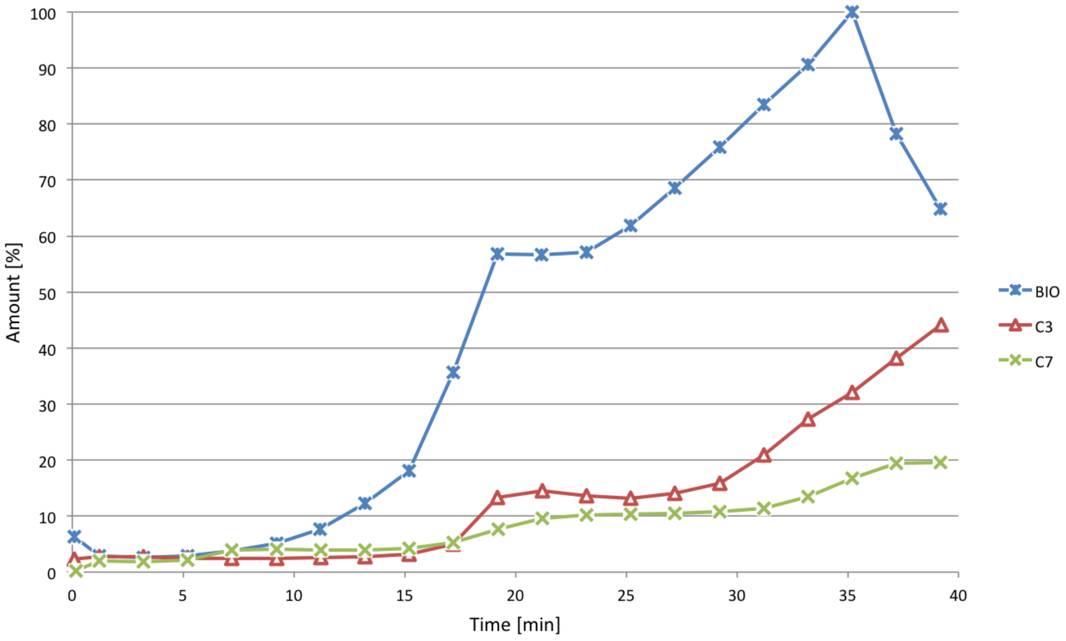

Figure 4.53: The peak areas obtained from the CO_2 extracted-ion chromatogram of C3, C7 and BIO corresponding to amount of CO_2. The amount is given as a function of time during heating to 1000 °C. The curves are normalized to the highest peak area of BIO during the heating to 1000 °C.

4.6 Multiple Linear Regression

4.6.1 Porosity

The relationship between the number of independent variables included in the optimum multiple linear regression (MLR) analysis, and the root mean square error (RMSE) difference between the calculated and the experimental values is presented in Figure 4.54. The content of ash, hydrogen, sulfur and nitrogen, as well as the interlayer spacing and the BET surface area were considered to calculate the total porosity of anthracite A11. The non-calcined anthracite and the anthracite calcined at 600, 1100, 1800 and 2650 °C were included in this study.

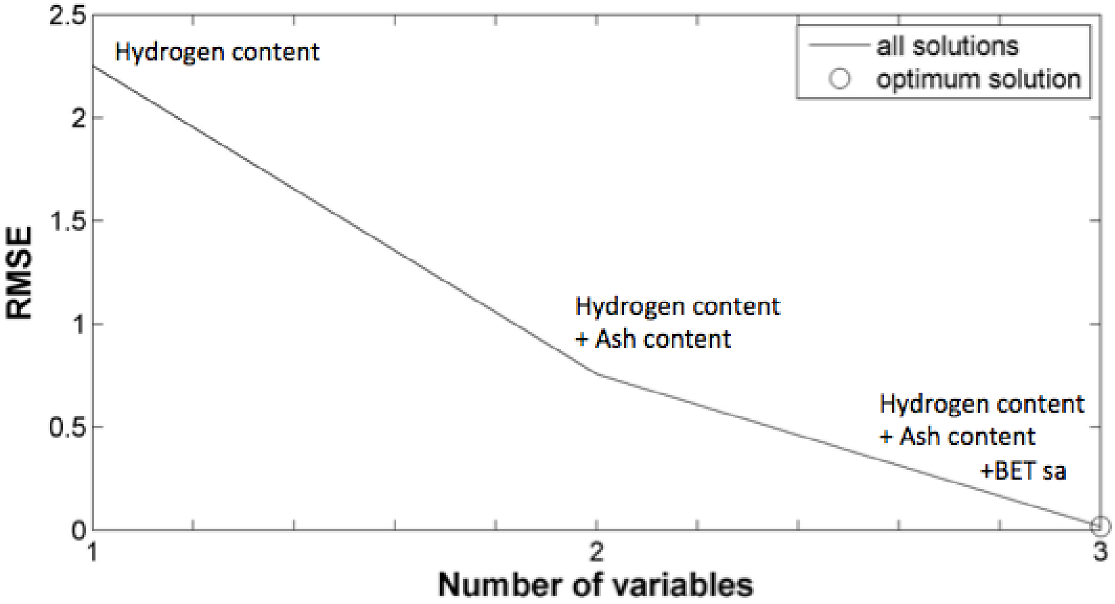

Figure 4.54: RMSE difference between the calculated porosity and the experimental porosity of A11 as a function of the number of independent variables included in the MLR solution.

From Figure 4.54 it can be seen that when considering only one independent variable for the MLR solution, the RMSE difference between the calculated porosity and the experimental values is about 2.3 %. By increasing the number of independent variables the deviation decreases.

The optimum solutions are given in Equation 4.55, 4.56 and 4.57 for 1, 2 and 3 independent variables, respectively.

$$\text{Total porosity [\%]} = 10.0577 + (1.28833 \cdot \text{Hydrogen [\%]}) \tag{4.1}$$

$$\text{Total porosity [\%]} = 13.8308 + (-2.05091 \cdot \text{Ash [\%]}) + (1.6731 \cdot \text{Hydrogen [\%]}) \tag{4.2}$$

$$\begin{aligned} \text{Total porosity [\%]} = 14.4819 + (-2.51264 \cdot \text{Ash [\%]}) \\ +(2.37617 \cdot \text{Hydrogen [\%]}) + (-0.220151 \cdot \text{BET surface area [m}^2\,\text{g}^{-1}]) \end{aligned} \tag{4.3}$$

The optimum solution with one independent variable depends on the hydrogen content of the sample. The optimum solution for this is shown in Equation 4.1. The values calculated from using this equation are given in Figure 4.55 together with the experimental porosity of the samples.

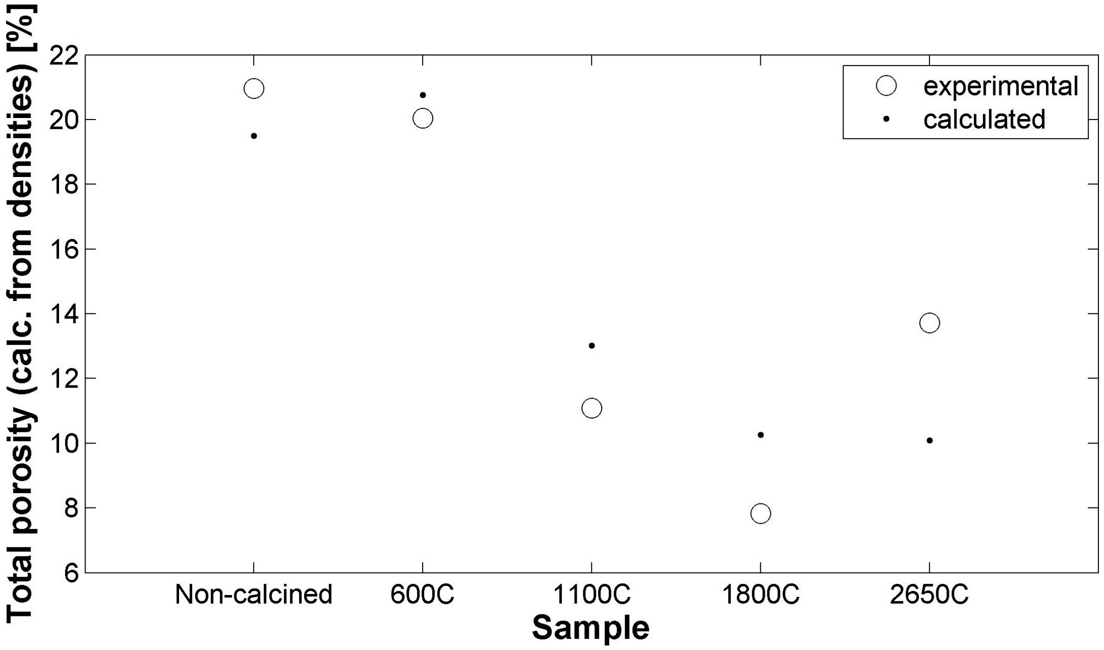

Figure 4.55: Calculated versus experimental porosity with an optimum solution with 1 independent variable.

For the most optimum solution with a RMSE difference of zero, the independent variables are the hydrogen content, the ash content and the BET surface area of the anthracite sample. The calculated versus actual porosities are shown in Figure 4.57.

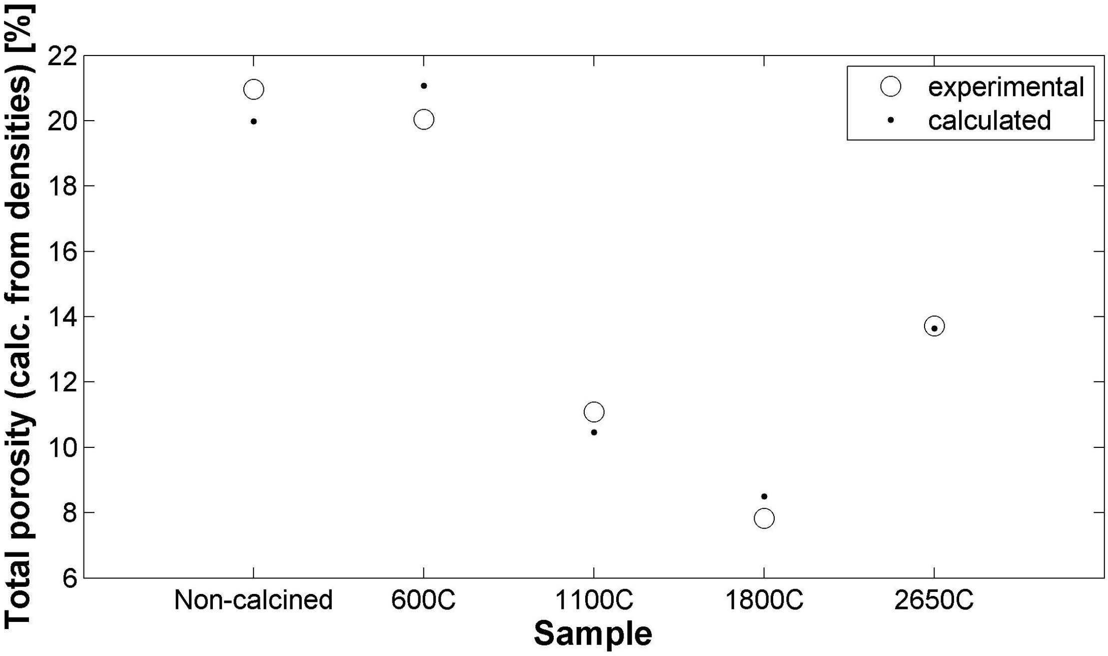

Figure 4.56: Calculated versus experimental porosity with an optimum solution with 2 independent variables.

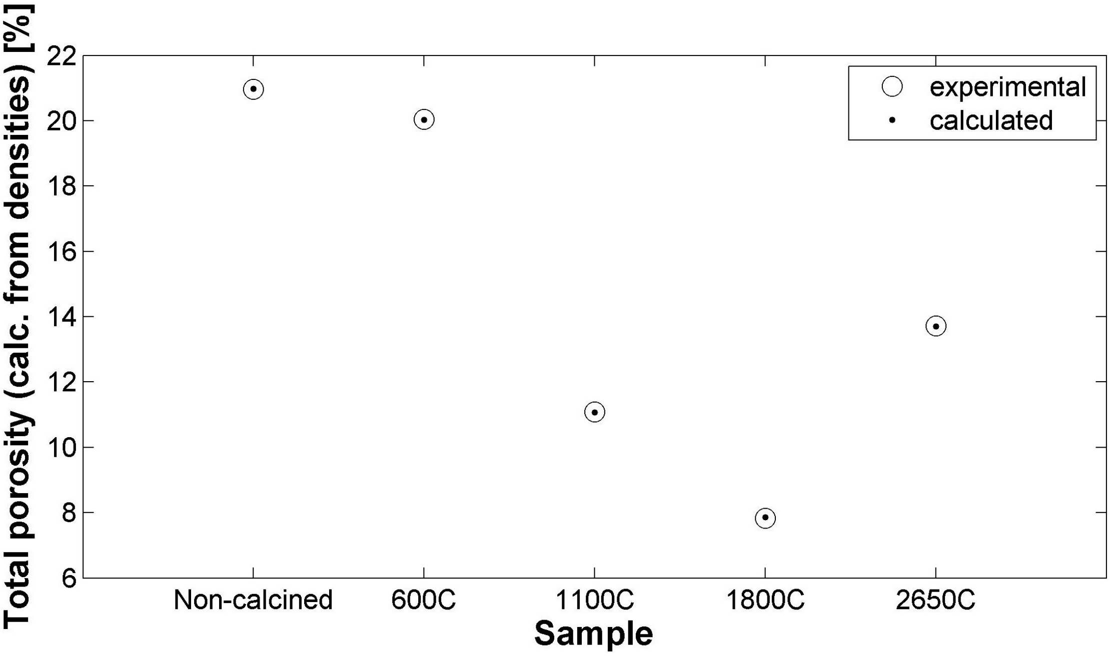

Figure 4.57: Calculated versus experimental porosity with an optimum solution with 3 independent variables.

4.6.2 Expansion

The relationship between the number of independent variables included in the optimum multiple linear regression analysis, and the root mean square error difference between the calculated and the experimental values is presented in Figure 4.58. The content of volatiles, ash, fixed carbon and sulfur, as well as the interlayer spacing were considered to calculate the expansion at 1400 °C during the first temperature cycle for the material. The two non-calcined anthracites and the anthracites calcined at 600 °C were included in this study.

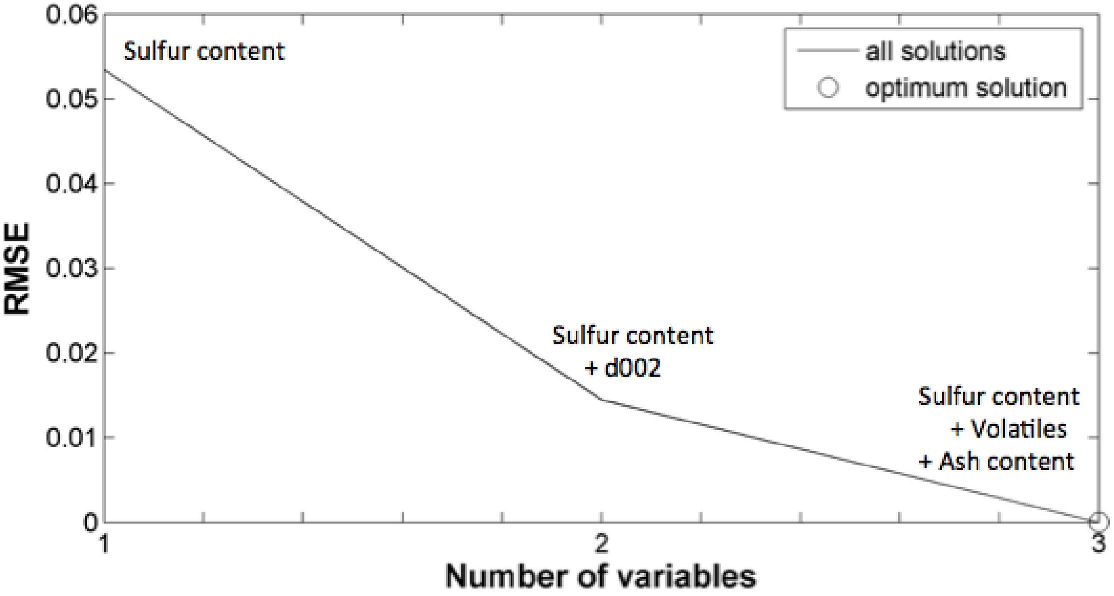

Figure 4.58: RMSE difference between the calculated expansion at 1400 °C and the experimantal expansion for A11 and A19 as a function of the number of independent variables included in the MLR solution.

As can be seen from the figure, a MLR solution with only one independent variable will give a RMSE difference of about 0.05 % between the calculated and the actual value. However, by increasing the number of independent variables to three, a RMSE difference of 0 might be obtained.

Figure 4.59, 4.60 and 4.61 show the calculated versus the actual values for a optimum solution of 1, 2 and 3 independent variables, respectively. The optimum equations are given in Equation 4.4, 4.5 and 4.6.

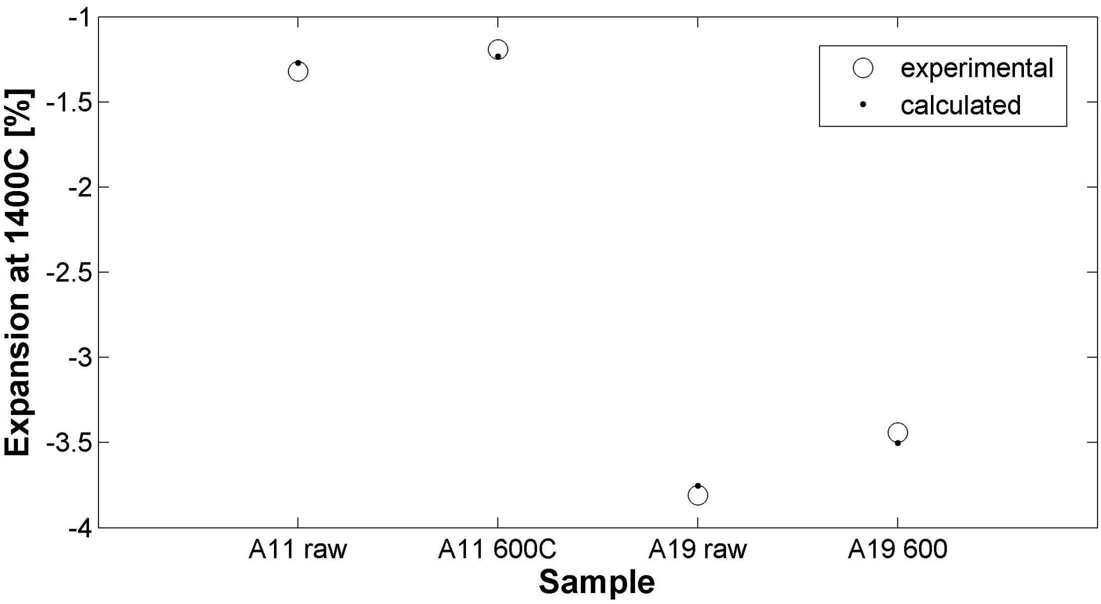

Figure 4.59: Calculated versus experimental expansion at 1400 °C during the first temperature cycle with an optimum solution with 1 independent variable.

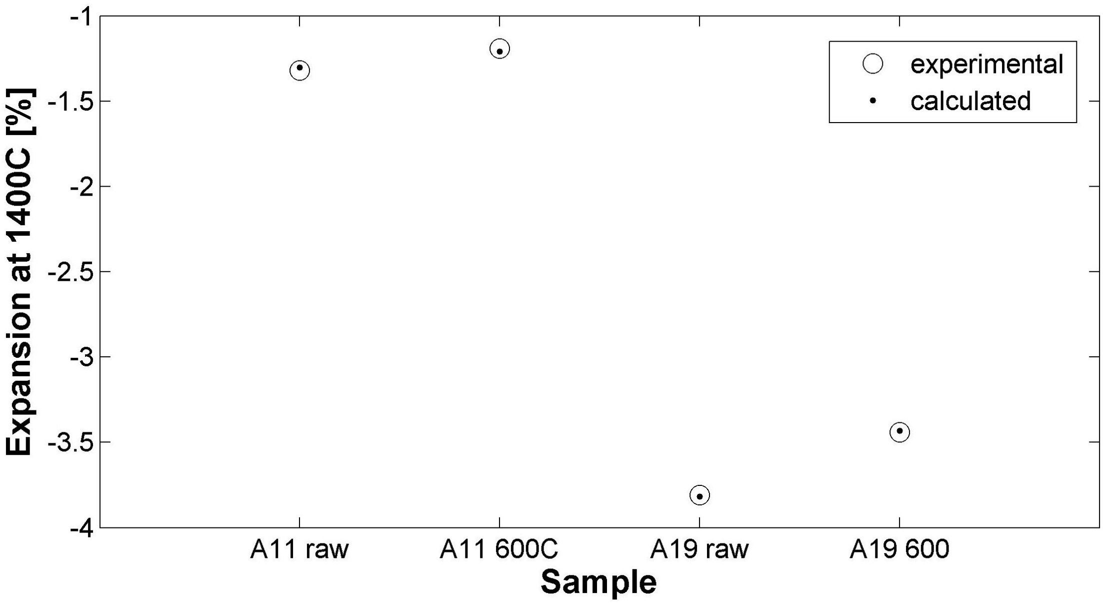

Figure 4.60: Calculated versus experimental expansion at 1400 °C during the first temperature cycle with an optimum solution with 2 independent variables.

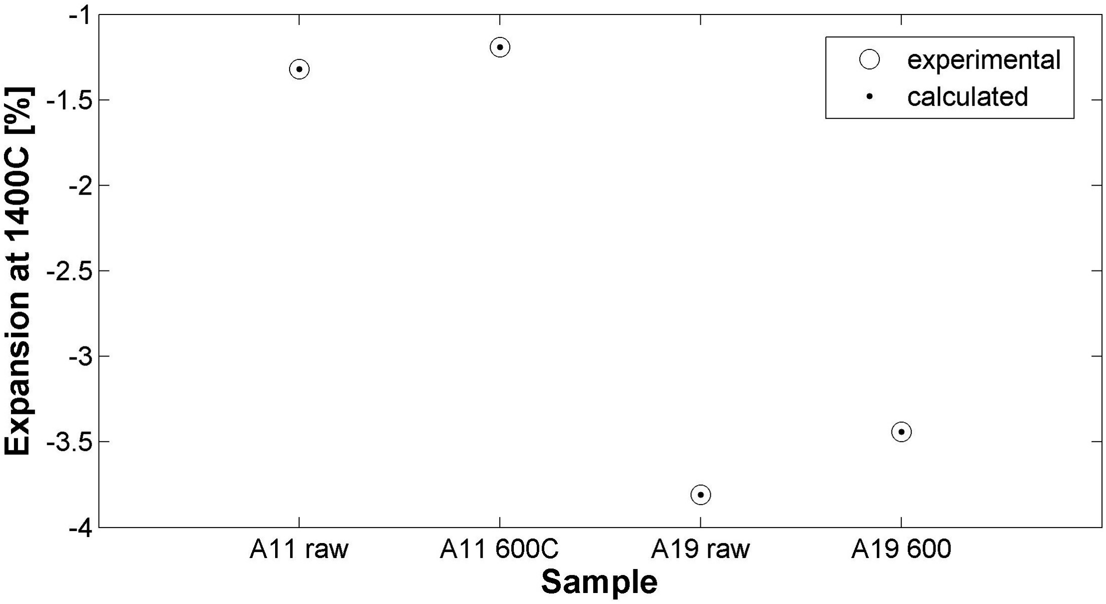

Figure 4.61: Calculated versus actual expansion at 1400 °C during the first temperature cycle with an optimum solution with 3 independent variables.

$$\text{Expansion at } 1400\,^{\circ}\text{C } [\%] = -0.69329 + (-3.6015 \cdot \text{Sulfur } [\%]) \tag{4.4}$$

$$\begin{split}\text{Expansion at } 1400\,^{\circ}\text{C } [\%] = 17.4091 + (-4.02395 \cdot \text{Sulfur } [\%]) \\ +(-5.20655 \cdot d_{002})\end{split} \tag{4.5}$$

$$\begin{split}\text{Expansion at } 1400\,^{\circ}\text{C } [\%] = -0.74279 + (0.04992 \cdot \text{Volatiles } [\%]) \\ +(-0.033028 \cdot \text{Ash } [\%]) + (-3.7568 \cdot \text{Sulfur } [\%])\end{split} \tag{4.6}$$

Chapter 5

Discussion

In this chapter a discussion of the previously mentioned results will be provided. The surface area and the porosity of anthracite A11 will be discussed, as well as the thermal expansion behaviour of single grains. The thermal expansion behaviour of pellets of all materials will also be discussed in this chapter, in addition to the mass loss during heating with corresponding off-gases.

5.1 Surface Area and Porosity

Both the BET surface areas obtained from previous work [33] and during this thesis work are given in Figure 5.1, where the red dots represent the previous work and the blue dots represent the new measurements. During the previous work, only BET surface areas from A11 calcined at 1100, 1800 and 2560 °C were obtained. As can be seen from the figure, the values correlate for these samples. The standard deviation for the increasing temperature samples are 0.1, 0.2 and 1.0 $\mathrm{m^2\,g^{-1}}$, respectively.

During this thesis work, BET surface area measurements were also obtained from the non-calcined material of A11 and A11 calcined at 600 °C. The values for these two samples are a lot higher than for the materials calcined at 1100, 1800 and 2650 °C, and indicates higher porosities. The big decrease in surface area between 600 and 1100 °C might be due to pores collapsing in this temperature range. According to Okolo et al. [30] are the pores covered by N_2 gas adsorption

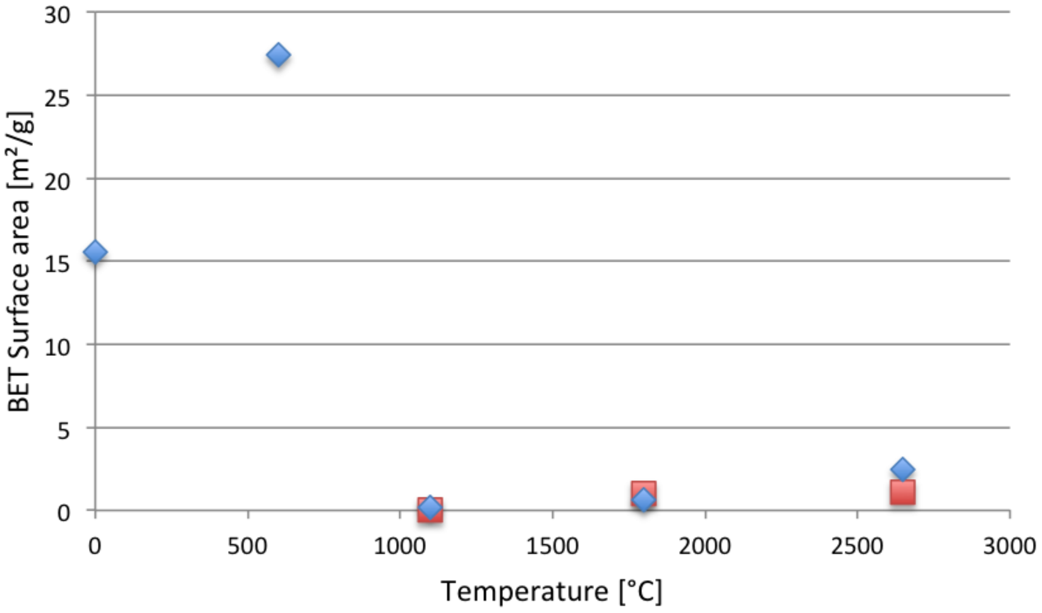

Figure 5.1: BET Surface area given as a function of calcining temperature. The red dots represent measurements carried out in previous work [33], while the blue dots represent the new measurements.

limited to those with a diameter between 1.7 and 50 nm. This implies that the possible collapse of pores between 600 and 1100 °C measured by N_2 gas adsorption are of micro- and mesopore-size.

Another explanation might be that smaller pores coalesce into each other to form bigger pores in the temperature range of 600 to 1100 °C. This would explain the decrease in surface area, however, this would not affect the total porosity.

The main motivation for the additional density measurements and surface area measurements carried out in this thesis were the difference in the porosities obtained by different methods in the previous work. During the specialization project [33], the porosity of anthracite A11 was calculated from density measurements and obtained by image analysis of light micrographs. These results are shown in Figure 2.12, Section 2.5.

While the porosity obtained from ImageJ increases with increasing calcining temperature, the porosity from the density measurements first decrease until 1800 °C before it increases between 1800 and 2650 °C. For all samples, the porosity obtained from density measurements is higher than the porosity from the image analysis. This might be explained by the fact that the porosity obtained from density measurements cover the full pore range from micropores through macropores, while the porosity obtained from image analysis only cover macropores.

The difference in porosity is greatest for the non-calcined material and the material calcined at 600 °C. This might be explained by the high surface areas indicating higher micro- and mesoporosity for these samples. By adding the detection ranges of the image analysis and the N_2 gas adsorption, pores in the micro range with a diameter grater than 1.7 nm, mesopores and macropores are included. However, there will still be pores not covered by any of these techniques in the lower micropore range, pores with a diameter less than 1.7 nm.

The scattered values of the absolute and envelope density measurements of A11, shown in Figure 5.2 and 5.3 respectively, indicate a high uncertainty connected to the porosity calculations. Here, the envelope density measurements from both the previous and present work are included. For the absolute density, the average value increases with increasing temperature with the exception of the material calcined at 1800 °C. The average value of envelope density also increases with increasing temperature, but here, the outlier value belongs to the material calcined at 1100 °C.

As can be seen from the figures, the variation in the density measurements decreases with increasing calcining temperature, especially for the absolute density. This might be explained by volatiles and ash components still present at lower temperatures with an inhomogeneous distribution causing a larger variability within the same temperature sample.

For the envelope density measurements, the quasi-fluid displacement medium used had a grain size of 500 µm or less. This means that small surface pores would not be measured by this medium, also causing a grater uncertainty in the measurements.

The porosities calculated with the the average envelope density values from both previous and present work are given in Figure 5.4. Here, the error bars represent the porosities calculated with different combinations of the highest and lowest densities in order to see the maximum variation in porosity calculations.

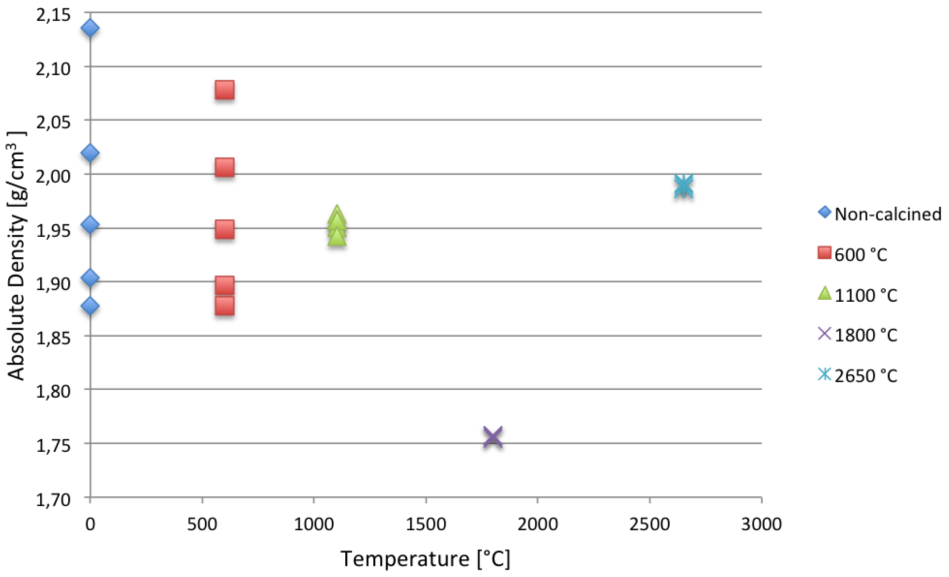

Figure 5.2: Scattered values of absolute density measurements.

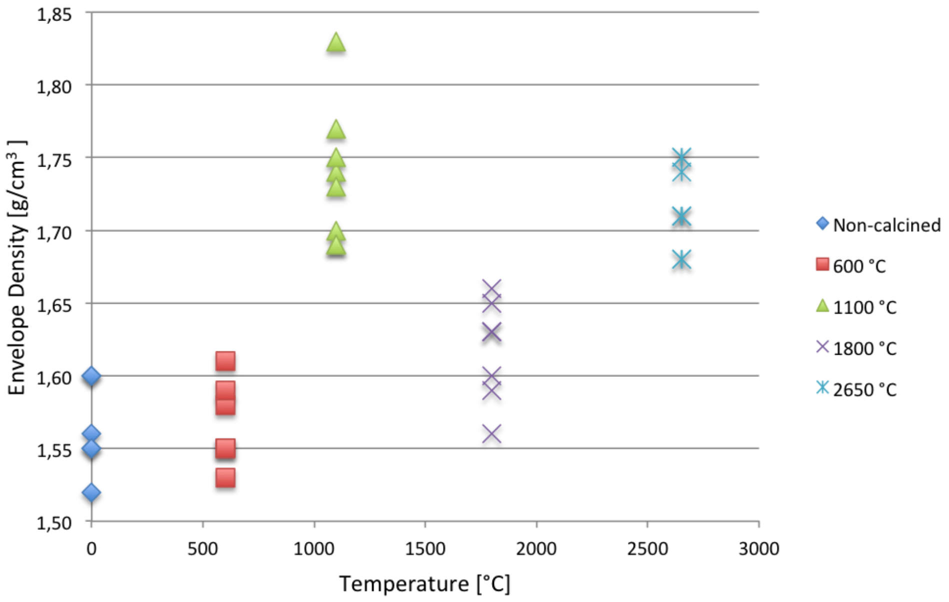

Figure 5.3: Scattered values of envelope density measurements.

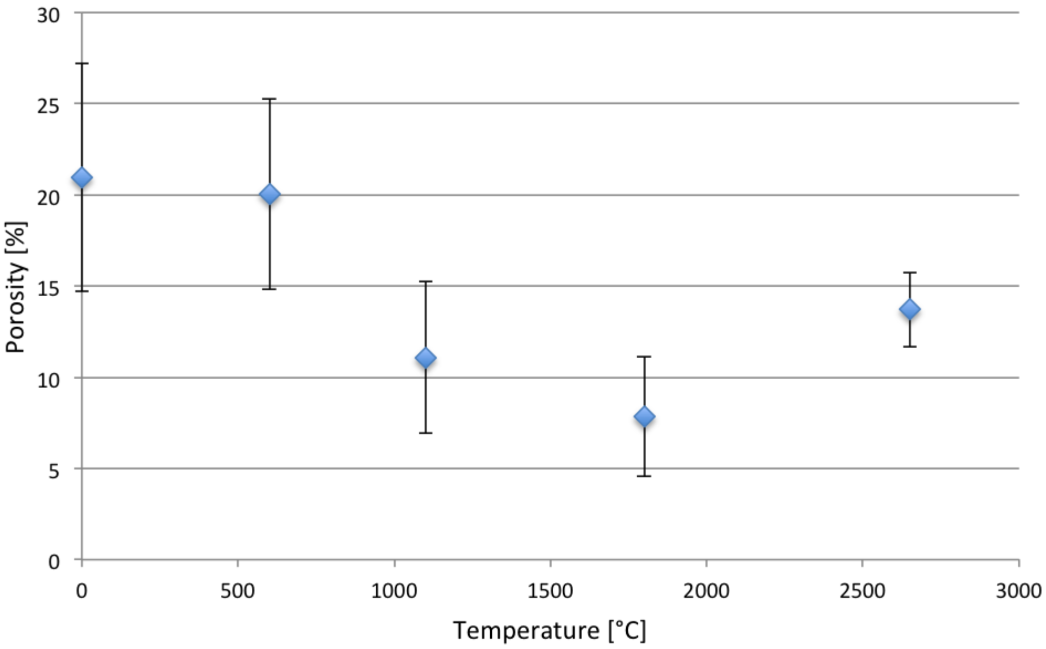

Figure 5.4: Total porosity calculated from density measurements. The error bars represent the maximum variations when using the highest and lowest density values in the porosity calculations.

This uncertainty was also pointed out in the previous work, where it was argued that the trend of the porosity values would still be the same even with variations in the density values. If assuming the trend in the porosity, where there is a decrease up to 1800 °C and an increase between 1800 and 2650 °C, is true, then other properties should be taken into considerations to describe the trend.

The decrease in porosity between 600 and 1800 °C might also be explained by volatiles and ash components leaving the carbon matrix within this temperature range, causing a significant shrinkage and making the material more dense. This shrinkage can be seen from the thermomechanical analysis in Section 4.4 and will be further discussed below.

As mentioned in Section 2.2.2, hydrogen is mostly found as CH_4, water and other hydrocarbons at the surface of the anthracite particles. The hydrogen is driven off around 800-1000 °C, which is confirmed in Figure 3.4 (c), Section 3.1. Here, it can be seen that the hydrogen is removed from A11 and A19 within this temperatur range, which might also describe the decrease in surface area. In the figure it can also be seen that there is an increase in hydrogen content between the non-calcined material and the material calcined at 600 °C corresponding to the increase in BET surface area for the same samples. The samples should be water-free after calcination since they were kept in sealed zip-lock bags, but the high hydrogen content may indicate that the material has picked up some humidity from the air before the measurements were carried out. However, this increase in hydrogen content should be further investigated.

In the previous work it was also argued that the interlayer spacing, d_{002}, affected the absolute density, and hence also the calculated total porosity. Other possible sources of influence mentioned were the hydrogen and ash removal. It was argued that the hydrogen and ash components leaving the carbon matrix at different temperatures would impact the absolute density and hence also the total porosity.

In order to investigate this further, an exploratory multiple linear regression analysis was carried out. These results indicated that an optimum solution including the hydrogen content, the ash content and the BET surface area could be used to calculate the porosity with a RMSE difference between the calculated and actual values of zero. This supports the argumentation carried out in the previous work.

An equation with only one independent variable, Equation 4.1 with the hydrogen content, could be used to calculate the porosity with a RMSE difference of about 2.3 %. This implies that the hydrogen content is the most important independent parameter for calculation of the total porosity. However, this multiple linear regression analysis is only exploratory, but it still gives a nice indication.

5.2 Dimensional Behaviour during Heating

5.2.1 Dilatometry

When the dilatometry experiments were carried out on the single grains, the material was heated up to about 1550 °C. For the material calcined at 1100 °C, this is 450 degrees higher than the material has reached before. Hence, additional changes in the structure might occur. For the materials calcined at 1800 and 2650 °C, the samples have already been at higher temperatures and no structural change should occur during the course of the experiments.

As can be seen from Figure 4.1, expansion of the single grains only occur above 800 °C. When cooling down, the contraction only happen above 800 °C as well. All three samples have previously been treated to temperatures above 800 °C, so all volatiles are already removed from the carbon matrix and no structural changes should occur. This indicate that the dimensional changes observed below 800 °C are due to inaccuracies in the measurements. By removing the data points below 800 °C and normalizing the data to the expansion at the maximum temperature, the samples can better be compared. This is shown in Figure 5.5 and 5.6, where the expansion is given as a function of time and temperature, respectively.

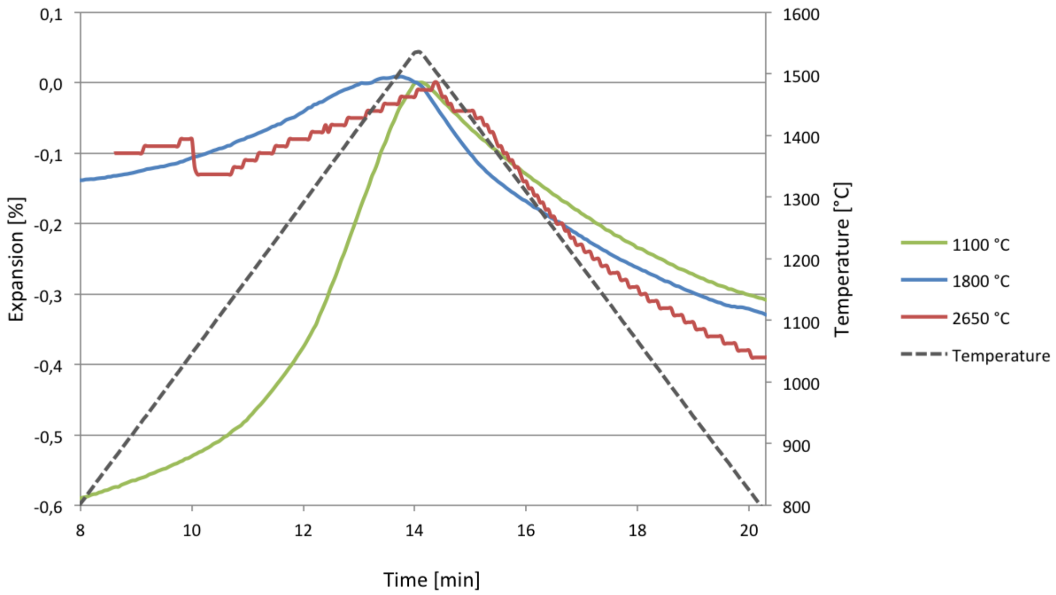

Figure 5.5: Expansion of A11 single grains above 800 °C normalized to maximum expansion.

As can be seen from the figures, the slope is similar for the materials calcined at 1800 and 2650 °C, while the material calcined at 1100 °C has a much higher slope during heating. This is also confirmed by the average TEC values, where the TEC is 15.4 $\cdot 10^{-6}$ °C^{-1} for the material calcined at 1100 °C, and 3.4 and 2.6 $\cdot 10^{-6}$ °C^{-1} for the materials calcined at 1800 and 2650 °C, respectively. These TEC values are close to the TEC of graphite, which is 2-6 $\cdot 10^{-6}$ °C^{-1}, and indicates

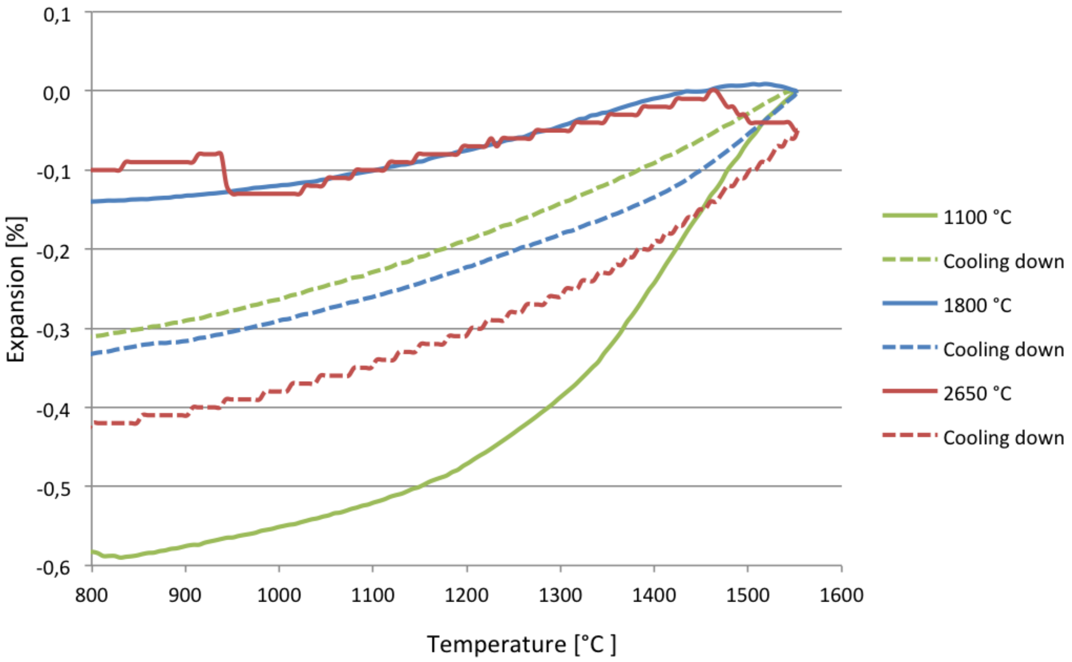

Figure 5.6: Dilatation graph of A11 single grains above 800 °C normalized to maximum expansion.

graphitization of the material calcined at 1800 and 2650 °C. During cooling, the slope is similar for all three samples, which means that at 1550 °C the changes has already occurred in the structure.

Indicated by the Figure 5.5 and 5.6, the material calcined at 1100 °C expand about 0.6 % between 800 and 1550 °C, while the materials calcined at 1800 and 2650 °C both expand about 0.1 %. During cooling all samples contract about 0.3 % within the same temperature range.

In previous work, single grains of A11 calcined at 1100 and 2650 °C were also tested. Comparison between the same temperature samples are given in Figure 5.7 and 5.8, for 1100 and 2650 °C, respectively.

For the material calcined at 1100 °C, there is a difference in the slope during heating between the two measurements. The slope is higher in the present work. This can also be seen from the TECs, where the average value from the previous work is $10.0 \cdot 10^{-6}$ $°C^{-1}$, while in the present work it is $15.4 \cdot 10^{-6}$ $°C^{-1}$. In the previous work, the material contracts about the same amount during cooling as it

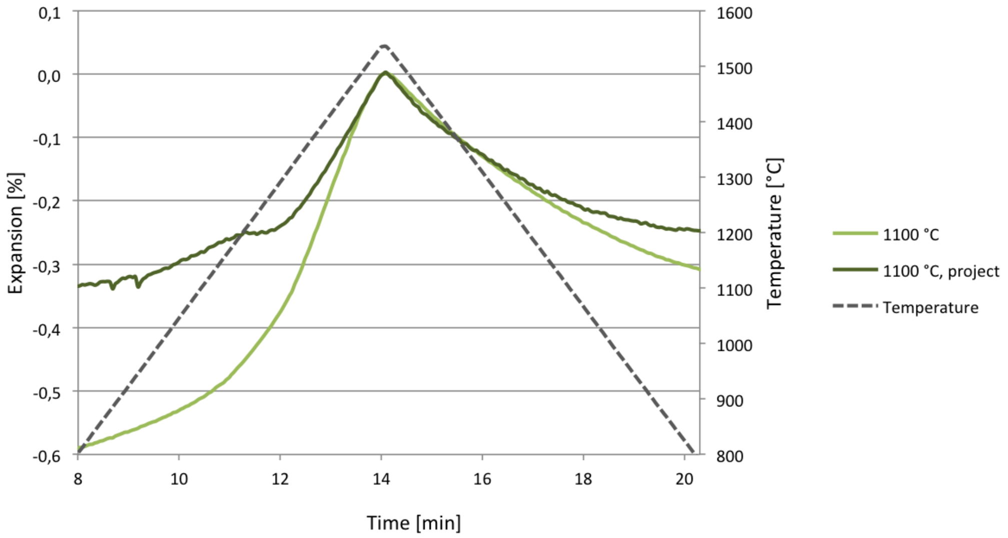

(a)

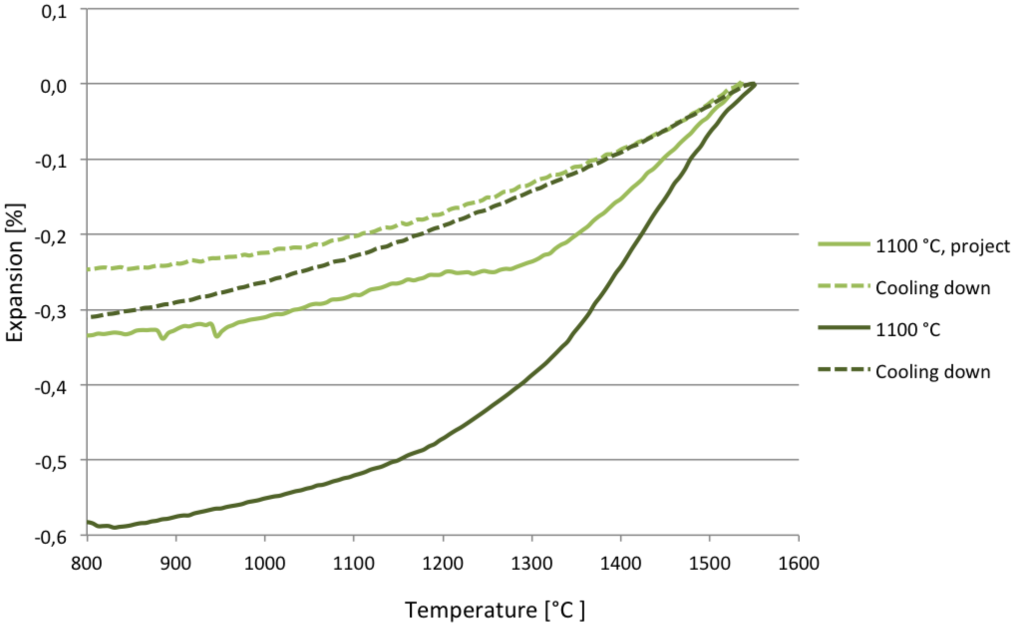

(b)

Figure 5.7: The thermal expansion of single grains of A11 calcined at 1100 °C as a function of (a) time and (b) temperature.

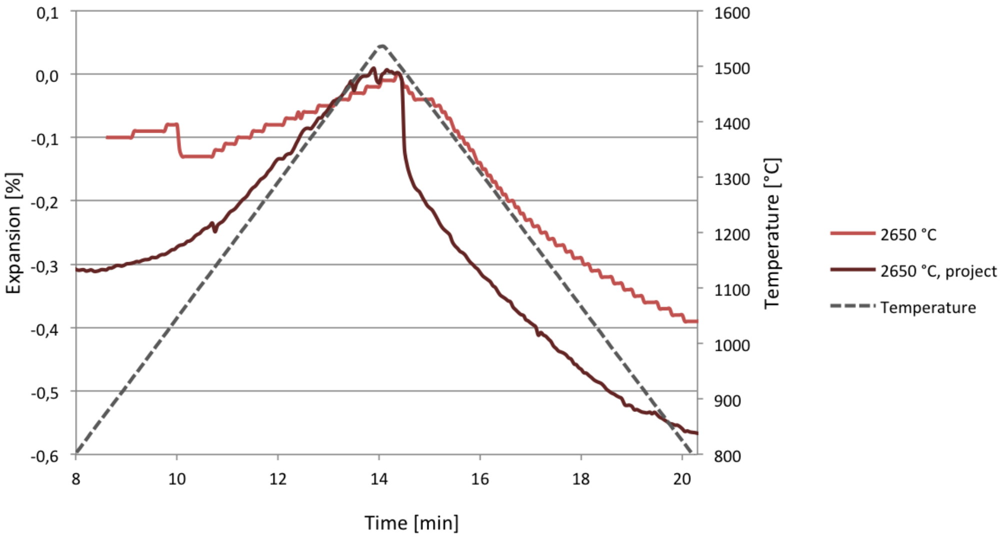

(a)

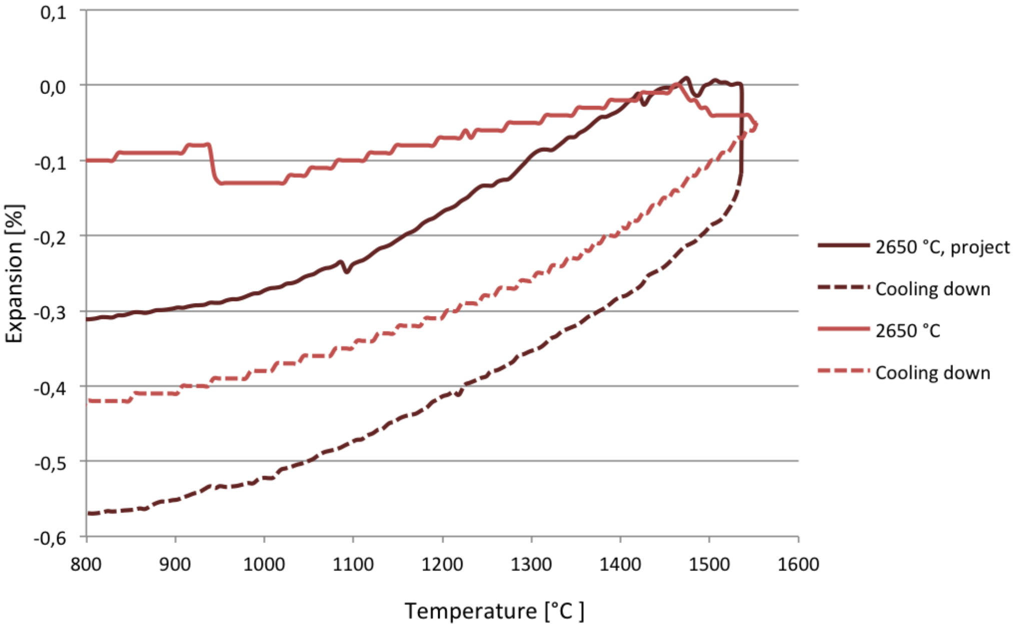

(b)

Figure 5.8: The thermal expansion of single grains of A11 calcined at 2650 °C as a function of (a) time and (b) temperature.

expands during heating in the temperature range of 800 to 1550 °C. The maximum expansion is about 0.3 %. In the present work the contraction during cooling is about 0.3 %, while the expansion within the same temperature range is 0.6 %.

Between the two experiments carried out for the material calcined at 2650 °C, a difference can also be observed. The slope is higher from the previous work, with a TEC of 6.4 $\cdot 10^{-6}$ °C^{-1}. For the present work, the TEC is 2.6 $\cdot 10^{-6}$ °C^{-1}. During heating the material was observed to expand 0.3 and 0.1 % for the previous and present work, respectively, while the contraction was about 0.6 and 0.4 %.

The inconsistencies between the previous and present work for both temperature samples, as well as difference in heating versus cooling within the same temperature ranges, indicate inaccurate measurements. While the length measurements of each grain, given in Table 4.2, suggest no change, the instrument suggests otherwise. A total expansion of about 0.4 % for the non-calcined material, and a shrinkage of 0.2 and 0.4 % for the materials calcined at 1800 and 2650 °C is measured by the instrument during the course of the experiments.

This indicates that that the dilatometer used in these experiments does not give an accurate picture of the expansion of single grains. Due to alumina having a greater TEC than graphite, 8.1 $\cdot 10^{-6}$ °C^{-1} versus 2-6 $\cdot 10^{-6}$ °C^{-1}, there will be a greater expansion in the distance piece than the actual sample. The length of the distance piece is greater than the length of the single grains, meaning that the uncertainty in the measurements will affect the anthracite grains more than the distance piece. However, the results would still give an indication, especially of the trend in TEC between the different temperature samples.

From Figure 4.3 it can be seen that above 1100 °C there is an increase in the TEC of the material calcined at 1100 °C. Below this temperature, the TEC is stable. This is in consistence with the fact that the material previously has been heated to 1100 °C, and the change in TEC only occur above this. The TECs of the materials calcined at 1800 and 2650 °C are more consistent throughout the experiment, with only a small increase towards the maximum temperature. There is a big decrease in the TEC values between 15.4 $\cdot 10^{-6}$ °C^{-1} at 1100 °C and 3.4 $\cdot 10^{-6}$ °C^{-1} at 1800 °C. A similar decrease was also pointed out in the previous work, between a material that had been heated to 1550 °C with a TEC of 10.6 $\cdot 10^{-6}$ °C^{-1} and the material calcined at 2650 °C with a TEC of 6.4 $\cdot 10^{-6}$ °C^{-1}.

It was argued that the change in the TEC between 1550 and 2650 °C indicates a change in the material. A possible explanation for this is the third stage of the graphitization, as mentioned in Section 2.2.3, where the neighbouring columns start to coalesce above 1500 °C. This might also be confirmed by the increase in the crystallite size (L_c) above 1400 °C. Due to the inclusion of the material calcined at 1800 °C in the present work, which led to a TEC of $3.4 \cdot 10^{-6}$ °C^{-1}, the argued structural change between 1550 and 2650 °C might now bee narrowed to a temperature range between 1550 and 1800 °C.

5.2.2 Thermomechanical Analysis

During the course of the thermomechanical experiments the pelletized material was heated to 1400 °C. As previously mentioned in Section 2.2.2, volatiles are removed from the carbon matrix around 800 to 1000 °C. This means that the volatiles, especially hydrogen, will be driven off during the experiments. This is true for all the non-calcined materials, and for the materials calcined at 600, 800 and 1000 °C. For the anthracites calcined at 1200 °C or higher, the volatiles have already been removed.

From Figure 4.6 and 4.7 shrinkage of A11 during the first temperature cycle can be observed. For the non-calcined material of A11, and A11 calcined at 600, 800 and 1000 °C, the shrinkage decreases with increasing calcining temperature. The relationship between the calcining temperature and the shrinkage can be seen in Figure 5.9. For the materials calcined at 1200 and 2000 °C no shrinkage is observed.

The figure shows a linear relationship between the calcining temperature of A11 and the shrinkage during the first temperature cycle for the materials calcined at 600 to 1200 °C. The shrinkage, and also this relationship, might be explained by volatiles leaving the carbon matrix since the volatiles are driven off at about 800-1000 °C. It could also be structural changes, however not structural changes that will lead to graphitization but structural changes in the amorphous carbon material. There are no big differences between the non-calcined material and the material calcined at 600 °C, or the materials calcined at 1200 and 2000 °C.

Figure 5.10 shows the relationship between the shrinkage and the volatile content of anthracite A11. The volatiles in this case, are represented by the hydrogen,

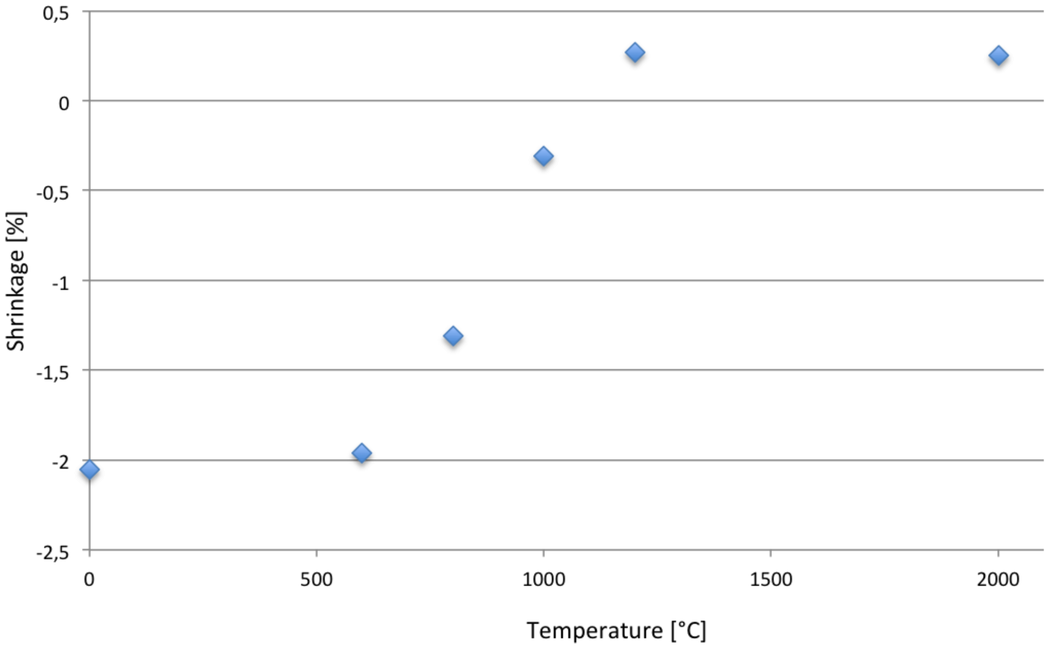

Figure 5.9: The relationship between the shrinkage and the calcining temperature of anthracite A11.

nitrogen and sulfur content of the different temperature samples. This confirms that there might be a linear relationship between the shrinkage and the volatile content for the materials calcined in the temperature region where the volatiles are driven off.

An exploratory multiple linear regression analysis was carried out in order to correlate the expansion at 1400 °C during the first temperature cycle to other coal characteristics. These expansions are given in Table 4.6 and 4.8 for anthracite A11 and A19, respectively. The results indicates that even an optimum solution with only one independent variable would give a very low RMSE difference between the experimental and calculated expansion values. This difference can be seen in Figure 4.59. This shows that the sulfur content is by far the most important parameter to consider when it comes to thermal expansion of the anthracites.

By also adding the interlayer spacing or the volatile and ash content into the optimum equation, the RMSE difference is further decreased. The results indicate that a combination of the sulfur, ash and volatile content is the best fit to ex-

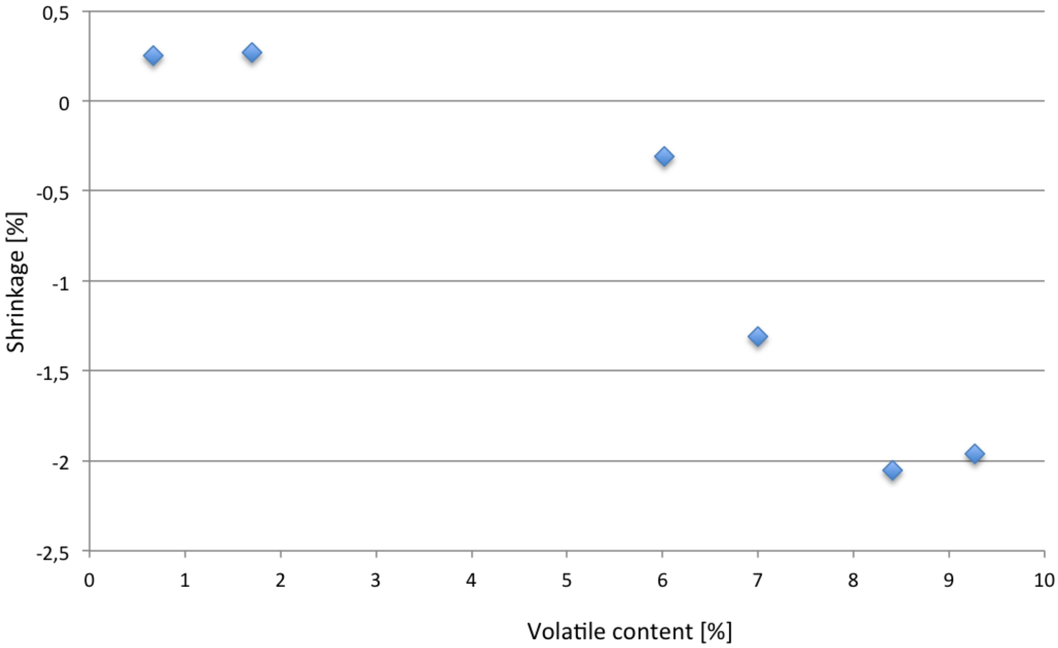

Figure 5.10: The relationship between the shrinkage and the volatile content for anthracite A11.

plain the expansion of the non-calcined anthracites and the anthracites calcined at 600 °C. The multiple linear regression analysis is only exploratory, but gives a good indication of what affects the expansion the most. The results here indicate that the sulfur content could be used as a screening parameter to assess if a new anthracite can be used or not in production to prepare calcined anthracite for use. Further investigations of the correlation between the expansion and the sulfur content should be carried out.

During the second temperature cycle, all A11 samles contract the same amount during cooling as they expand during heating. This is true also for the first temperature cycle of the materials calcined at 1200 and 2000 °C. The materials have previously been heated to temperatures equal to or higher than the maximum temperature of the experiment, mening that no additional changes will occur. The expansion during the second temperature cycle for all A11 samples are given in Figure 5.11 and 5.12 as a function of time and temperature, respectively. All samples are normalized to 0 % expansion at the beginning of the second heating.

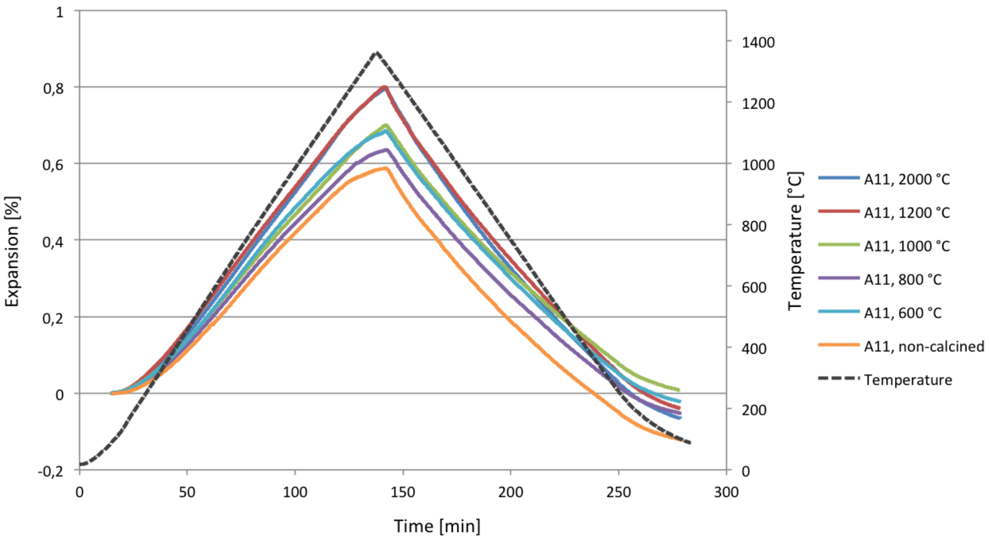

Figure 5.11: The expansion during the second temperature cycle of the A11 samples.

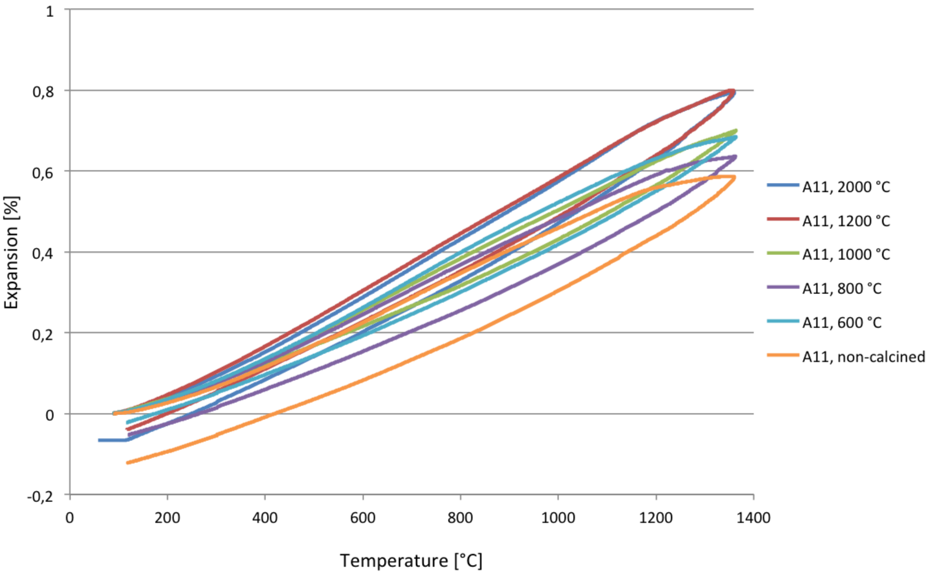

Figure 5.12: Dilatation during the second temperature cycle of the A11 samples.

As can be seen from the figures, the expansions of the materials calcined at 1200 and 2000 °C are identical. This expansion is 0.8 %. The non-calcined material has the lowest expansion of 0.6 % during the second temperature cycle. This is also in compliance with the finding of Beukes et al. [35], where they found that the expansion of anthracite is 0.6 to 1 % at 1400 °C.

For the anthracite A19, the non-calcined material and the material calcined at 600 °C also undergoes a change during the first temperature cycle, when volatiles are removed. A shrinkage of 4.7 and 4.3 % is observed. During the second heating to 1400 °C, no additional changes occur. For the material calcined at 1800 °C, no changes are observed during any of the temperature cycles. The material contracts the same amount during cooling as it expands during heating.

The second heating of all samples of A19 are given in Figure 5.13, where the expansion is given as a function of temperature. Similar to such of A11, the material with the highest calcining temperature expands more during the second temperature cycle, in this case 0.9 %. The second temperature cycle is identical for the non-calcined material and the material calcined at 600 °C, with an expansion of 0.7 % at 1400 °C.

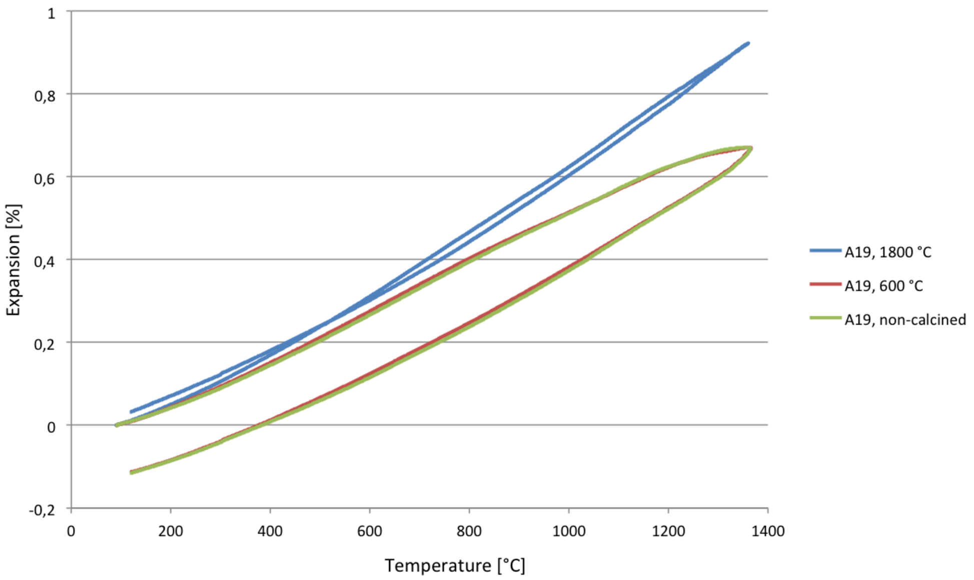

Figure 5.13: The dilatation graph for the second temperature cycle of the A19 samples.

If comparing the two non-calcined anthracites to the two cokes and the charcoal, similar behaviour is observed. The dilatation graphs of all samples are given in Figure 5.14, where the expansion is given as a function of temperature. During the first temperature cycle, there is an expansion between 500 and 800 °C for A11, A19, C7 and BIO, followed by a shrinkage. A11 and C7 show very similar behaviour which might be explained by the similarities in volatile content, both of about 2 %. The volatile content is believed to impact the shrinkage the most. This is supported by the close to linear relationship given in Figure 5.15, where the shrinkage during the first temperature cycle is given as a function of the volatile content of all samples. Here, the two anthracites calcined at 600 °C are also included.

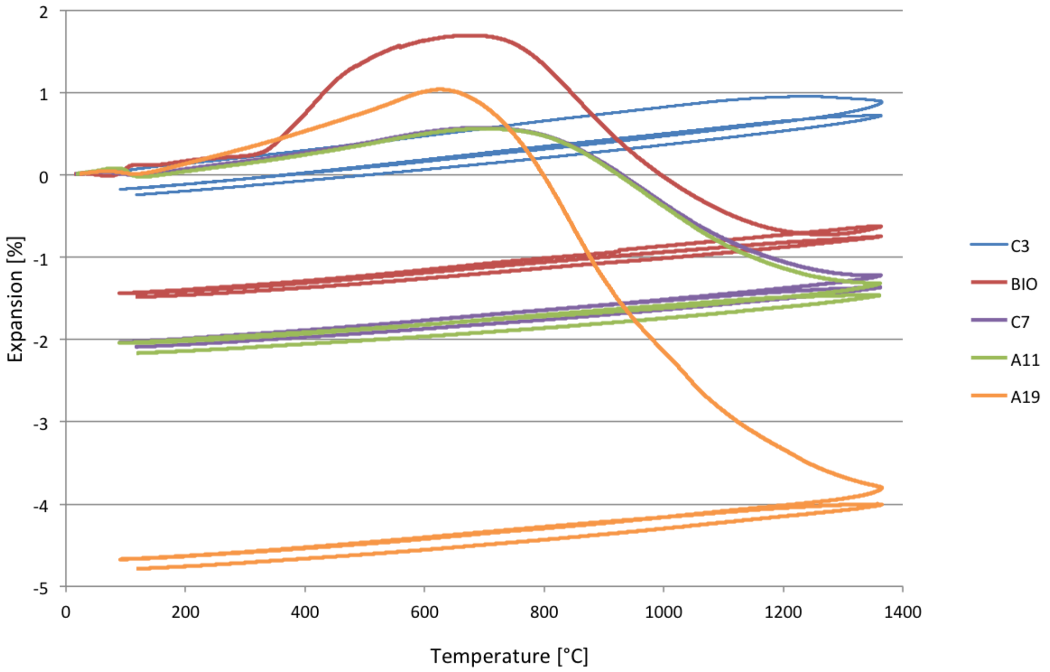

Figure 5.14: The dilatation graphs of the non-calcined anthracites, the charcoal ant the cokes.

As can be seen from Figure 5.15, BIO is an outlier with a volatile content of 14 % and only a 0.6 % shrinkage. The linear relationship between the other samples can easier be seen in Figure 5.16, where BIO is left out.

C3 stands out from the other samples by contracting the same amount during

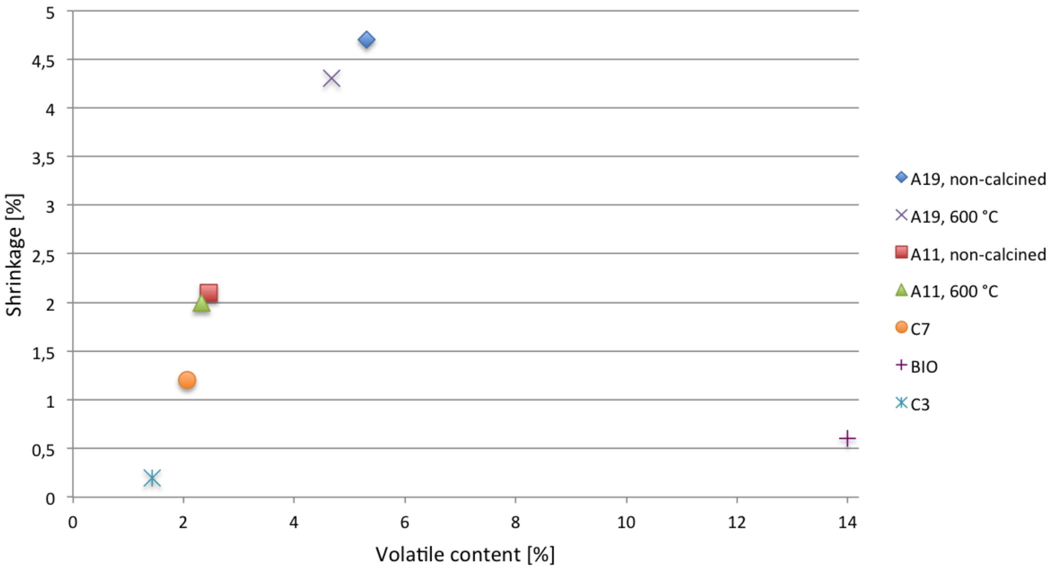

Figure 5.15: The relationship between the shrinkage during the first heating and the volatile content of each sample.

cooling as it expands during heating for both temperature cycles. This implies that the coking temperature used in the coking process is sufficiently high to remove close all volatiles, and higher than that of C7.

By considering only the second temperature cycle, as shown in Figure 5.17, it can be seen that the expansion is similar for all samples during the second heating to 1400 °C. The C3 coke has the highest expansion of 0.9 %, while the A11 has the lowest expansion of 0.6 %. For A19, BIO and C7, they all expand about the same amount at 1400 °C of 0.7 %.

This implies that the difference in the materials doesn't matter as much anymore, after the material has been heated the first time. Charcoal, coke or anthracite, they all expand 0.6 - 0.9 % at 1400 °C, which complies with the findings of Beukes et al. [35] for three different anthracites.

From Figure 4.7, it can be seen that the dilatation and hence also the TEC is equal for both temperature cycles of A11 calcined at 1200 and 2000 °C. However, from the TEC calculations the TEC during the first temperature cycle is about $8.5 \cdot 10^{-6}$ °C^{-1} for both samples, and $7.0 \cdot 10^{-6}$ °C^{-1} for the second heating.

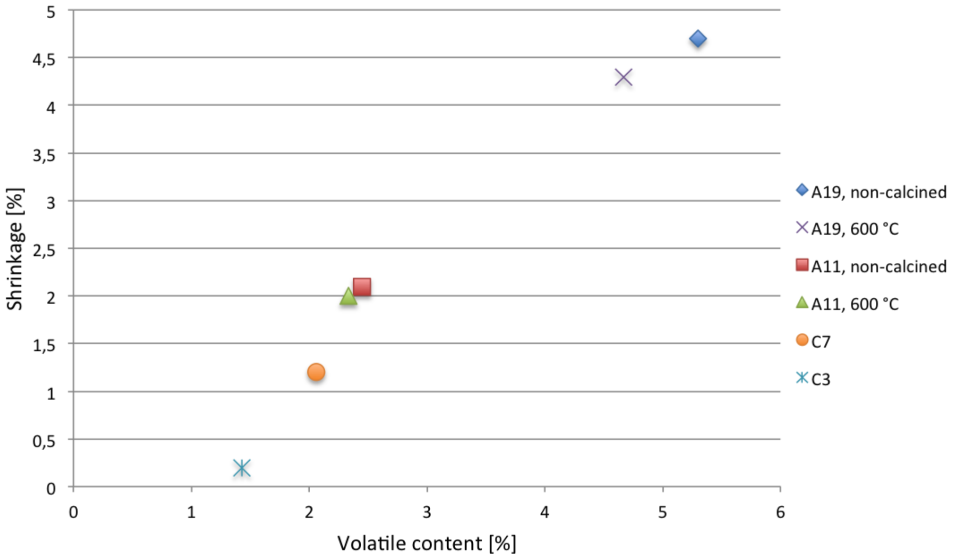

Figure 5.16: The relationship between the shrinkage during the first heating and the volatile content of each sample. Here, BIO is left out to better see the linear relationship for the other samples.

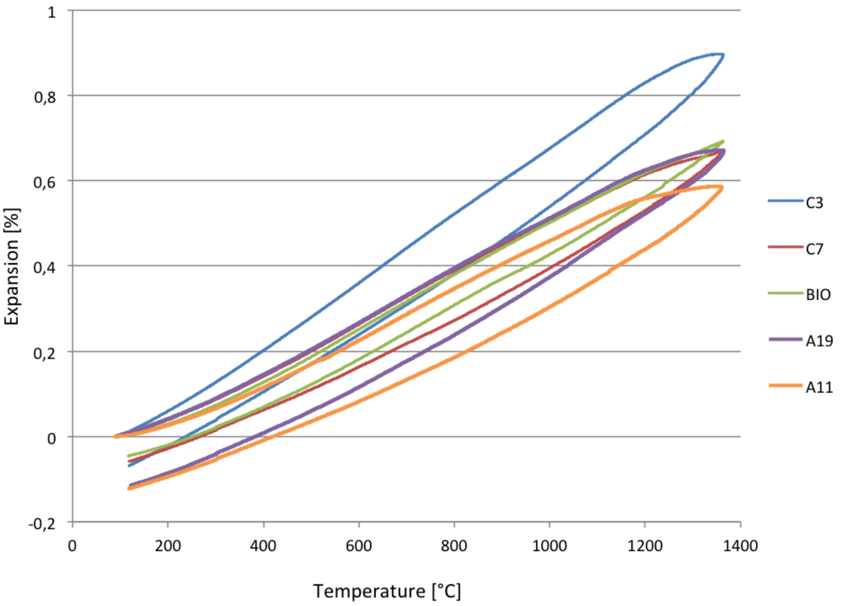

Figure 5.17: The dilatation graphs for the second temperature cycle of the non-calcined anthracites, the charcoal and the cokes.

A small difference in the expansion data might lead to a bigger difference in the TEC calculations. However, only a small standard deviation of 0.4 $\cdot 10^{-6}$ °C^{-1} during the first heating and 0.3 $\cdot 10^{-6}$ °C^{-1} during the second heating is observed for A11 calcined at 1200 and 2000 °C. This means that even with the deviations, the TEC values are higher during the fist heating.

For the TEC values of A11 calcined at 1000, 1200 and 2000 °C, the same trend can be seen for both the first and the second temperature cycle, where there is a small increase in TEC values up to about 400 °C, and a small decrease above 1100 °C. However, during the first temperature cycle, there is a small increase in the TEC values for the material calcined at 1200 and 2000 °C close to the maximum temperature, this is marked in Figure 5.18. This is only true for the last two calculated points, whereas the trend shows otherwise with a small decrease in TEC values above 1100 °C. Hence, these values should be excluded.

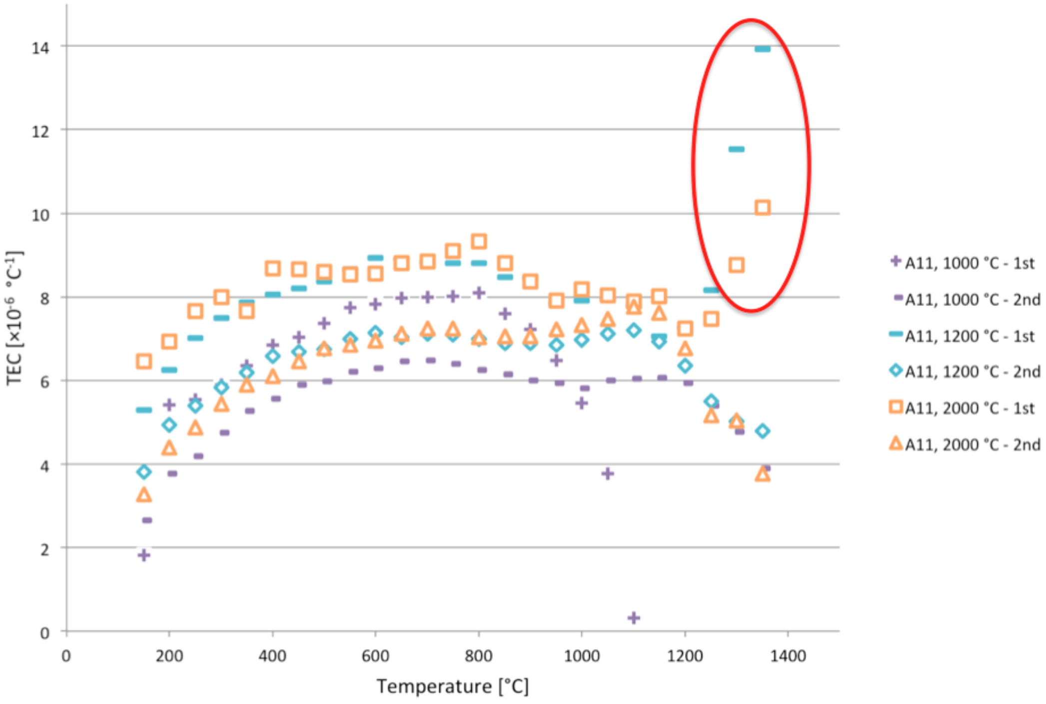

Figure 5.18: The thermal expansion coefficients of A11 calcined at 1000, 1200 and 2000 °C

From the TEC graphs in Section 4.4, it can be seen that there is an increase in the TEC values up to 400 °C and a decrease above 1100 °C during the second temperature cycle. This is true for all samples. One reason for this might be the delay due to heat transfer in the temperature regions where the temperature changes from cooling to heating and vice versa. The average TEC values are therefore calculated in the temperature range of 400 to 1100 °C, where the TECs are more stable. This is shown in Figure 5.19.

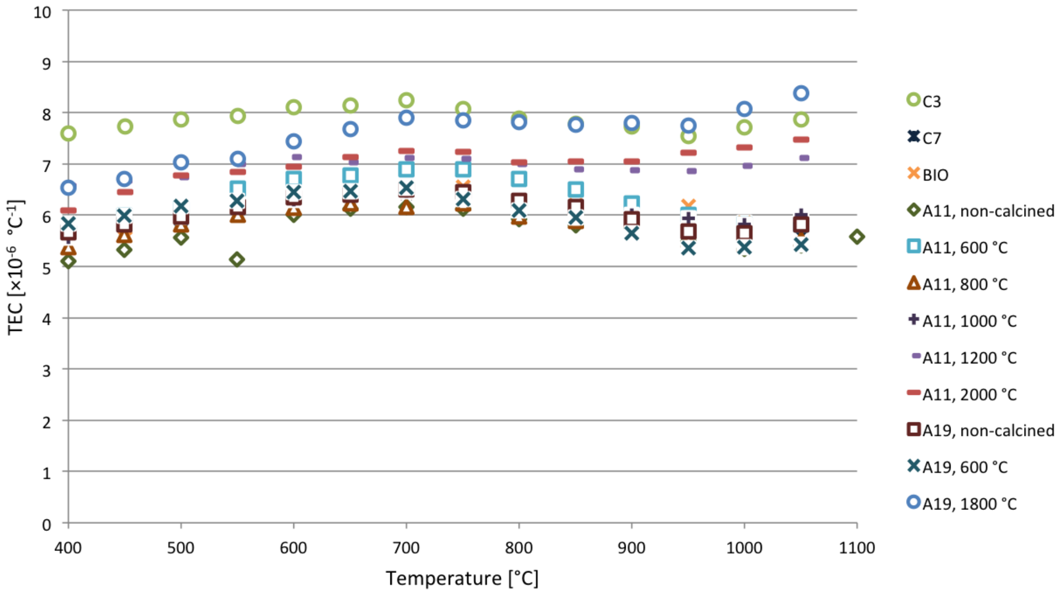

Figure 5.19: The thermal expansion coefficients of all samples during the second heating from 400 to 1100 °C.

As can be seen from the figure, the TEC values are similar for all samples after they have reached 1400 °C once. The TEC values are all in the region of 5 to 8 $\cdot 10^{-6}$ °C^{-1} with standard deviations ranging from 0.2 to 0.6 $\cdot 10^{-6}$ °C^{-1}. This also confirms that the materials are very similar after they have reached a certain temperature once.

By considering the TECs calculated from the first heating to 1400 °C, a greater difference between the different samples can be observed. Due to the big variations and the high values of the TECs obtained from the BIO sample, an average TEC was not calculated. The TECs obtained from the first heating of the different samples are summarized in Figure 5.20. Here, the higher temperature samples are excluded due to them showing the same trend in TEC values as the second temperature cycle, discussed above.

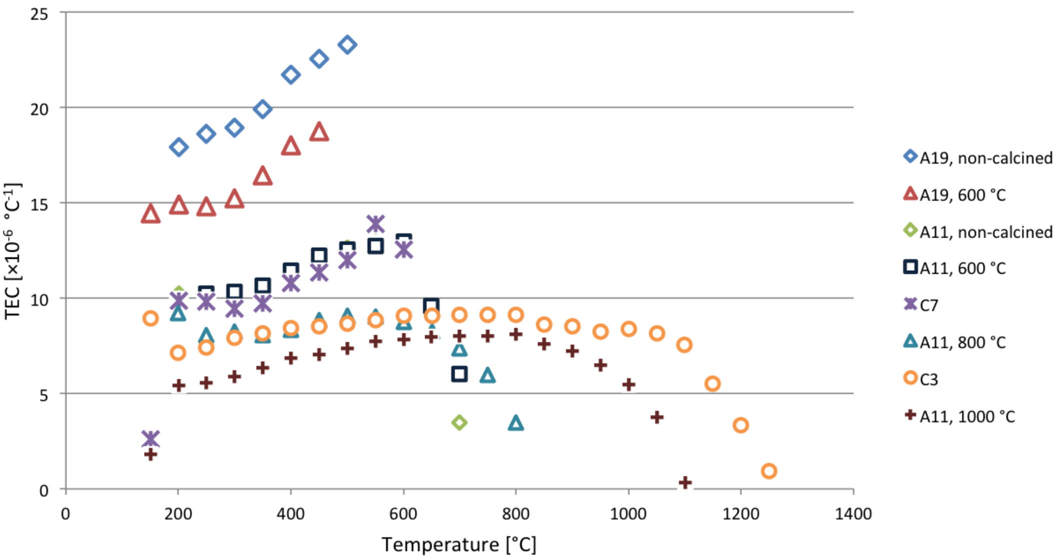

Figure 5.20: The thermal expansion coefficients obtained from the heating of the different samples during the first temperature cycle.

From the figure, it can be seen that the non-calcined material of A19 and A19 calcined at 600 °C have the highest TEC values during the fist temperature cycle with an average of 20 and 16 $\cdot 10^{-6}$ $°C^{-1}$, respectively. The TECs of C7, non-calcined A11 and A11 calcined at 600 °C are all very similar with an average of about 11 $\cdot 10^{-6}$ $°C^{-1}$. This might be explained by the amount of volatiles leaving the carbon matrix during the first temperature cycle. The non-calcined material of A19 has the highest amount of volatiles, followed by A19 calcined at 600 °C.

This is supported by the close to linear relationship between the average TEC from the first heating and the volatile content of the samples given in Figure 5.21.

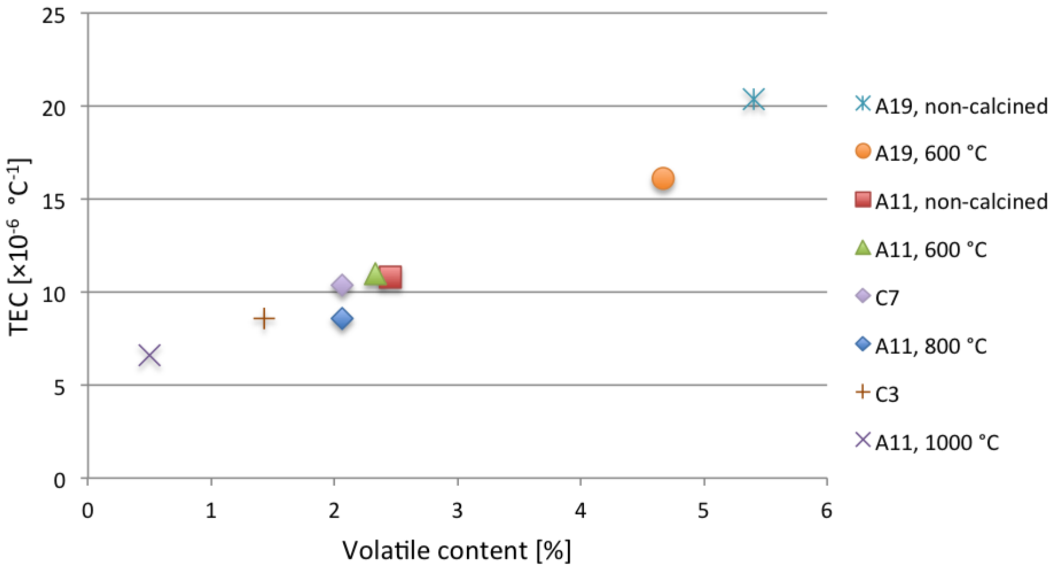

Figure 5.21: The average thermal expansion coefficients from the first heating given as a function of the volatile content of each sample.

5.2.3 The Expansion of Single Grains versus Pellets

The difference between the expansion of the single grains and pelletized material of A11 is shown in Figure 5.22 and 5.23 for the non-calcined material and the material calcined at 600 °C, respectively.

As can be seen from the figures, a bigger shrinkage is observed for the single grains than the pelletized material for both temperature samples. For the non-calcined material, the measured shrinkage is about 2 % for the pelletized material, while the dilatometer shows a shrinkage of 4.5 % for the single grain.

A shrinkage of about 2 and 3 % is observed for the material calcined at 600 °C with the two different approaches. Some of this difference might be explained by the fact that the temperature used in the dilatometer was 1550 °C, while the maximum temperature for the TMA experiments were 1400 °C. With a higher temperature, additional reactions might take place resulting in a bigger mass loss and higher shrinkage.

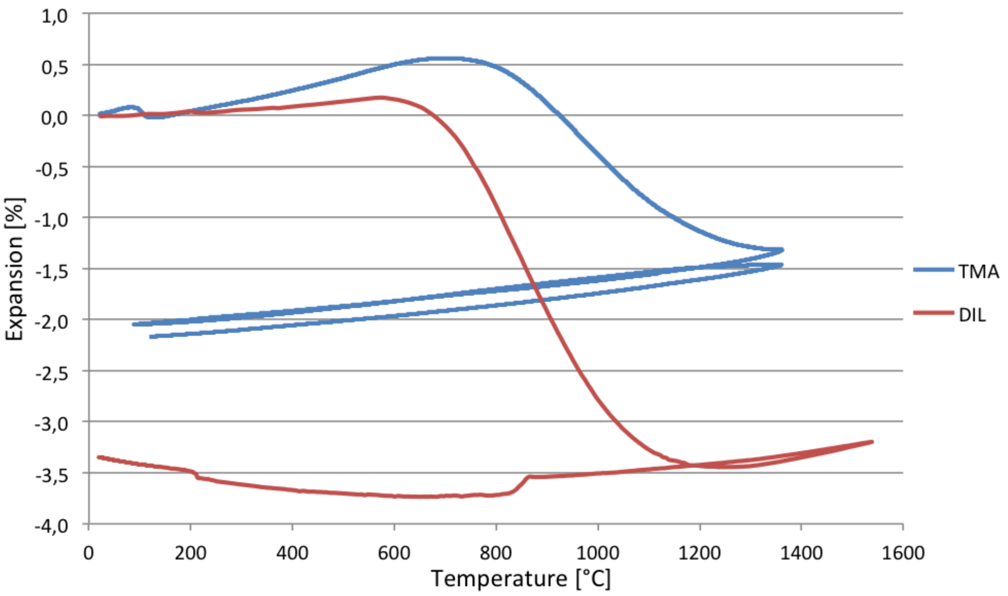

Figure 5.22: Dilatation graphs of the non-calcined A11. Pellets from TMA and single grain from dilatometry.

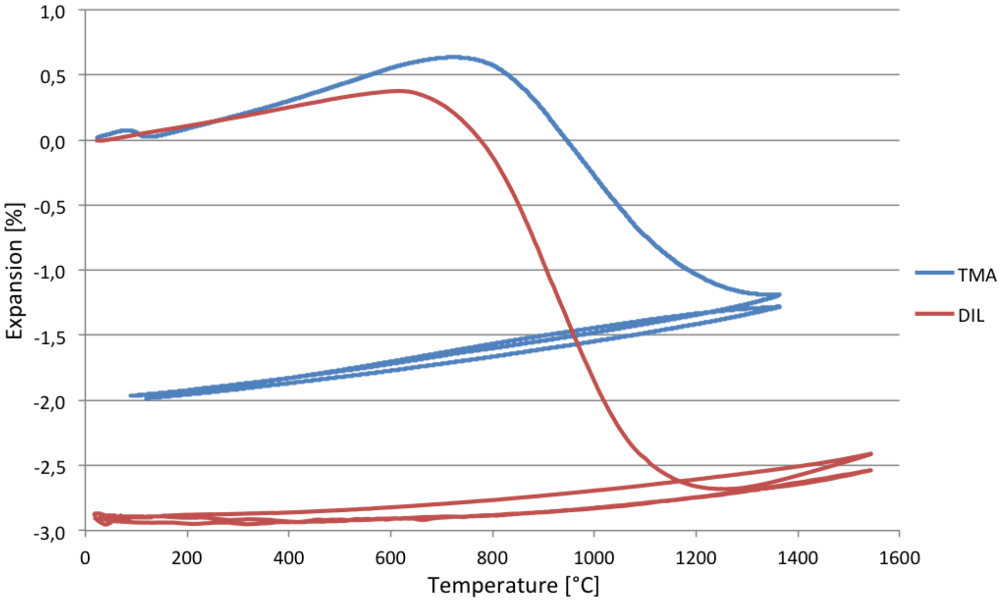

Figure 5.23: Dilatation graphs of A11 calcined at 600 °C. Pellets from TMA and single grain from dilatometry.

The heating rate used in the dilatometer was about 115 degrees per hour, which corresponds to about 2 degrees per minute. The heating rate utilized in the TMA was 10 degrees per minute. The difference in heating rate and hence also the retention time might also contribute to the difference in shrinkage between the two methods. A lower heating rate and longer retention time would give reactions more time to take place, resulting in a bigger mass loss and higher shrinkage.

The atmosphere used in both cases was N_2, so this is not believed to influence the results.

There is also a big difference in the TEC values calculated from the two different methods, where the TECs calculated from the dilatometry are generally lower than from the TMA experiments. Again, the temperature range would affect these results. For the dilatometry experiments it was argued that the measurements were inaccurate below 800 °C, hence the average TEC was calculated closer to the maximum temperature in the range of about 1200 to 1500 °C.

As discussed above, the average TECs from the TMA experiments were calculated from the temperature range of 400 to 1100 °C. This means that the TECs could not really be compared.

For the dilatometry experiments, only one heating up to 1550 °C was carried out for each grain, with an exception of the material calcined at 600 °C, which was heated twice. By looking at the dilatation graphs from 800 °C in Figure 5.24, it can be seen that the slope and hence the TEC is higher for the TMA experiment. The average TEC values between 800 and 1200 °C are 5.9 and 3.3 $\cdot 10^{-6}$ °C^{-1} for the pelletized material and the single grain, respectively, with a standard deviation of 0.5 and 1.1 $\cdot 10^{-6}$ °C^{-1}. However, at 1400 °C, it can be seen that the difference between the expansions is not very big. Normalized to the expansion at 800 °C, the expansion is 0.23 % for the pelletized material and 0.28 % for the single grain.

The same change in TEC between materials heated to 1550 and 1800 °C for the single grains, cannot bee seen for the pelletized material. One reason for this might be the difference in the temperature ranges from where the TEC was calculated, or the uncertainties connected to the calculations.

As discussed above, there is a big difference between single grains of the same temperature samples. For two pellets of the same material, the expansion data obtained from the TMA measurements are very similar, hence the repeatability is

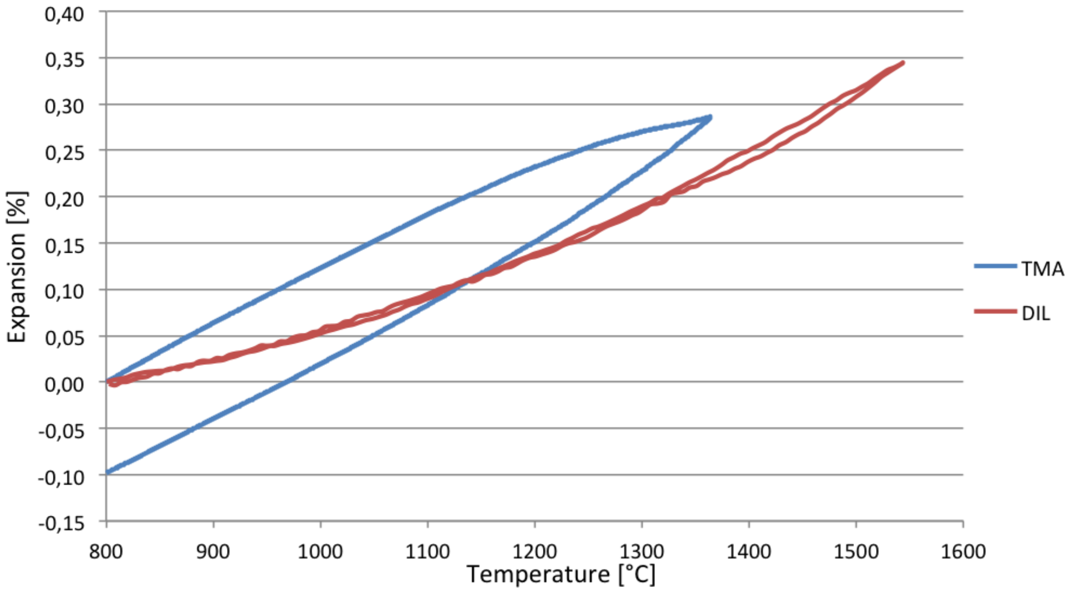

Figure 5.24: Dilatation graphs of the second heating of A11 calcined at 600 °C. The datas are normalized to the expansion at 800 °C for both the single grain and the pelletized material.

high. Therefore, it is believed that the TMA results are more trustworthy than the dilatometer.

5.3 Mass Loss during Heating

The mass loss of the non-calcined material of A11 during heated to 900, 1000 and 1500 °C in the STA 449 F3 Jupiter and the Elite tube furnace are summarized in Figure 5.25. The mass as a function of calcining temperature is also given, and can be seen as the yellow line.

A big difference between the two furnaces during heating to 1500 °C can be seen. While the total mass loss at 1500 °C in the STA furnace is 7.6 %, the mass loss in the tube furnace is only 3.4 %. At 1000 °C however, the difference is smaller with a mass loss of 2.2 and 3.2 % from the two runs with the STA furnace, and a mass loss of 1.6 % from the tube furnace. A mass loss of about 3 % at 1000 °C for the non-calcined A11 complies with the volatile content of 2.5 %.

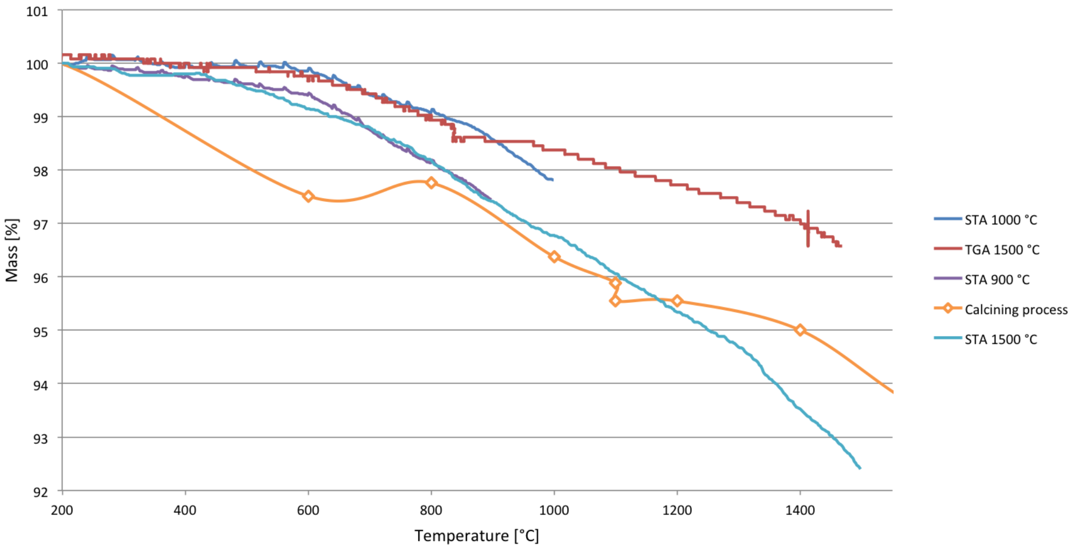

Figure 5.25: Mass of the non-calcined material of A11 as a function of temperature.

As can be seen from the Figure 5.25, there are very small differences between the different runs in the STA furnace. In addition, the mass loss during heating to 1500 °C is very similar to the mass loss during the calcining process.

This is also true for the non-calcined material of A19 during heating in the STA furnace. The mass of the non-calcined A19 during heating to 900, 1000 and 1500 °C can be seen in Figure 5.26, together with the mass loss from the calcining process. For the calcining process and the heating to 1500 °C, the mass loss is almost identical. A mass loss of about 5 % at 1000 °C for the non-calcined A19 complies with the volatile content of 5.4 %.

The derivative of mass is similar for both anthracites, with an increase above 600 °C. However, there is a higher increase for A19 than A11. This might be explained by the higher amount of volatiles leaving the carbon matrix in this temperature range for A19, and the higher mass loss.

For the two cokes, C3 and C7, the derivative of mass is also similar. In this case, the increase starts at about 500 °C. The increase is higher for C7 than C3, in compliance with the higher volatile content. BIO has the highest derivative of mass, supported by the highest mass loss during heating to 1000 °C and the highest volatile content of 14 %. In this case, there are two increases, one at about 300 °C

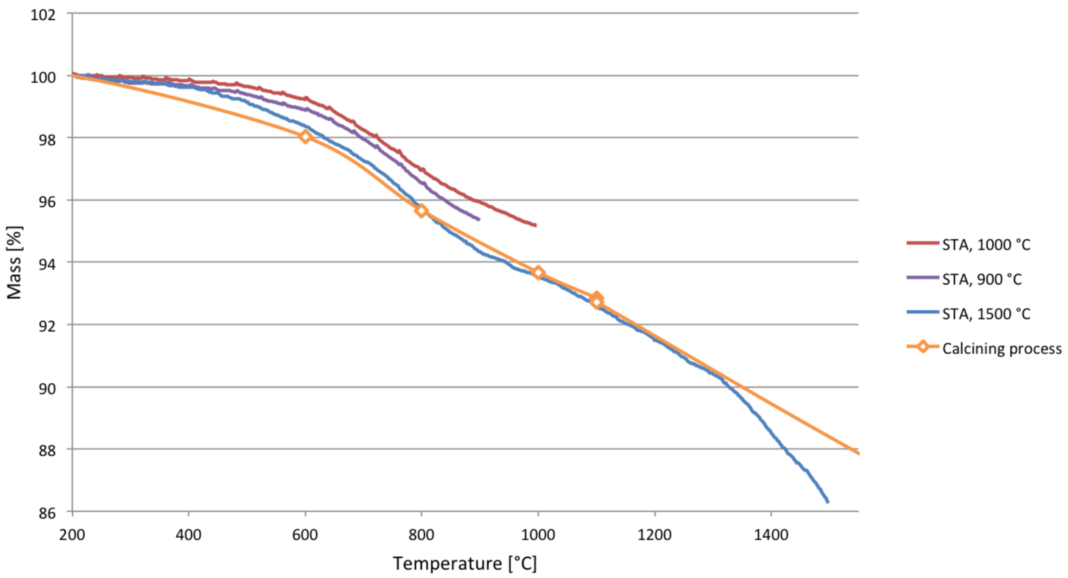

Figure 5.26: Mass of the non-calcined material of A19 as a function of temperature.

and one at 500 °C. This indicates that there are two different events resulting in mass loss.

All the Gram-Schmidt curves representing the intensity of the evolved gas follow the same trend as the derivative of mass for each sample. However, at temperatures above 800 °C where the derivative of mass decreases, the Gram-Schmidt curves continue to increase.

The mass loss of C3, C7 and BIO during heating to 1000 and 1500 °C in the STA and tube furnace is given in Figure 5.27. The heating of C7 and BIO to 1500 °C were carried out in the Elite tube furnace, and especially for the BIO sample, there is a big difference between the two furnaces. This also confirms the inaccuracies connected to the weight measurements during heating in the Elite tube furnace.

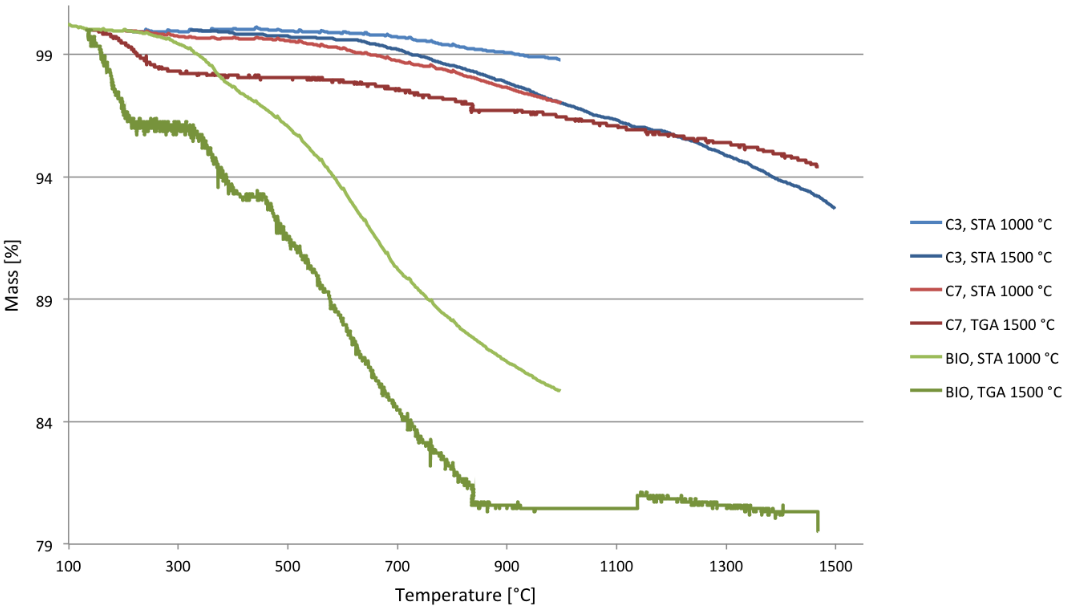

Figure 5.27: Mass of C3, C7 and BIO as a function of temperature.

The noise in the TG measurements from the Elite tube furnace in combination with the big differences to the TG measurements from the STA 449 F3 Jupiter, implies that the tube furnace does not give a correct picture of the mass loss during heating. However, it might give an indication of mass loss and show trends.

The STA show a better correlation between different runs of the same temperature sample, as seen in Figure 5.25 and 5.26. It also correlates better with the mass loss during the calcining process of A11 and A19. It it therefore believed to be a more accurate method.

Figure 5.28 shows the mass loss during heating to 1000 °C for the non-calcined anthracites, the charcoal and the cokes. As can be seen from the figure, BIO has the highest mass loss of about 15 %, followed by A19, C7, A11 and C3 with a mass losses of 4.8, 3.0, 2.2 and 1.2 % respectively.

A close to linear relationship between the mass loss at 1000 °C and the volatile content of each sample can be seen in Figure 5.29, indicating that the mass loss below 1000 °C is mostly due to volatiles leaving the carbon matrix.

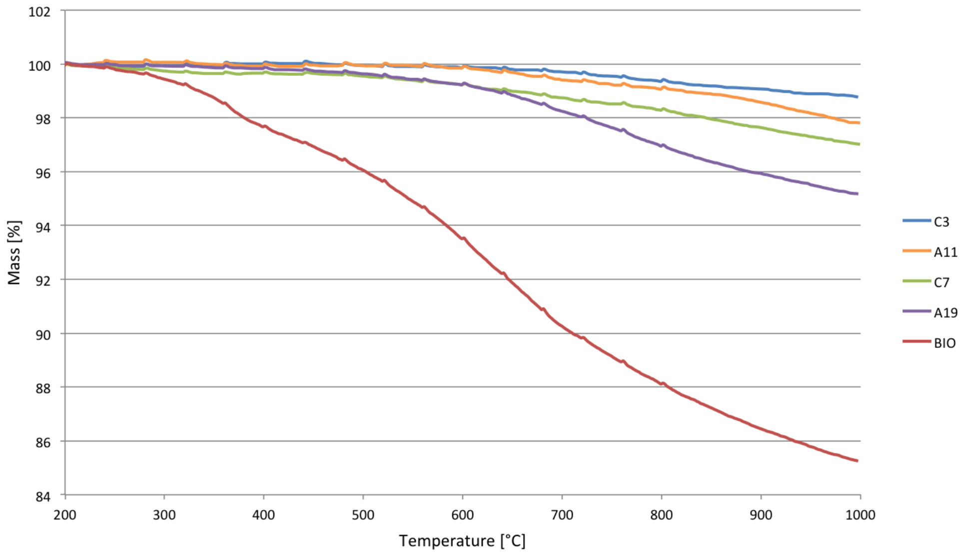

Figure 5.28: Mass of the non-calcined anthracites, the charcoal and the cokes as a function of temperature.

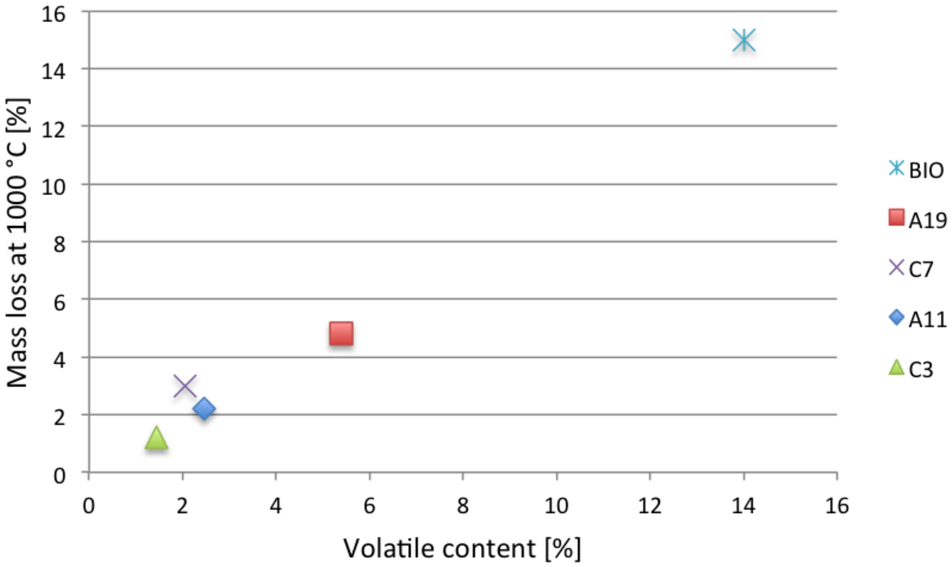

Figure 5.29: Relationship between the mass loss at 1000 °C and the volatile content of the non-calcined anthracites, the cokes and the charcoal.

5.4 Evolved Gases

For anthracite A11, there is a bigger mass loss for the material calcined at 600 °C than for the non-calcined material. This is also seen in the evolved gases, where the amount of evolved gas is about twice that of the non-calcined A11. There are very small differences between the non-calcined A11 and A11 calcined at 600 °C, with a mass loss of 2.2 and 2.4 %, respectively. Hence, the difference in mass loss might be explained by small variations in the material, or by the measurement itself.

For both anthracites, both the non-calcined material and the material calcined at 600 °C, the amount of CO_2 increases with increasing temperature and CO appears around 700-800 °C. This is also true for the two cokes and the charcoal. This might be explained by the two equations, 5.1 and 5.2, which show possible reactions of carbon with oxygen.

$$\mathrm{C\,(gr) + O_2(g) = CO_2(g)} \tag{5.1}$$

$$\Delta G^\circ_{5.1} = -394100 - 0.84T$$

$$\mathrm{2\,C\,(gr) + O_2(g) = 2\,CO\,(g)} \tag{5.2}$$

$$\Delta G^\circ_{5.2} = -223400 - 175.3T$$

Reaction 5.1 - 5.2 gives:

$$\mathrm{2\,CO\,(g) + O_2(g) = 2\,CO_2(g)} \tag{5.3}$$

Whit a Gibbs free energy of:

$$\Delta G^\circ_{5.3} = -564800 + 173.62T$$

$$\Delta G^\circ_{5.3} = 0 \text{ at } T = 2955°\text{C}$$

Additionally, reaction 5.2 - 5.1 yields:

$$\mathrm{C\,(gr) + CO_2(g) = 2\,CO\,(g)} \tag{5.4}$$

With a Gibbs free energy of:

$$\Delta G^\circ_{5.4} = 170700 - 174.5T$$

$$\Delta G^\circ_{5.4} = 0 \text{ at } T = 705°\text{C}$$

It can be seen that reaction 5.3 is spontaneous up until 3000 °C, while reaction 5.4 only is spontaneous above 700 °C. Hence, this complies with the fact that CO appears around 700 °C for all samples.

However, by looking at the equilibrium curve for CO_2 and CO in Figure 5.30, it can be seen that when the amount of CO increases, the amount of CO_2 should decrease. This is not the case for any of the samples, as the amount of CO_2 continue to increase with increasing temperature.

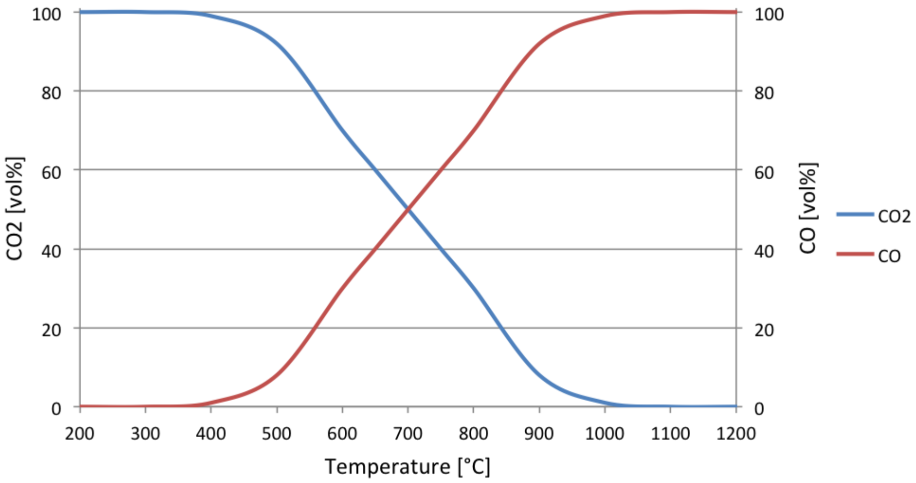

Figure 5.30: Equilibrium curve for CO_2 and CO.

The fact that there is an inert atmosphere of He inside the furnace should hinder the oxidation of carbon to carbon dioxide and carbon monoxide. The evolution of CO_2 and CO might then be explained by the carbon reacting with oxygen already present in the carbon matrix during heating. Another possible explanation is that there might be a leakage in the furnace resulting in oxygen reaching the carbon sample, forming an oxidation reaction. Oxides of the ash components might also release O_2 at higher temperatures. However, as described in Section 2.2.2, this temperature is usually required to be higher than 1000 °C.

Figure 5.31 compares the amount of CO_2 for both non-calcined anthracites, the charcoal and the cokes. The amount is normalized to the maximum amount of CO_2 for the BIO sample. As can be seen from the figure, there is a great correlation between the two methods, GC-MS and FTIR, for all samples.

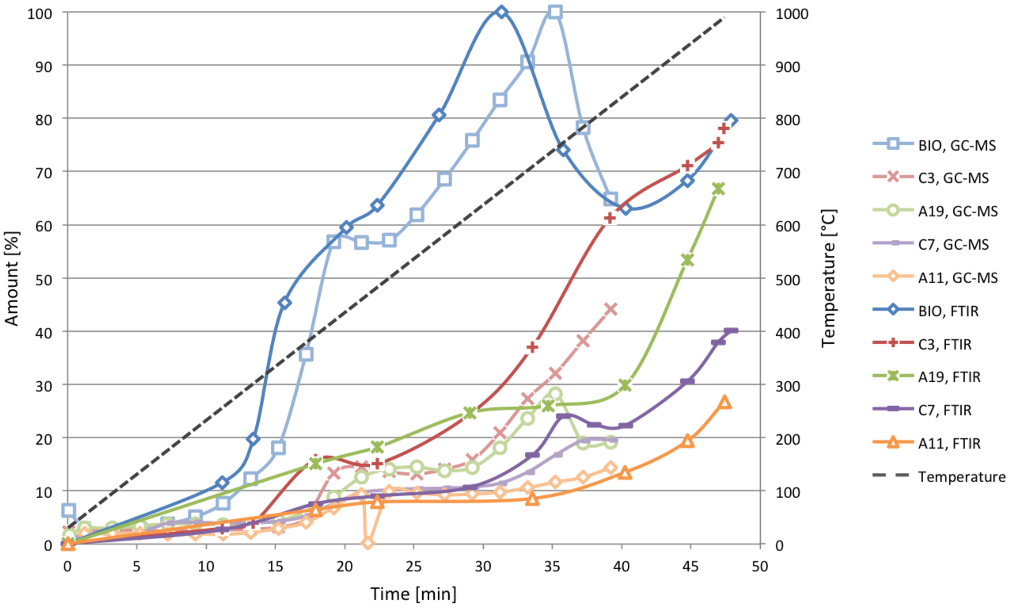

Figure 5.31: Amount of CO_2 for all samples given as a function of temperature. All samples are normalized to the maximum amount of CO_2 for BIO.

Even though C3 has the lowest content of volatiles and BIO has the highest, at the the maximum temperature of 1000 °C the amount of CO_2 is the same according to the FTIR results.

From the extracted-ion chromatograms, the amount of CO_2 from BIO is somewhat higher than of C3. A11 and C7 have the lowest amount in both cases, and show very similar behaviour. The similar behaviour between non-calcined A11 and C7 might be explained by similar volatile content, and is also seen in the thermomechanical analysis mentioned above.

Arenillas et al. [27] also investigated the off-gases of anthracite and bituminous coal, and very little hydrocarbons were detected as described in Section 2.4. However, a higer amount of hydrocarbons were detected for the bituminous coals than for the anthracite, as they contain a much higher amount of volatiles. The anthracite in this case contained about 4 % of volatiles, which is about double of that for A11, and a little less of that for A19. High hydrogen content of the anthracites is also seen from Figure 3.4, Section 3.1. However, no hydrocarbons were detected from A11 and A19 from the GC-MS.

The method used by Arenillas et al. was a mass-spectrometer connected to the TG furnace. This method differs from the method used in this thesis work by the fact that the mass-spectrometer was directly connected to the TG furnace, while in this thesis work the mass-spectrometer was connected to a gas chromatography column as a intermediate between the MS and the TG furnace. The column might cause a dilution of the off-gases, and might explain why no hydrocarbons were detected from the A11 and A19.

The FTIR spectra of A11 are very similar for both temperature samples. However, for the non-calcined material, a peak around 3000 cm^{-1} is observed at about 700 °C. This peak was not recognized by the software library, but is at the same wavenumber as PAHs would occur, as described in Section 2.4. This gives an indication of PAHs present in the non-calcined material, which is then driven off around this temperature. For the material calcined at 600 °C no such peak is observed, which might indicate that PAHs were driven off during the calcining process. Similar peaks are observed for the charcoal and both temperature samples of A19, also in the same temperature rang.

The hydrocarbons detected by Arenillas et al. were detected mainly between 600 to 800 °C, as showed in Figure 2.9. This is in compliance with the peaks around 3000 cm^{-1} in the FTIR spectra appearing in the same temperature range for the non-calcined anthracites, A19 calcined at 600 °C and the charcoal.

No such peaks were detected for the cokes or A11 calcined at 600 °C. This might be explained by the fact that the cokes already have been to temperatures higher than 600 to 800 °C during the coking process where bituminous coal is transformed to metallurgical coke. For A11 calcined at 600 °C, the calcining temperature might have been sufficient to remove hydrocarbons present in the material. Another reason might be that the amount of hydrocarbons present in the carbon matrix of A11 calcined at 600 °C was not high enough to impact the FTIR spectrum with a detection limit of about 10 ppm.

Due to the overlap in values of CO and N_2 for the mass spectroscopy, and the fact that no hydrocarbons were detected by this method, FTIR is believed to be the better method to detect evolved gases from carbon materials during heating. Mass-spectroscopy usually has a detection limit of 1 ppm, but the chromatography column increases the detection limit. For FTIR the detection limit is 10ppm. Hence GC-MS is believed to have a higher limit than FTIR. Another posibillity would be to use high-performance liquid chromatography with fluorescence detector (HPLC-FLD).

One reason for the low amount of hydrocarbons in the anthracites might be that during the formation of anthracitic coal, high temperatures and pressure is obtained in the earths crust. This might result in lighter PAHs with lower evaporation temperatures to leave the carbon matrix while still in the earths crust, leaving only heavier PAHs with higher evaporation temperatures in the coal. This gives a possible explanation to the low amount of PAHs in the anthracites, and to why they only are detected at higher temperatures around 600 to 800 °C.

Chapter 6

Conclusions and Suggested Further Work

6.1 Conclusions

In compliance with the previous work, the porosity of A11 calculated from density measurements were found to decrease with increasing calcining temperature up to 1800 °C. Between 1800 and 2650 °C there is an increase in the porosity.

The optimum equation for the total porosity of A11 contains hydrogen content, ash content and BET surface area. This gives a root mean square error of zero.

The BET surface area of A11 was found to increase between the non-calcined material and the material calcined at 600 °C. A big decrease from 27.4 to 0.2 $\mathrm{m^2\,g^{-1}}$ was found between the material calcined at 600 and 1100 °C. From 1100 and up to 2650 °C there is a small, gradual increase in the BET surface area with increasing calcining temperature.

From the dilatometry experiments the thermal expansion coefficient of single grains were found to decrease with increasing calcining temperature. A11 calcined at 1800 and 2650 °C both had a TEC close to the TEC of graphite of about $3 \cdot 10^{-6}$ $^{\circ}\mathrm{C}^{-1}$, indicating graphitization of the materials. The material calcined at 1100 °C showed a higher TEC value.

During the thermomechanical analysis of the pelletized material a shrinkage was found during the first heating to 1400 °C due to volatiles leaving the carbon matrix. The non-calcined A11 and A11 calcined at 600, 800 and 1000 °C show a trend where the shrinkage decrease with increasing calcining temperature. A linear relationship between the shrinkage and the volatile content was found in the temperature range where volatiles leave the carbon matrix. Similar shrinkage was found for the non-calcined A19, A19 calcined at 600 °C, C7 and BIO.

Before the shrinkage during the first heating, there was an expansion in the temperature range of about 200 to 500 °C where the TEC increases with increasing temperature. The average TECs obtained from these expansions show a linear relationship with the volatile content of the material.

Multiple linear regression shows that sulfur is by far the most important parameter to consider for the thermal behaviour during the first heating. A root mean square error of zero was obtained by also including ash and volatile content in the optimum solution. The sulfur content could be used as a screening parameter to assess if a new anthracite can be used or not in production to prepare calcined anthracite for use.

No shrinkage was observed during the first heating for C3 or the anthracites calcined at 1200 °C or higher.

For the second heating all A11 materials were found to contract the same amount during cooling as they expand during heating. The expansion at 1400 °C was found to be between 0.6 and 0.9 % for all samples.

The TEC values during the second heating were found to be very stable between 400 and 1100 °C. For all samples the TEC values were found to lay between 5 and 8 $\cdot 10^{-6}$ $°C^{-1}$, indicating graphitization.

C3 and the anthracites calcined at 1200 °C and higher, all show similar behaviour during both temperature cycles. However, a small decrease in TEC between the two temperature cycles was found.

A high reproducibility was found for the thermal behaviour experiments carried out in the Exstar SS6300 TMA, this is considered the preferable instrument for thermal expansion considerations.

The mass loss measured by STA 449 F3 Jupiter during heating to 1500 °C complies with mass loss from the calcining process for A11 and A19.

The mass loss at 1000 °C complies with the volatile content for all materials, and a linear relationship between the volatile content and the mas loss at 1000 °C was found.

The derivative of mass curves show the highest increase around 600-700 °C for all samples. The increase is higher for A19 than for A11 samples due to the higher volatile content.

There is a big difference between the mass loss measured by the STA 449 F3 Jupiter and the Elite tube furnace. The STA is more accurate and the results are reproducible.

By Fourier transformed infrared analysis CO_2, CO and H_2O were detected for all samples, with the exception of C3 where H_2O was not detected. The amount of CO_2 increase with increasing temperature. CO appears around 700 °C for all samples and the amount increases with increasing temperature.

Only CO_2 was detected by gas chromatography with mass spectrometry. The amount was found to increase with increasing temperature for all samples. Highest amount was found for BIO.

There is a good correlation of CO_2 analysis between the FTIR and the GC-MS for all samples.

Due to the increase of CO_2 also above 700 °C indicating access to oxygen, it can be concluded that the off-gas analysis connected to the STA is not satisfactory. Hence, the method should be further developed.

Indication of polycyclic aromatic hydrocarbons around 600-700 °C from the FTIR spectra for the non-calcined anthracites, A19 calcined at 600 °C and BIO.

6.2 Suggested Further Work

As a continuation of this work, it is suggested to do additional porosity measurements of A11 with calcining temperatures between 600 and 1100 °C. This should be done in order to investigate the possible collapse of micropores in this temperature range. Other ways of measuring porosity such as Small Angle X-ray Scattering (SAXS) or CO_2 gas adsorption could also be conducted. SAXS would cover the pore range 0.3 - 60 000 nm, also including closed pores, while CO_2 gas adsorption would cover pores with a diameter of 0.3 - 0.5 nm. Both methods then cover the lower micropore range, which would be of special interest regarding the collapse of pores.

It would be interesting to see how the calcining temperature affects the wettability of binder to the anthracite grains, and to find possible relations between the surface roughness/open porosity and the wettability.

Single grains of the anthracites calcined at different temperatures should also be investigated by using Exstar SS6300 TMA in order to compare better with the pelletized material.

For the thermal expansion investigations, it was suggested that the sulfur content played the biggest part in the thermal behaviour of pelletized anthracite. This should be investigated further, also by looking at the sulfur content of other carbon materials. It would be interesting to see whether the organically or inorganically bound sulfur plays the biggest role during heating, when leaving the carbon matrix.

The thermal expansion can also be connected to thermal stresses. The anthracites calcined at different temperatures should also be looked at in combination with the binder, coal tar pitch, in order to determine how e.g. an anthracite with a low calcining temperature will contribute to additional stresses in a Søderberg electrode. Since a material with a lower calcining temperature most likely still will contain volatiles, these will leave the carbon matrix during the first heating and contribute to additional shrinkage, while anthracites calcined at higher temperatures, as previously discussed, will expand about 1 %. In this thesis work only the thermal expansion up to 1400 °C was investigated due to furnace limitetions. However, since the temperature inside a furnace can reach much higher temperatures during operation, it would be interesting to see how the thermal behaviour is at even higher temperatures.

Bibliography

[1] Elkem Carbon Jesse White. Calcining process fundamentals. Personal communication, 2016.

[2] Hogne Linga and Ivar Skogland. *Fremstilling av Karbonmaterialer*. Elektrokemiske Arbeidsgiverforening i samarbeid med Norsk Korrespondanseskole, 1985.

[3] Fagkurs Elkem Carbon. *Produksjon av Søderbergmasse og andre Karbonmaterialer*. Elkem Carbon, 1982.

[4] Britannica Encyclopædia. Coal. `https://www.britannica.com/science/coal-fossil-fuel`, 10 2016. Accessed: 14.10.2016.

[5] John W. Patrick. *Porosity in Carbons*. Edward Arnold, 1995.

[6] The American Society for Testing and Materials. Standard classification of coals by rank. ASTM Book of Standards.

[7] Harry Marsh and Francisco Rodriguez Reinoso. *Science of Carbon Materials*. Publicaciones Universidad de Alicante, 2000.

[8] `http://geology.com/rocks/coal.shtml`. Accessed: 10.04.2017.

[9] Britannica Encyclopædia. Coal utilization. `https://www.britannica.com/topic/coal-utilization-122944`, 9 2012. Accessed: 27.09.2016.

[10] The American Society for Testing and Materials. Standard test method for hardgrove grindability index (hgi) of petroleum coke. ASTM Book of Standards.

[11] `http://www.dietmar-schulze.de/entmie.html`. Accessed: 06.12.2016.

[12] Harry Marsh. *Carbon*, 29(6):703–704, 1991.

[13] Xavier Bourrat. Electrically conductive grades of carbon black: Structure and properties. *Carbon*, 31(2):287–302, 1993.

[14] Xavier Bourrant. Structure of carbons and carbon artefacts. pages 1–87, 2000.

[15] MA Dıez, R Alvarez, and C Barriocanal. Coal for metallurgical coke production: predictions of coke quality and future requirements for cokemaking. *International Journal of Coal Geology*, 50(1):389–412, 2002.

[16] Joalet Dalene Steenkamp. *Chemical wear of carbon-based refractory materials in a silicomanganese furnace tap-hole.* PhD thesis, University of Pretoria, 2014.

[17] P-Y Brisson, H Darmstadt, M Fafard, A Adnot, G Servant, and G Soucy. X-ray photoelectron spectroscopy study of sodium reactions in carbon cathode blocks of aluminium oxide reduction cells. *Carbon*, 44(8):1438–1447, 2006.

[18] Aluminium for the Future Generations. Anode production. `http://primary.world-aluminium.org/processes/anode-production.html`. Accessed: 05.12.2016.

[19] Byeong-Kyu Lee (2010). Sources, distribution and toxicity of polyaromatic hydrocarbons (pahs) in particulate matter. `https://www.intechopen.com/books/air-pollution/sources-distribution-and-toxicity-of-polyaromatic-hydrocarbons-pahs-in-particulate-matter`. Accessed: 12.04.2017.

[20] Toxipedia Aleksandra Buha. Polycyclic aromatic hydrocarbons. `http://www.toxipedia.org/display/toxipedia/Polycyclic+Aromatic+Hydrocarbons`. Accessed: 14.04.2017.

[21] T Ramdahl, I Alfheim, and A Bjørseth. Pah emission from various sources and their evolution over the last decades. *Mobile Source Emissions Including Polycyclic Organic Species*, pages 277–297, 1983.

[22] RK Bentsen, K Halgard, H Notø, HL Daae, and S Øvrebø. Correlation between urinary 1-hydroxypyrene and ambient air pyrene measured with an in-

halable aerosol sampler and a total dust sampler in an electrode paste plant. *Science of the total environment*, 212(1):59–67, 1998.

[23] R.K Bentsen, H. Notø, K. Halgard, and S. Øverbø. The effect of dust-protective respirator mask and the relevance of work category on urinary 1-hydroxypyrene concentration in pah exposed electrode paste pland workers. *Pergamon*, 42(2):135–144, 1998.

[24] AM Mastral, MS Callen, and T1 Garcia. Toxic organic emissions from coal combustion. *Fuel processing technology*, 67(1):1–10, 2000.

[25] `https://www.researchgate.net/figure/227550905_fig2_Figure-2-Examples-of-carcinogenic-polycyclic-aromatic-hydrocarbons`. Accessed: 14.04.2017.

[26] AP Radlinski, Maria Mastalerz, AL Hinde, Martin Hainbuchner, Helmut Rauch, Matthias Baron, JS Lin, L Fan, and P Thiyagarajan. Application of saxs and sans in evaluation of porosity, pore size distribution and surface area of coal. *International Journal of Coal Geology*, 59(3):245–271, 2004.

[27] A Arenillas, F Rubiera, and JJ Pis. Simultaneous thermogravimetric–mass spectrometric study on the pyrolysis behaviour of different rank coals. *Journal of Analytical and Applied Pyrolysis*, 50(1):31–46, 1999.

[28] Ana Maria Mastral, Marisol Callen, and Ramón Murillo. Assessment of pah emissions as a function of coal combustion variables. *Fuel*, 75(13):1533–1536, 1996.

[29] D.W. van Krevelen. *Coal: Typology-Physics-Chemistry-Constitution.* Elsevier Science, 3rd edition, 1993.

[30] Gregory N Okolo, Raymond C Everson, Hein WJP Neomagus, Mokone J Roberts, and Richard Sakurovs. Comparing the porosity and surface areas of coal as measured by gas adsorption, mercury intrusion and saxs techniques. *Fuel*, 141:293–304, 2015.

[31] CF Rodrigues and MJ Lemos De Sousa. The measurement of coal porosity with different gases. *International Journal of Coal Geology*, 48(3):245–251, 2002.

[32] G Liu, P Benyon, KE Benfell, GW Bryant, AG Tate, RK Boyd, DJ Harris, and TF Wall. The porous structure of bituminous coal chars and its influence on combustion and gasification under chemically controlled conditions. *Fuel*, 79(6):617–626, 2000.

[33] Katrine Holm. The properties of calcined anthracite. Specialization Project, The Norwegian University of Science and Technology, NTNU, 2016.

[34] J Alcaniz-Monge, D Cazorla-Amoros, and A Linares-Solano. Characterisation of coal tar pitches by thermal analysis, infrared spectroscopy and solvent fractionation. *Fuel*, 80(1):41–48, 2001.

[35] JP Beukes, H Roos, L Shoko, PG Van Zyl, HWJP Neomagus, CA Strydom, and NF Dawson. The use of thermomechanical analysis to characterise söderberg electrode paste raw materials. *Minerals Engineering*, 46:167–176, 2013.

[36] POCO Graphite Inc. *Properties and Characteristics of Graphite*, 2015.

[37] `http://www.glass-ts.com/dilatometry-thermal-expansion`. Accessed: 16.04.2017.

[38] The Engineering Toolbox. Coefficients of linear thermal expansion. `http://www.engineeringtoolbox.com/linear-expansion-coefficients-d_95.html`. Accesses: 15.12.2016.

[39] Ove Paulsen. *Dilatometer Netzsch 402E manual.* SINTEF Materials and Chemistry, Trondheim, 2000.

[40] Micromeritics. Density measurements. Density Brochure, 2001.

[41] Britannica Encyclopædia. Archimedes' principle. `https://www.britannica.com/science/Archimedes-principle`, 8 2016. Accessed: 03.11.2016.

[42] Determining volume and density for particle technologists by micromeritics. `http://www.azonano.com/article.aspx?ArticleID=2637`. Accessed: 07.12.2016.

[43] Stephen Brunauer, P.H. Emmett, and Edward Teller. Adsorption of gases in multimolecular layers. *Journal of the American Chemical Society*, 60(2):309–319.

[44] Hitachi High-Tech Science Corporation. *Dynamic Load Thermomechanical Analyzer Module, Operation Manual TMA/SS6300*. SII NanoTechnology Inc., 2.3 edition, 7 2007.

[45] PerkinElmer Inc. *Thermogravimetric Analysis (TGA) - A beginner's guide*, 2010.

[46] PerkinElmer Inc. *Differential Scanning Calorimetry (DSC) - A beginner's guide*, 2014.

[47] NETZSCH. Simultaneous thermal analyzer - sta 449 f3 jupiter. NETZSCH Brochure.

[48] W Xie and W-P Pan. Thermal characterization of materials using evolved gas analysis. *Journal of Thermal Analysis and Calorimetry*, 65(3):669–685, 2001.

[49] NETZSCH. Coupling to fourier transform infrared spectrometers ft-ir. NETZSCH Brochure.

[50] `https://chem.libretexts.org/Core/Physical_and_Theoretical_Chemistry/Spectroscopy/Vibrational_Spectroscopy/Infrared_Spectroscopy/How_an_FTIR_Spectrometer_Operates`. Accessed: 16.05.2017.

[51] LJ Allamandola, AGGM Tielens, and JR Barker. Interstellar polycyclic aromatic hydrocarbons-the infrared emission bands, the excitation/emission mechanism, and the astrophysical implications. *The Astrophysical Journal Supplement Series*, 71:733–775, 1989.

[52] Scott A Sandford and Max P Bernstein. The infrared spectra of polycyclic aromatic hydrocarbons with excess peripheral h atoms (h n-pahs) and their relation to the 3.4 and 6.9 μm pah emission features. *The Astrophysical Journal Supplement Series*, 205(1):8, 2013.

[53] ELJ Kleynhans, JP Beukes, PG Van Zyl, JR Bunt, NSB Nkosi, and M Venter. The effect of carbonaceous reductant selection on chromite pre-reduction. *Metallurgical and Materials Transactions B*, pages 1–14, 2016.

[54] SP Du Preez, JP Beukes, and PG Van Zyl. Cr (vi) generation during flaring of co-rich off-gas from closed ferrochromium submerged arc furnaces. *Metallurgical and Materials Transactions B*, 46(2):1002–1010, 2015.

[55] L Shoko, JP Beukes, CA Strydom, B Larsen, and L Lindstad. Predicting the toluene-and quinoline insoluble contents of coal tar pitches used as binders in söderberg electrodes. *International Journal of Mineral Processing*, 144:46–49, 2015.

Appendix A

Experimental Data from experiments carried out at Elkem Carbon Fiskaa

Table A.1 through A.6 gives the experimental data from some of the experiments carried out at Elkem Carbon Fiskaa during the period of June and July 2016. Two anthracites, A11 and A19, were calcined at different temperatures and characterized.

Table A.1: Weight loss during calcination for A11 and A19.

Sample	Temperature [°C]	Furnace	Retention time [h]	Weight loss [%]
A11	0	-	-	0
A11	600	1	1	2.5
A11	800	1	1	2.2
A11	1000	1	1	3.6
A11	1100	1	1	4.1
A11	1100	1	2	4.4
A11	1100	1	8	5.1
A11	1100	2	1	4.5
A11	1200	2	1	4.5
A11	1400	2	1	5.0
A11	1600	2	1	6.5
A11	1800	2	1	7.1
A11	2000	2	1	8.0
A11	2300	2	1	8.2
A11	2650	2	1	10.1
A19	0	-	-	0
A19	600	1	1	2.0
A19	800	1	1	4.3
A19	1000	1	1	6.3
A19	1100	1	1	7.2
A19	1100	1	2	7.1
A19	1100	1	8	11.2
A19	1100	2	1	7.3
A19	1800	2	1	14.6
A19	2650	2	1	21.8

Table A.2: The absolute density measurements of A11 and A19 given in $\mathrm{g\,cm^{-3}}$.

Sample	Average [$\mathrm{g\,cm^{-3}}$]	Std. deviation
A11, non-calcined	1.9780	0.0925
A11, 600 °C, Funace 1, 1h	1.9615	0.0823
A11, 800 °C, Funace 1, 1h	2.0145	0.0936
A11, 1000 °C, Funace 1, 1h	2.0938	0.0512
A11, 1100 °C, Funace 1, 1h	2.0186	0.0065
A11, 1100 °C, Funace 1, 2h	1.9937	0.0091
A11, 1100 °C, Funace 1, 8h	1.8966	0.0045
A11, 1100 °C, Funace 2, 1h	1.9543	0.0072
A11, 1200 °C, Funace 2, 1h	1.7944	0.0035
A11, 1400 °C, Funace 2, 1h	1.7607	0.0018
A11, 1600 °C, Funace 2, 1h	1.7564	0.0021
A11, 1800 °C, Funace 2, 1h	1.7563	0.0011
A11, 2000 °C, Funace 2, 1h	1.7734	0.0006
A11, 2300 °C, Funace 2, 1h	1.8633	0.0033
A11, 2650 °C, Funace 2, 1h	1.9891	0.0024
A19, non-calcined	1.6644	0.0319
A19, 600 °C, Funace 1, 1h	1.6720	0.0287
A19, 800 °C, Funace 1, 1h	2.1030	0.1182
A19, 1000 °C, Funace 1, 1h	2.1065	0.0311
A19, 1100 °C, Funace 1, 1h	2.0332	0.0247
A19, 1100 °C, Funace 1, 2h	1.9951	0.0037
A19, 1100 °C, Funace 1, 8h	1.9598	0.0126
A19, 1100 °C, Funace 2, 1h	1.9525	0.0076
A19, 1800 °C, Funace 2, 1h	1.8795	0.0042
A19, 2650 °C, Funace 2, 1h	2.1816	0.0035

Table A.3: The absolute density measurements of selected samples of A11 given in g cm^{-3}. The average value and standard deviation is also given.

Sample	1	2	3	4	5	Average [g cm^{-3}]	Std. dev.
A11, non-caclined	2.14	2.02	1.95	1.90	1.88	1.98	0.10
A11, 600 °C	2.07	2.01	1.95	1.96	1.94	1.96	0.08
A11, 1100 °C	1.95	1.96	1.96	1.96	1.94	1.95	0.01
A11, 1800 °C	1.76	1.75	1.75	1.76	1.76	1.76	0.001
A11, 2650 °C	1.99	1.99	1.99	1.99	1.99	1.99	0.002

Table A.4: Volatile content of the non-calcined material and the material calcined at 600 and 800°C.

Sample	Temperature [°C]	Furnace	Retention time [h]	Volatiles [%]	Std. deviation
A11	0	-	-	2.45	0.11
A11	600	1	1	2.33	0.09
A11	800	2	1	2.06	0.02
A19	0	-	-	5.37	0.16
A19	600	1	1	4.47	0.14
A19	800	2	1	2.81	0.67

Table A.5: The sulfur, hydrogen and nitrogen of A11 and A19.

Sample	Temperature [°C]	Furnace	Retention time [h]	Sulfur [%]	Hydrogen [%]	Nitrogen [%]
A11	0	-	-	0.16	7.33	0.92
A11	600	1	1	0.15	8.32	0.81
A11	800	1	1	0.13	6.06	0.81
A11	1000	1	1	0.13	5.59	1.23
A11	1100	1	1	0.12	2.30	0.89
A11	1100	1	2	0.12	2.03	0.80
A11	1100	1	8	0.13	1.66	0.73
A11	1100	2	1	0.12	1.90	0.85
A11	1200	2	1	0.17	0.91	0.61
A11	1400	2	1	0.12	0.71	0.83
A11	1600	2	1	0.10	0.33	0.55
A11	1800	2	1	0.10	0.16	0.67
A11	2000	2	1	0.08	0.12	0.47
A11	2300	2	1	0.04	0.08	0.24
A11	2650	2	1	0.00	0.03	0.08
A19	0	-	-	0.85	5.35	0.42
A19	600	1	1	0.78	9.76	1.35
A19	800	1	1	0.75	8.92	1.82
A19	1000	1	1	0.76	2.84	1.14
A19	1100	1	1	0.72	1.94	1.12
A19	1100	1	2	0.72	1.67	0.90
A19	1100	1	8	0.78	1.45	0.85
A19	1100	2	1	0.67	1.78	0.80
A19	1800	2	1	0.45	0.13	0.26
A19	2650	2	1	0.00	0.02	0.03

Table A.6: XRD results. The peak position, crystallite size and interlayar spacing of A11 and A19 anthracites.

Sample	Temperature [°C]	Furnace	Retention time [h]	Peak pos.	Cryst.size (Lc) [Å]	d_{002} [Å]
A11	0	-	-	25.65	13.78	3.47
A11	600	1	1	25.72	13.59	3.46
A11	800	1	1	25.42	12.15	3.50
A11	1000	1	1	25.26	11.95	3.52
A11	1100	1	1	25.26	12.63	3.52
A11	1100	1	2	25.35	12.88	3.51
A11	1100	1	8	25.56	13.94	3.48
A11	1100	2	1	25.34	13.29	3.51
A11	1200	2	1	25.68	15.65	3.47
A11	1400	2	1	25.68	20.97	3.47
A11	1600	2	1	25.74	25.25	3.46
A11	1800	2	1	25.87	30.76	3.44
A11	2000	2	1	26.01	43.34	3.42
A11	2300	2	1	26.34	107.24	3.38
A11	2650	2	1	26.47	174.03	3.36
A19	0	-	-	26.06	15.23	3.42
A19	600	1	1	26.21	13.74	3.40
A19	800	1	1	25.61	10.79	3.48
A19	1000	1	1	25.77	12.32	3.45
A19	1100	1	1	25.66	12.93	3.47
A19	1100	1	2	25.88	14.29	3.44
A19	1100	1	8	25.90	14.90	3.44
A19	1100	2	1	25.93	14.86	3.43
A19	1800	2	1	26.10	43.71	3.41
A19	2650	2	1	26.51	256.03	3.36

Appendix B

Crucible Correction for TMA Measurements

In order to protect the probe from the sample, a small crucible was used. The expansion data from the crucible is given in Figure B.1. The graph is based on the average of two measurements. Corrections for the crucible expansion were made for all the tested samples by subtracting the crucible expansion from the sample expansion.

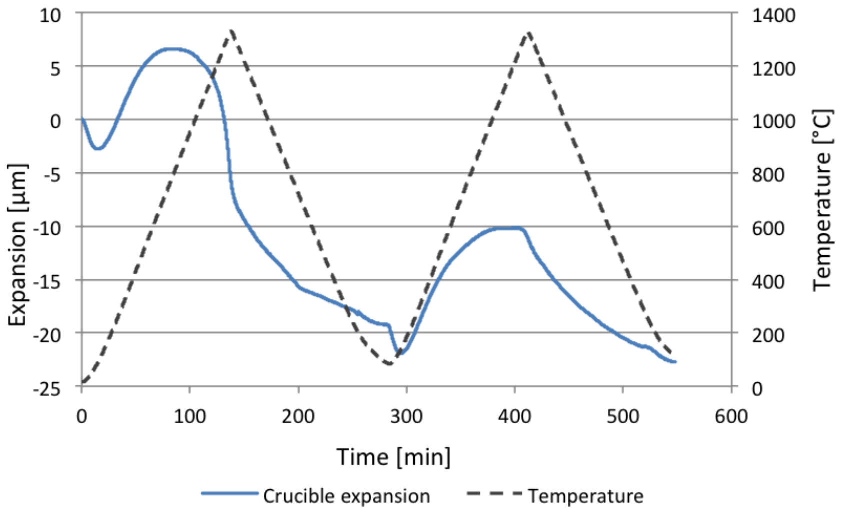

Figure B.1: Expansion data from crucible used in thermaomechanical analysis experiments. The data is used for correction of the samples analyzed.

Appendix C

Calibration for DSC Curves

The DSC data from the blank run in the STA 449 F3 Jupiter heated to 1500 °C is given in Figure C.1.

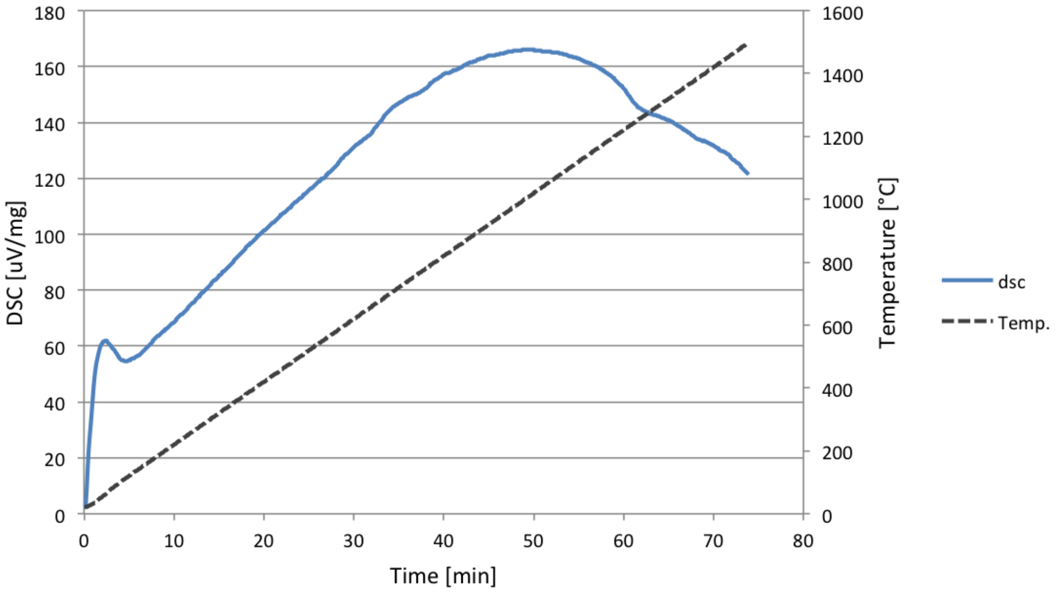

Figure C.1: DCS curve from blank run, STA 449 F3 Jupiter.

Appendix D

The Effect of Crucible Lids during Thermogravimetric Experiments

The effect of crucible lids during the thermogravimetric experiments in STA 449 F3 Jupiter were investigated. This was done in order to determine whether the lid would have an impact on the results or not.

The results are given in Figure D.1, where the thermogravimetric data and the DSC curve from heating A11 to 1500 °C with a crucible lid is given as the blue lines. A and B represent two runs of A11 without crucible lids.

From the figure it can be seen that there is a higher mass loss from the runs without a crucible lids. For the DSC curves, both A and B differ from the run with crucible lid, and from each other. From this it was decided to continue to use a crucible lid when running samples in the STA 449 F3 Jupiter, and rather set the maximum temperature to 1000 °C to avoid fusion of lids.

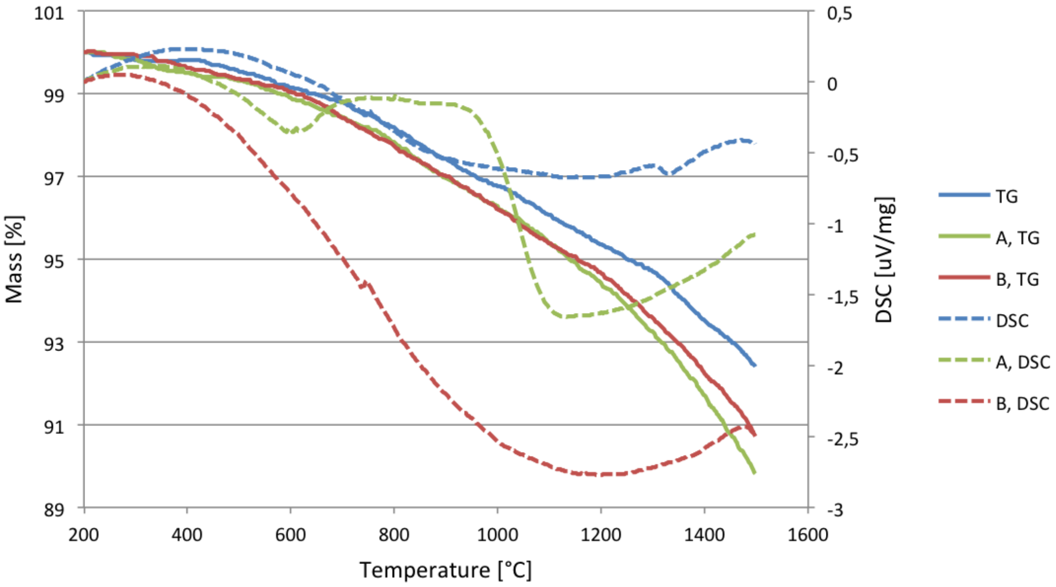

Figure D.1: DCS curve from blank run, STA 449 F3 Jupiter.

Appendix E

Thermogravimetric Data, 430 °C

From the STA 449 F3 Jupiter runs of non-calcined A11 to 430 °C, the thermogravimetric results are given in Figure E.1. The temperature is given as the dotted lines.

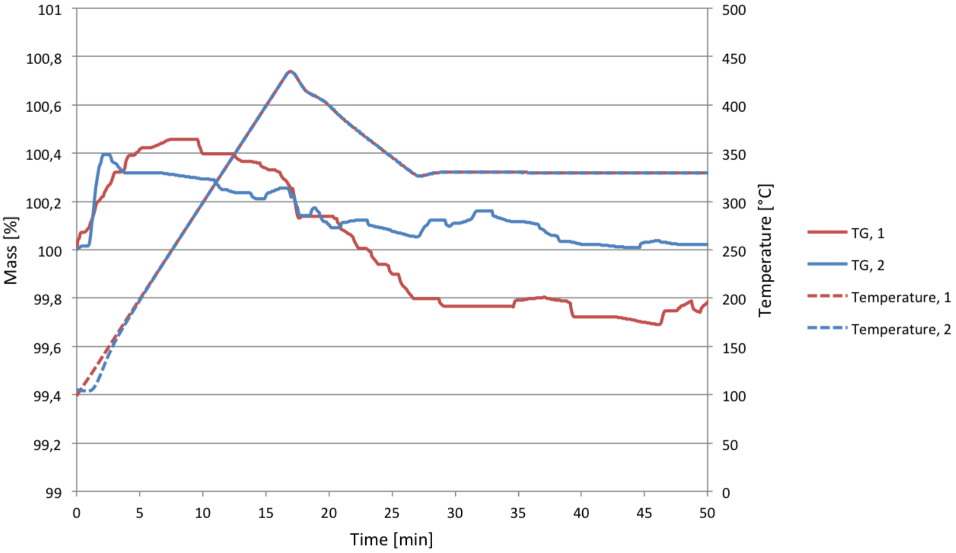

Figure E.1: Thermogravimetric data from A11 heated to 430 °C in the STA 449 F3 Jupiter.

As can be seen from the figure, there is not much mass loss during the experiments. Hence, no off-gases were detected by the GC-MS.

Appendix F

Experimental Data from Thermomechanical Analysis of Pelletized Material

Figure F.1 through F.11 show both runs of the pelletized materials in the Exstar SS6300 TMA. The temperature profile is given in Figure F.12. As can be seen from the figures, there is a high repeatability in the experiments.

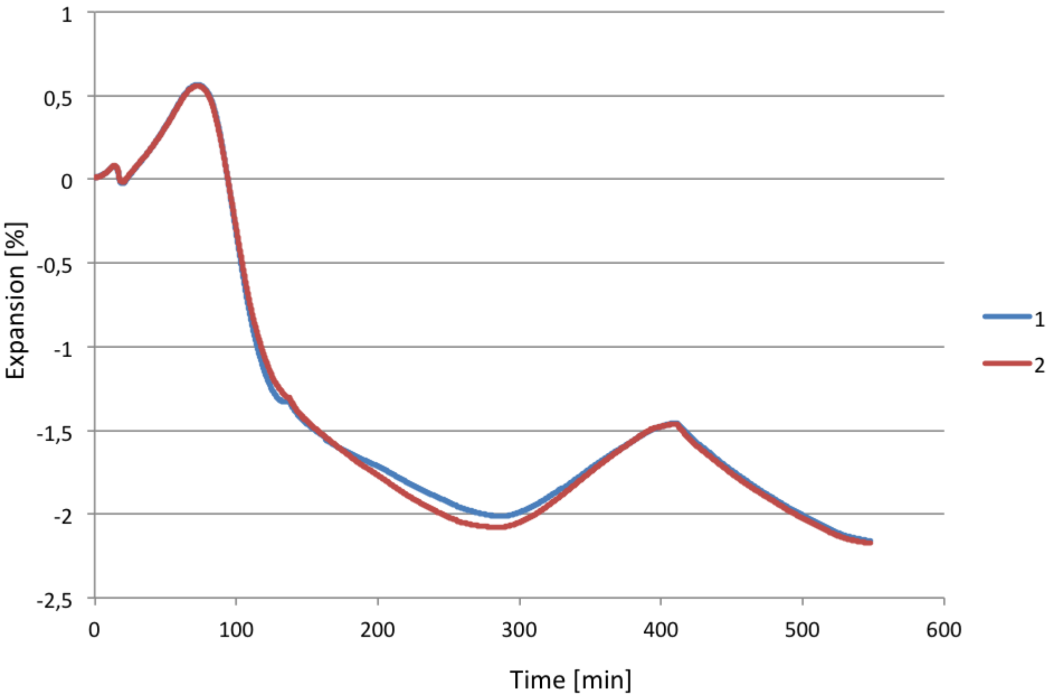

Figure F.1: The two TMA runs of the non-calcined A11.

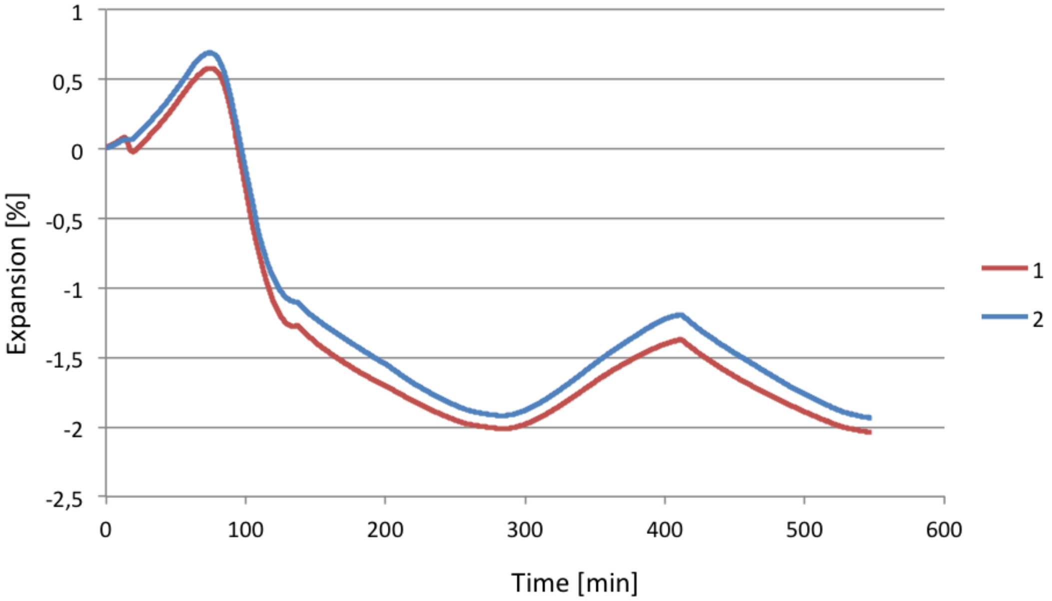

Figure F.2: The two TMA runs of A11 calcined at 600 °C.

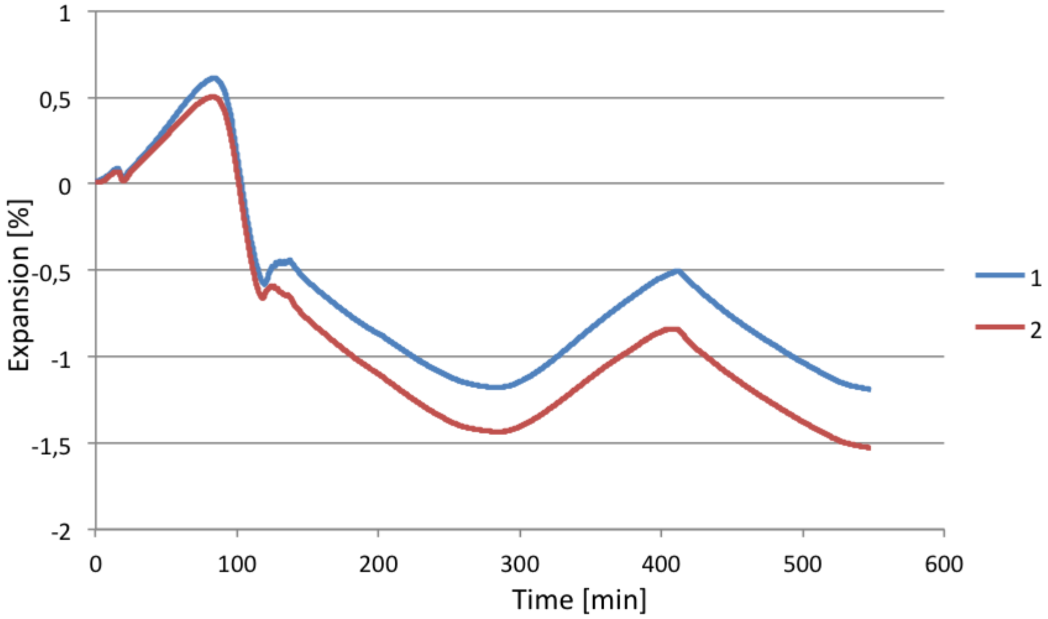

Figure F.3: The two TMA runs of A11 calcined at 800 °C.

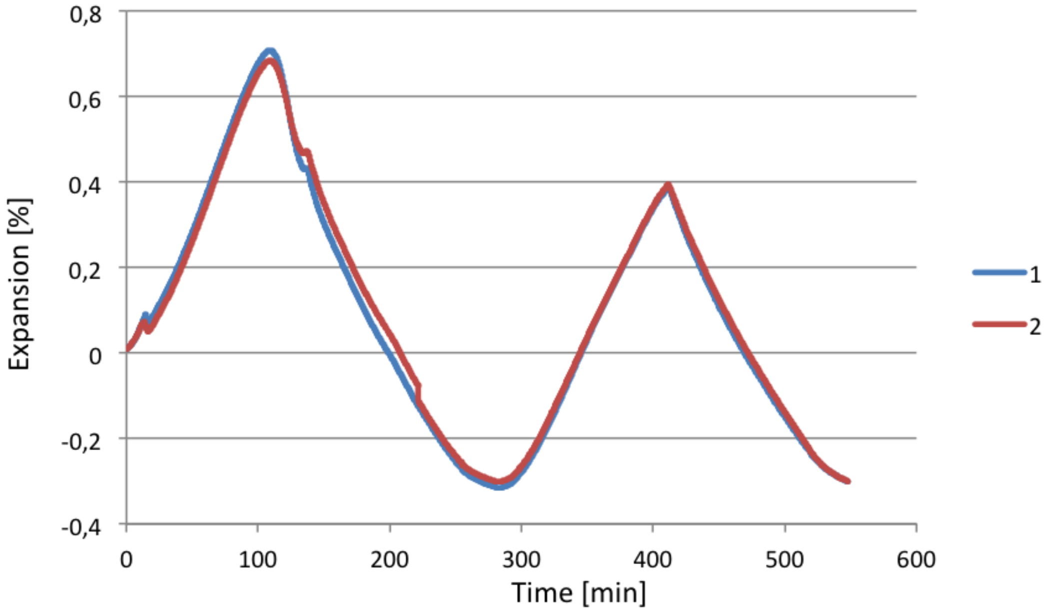

Figure F.4: The two TMA runs of A11 calcined at 1000 °C.

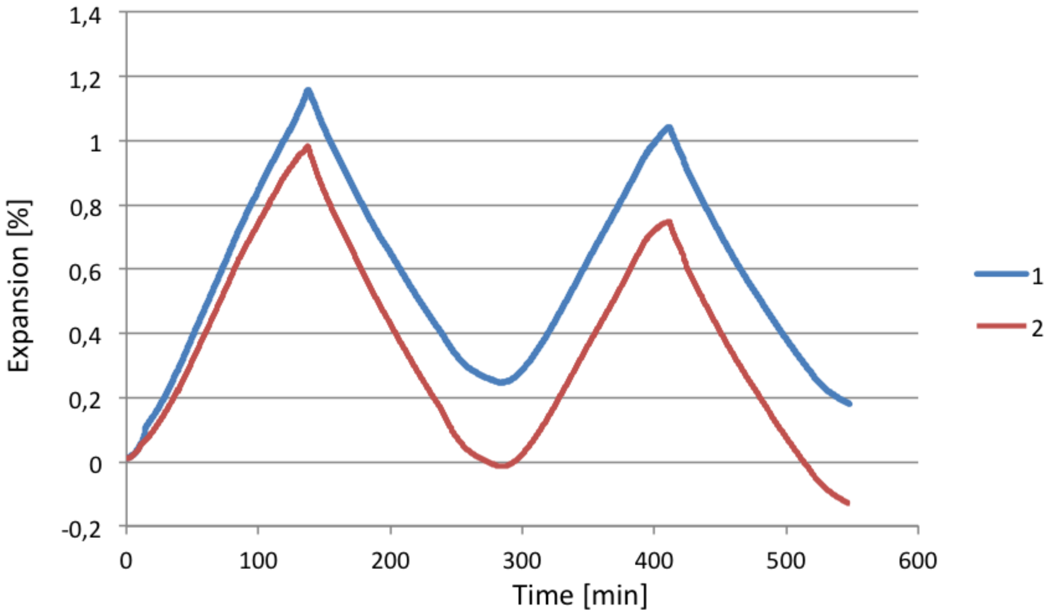

Figure F.5: The two TMA runs of A11 calcined at 2000 °C.

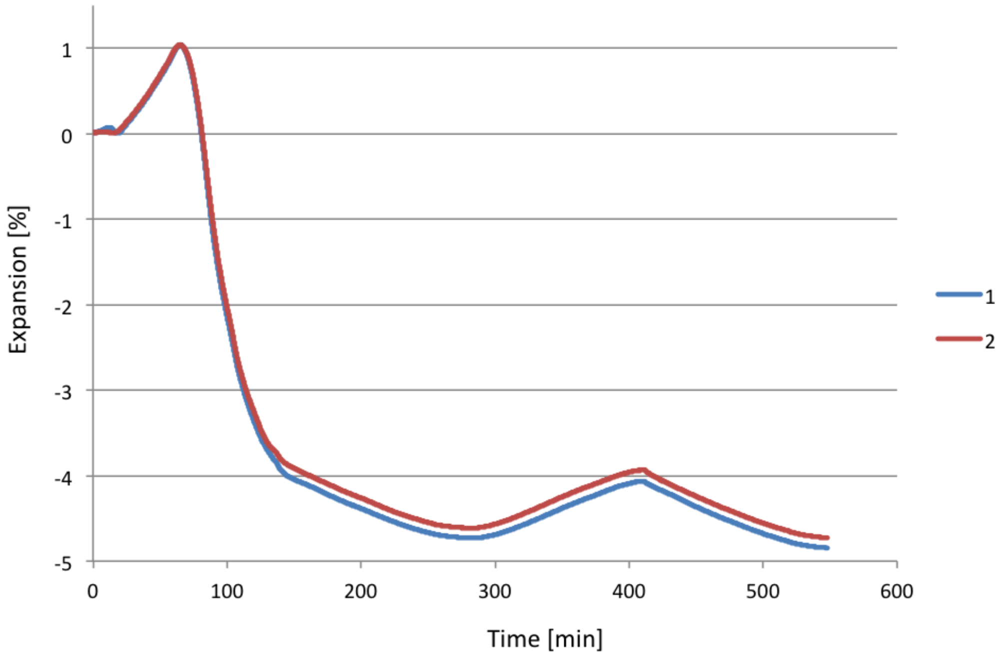

Figure F.6: The two TMA runs of the non-calcined A19.

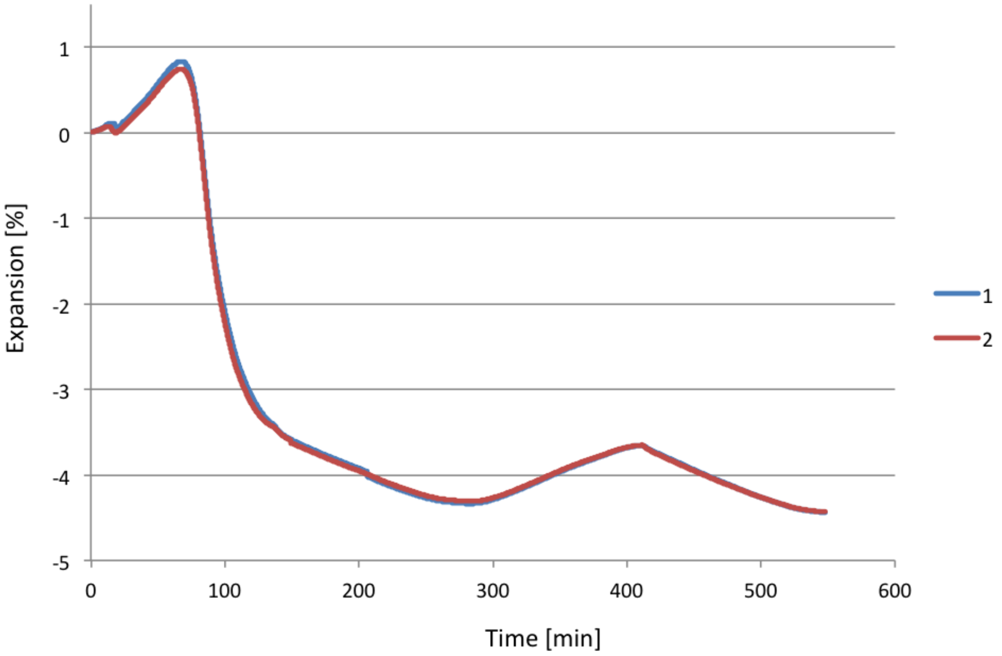

Figure F.7: The two TMA runs of A19 calcined at 600 °C.

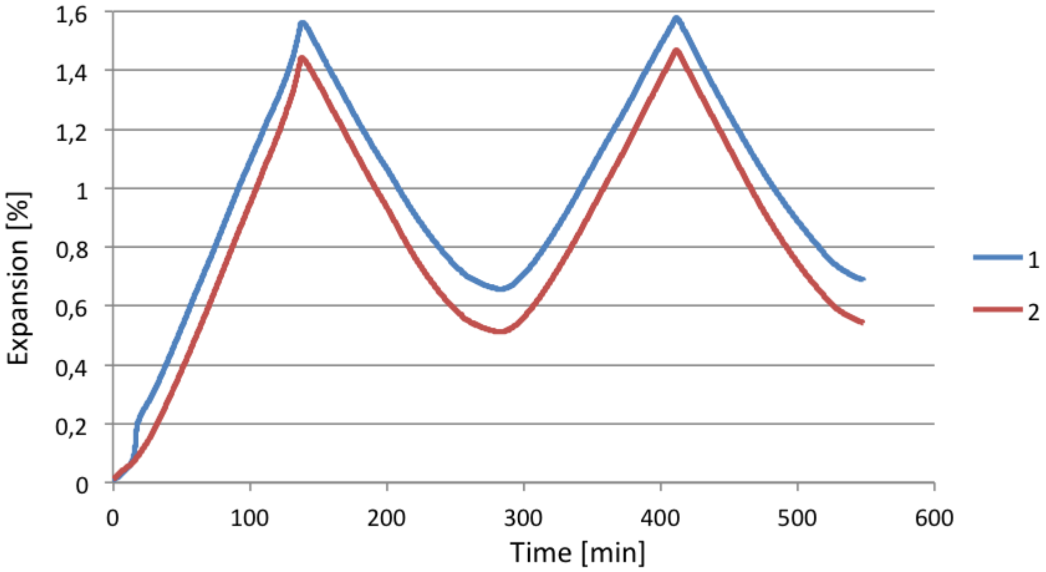

Figure F.8: The two TMA runs of A19 calcined at 1800 °C.

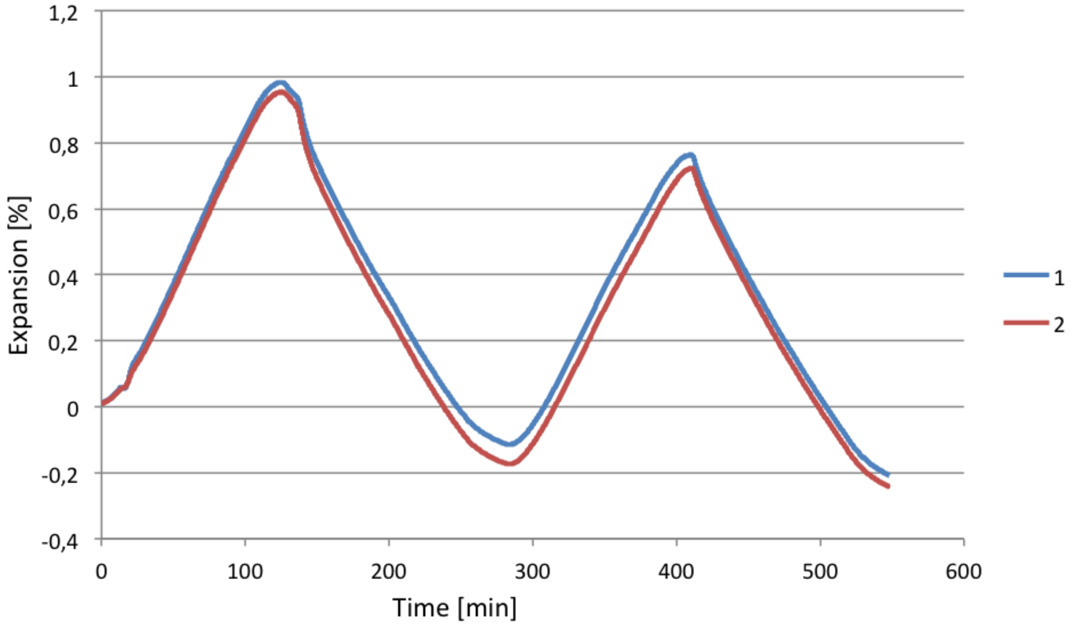

Figure F.9: The two TMA runs of C3.

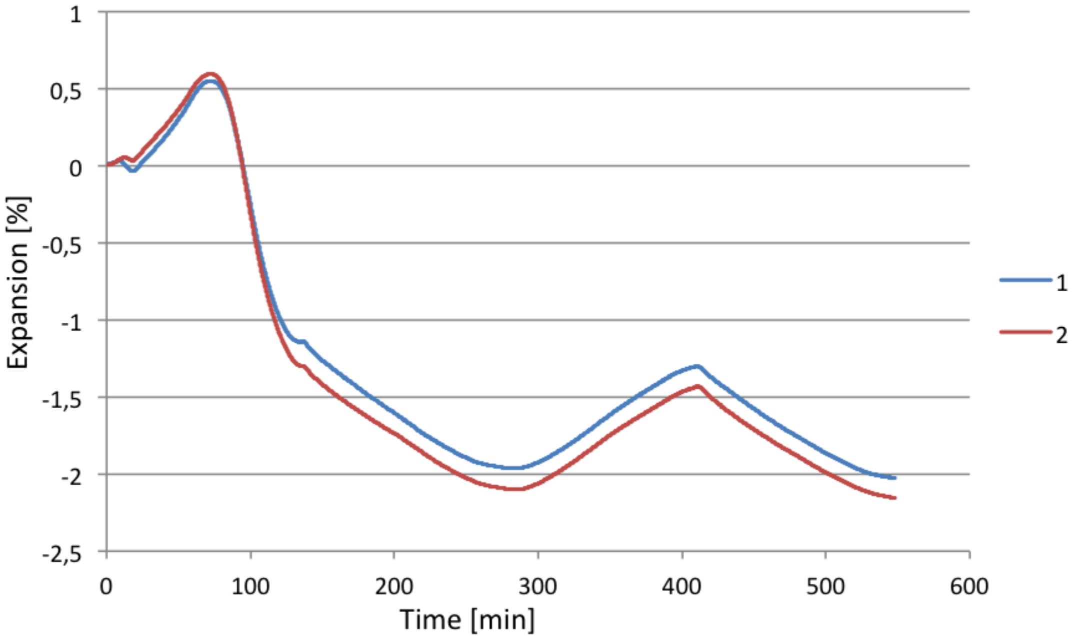

Figure F.10: The two TMA runs of C7.

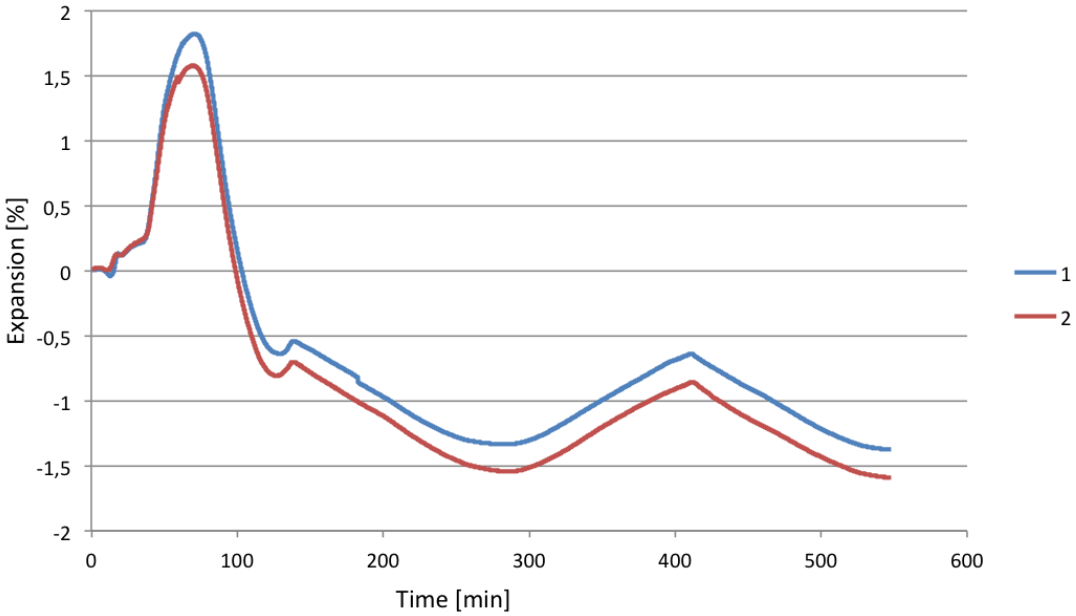

Figure F.11: The two TMA runs of BIO.

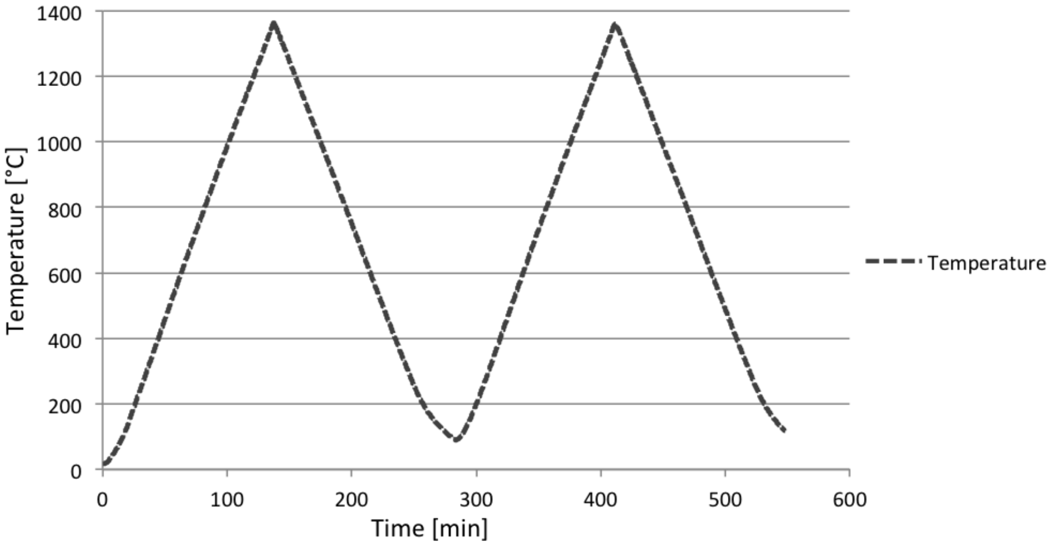

Figure F.12: The temperature profile of the TMA runs.

Appendix G

Thermogravimetric Results from Elite Tube Furnace

The unsmoothened thermogravimetric data from the heating of A11, C7 and BIO to 1500 °C in the Elite tube furnace can be seen in Figure G.1. The curved show a lot of noise for the Elite tube furnace.

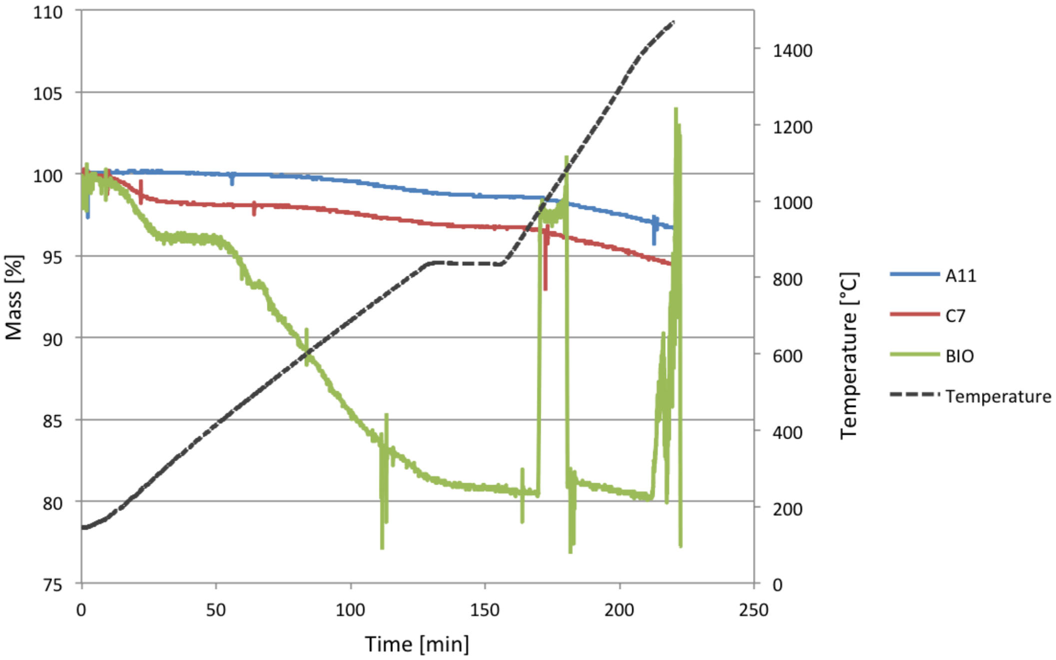

Figure G.1: The unsmoothened thermogravimetric results of A11, C7 and BIO from the Elite tube furnace heated to 1500 °C.

Appendix H

Experimental Data from Gas Chromatograhpy with Mass-Spectroscopy

Table H.1 through H.9 give the retention times, peak heights and peak areas for CO_2 obtained from the GC-MS experiments. For the peak areas given in percentage, the areas are normalized to the highest peak area for each sample.

Table H.1: Retention time, peak height and peak area obtained for CO_2 from the non-calcined A11 heated to 900 °C.

Peak	Start	RT	End	Height	Area	Area %
1	0.16	0.19	0.37	1068.13	7043.29	1.27
2	1.22	1.24	1.27	70171.14	54684.7	9.90
3	3.20	3.23	3.28	83584.89	63036.37	11.41
4	5.21	5.23	5.28	76549.74	59308.76	10.73
5	7.21	7.22	7.28	78119.68	63987.80	11.58
6	9.19	9.23	9.26	97936.31	87753.68	15.88
7	11.21	11.23	11.26	127472.47	100724.21	18.23
8	13.21	13.23	13.27	135076.41	102497.29	18.55
9	15.21	15.23	15.27	143285.32	101533.55	18.38
10	17.20	17.23	17.26	147073.92	104060.16	18.83
11	19.21	19.23	19.26	163835.08	115283.58	20.87
12	21.21	21.23	21.31	243966.93	173209.60	31.35
13	23.21	23.23	23.27	317356.16	239853.52	43.41
14	25.21	25.23	25.29	333534.59	281151.76	50.89
15	27.21	27.23	27.27	327856.32	263076.46	47.61
16	29.21	29.23	29.27	343299.48	262400.49	47.49
17	31.20	31.23	31.27	406085.61	288017.21	52.13
18	33.20	33.23	33.27	493941.60	337662.42	61.11
19	35.20	35.23	35.26	594260.19	406868.32	73.64
20	37.20	37.23	37.29	697122.51	504700.65	91.35
21	39.20	39.23	39.27	796043.51	552514.64	100.00

Table H.2: Retention time, peak height and peak area obtained for CO_2 from the non-calcined A11 heated to 1000 °C.

Peak	Start	RT	End	Height	Area	Area %
1	1.21	1.24	1.30	56064.56	50804.52	14.06
2	3.21	3.23	3.28	68047.37	50855.88	14.07
3	5.21	5.23	5.26	66747.93	51134.64	14.15
4	7.21	7.23	7.27	66188.88	48467.13	13.41
5	9.21	9.23	9.26	58130.69	47885.35	13.25
6	11.20	11.23	11.26	61451.33	45691.90	12.64
7	13.20	13.23	13.27	60629.46	54757.65	15.15
8	15.20	15.23	15.26	105415.56	73973.35	20.47
9	17.21	17.23	17.27	118976.91	101632.72	28.13
10	19.21	19.23	19.27	250667.95	171577.71	47.48
11	21.20	21.23	21.27	264139.75	234889.88	65.00
12	21.65	21.70	21.72	3204.48	4038.48	1.12
13	23.21	23.23	23.27	361956.12	248115.11	68.66
14	25.20	25.23	25.29	281090.37	241083.07	66.72
15	27.21	27.23	27.27	339784.75	232572.80	64.36
16	29.21	29.23	29.29	294364.07	236753.54	65.52
17	31.21	31.23	31.26	351830.21	245146.83	67.84
18	33.21	33.23	33.27	346164.84	266955.52	73.88
19	35.21	35.23	35.26	423184.13	293088.35	81.11
20	37.21	37.23	37.27	405568.49	316062.96	87.47
21	39.20	39.22	39.30	477747.82	361347.01	100.00

Table H.3: Retention time, peak height and peak area obtained for CO_2 from A11 calcined at 600 °C heated to 1000 °C.

Peak	Start	RT	End	Height	Area	Area %
1	0.10	0.24	0.44	3541.16	35982.53	4.92
2	1.20	1.24	1.28	77645.24	69509.01	9.51
3	3.21	3.23	3.28	72714.10	63528.04	8.69
4	5.21	5.23	5.27	168560.93	120886.07	16.53
5	7.21	7.23	7.28	182189.5	143027.02	19.56
6	9.21	9.23	9.27	175966.48	131679.74	18.01
7	11.20	11.23	11.27	151899.55	114869.30	15.71
8	13.21	13.23	13.27	141611.65	105833.25	14.47
9	15.22	15.23	15.30	178870.07	131781.30	18.02
10	17.21	17.23	17.27	198553.04	155264.16	21.23
11	19.20	19.23	19.30	249806.00	180880.88	24.74
12	21.21	21.23	21.27	258903.98	206168.42	28.19
13	23.20	23.23	23.27	322622.77	226750.29	31.01
14	25.21	25.23	25.26	293153.52	236503.56	32.34
15	27.20	27.23	27.27	367946.39	256522.07	35.08
16	29.21	29.23	29.27	350554.01	296695.52	40.57
17	31.21	31.23	31.27	533775.09	371080.58	50.75
18	33.21	33.23	33.29	546138.41	475357.14	65.01
19	35.21	35.23	35.27	861343.87	594160.38	81.25
20	37.20	37.23	37.27	804920.78	695239.74	95.08
21	39.21	39.23	39.28	875154.14	731237.74	100.00

Table H.4: Retention time, peak height and peak area obtained for CO_2 from the non-calcined A19 heated to 900 °C.

Peak	Start	RT	End	Height	Area	Area %
1	0.11	0.21	0.72	7380.66	112266.03	7.53
2	1.22	1.24	1.28	99100.43	77812.54	5.22
3	3.21	3.23	3.28	109649.25	87056.70	5.84
4	5.21	5.23	5.27	103135.62	88145.28	5.91
5	7.21	7.23	7.29	118583.26	107749.86	7.22
6	9.19	9.23	9.27	121198.94	107516.91	7.21
7	11.21	11.23	11.27	134638.92	108824.44	7.29
8	13.21	13.23	13.27	149750.88	112357.49	7.53
9	15.20	15.23	15.26	167227.92	124474.54	8.34
10	17.21	17.23	17.27	206992.11	150628.47	10.10
11	19.20	19.23	19.26	323424.65	236770.63	15.87
12	21.20	21.23	21.28	430440.31	333620.54	22.36
13	23.21	23.23	23.29	577224.06	477464.04	32.00
14	25.20	25.23	25.27	616551.25	541380.96	36.29
15	27.21	27.23	27.27	652724.01	528659.06	35.44
16	29.21	29.23	29.27	732535.18	558004.42	37.40
17	31.21	31.23	31.27	1000622.38	722611.58	48.44
18	33.20	33.23	33.27	1380028.56	984409.77	65.98
19	35.20	35.23	35.27	1758536.35	1265902.52	84.85
20	37.20	37.23	37.29	1974097.16	1491904.48	100.00
21	39.20	39.23	39.27	1933800.10	1383285.55	92.72

Table H.5: Retention time, peak height and peak area obtained for CO_2 from the non-calcined A19 heated to 1000 °C.

Peak	Start	RT	End	Height	Area	Area %
1	0.13	0.22	0.54	3582.81	41201.39	5.8
2	1.20	1.24	1.28	80513.84	75788.18	10.67
3	3.21	3.23	3.29	91086.55	74857.26	10.54
4	5.20	5.23	5.26	116716.33	85877.94	12.09
5	7.21	7.23	7.27	130338.63	94981.73	13.37
6	9.21	9.23	9.27	120333.61	95443.28	13.44
7	11.21	11.23	11.27	128287.72	93163.68	13.12
8	13.21	13.23	13.27	121366.13	99388.18	13.99
9	15.20	15.23	15.26	153359.61	110783.21	15.6
10	17.21	17.23	17.27	181044.49	153278.78	21.58
11	19.20	19.23	19.27	316823.19	223191.75	31.42
12	21.21	21.23	21.27	385606.89	317126.19	44.64
13	23.20	23.23	23.27	518768.57	356185.17	50.14
14	25.21	25.23	25.27	426745.89	364334.55	51.29
15	27.20	27.23	27.27	504992.69	347426.89	48.91
16	29.21	29.23	29.28	418684.63	362333.88	51.01
17	31.20	31.23	31.27	656053.34	453906.26	63.9
18	33.21	33.23	33.29	736214.16	596399.07	83.96
19	35.21	35.23	35.27	1028410.74	710345.04	100
20	37.21	37.23	37.29	570692.25	480042.62	67.58
21	39.20	39.22	39.30	620086.61	481027.86	67.72

Table H.6: Retention time, peak height and peak area obtained for CO_2 from A11 calcined at 600 °C heated to 1000 °C.

Peak	Start	RT	End	Height	Area	Area %
1	0.13	0.23	0.42	1589.74	12914.22	3.39
2	1.22	1.24	1.28	53051.70	44419.62	11.64
3	3.21	3.23	3.23	50485.91	39480.30	10.35
4	5.21	5.23	5.27	67798.82	52746.08	13.83
5	7.20	7.23	7.26	94900.60	67555.82	17.71
6	9.21	9.23	9.27	87102.66	73101.19	19.16
7	11.22	11.23	11.26	110581.48	78447.01	20.56
8	13.21	13.23	13.27	107099.33	88241.89	23.13
9	15.22	15.23	15.26	150256.41	104774.47	27.46
10	17.21	17.23	17.27	167402.01	143248.46	37.55
11	19.21	19.23	19.27	244437.63	170537.43	44.7
12	21.19	21.23	21.26	221278.79	194241.48	50.91
13	23.20	23.23	23.27	295741.26	204186.68	53.52
14	25.21	25.23	25.31	244895.32	209880.46	55.01
15	27.20	27.23	27.27	329386.71	227392.22	59.6
16	29.21	29.23	29.29	318407.83	264194.55	69.25
17	31.21	31.23	31.27	460627.73	320861.53	84.1
18	33.21	33.23	33.27	478546.07	381508.37	100.00
19	35.20	35.23	35.27	398668.60	279356.40	73.22
20	37.21	37.23	37.28	436027.88	341351.36	89.47
21	39.20	39.22	39.27	454487.67	338886.24	88.83

Table H.7: Retention time, peak height and peak area obtained for CO_2 from C3 heated to 1000 °C.

Peak	Start	RT	End	Height	Area	Area %
1	0.11	0.24	0.61	4319.40	59171.52	5.32
2	1.22	1.24	1.30	72982.99	67957.60	6.11
3	3.21	3.23	3.29	86361.69	68621.36	6.17
4	5.21	5.23	5.27	83154.46	63455.20	5.71
5	7.21	7.23	7.29	82096.98	61649.17	5.54
6	9.21	9.23	9.27	79331.59	62613.42	5.63
7	11.21	11.23	11.30	88593.59	66102.84	5.94
8	13.20	13.23	13.27	87122.87	70892.11	6.37
9	15.20	15.23	15.31	105008.12	80145.86	7.21
10	17.20	17.23	17.26	151807.18	125841.38	11.31
11	19.20	19.23	19.27	477740.49	335739.33	30.19
12	21.21	21.23	21.26	427046.14	367149.91	33.01
13	23.21	23.23	23.27	490147.33	342135.99	30.76
14	25.19	25.23	25.26	382452.53	331311.55	29.79
15	27.20	27.23	27.27	512658.68	354715.06	31.89
16	29.21	29.23	29.28	458231.30	398751.39	35.85
17	31.20	31.23	31.27	760785.31	525749.18	47.27
18	33.21	33.23	33.29	835331.22	689060.18	61.95
19	35.20	35.23	35.27	1167239.28	807567.64	72.61
20	37.21	37.23	37.31	1125640.79	962695.36	86.55
21	39.21	39.22	39.30	1431859.95	1112250.52	100.00

Table H.8: Retention time, peak height and peak area obtained for CO_2 from C7 heated to 1000 °C.

Peak	Start	RT	End	Height	Area	Area %
1	0.15	0.26	0.31	1107.97	6698.43	1.36
2	1.22	1.24	1.28	61391.07	50374.30	10.20
3	3.21	3.23	3.28	62289.99	47478.38	9.61
4	5.21	5.23	5.26	66208.10	53071.98	10.74
5	7.21	7.23	7.26	140699.88	98301.77	19.90
6	9.21	9.23	9.27	121299.05	102274.07	20.70
7	11.21	11.23	11.26	143741.63	99455.11	20.13
8	13.21	13.23	13.26	117102.19	100927.32	20.43
9	15.21	15.23	15.26	154071.65	107530.82	21.77
10	17.21	17.22	17.29	149433.09	132906.39	26.91
11	19.21	19.23	19.27	275344.06	191999.96	38.87
12	21.21	21.22	21.27	289299.49	243093.77	49.21
13	23.20	23.23	23.27	371681.08	256955.03	52.02
14	25.21	25.23	25.27	330555.09	262156.04	53.07
15	27.20	27.23	27.27	378091.57	264759.32	53.60
16	29.21	29.23	29.30	353494.02	270555.28	54.77
17	31.21	31.23	31.27	412716.27	288031.50	58.31
18	33.21	33.23	33.28	453405.66	341134.69	69.06
19	35.21	35.23	35.27	589451.86	421078.62	85.24
20	37.21	37.23	37.30	649358.52	490934.85	99.38
21	39.20	39.22	39.28	671707.59	493978.96	100.00

Table H.9: Retention time, peak height and peak area obtained for CO_2 from BIO heated to 1000 °C.

Peak	Start	RT	End	Height	Area	Area %
1	0.10	0.26	0.96	8662.57	160609.36	6.37
2	1.20	1.24	1.28	75282.78	74903.24	2.97
3	3.20	3.23	3.29	70819.50	65064.21	2.58
4	5.21	5.23	5.27	89921.96	72239.03	2.87
5	7.21	7.23	7.29	119653.52	95788.17	3.80
6	9.21	9.23	9.27	161882.24	128799.29	5.11
7	11.20	11.23	11.30	247823.14	191183.79	7.59
8	13.21	13.23	13.27	387566.00	307912.76	12.22
9	15.20	15.23	15.28	613352.04	455381.19	18.07
10	17.21	17.23	17.27	1109051.19	899587.87	35.71
11	19.20	19.23	19.27	1973279.81	1433341.63	56.89
12	21.19	21.23	21.27	1669859.47	1429440.64	56.74
13	23.20	23.23	23.27	1993130.43	1437512.11	57.06
14	25.19	25.23	25.27	1809587.86	1560807.93	61.95
15	27.21	27.23	27.27	2402734.69	1727363.42	68.56
16	29.21	29.23	29.31	2213982.48	1910805.26	75.84
17	31.21	31.23	31.27	2907076.81	2104476.13	83.53
18	33.21	33.23	33.31	2741080.76	2284019.25	90.66
19	35.21	35.23	35.27	3452561.17	2519461.41	100.00
20	37.21	37.23	37.31	2393639.99	1971277.04	78.24
21	39.20	39.22	39.30	2065951.16	1632518.11	64.80